The Dissertation Committee for Caleb Tyler Alexander Certifies that this is the approved version of the following dissertation:

Perovskite Oxides for Metal-Air Batteries and Pseudocapacitor Applications

Committee:

Keith P. Johnston Supervisor

Keith J. Stevenson, Co-Supervisor

Delia Milliron

Gyeong Hwang

Perovskite Oxides for Metal-Air Batteries and Pseudocapacitor Applications

by

Caleb Tyler Alexander

Dissertation

Presented to the Faculty of the Graduate School of

The University of Texas at Austin

in Partial Fulfillment

of the Requirements

for the Degree of

Doctor of Philosophy

The University of Texas at Austin

May 2019

Dedication

To God for His works and what He has done in my life. I am not the man I used to be.

Acknowledgements

There were so many brilliant scientists involved in the development of this work. Firstly, I would like to thank Dr. Keith Stevenson for his unwavering support, intellectual discussions from across the world, inspiring me to do great work and constant dedication to his students even to his group's black sheep (the lone chemical engineer :P). I would also like to thank Dr. Keith Johnston for challenging me to grow where I was weak with the journal clubbing sessions and for the intellectual freedom and support to do great work.

There are also many graduate students I would like to thank as well. First, I would like to thank Dr. Tyler Mefford and Dr. William Hardin for mentoring me and being my friends. They were dearly missed after they graduated and moved on to greener pastures. I would also like to thank Himmi Nallan, Olja Simoska, Angela Chen, Dr. Ehsan Morasi, Bezhad Chang, Dr. Robin Forslund, Dr. Amro Elhad, Dr. Andrew Worthen, Dr. Bobby Stover, Dr. Jessica Hung, Dr. Bart Dear, Amjad Chowdhury, Shehab Alzobaidi, Dr. Mohammad Iqbal, Dr. Sudipta Gupta, and Chang Da for being my friends and colleagues during my time in graduate school.

Abstract

Perovskite Oxides for Metal-Air Batteries and Pseudocapacitor Applications

Caleb Tyler Alexander, Ph. D.

The University of Texas at Austin, 2019

Supervisors: Keith P. Johnston, Keith J. Stevenson

Wind and solar energy's rapid development has created a significant need for low-cost energy storage to enable renewables at grid level. To meet these challenges, metal-air batteries and fuel cells are being considered for base-load energy storage while high power applications like frequency regulation and uninterruptable power supplies (UPS) can be addressed using high energy pseudocapacitors. The major bottleneck to metal-air battery and fuel cell commercialization is the sluggish oxygen reactions at the positive electrode that are industrially catalyzed using expensive precious metal catalysts like Pt and IrO_2. Here, the aim is to replace precious metal-catalysts with low-cost $LaNiO_3$ perovskites and N-doped CNTs in alkaline conditions and study their synergistic interactions and composite stability. The work is continued by studying the anion-intercalation pseudocapacitance in a perovskite oxide library with composition $La_{1-x}Sr_xBO_{3-\delta}$ (B = Mn, Fe, Co; $0 \leq x \leq 1$) and found that increasing oxygen vacancy content universally increases the pseudocapacitance while the B-site element controlled the redox potential. The most pseudocapacitive materials were then used to make the first all perovskite asymmetric pseudocapacitors with a maximum energy density of 31 Wh kg^{-1}. This work was followed by using the principles learned to further extent the redox

voltage potential difference using $LaNi_{1-x}Fe_xO_{3-\delta}$ and brownmillerite-$SrFeO_{2.5}$ to make an asymmetric pseudocapacitor. Doing this, the redox discharge potential was pushed all the way to 1.1 V which is the highest asymmetric pseudocapacitor discharge peak potential reported to date.

Table of Contents

List of Tables

List of Figures

List of Illustrations

Chapter 1: Introduction

According to the UN climate change report released in early 2019, humanity needs to cut its CO_2 emissions from 40 $Gton_{CO2}$ yr^{-1} to 20 $Gton_{CO2}$ yr^{-1} by 2030 and down to net-zero carbon emissions by 2050 to avoid global climate change's worst effects.[1] Humanity's power demand was 19.4 TW (170,000 TWh yr^{-1}) in 2015 and is projected to grow to 24.8 TW (217,600 TWh yr^{-1}) by 2040.[2] Due to this enormous size, a truly global scale infrastructure change is going to be required to hit these emissions targets. The good news is that wind and solar power production are each growing exponentially[3] as shown in Figure 1.1.

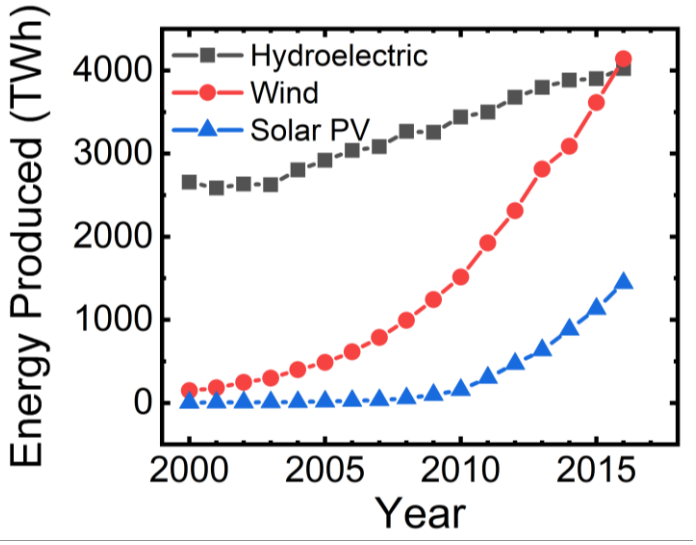

Figure 1.1 | Global renewable energy production over time.[3]

The main challenge to maintain and encourage this exponential growth is solar and wind's intermittency thus requiring low-cost, long lasting energy storage. Hydroelectric dams are an efficient way of storing excess wind and solar energy, but there are only so many rivers that can be dammed to store energy, not to mention the damage to local environments. Electrochemical energy storage (e.g. batteries and supercapacitors) could be a scalable solution to tackle the intermittency challenge.

Electrochemical energy storage involves extracting and storing energy using chemicals *and* electrons that allow it to avoid the thermodynamic efficiency limitations that a heat engine would have and thus allow for high efficiencies. The thermodynamic efficiency of any electrochemical energy reaction is given in equation 1 as:[4]

$$\eta = \frac{\Delta G_{rxn}}{\Delta H_{rxn}} \quad (1)$$

where η is the energy efficiency, ΔG_{rxn} is the Gibbs free energy of reaction and ΔH_{rxn} is the enthalpy of reaction. Depending on the redox reactions chosen and cell operation conditions the efficiencies can be on the order of 50-95%.

1.1 Electrochemical Energy Storage

The total energy that can be stored electrochemically (U [Wh kg^{-1}]) is given by equation 2:

$$U = QV_{cell} \quad (2)$$

where Q is the charge stored per unit mass and V_{cell} is the voltage difference (e.g electric potential difference) between electrodes. Voltage is also referred to as an electrical potential because it corresponds to the *potential* for each electron to carry energy. More simply, the cell voltage is the amount of energy each charge carries so by multiplying the cell voltage by the total charge carried yields the total energy stored.

"Energy" is a rather abstract concept and it is difficult to determine the *absolute* amount of energy contained in something, but it is far easier to tell the energy difference of one state relative to an arbitrary reference state like when we can tell if the weather gets hotter or colder. Similarly, different electrochemical (redox) reactions have unique standard reduction equilibrium potentials (E^o) that can be measured relative to a reference electrode (R.E.). Redox reactions are written by convention as a reduction reaction according to equation 3:

$$Ox + n * e^- \leftrightarrow Red \;\; E^o vs\; R.E. \quad (3)$$

where *Ox* is an oxidized species, *n* is the number of electrons transferred per mole of reaction and *Red* is the reduced species. The reference state is typically defined as when all involved species have an activity (a_i) or partial pressure (P_i) equal to 1 M or 1 atm respectively in water.

A common reference electrode that E^o can be reported relative to is the Standard Hydrogen Electrode (SHE) that is the hydrogen reaction:

$$2H^+ + 2e^- \leftrightarrow H_2 \quad E^o_{H^+/H_2} \equiv 0.000\ V\ vs\ SHE \tag{4}$$

where the reference pressure and concentration are 1 bar and 1 M H^+ (pH=0) for all temperatures and pH values. The normal hydrogen electrode (NHE) is the same as SHE except the reference pressure is 1 atm and E^o values are more commonly reported relative to NHE than SHE for convenience.[5] The change in a redox reaction's equilibrium potential (E; e.g. "Nernst potential") caused by the relative species not being at unit activity is governed by the Nernst equation:[5]

$$E = E^o - \frac{RT}{nF}\ln(\frac{[red]}{[ox]}) \tag{5}$$

where *R* is the ideal gas constant (8.314 J $mol^{-1}K^{-1}$), *T* is the temperature (K), *n* is the number of electrons transferred per mole of reaction, *F* is the Faraday constant (96485 C/mol e^-), [*red*] is the activity (or concentration for dilute) reduced species, and [*ox*] is the oxidized species' activity. For example, the Regular Hydrogen Electrode (RHE) is a convenient reference electrode (with P_{H2} = 1 atm) that adjusts for the solution pH according to equations 6-8:

$$E_{RHE} = E^o_{H^+/H_2} - \frac{RT}{2F}\ln\left(\frac{P_{H_2}=1}{[H^+]^2}\right) \tag{6}$$

$$E_{RHE} = 0.000V + \frac{2.303RT}{F}log_{10}([H^+]) \tag{7}$$

$$E_{RHE} = -\frac{2.303RT}{F}pH\ \ V\ vs\ NHE \tag{8}$$

RHE is a very convenient reference to use when working with redox reactions that are pH dependent like the oxygen evolution and reduction reaction (OER/ORR). Because the pH redox potential dependence is the same in RHE, the equilibrium potential versus RHE will be constant at all pH values. More practical reference electrodes that don't require saturating the electrolyte with H_2 are Hg/HgO (1 M KOH) for alkaline solutions, and Ag/AgCl (saturated KCl) and Hg/HCl (SCE; saturated KCl) for neutral and acidic solutions.[6] A common reference electrode for studying batteries is the Li^+/Li (E^o = -3.04 V vs NHE) couple in an organic electrolyte with 1 M Li^+.

A potentiostat can control the applied potential to the working electrode and study the various redox reactions of interest. If an applied potential is lower than the redox reaction's Nernst potential, E, then the reduction reaction would dominate, and electrons would be *donated* to solution. Conversely, if the applied potential is above the redox reaction's Nernst potential then the oxidation reaction would dominate, and electrons would be *taken* from solution. The number of possible electrode combinations is immense, and a summary various electrochemical energy storage technologies' performance is shown in Figure 1.2

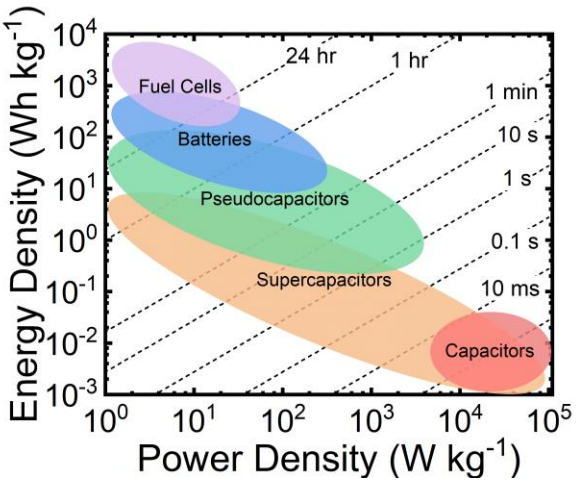

Figure 1.2 | Ragone plot of various electrochemical energy storage technologies.

1.2 Battery, Supercapacitor and Pseudocapacitor Characteristics

1.2.1 Batteries and Fuel Cells

The fundamental charge storage mechanism in batteries and fuel cells involves faradaic charge transfer where charge is transferred across the double layer at the electrode-electrolyte interface. For example, $Li_{1-x}CoO_2$ lithiation to $LiCoO_2$ given as:

$$Li_{1-x}CoO_2 + xLi^+ + e^- \leftrightarrow LiCoO_2 \quad E^o \sim 3.4\ V\ vs\ Li/Li^+ \tag{9}$$

is a faradaic reaction that serves as the positive electrode in our cell phones. For a conversion reaction like equation 9, the potential can be expressed at a function of filled site fraction (θ) as:[7,8]

$$E = 3.4\ V - \frac{RT}{nF}\ln\left(\frac{\theta}{1-\theta}\right)\ V\ vs\ Li/Li^+ \tag{10}$$

The theoretical amount of charge that a battery or fuel cell reaction can hold is given by:[7]

$$Q = \frac{nF}{m} \tag{11}$$

where m is the molecular weight of the species involved in the redox reaction. This suggests that the reactants and products of the reactions should have a low molecular weight to increase the device's energy density which is illustrated graphically as the shaded region in Figure 1.3.

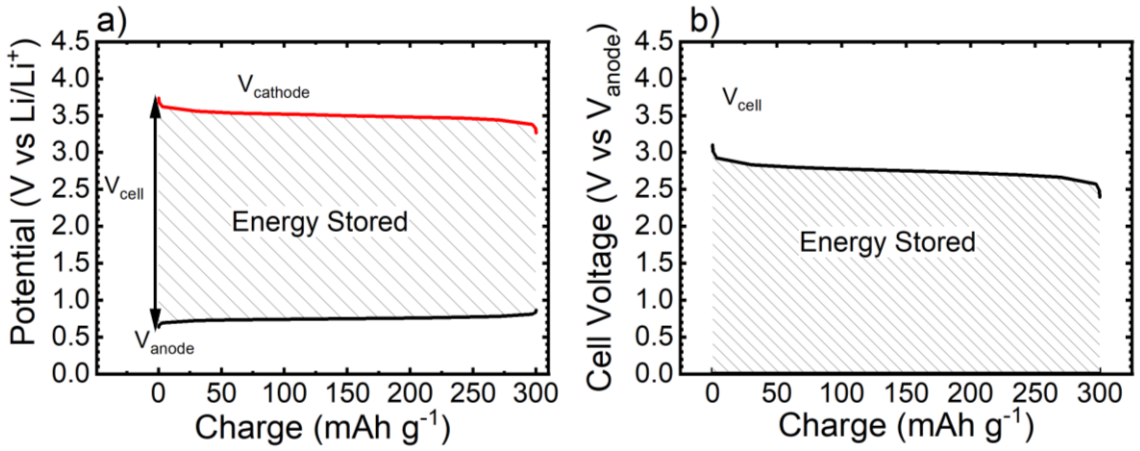

Figure 1.3 | Energy stored electrochemically in a battery.

A battery discharge reaction is shown with (a) the cathode and anode potentials in a three-electrode configuration and alternatively as (b) the cell voltage versus the charge output. The shaded regions represent the total energy the device stores.

Faradaic processes involving charge transfer across the electrode-electrolyte interface are typically accompanied by phase transitions, diffusion limitations and side reactions. These limitations tend to make charge transfer irreversible (or slow) such that they require a large overpotential to achieve significant current densities. Diffusion limitations are typically observed when the measured current (i) is proportional to the square root of the potential scan rate, υ, ($i \sim \upsilon^{0.5}$).[5]

1.2.2 Electrical Double Layer Capacitors (EDLCs) and Supercapacitors

In contrast to faradaic processes, energy can also be stored in capacitors via non-faradaic processes. In a classic parallel plate capacitor, two metal plates are separated by a dielectric material with a relative dielectric constant (ε) separated by a distance (d) that is typically on the order of 50 μm as shown in Illustration 1.1a.

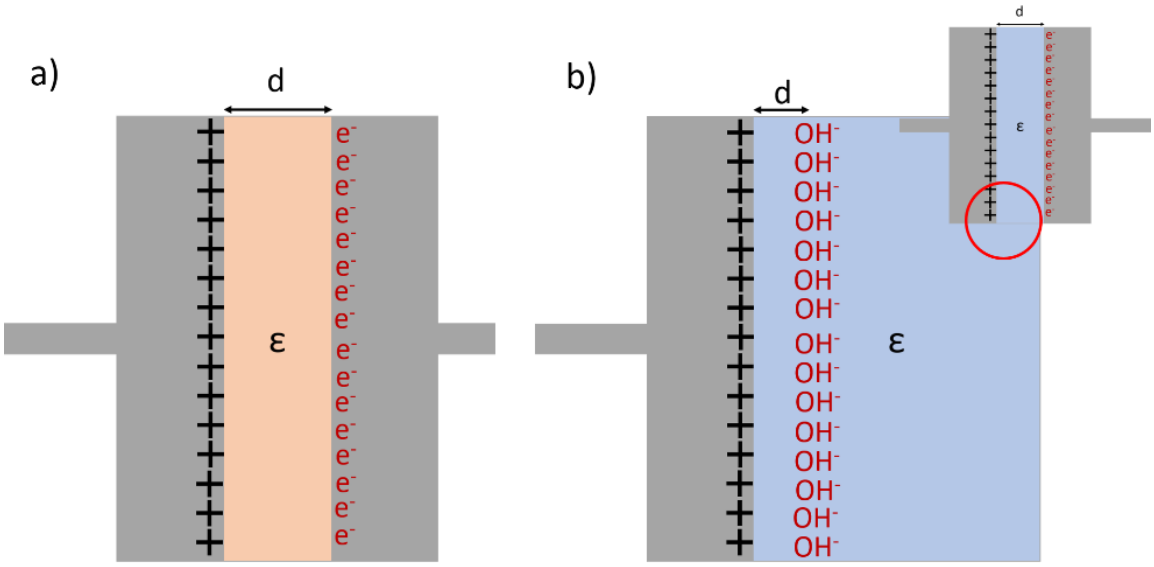

Illustration 1.1 | Capacitor schematic design.

A schematic is given for a (a) parallel plate capacitor and a (b) supercapacitor.

Applying a potential (V_{cell}) between the metal plates in Illustration 1.1a causes charge to accumulate in the form of a capacitance due to electrostatics that is represented as:

$$C = \frac{\varepsilon\varepsilon_o A}{d} = \frac{\Delta Q}{\Delta V} \tag{12}$$

where ε_o is the permittivity of free space (8.85 x 10^{-12} F m^{-1}) and A is the area of the electrode-dielectric interface. The amount the charge separation distance, d, can be reduced in a parallel plate capacitor is limited due to mechanical considerations and dielectric break down. However, if the dielectric is a liquid electrolyte then the charge separation distance can be shrunk down to the order of nanometers in the electric double layer as shown in Illustration 1.1b which increases the capacitance by several orders of magnitude. This kind of capacitor is called an electric double layer capacitor (EDLC) or a supercapacitor for short. The non-faradaic nature of EDLCs result in their current being linearly proportional to the potential scan rate ($i \sim \upsilon^1$).[5,7]

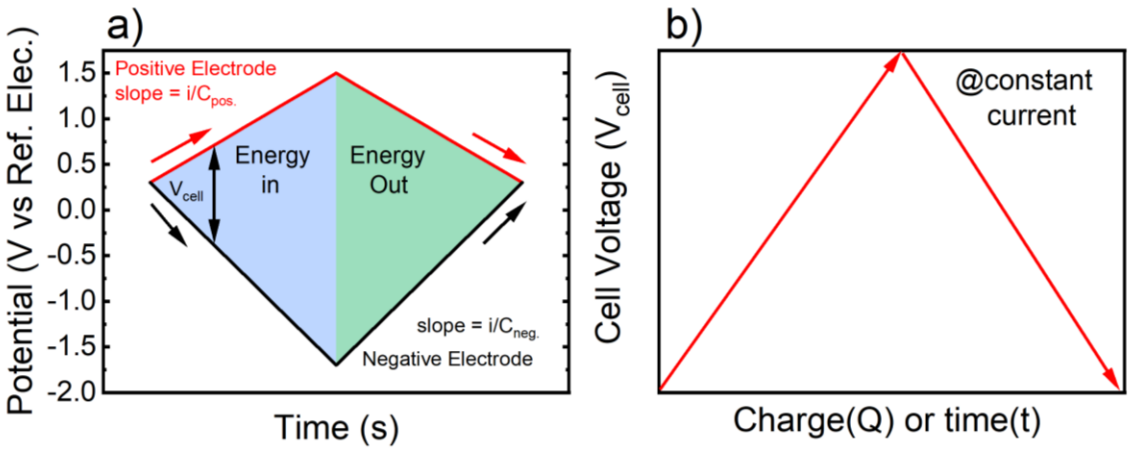

Figure 1.4 | Supercapacitor Charge-Discharge Characteristics.

A constant current, i, applied to a supercapacitor with its potential-time (or charge) plots shown in a (a) three-electrode configuration and (b) two-electrode configuration.

Typical supercapacitors are made using high surface area carbons to maximize their specific capacitance ($\hat{C}$) and therefore stored charge.[9,10] The energy density of a capacitor is given by:

$$U = \frac{1}{2}\hat{C}V_{cell}^2 \tag{13}$$

with an example of the stored energy and electrode potentials during operation shown in Figure 1.4. Equation 13 shows that a supercapacitor's energy density increases with the square of the cell voltage so developing strategies to increase V_{cell} is a good strategy to increase the energy stored in a device.

Because supercapacitors store charge non-faradaically, they avoid the irreversible reactions that batteries and fuel cell experience which allows them to charge and discharge at high rates. The lack of irreversible faradaic reactions also allows supercapacitors to cycle nearly indefinitely, but also at the cost of energy density as shown in Figure 1.2 because the charge is only stored at the electrode material's surface instead of within the electrode bulk like in a battery.

1.2.3 Pseudocapacitors

Pseudocapacitors are an intermediary form of charge storage that sits between batteries and supercapacitors in that they store charge faradaically-thus allowing them to store more energy than a supercapacitor-but that charge is stored near the surface like a supercapacitor which allows them to charge and discharge much more quickly than a battery. There are four known pseudocapacitive mechanisms each of which has a potential governed by a form of equation 10, but with their own unique standard reduction potential.[7,8]

The first mechanism concerns underpotential deposition or adsorption pseudocapacitance like that of Pb on Au[11] or hydrogen on a Pt surface according to:[12,13]

$$Pt(H_2O)_x + H^+ + e^- \leftrightarrow Pt(H) + xH_2O \quad (14)$$

The second mechanism is a general redox pseudocapacitance typically at metal oxides like (MnO_2[7] and RuO_2[14]) or metal hydroxides like $Ni(OH)_2$[15] according to:

$$NiOOH + e^- + H_2O \leftrightarrow Ni(OH)_2 + OH^- \quad (15)$$

The third mechanism involves cation intercalation pseudocapacitance. For example, Li intercalation into Li_xTiS_2 behaves reversibly according to:[16]

$$Li_xTiS_2 + xLi^+ + e^- \leftrightarrow LiTiS_2 \quad (16)$$

The fourth and last mechanism is anion intercalation pseudocapacitance and was first discovered in our group for oxygen deficient $LaMnO_{3-\delta}$ in alkaline solutions according to:[17]

$$La\left[Mn^{z+}_{1-2\delta}; Mn^{(z+1)+}_{2\delta}\right]O_{3-\delta} + 2\delta e^- + \delta H_2O \leftrightarrow La[Mn^{z+}]O_3 + 2\delta OH^- \quad (17)$$

Several chapters of this dissertation are devoted to further exploring the perovskites phase space for anion intercalation pseudocapacitors.

The electrochemical characteristics for these electrochemical energy devices are summarized in Figure 1.5.

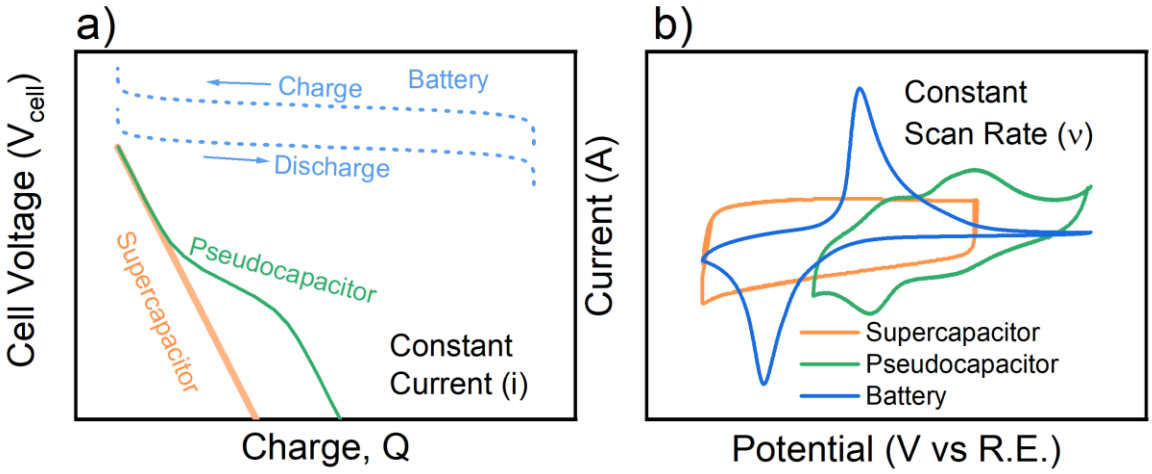

Figure 1.5 | Electrochemical behavior of batteries, supercapacitors and pseudocapacitors. The characteristic behavior of batteries, supercapacitors and pseudocapacitors are shown as (a) potential-charge plots and (b) current-potential plots.

1.3 Metal-Air Batteries and Fuel Cells

Metal-air batteries, fuel cells and water electrolysis operate according to the same basic principles as batteries except, instead of storing charge faradaically via an intercalation mechanism, their energy is stored chemically and accessed via faradaic charge transfer using electrocatalysts. Metal-air batteries and fuel cells are attractive energy storage technologies because they can store 3-5x more energy per mass than conventional Li-ion batteries.[4,18–20] In a hydrogen fuel cell or water electrolyzer, the negative electrode is the hydrogen reaction given in equation 4 above. The negative electrode for a metal-air battery is any metal that electrochemically dissolves and electroplates with Zn metal in alkaline solution being an example:

$$Zn(OH)_4^{2-} + 2e^- \leftrightarrow Zn_{(s)} + 4OH^- \; E^o_{Zn(OH)_4^{2-}/Zn} = -1.20\,V\; vs\; NHE \quad (18)$$

While metal-air batteries and fuel cells/water electrolyzers have different negative electrodes they have in common the oxygen evolution and reduction reaction (OER and ORR respectively) as their positive electrode according to:

$$O_2 + 2H_2O + 4e^- \leftrightarrow 4OH^- \; E^o_{O_2/OH^-} = 0.401\, V\, vs\, SHE\; (pH = 14) \quad (19)$$

The more convenient way of reporting the OER/ORR equilibrium potential ($E_{O2/OH-}$) is as 1.23 V vs RHE which is constant regardless of the solution pH as discussed above. Current-potential curves for the hydrogen and oxygen reaction are shown in Figure 1.6.

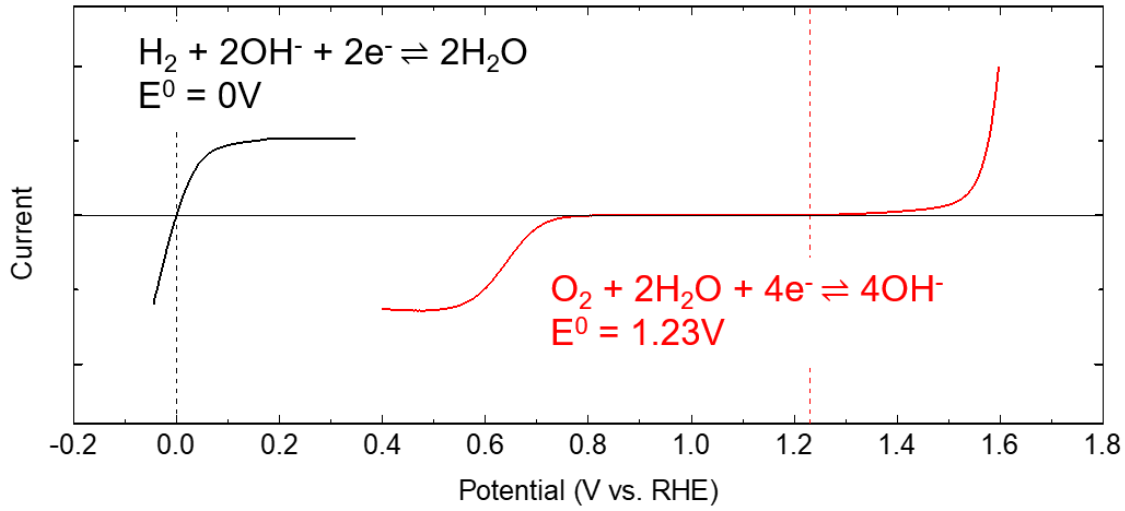

Figure 1.6 | Hydrogen and oxygen redox reactions for a H2 fuel cell and water electrolysis.

The hydrogen reaction only involves two electron and two proton transfers which makes it a relatively reversible reaction that only requires a small overpotential to get a significant current as shown in Figure 1.6. The OER/ORR is the opposite. The more elementary steps a reaction has means there are more possible energetic barriers to the net reaction proceeding quickly and reversibly. The OER/ORR involves four electron transfers and four proton transfers which results in the large overpotential for both the forward and backwards reactions as illustrated in Figure 1.6. Thus, the OER/ORR require

active electrocatalysts to lower the overpotentials and thus waste much less energy during operation.

The problem is that electrocatalysts used in industry for these reactions are precious metals like Pt, IrO_2 and RuO_2, and their high cost limits them from being commercially viable for low-cost energy storage on a global scale. However, an opportunity lies in operating these reactions in alkaline conditions where low-cost transition metals, oxides and hydroxides are thermodynamically resistant to corrosion dissolution and can be used to design active electrocatalysts. Before designing catalysts for these reactions, it would help to understand the OER and ORR mechanisms.

1.3.1 OER Mechanism

Several years ago, former students in our group proposed[21,22] and then confirmed along with others a more efficient lattice oxygen mechanism (LOM) that takes place for highly active OER electrocatalysts.[23–25] They found that designing electrocatalysts with a heavily oxidized transition metal with a high electronegativity will lower the material's Fermi energy (or highest energy electrons in a solid) until it dips into its O 2p energy band. Due to Fermi level pinning at the top of the O 2p band,[26] the Fermi energy dipping into the O 2p band makes emitting O_2 from the lattice and forming oxygen vacancies thermodynamically favorable.[23,24] Favorable oxygen vacancies formation thus allows lattice oxygen to participate in the OER mechanism with a lower energy barrier than the previously prevailing adsorbate exchange mechanism (AEM).[23–25] The LOM mechanism was suggested to follow the steps below (20-23)[23]:

$$M^{3+}\text{-}OH + M^{3+}\text{-}O^{-} + OH^{-} \rightarrow M^{3+}\text{-}O_2^{-} + M^{3+}\text{-}[V] + H_2O + e^{-} \quad (20)$$

$$M^{3+}\text{-}O_2^{-} + OH^{-} \rightarrow M^{3+}\text{-}OH^{-} + O_2 + e^{-} \quad (21)$$

$$M^{3+}\text{-}[V] + OH^{-} \rightarrow M^{3+}\text{-}OH + e^{-} \quad (22)$$

$$M^{3+}\text{-}OH + M^{3+}\text{-}OH^{-} + OH^{-} \rightarrow M^{3+}\text{-}O^{-} + M^{3+}\text{-}OH + H_2O + e^{-} \quad (23)$$

1.3.2 ORR Mechanism

In alkaline conditions, the ORR follows one of three mechanistic pathways. The first is the direct four electron path according to equation 24:

$$O_2 + 2H_2O + 4e^- \leftrightarrow 4OH^- \; E^o_{O_2/OH^-} = 1.23\, V \; vs \; RHE \qquad (24)$$

The second pathway is the two-by-two pathway where O_2 is reduced to HO_2^- which is then electrochemically reduced to OH^- with each reduction requiring two electrons according to equations 25 and 26:

$$O_2 + H_2O + 2e^- \leftrightarrow HO_2^- + OH^- \; E^o_{O_2/HO_2^-} = 0.77\, V \; vs \; RHE \qquad (25)$$

$$HO_2^- + 2e^- \leftrightarrow 3OH^- E^o_{HO_2^-/OH^-} = 1.71\, V \; vs \; RHE \qquad (26)$$

After reaction 25 proceeds, reaction 26 is still kinetically limiting despite the huge thermodynamic driving force for it at the low ORR potentials.[27] The third pathway gets around this kinetically limited electron transfer step by chemically disproportionating HO_2^- according to reaction 27:

$$2HO_2^- \leftrightarrow \; O_2 + 2OH^- \qquad (27)$$

If reaction 27 is fast enough, the regenerated O_2 will be re-reduced to form peroxides and will effectively yield a net four electron transfer.[28,29] Thus the pathway following reactions 25 and 27 is thus appropriately named the "pseudo $4e^-$ pathway".

The direct four electron pathway typically occurs on metals like Pt and its alloys while the two-by-two and pseudo $4e^-$ pathways tend to be followed by most carbons and transition metal oxides.[30,31]

1.4 PEROVSKITES

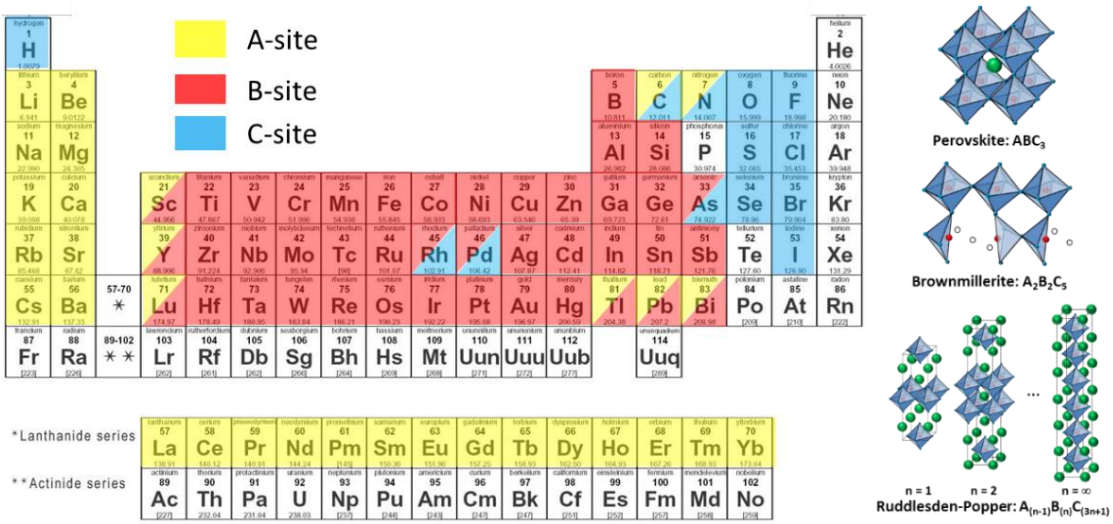

Figure 1.7 | Perovskite crystal structure, its relatives and its element utilization.

Perovskites have an ideally cubic ABC_3 primitive unit cell formula and can use approximately 90% of the periodic table, as shown in Fiugre 1.7, thus making it a useful platform to tune its properties and study various phenomenon. A lanthanide or alkali element typically sits in the A-site, while the B-site consists of transition metal elements or semimetal elements at the unit cell corners that are octahedrally coordinated by the C-sites. The C-sites are typically occupied by non-metal elements as shown in Figure 1.7. Here, perovskite oxides are studied here due to their high electrocatalytic activity[32,33], low cost, elemental versatility and simple synthesis.

Different elements in different oxidation states have different ionic radii which causes the perovskite octahedra to tilt and distort the lattice from its ideal cubic structure. These ionic size differences are related to each other through the Goldschmidt tolerance factor (t):

$$t = \frac{r_A + r_O}{\sqrt{2}(r_B + r_O)} \tag{28}$$

where r_A, r_O and r_B are the ionic radii of the A-site ion, the oxide ion and the B-site ion respectively. A perovskite takes on the ideally cubic structure with t = 1, but as t is increased it transforms into a rhombohedral (1 < t < 1.06) and hexagonal (t > 1.06) structure.[34] However, as t decreases, the cubic structure converts to a tetragonal structure followed by an orthorhombic structure from 0.7 < t < 1, but below t = 0.7 the perovskite structure becomes unstable.[34]

Perovskites' properties can be tuned as desired by strategically substituting different elements into the A and B sites. For example, replacing La^{3+} in the A-site with lower valence elements like Sr^{2+} thus leading to either the B-site transition metal oxidizing or to oxygen vacancy formation caused by electroneutrality constraints. As the oxygen vacancy content increases, the oxygen vacancies will begin to order[23] and will eventually form the Brownmillerite structure shown in Figure 1.7. Additionally, pushing the tolerance factor to deviate away from unity will decrease the M-O orbital overlap that narrows the electronic energy bands and decreases the material's electrical conductivity.

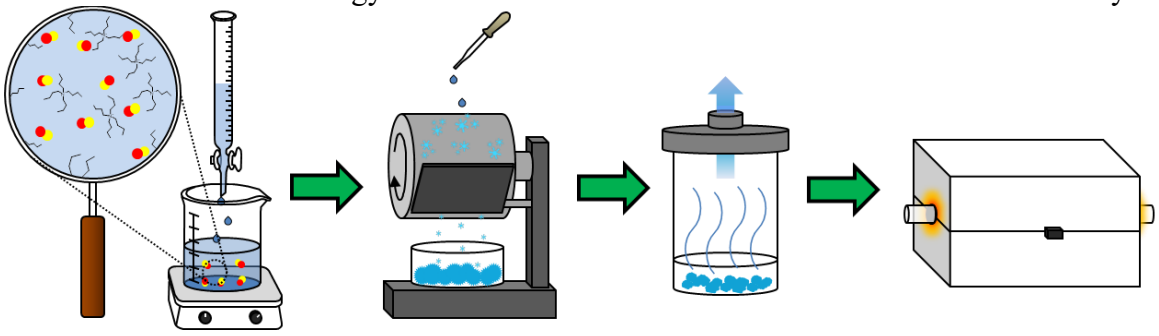

Figure 1.8 | Perovskite co-precipitation synthesis.

Perovskites can only form at high temperatures (700°C+) which causes particles to sinter together and lower their surface area for oxygen exchange in electrocatalysis or in intercalation pseudocapacitance. However, high surface area perovskites (~10 m^2 g^{-1}) can be made using a co-precipitation synthesis as shown in Figure 1.8. The synthesis

involves dripping a metal nitrate solution into an alkaline solution to cause metal hydroxide nuclei precipitation with its growth arrested using large capping ligands. The nanoparticles are then collected via centrifugation, washed three times, dispersed in deionized water via ultrasonication and solution sprayed and frozen onto a rotating drum at cryogenic temperatures. The ice containing the nanoparticles is then sublimed away in a freeze-dryer and the nanoparticles are then calcined in air at 700^{o}C or higher to form a phase pure perovskite.

1.5 OUTLINE

Chapter 2 involves the promise and development of metal-air batteries and fuel cells towards advancing low-cost, high energy density charge storage solutions for sustainable energy applications. To improve the activities and stabilities of electrocatalysts for the critical oxygen reduction and evolution reactions (ORR and OER respectively), a greater understanding is needed of the catalyst/carbon interactions and carbon stability. Herein, $LaNiO_3$ (LNO) is supported on nitrogen-doped carbon nanotubes (N-CNT) made via a high yield synthesis and is shown to lower the overpotential for both the OER and ORR markedly to enable a low bifunctional window of 0.81 V at only a 51 μg cm^{-2} mass loading. Furthermore, the addition of LNO to the N-CNTs improves the galvanostatic stability for the OER by almost two orders of magnitude. The nanoscale geometries of the perovskites and the CNTs enhance the number of metal-support and charge transfer interactions and thus the activity. The current contributions from carbon oxidation and even anodic iron leaching from carbon nanotubes during OER are quantitatively separated using rotating ring disk electrodes (RRDEs), Tafel slope analysis and ICP-OES. CTA synthesized all samples, performed all sample characterization and electrochemical testing except for taking the high resolution TEM and HAADF-STEM,

EDX and EELS which AMA performed. CTA wrote the paper and analyzed the data with assistance from KJS and KPJ.

Chapter 3 covers a perovskite oxide library with the composition $La_{1-x}Sr_xBO_{3-\delta}$ (x = 0-1; B = Fe, Mn, Co) that is synthesized and characterized to systematically study anion-based pseudocapacitance. The electrochemical capacitance of these materials was evaluated by cyclic voltammetry and galvanostatic charging/discharging in 1 M KOH. The results demonstrated greater oxygen vacancy content (δ), upon systematic incorporation of Sr^{2+}, linearly increases the surface-normalized pseudocapacitance with a slope controlled by the B-site element. $La_{0.2}Sr_{0.8}MnO_{2.7}$ exhibited the highest specific capacitance of 492 F g^{-1} at 5 mV s^{-1} relative to the Fe and Co oxides.

Chapter 4 uses the pseudocapacitive principles from Chapter 3 and successfully demonstrates the first all-perovskite asymmetric pseudocapacitors and characterized them in alkaline aqueous electrolytes. The asymmetric pseudocapacitor cell voltage could be increased by widening the difference between the B-site transition metal redox potentials in each electrode which resulted in a maximum voltage window of 2.0 V in 1 M KOH. Among the three pairs of asymmetric pseudocapacitors constructed from $SrCoO_{2.7}$, $La_{0.2}Sr_{0.8}MnO_{2.7}$, and Brownmillerite (BM)-$Sr_2Fe_2O_5$, the BM-$Sr_2Fe_2O_5$//$SrCoO_{2.7}$ combination performed the best with a high energy density of 31 Wh kg^{-1} at 450 W kg^{-1} and power density of 10,000 W kg^{-1} at 28 Wh kg^{-1}. For Chapters 3 and 4, CTA synthesized, characterized and electrochemically tested SCO, LSMO28 and BM-SFO, performed iodometric titrations on the iron series and made and tested the asymmetric pseudocapacitors. JTM contributed intellectually and took the cyclic voltammetry measurements of the perovskite library. JS synthesized the perovskite library and performed iodometric titration measurements on the cobalt and manganese series. RFP

synthesized the LFO sample. CTA analyzed data and wrote the paper with assistance from KJS and KPJ.

Chapter 5 explores the $LaNi_{1-x}Fe_xO_{3-\delta}$ (LNF; x=0, 0.15, 0.55) series perovskites and brownmillerite-$SrFeO_{2.5}$ (BM-SFO) to use Ni's high electronegativity combined with the inductive effect via iron substitution to make higher voltage anion based (a)symmetric pseudocapacitors. These materials were well characterized, and their capacitance was measured using cyclic voltammetry (CV) and galvanostatic charging and discharging (GCD) tests in 1 M KOH. The results showed that substituting Ni for Fe in the B-site increased the $Ni^{2+/3+}$ redox potential while the $Fe^{3+/4+}$ redox peaks shifted to lower potentials due to the inductive effect. The LNF materials had a surface anion-redox pseudocapacitance mechanism as opposed to a pseudocapacitive intercalation mechanism that enabled a $LaNi_{0.45}Fe_{0.55}O_{3-\delta}$ (LNF55) symmetric pseudocapacitor to discharge with high power (250,000 W kg^{-1}) with 4.3 Wh kg^{-1} and it had the largest discharge peak (1 V) for any symmetric anion-pseudocapacitor reported to date. The BM-SFO//LNF55 asymmetric pseudocapacitor had a 1.8 V potential window and the largest discharge voltage at 1.1 V of any anion-based aqueous pseudocapacitor reported to our knowledge to yield a 11.4 Wh kg^{-1} energy density at 453 W kg^{-1}. CTA synthesized, characterized and electrochemically tested all materials and asymmetric and symmetric pseudocapacitors in this work. CTA analyzed the data and wrote the paper with assistance from KJS and KPJ.

1.6 REFERENCES

(1) Intergovernmental Panel on Climate Change. *Global Warming of 1.5°C*; 2018.
(2) EIA - International Energy Outlook 2017 https://www.eia.gov/outlooks/archive/ieo17/ (accessed Apr 11, 2019).
(3) Ritchie, H.; Roser, M. Renewable Energy. *Our World Data* **2017**.
(4) O'Hayre, R. P.; Cha, S.-W.; Colella, W. G.; Prinz, F. B. *Fuel Cell Fundamentals*, Third edition.; Wiley: Hoboken, New Jersey, 2016.

(5) Bard, A. J. *Electroanalytical Chemistry: A Series of Advances:*; CRC Press, 1990.
(6) Smith, T. J.; Stevenson, K. J. Reference Electrodes. In *Handbook of Electrochemistry*; Elsevier, 2007; pp 73–110.
(7) Conway, B. E. *Electrochemical Supercapacitors: Scientific Fundamentals and Technological Applications*; Springer Science & Business Media, 2013.
(8) Conway, B. E. Two-Dimensional and Quasi-Two-Dimensional Isotherms for Li Intercalation and Upd Processes at Surfaces. *Electrochimica Acta* **1993**, *38* (9), 1249–1258. https://doi.org/10.1016/0013-4686(93)80055-5.
(9) Frackowiak, E.; Béguin, F. Carbon Materials for the Electrochemical Storage of Energy in Capacitors. *Carbon* **2001**, *39* (6), 937–950. https://doi.org/10.1016/S0008-6223(00)00183-4.
(10) Simon, P.; Gogotsi, Y. Materials for Electrochemical Capacitors. *Nat. Mater.* **2008**, *7* (11), 845–854. https://doi.org/10.1038/nmat2297.
(11) Engelsmann, K.; Lorenz, W. J.; Schmidt, E. Underpotential Deposition of Lead on Polycrystalline and Single-Crystal Gold Surfaces: Part I. Thermodynamics. *J. Electroanal. Chem. Interfacial Electrochem.* **1980**, *114* (1), 1–10. https://doi.org/10.1016/S0022-0728(80)80431-1.
(12) Gloaguen, F.; Léger, J.-M.; Lamy, C. An Electrochemical Quartz Crystal Microbalance Study of the Hydrogen Underpotential Deposition at a Pt Electrode. *J. Electroanal. Chem.* **1999**, *467* (1), 186–192. https://doi.org/10.1016/S0022-0728(98)00448-3.
(13) Tripković, A. V.; Popović, K. D.; Momčilović, J. D.; Dražić, D. M. Kinetic and Mechanistic Study of Methanol Oxidation on a Pt(100) Surface in Alkaline media1Dedicated to Professor Aleksandar R. Despić on the Occasion of His 70th birthday.1. *J. Electroanal. Chem.* **1998**, *448* (2), 173–181. https://doi.org/10.1016/S0022-0728(97)00141-1.
(14) Conway, B. E. Transition from "Supercapacitor" to "Battery" Behavior in Electrochemical Energy Storage. *J. Electrochem. Soc.* **1991**, *138* (6), 1539–1548. https://doi.org/10.1149/1.2085829.
(15) Brousse, T.; Bélanger, D.; Long, J. W. To Be or Not To Be Pseudocapacitive? *J. Electrochem. Soc.* **2015**, *162* (5), A5185–A5189. https://doi.org/10.1149/2.0201505jes.
(16) Conway, B. E.; Birss, V.; Wojtowicz, J. The Role and Utilization of Pseudocapacitance for Energy Storage by Supercapacitors. *J. Power Sources* **1997**, *66* (1–2), 1–14.
(17) Mefford, J. T.; Hardin, W. G.; Dai, S.; Johnston, K. P.; Stevenson, K. J. Anion Charge Storage through Oxygen Intercalation in LaMnO3 Perovskite Pseudocapacitor Electrodes. *Nat. Mater.* **2014**, *13* (7), 726–732. https://doi.org/10.1038/nmat4000.
(18) Christensen, J.; Albertus, P.; Sanchez-Carrera, R. S.; Lohmann, T.; Kozinsky, B.; Liedtke, R.; Ahmed, J.; Kojic, A. A Critical Review of Li/Air Batteries. *J. Electrochem. Soc.* **2011**, *159* (2), R1–R30. https://doi.org/10.1149/2.086202jes.

(19) Rahman, M. A.; Wang, X.; Wen, C. High Energy Density Metal-Air Batteries: A Review. *J. Electrochem. Soc.* **2013**, *160* (10), A1759–A1771. https://doi.org/10.1149/2.062310jes.
(20) Chen, Z.; Higgins, D.; Yu, A.; Zhang, L.; Zhang, J. A Review on Non-Precious Metal Electrocatalysts for PEM Fuel Cells. *Energy Environ. Sci.* **2011**, *4* (9), 3167. https://doi.org/10.1039/c0ee00558d.
(21) Hardin, W. G.; Slanac, D. A.; Wang, X.; Dai, S.; Johnston, K. P.; Stevenson, K. J. Highly Active, Nonprecious Metal Perovskite Electrocatalysts for Bifunctional Metal–Air Battery Electrodes. *J. Phys. Chem. Lett.* **2013**, *4* (8), 1254–1259. https://doi.org/10.1021/jz400595z.
(22) Hardin, W. G.; Mefford, J. T.; Slanac, D. A.; Patel, B. B.; Wang, X.; Dai, S.; Zhao, X.; Ruoff, R. S.; Johnston, K. P.; Stevenson, K. J. Tuning the Electrocatalytic Activity of Perovskites through Active Site Variation and Support Interactions. *Chem. Mater.* **2014**, *26* (11), 3368–3376. https://doi.org/10.1021/cm403785q.
(23) Mefford, J. T.; Rong, X.; Abakumov, A. M.; Hardin, W. G.; Dai, S.; Kolpak, A. M.; Johnston, K. P.; Stevenson, K. J. Water Electrolysis on La1-xSrxCoO3-δ Perovskite Electrocatalysts. *Nat. Commun.* **2016**, *7*, 11053. https://doi.org/10.1038/ncomms11053.
(24) Rong, X.; Parolin, J.; Kolpak, A. M. A Fundamental Relationship between Reaction Mechanism and Stability in Metal Oxide Catalysts for Oxygen Evolution. *ACS Catal.* **2016**, *6* (2), 1153–1158. https://doi.org/10.1021/acscatal.5b02432.
(25) Grimaud, A.; Diaz-Morales, O.; Han, B.; Hong, W. T.; Lee, Y.-L.; Giordano, L.; Stoerzinger, K. A.; Koper, M. T. M.; Shao-Horn, Y. Activating Lattice Oxygen Redox Reactions in Metal Oxides to Catalyse Oxygen Evolution. *Nat. Chem.* **2017**, *9*, 457. https://doi.org/10.1038/nchem.2695.
(26) Maiyalagan, T.; Jarvis, K. A.; Therese, S.; Ferreira, P. J.; Manthiram, A. Spinel-Type Lithium Cobalt Oxide as a Bifunctional Electrocatalyst for the Oxygen Evolution and Oxygen Reduction Reactions. *Nat. Commun.* **2014**, *5*, 3949. https://doi.org/10.1038/ncomms4949.
(27) Lovreček, B.; Batinic, M.; Čaja, J. The Electrochemical Oxygen Reduction on the Graphite Electrode. *Electrochimica Acta* **1983**, *28* (5), 685–690. https://doi.org/10.1016/0013-4686(83)85065-8.
(28) Maldonado, S.; Stevenson, K. J. Influence of Nitrogen Doping on Oxygen Reduction Electrocatalysis at Carbon Nanofiber Electrodes. *J. Phys. Chem. B* **2005**, *109* (10), 4707–4716. https://doi.org/10.1021/jp044442z.
(29) Wiggins-Camacho, J. D.; Stevenson, K. J. Mechanistic Discussion of the Oxygen Reduction Reaction at Nitrogen-Doped Carbon Nanotubes. *J. Phys. Chem. C* **2011**, *115* (40), 20002–20010. https://doi.org/10.1021/jp205336w.
(30) Yeager, E. Electrocatalysts for O2 Reduction. *Electrochimica Acta* **1984**, *29* (11), 1527–1537. https://doi.org/10.1016/0013-4686(84)85006-9.
(31) Poux, T.; Napolskiy, F. S.; Dintzer, T.; Kéranguéven, G.; Istomin, S. Y.; Tsirlina, G. A.; Antipov, E. V.; Savinova, E. R. Dual Role of Carbon in the Catalytic Layers of

Perovskite/carbon Composites for the Electrocatalytic Oxygen Reduction Reaction. *Catal. Today* **2012**, *189* (1), 83–92. https://doi.org/10.1016/j.cattod.2012.04.046.
(32) Matsumoto, Y.; Sato, E. Electrocatalytic Properties of Transition Metal Oxides for Oxygen Evolution Reaction. *Mater. Chem. Phys.* **1986**, *14* (5), 397–426.
(33) Bockris, J. O.; Otagawa, T. The Electrocatalysis of Oxygen Evolution on Perovskites. *J. Electrochem. Soc.* **1984**, *131* (2), 290–302. https://doi.org/10.1149/1.2115565.
(34) Richter, J.; Holtappels, P.; Graule, T.; Nakamura, T.; Gauckler, L. J. Materials Design for Perovskite SOFC Cathodes. *Monatshefte Für Chem. - Chem. Mon.* **2009**, *140* (9), 985–999. https://doi.org/10.1007/s00706-009-0153-3.

Chapter 2: Role of the Carbon Support on the Oxygen Reduction and Evolution Activities in $LaNiO_3$ Composite Electrodes in Alkaline Solution[1]

2.1: INTRODUCTION

Sustainable sources of energy such as solar and wind, along with electric vehicles, need high energy density, low-cost energy storage to become economically viable[1]. For example, metal-air batteries show a great deal of promise as a route to increasing energy storage capabilities by reducing oxygen from air at the cathode to yield a theoretical energy density three to six times larger than conventional lithium insertion batteries[2]. The major bottlenecks for these devices, however, are the sluggish kinetics of the oxygen evolution reaction and oxygen reduction reaction (OER and ORR, respectively) which require a large overpotential to facilitate pragmatic current densities.[2,3] Additionally, the high cost of standard precious metal Pt and Ir OER and ORR catalysts is detrimental to wide-scale adoption.[4] A low-cost alternative to precious metals are perovskite oxides that have the formula $ABO_{3-\delta}$ where A is a lanthanide or alkaline earth element and B is a transition metal element[5,6]. Perovskite oxides have been shown to be catalytically active for both reactions,[7,8] have high oxygen diffusivity, [9,10] and may be synthesized using a wide variety of elemental compositions[7,11] for facile tuning of catalytic properties.

[1] Adapted with permission from C. T. Alexander, A. M. Abakumov, R. P. Forslund, K. P. Johnston and K. J. Stevenson. Role of the Carbon Support on the Oxygen Reduction and Evolution Activities in $LaNiO_3$ Composite Electrodes in Alkaline Solution. ACS Appl. Energy Mater. 2018, 1, 1549−1558. Copyright © 2018 American Chemical Society. C. T. Alexander synthesized the materials, processed and analyzed data and wrote the manuscript. A. M. Abakumov took the high resolution-TEM images and EELS data, R. P. Forslund assisted in sample synthesis, K. P. Johnston and K. J. Stevenson assisted in writing the manuscript.

Several studies have shown that perovskites are highly active ORR catalysts, particularly when supported on N-doped carbons.[11–14] In alkaline conditions, the ORR proceeds by one of two major pathways, either the direct four electron route:

$$O_2 + H_2O + 4e^- \rightarrow 4OH^- \; E^o = +0.401\, V \; vs \; NHE \qquad (1)$$

or by an initial two electron process where oxygen is first reduced to hydroperoxide:

$$O_2 + H_2O + 2e^- \rightarrow HO_2^- + OH^- \; E^o = -0.065\, V \; vs \; NHE \quad (2)$$

followed by electrochemical reduction to OH- to complete what is commonly referred to as the 'two by two process':

$$HO_2^- + H_2O + 2e^- \rightarrow 3OH^- \; E^o = +0.867\, V \; vs \; NHE. \qquad (3)$$

Furthermore, the hydroperoxide may be chemically disproportionated to O2 and OH- resulting in the 'pseudo-four electron process':

$$2HO_2^- \rightarrow O_2 + 2OH^- \qquad (4)$$

A more detailed description of the reaction 2 mechanism is briefly discussed in Appendix A1.1. The direct four electron pathway typically occurs on materials such as Pt and its alloys while the hydroperoxide route typically occurs on most carbons and transition metal oxides.[15,16] In particular, N-doped carbon materials have been shown to be highly active for the ORR via the pseudo-four electron pathway.[13,17]

In contrast to the ORR, the OER has been shown to be more active on metal oxides and especially perovskites[7,18–20] relative to precious group metals. The adsorbate evolution mechanism (AEM) has been the most commonly accepted OER mechanism on perovskites since the work of Bockris and Otagawa,[8] but recently a new lattice oxygen

mediated (LOM) mechanism has been demonstrated for certain perovskites containing oxygen vacancies.[19,21,22] The LOM mechanism occurs by utilizing lattice oxygen when the Fermi level dips into overlapping transition metal 3d and oxygen 2p bands that result in oxygen vacancies and a net lower activation energy barrier. Whereas these studies have been performed for perovskites mixed with supports including mesoporous N-doped carbon[11,19] and Vulcan carbon,[19] acetylene black[7] and Ketjenblack,[23] relatively few OER studies investigating perovskites have utilized carbon nanotubes which offer the benefit of highly accessible surface areas and higher electronic conductivities.[24–26]

Recent gains in characterizing the OER mechanism on perovskites provide a foundation for current attempts at understanding perovskite catalyst-support interactions.[27] One approach to promote charge transfer between the catalyst support and perovskite is to form covalent bonds between transition metals and carbon, as reported for C-O-Mn bonds for $LaMnO_3$ perovskites to enhance the ORR.[28] However, a major challenge in forming perovskite-carbon hybrids with chemical bonds is the need for calcination at elevated temperatures to form the crystalline perovskite phase that often cannot be done in the presence of a support as it leads to preferential gasification of the carbon support. A promising alternative strategy to promote OER activity is to design the carbon support to be highly conductive, graphitic and have a morphology suitable to best electrically wire the perovskite catalysts to the electrode.

The stability of catalyst/carbon composites is a major challenge for the OER as the carbon support is thermodynamically unstable above ~0.09 V vs RHE and may be (electro)chemically oxidized to either CO or CO_2 .[29,30] In an effort to solve this problem

considerable efforts have been made to compensate for this thermodynamic instability by separating the OER and ORR half reactions[20], increasing the mass loading,[31] coating the carbon with TiO_2.[32,33] Efforts have also been made to slow the kinetic rate of carbon oxidation by designing perovskite composites with more stable, graphitic carbon supports.[25–27] The recently reported stability of various carbon-supported perovskites in rechargeable Zn-air batteries during cycling provides evidence that carbon may be used as a stable support under OER conditions[23,24]. In a study of the direct growth of N-CNTs on the surface of a $LaCoO_3$, the nanotube structure did not change after 37 h of galvanostatic polarization, but the degree of carbon oxidation was not quantified[25]. While these approaches have proven fruitful, it would be beneficial to measure directly the selectivity for the OER versus carbon oxidation to better understand the OER activity and how to improve catalyst stability.

Herein, we report a systematic study of the effect of carbon supports on the OER and ORR activity for a nanostructured electrocatalyst, $LaNiO_3$ (LNO). LNO was chosen because it is highly active for the OER[18], can be reproducibly synthesized, and has been benchmarked versus other catalytically active, non-precious metal systems[11,18]. The high surface area and large aspect ratio of CNTs and N-CNTs in addition to the nanoscale geometries of the LNO are expected to raise the activities by enhancing the number of metal-support interactions and the overall electrical conductivity[27]. Additionally, N-CNTs are known to be highly effective supports for the ORR via the pseudo-four electron pathway in which the nitrogen functionality acts to increase the rate of the first two electron transfers[17,34]. The bifunctional window (the difference in potentials to reach 10

mA/cm^2_{geo} for the OER and 3 mA/cm^2_{geo} for the ORR [35]) for $LaNiO_3$ supported on N-CNTs was found to be only 0.81 V for the N-CNT/LNO composite at only 51 μg cm^{-2} loading, the lowest value reported to date for $LaNiO_3$. For the OER, we present a comprehensive methodology to delineate the effects of iron corrosion from the CNT supports, carbon corrosion, and oxygen evolution by combining RRDE measurements, Tafel slope analysis, and Fe concentration measurements with ICP-OES.

2.2: EXPERIMENTAL

2.2.1: Chemicals

All chemicals were used as received. Lanthanum (III) nitrate hexahydrate (99.995%), nickel (II) nitrate hexahydrate (99%) were purchased from ARCOS Organics. 5 wt % Nafion solution in lower alcohols, diethylene glycol (DEG, 99%), m-xylene (>99%) and ammonia gas (99.98%) were purchased from Sigma-Aldrich. Citric acid (100%), pyridine (99.9%), and ethanol (Absolute 200 proof) were purchased from Fischer Scientific and ferrocene (99%) was obtained from Alfa Aesar. Oxygen (research grade, 99.999% purity), argon (research grade, 99.999% purity) and hydrogen (research grade, 99.999% purity) were obtained from Praxair. Millipore deionized water (18 MΩ cm) was used. Vulcan Carbon XC-72R (VC) was purchased from Cabot Corp.

2.2.2: N-CNT/CNT Synthesis

Nitrogen doped and non-doped carbon nanotubes were produced from a combination of prior floating catalyst CVD methods to increase total yield[34,36] using two

single-zone tube furnaces (Carbolite Model HST 12/35/200/2416CG). 104.3 mg of ferrocene was placed in a small vial, capped with a rubber septum, and flushed with Ar to remove oxygen. 1 mL of pyridine was added to the vial to make a 9.6 wt% ferrocene solution. 1.0 mL of solution was loaded into a gas tight glass syringe (Hamilton 81320) and then interfaced with plastic tubing that led to the inlet of a sealed quartz tube (22 mm ID, 19.7 cm reaction zone length) as shown in Figure A1. The first zone and second zone were heated to 200ºC and 760ºC, respectively, followed by a five-minute hold to reach equilibrium while Ar was purged at 200 sccm. The NH_3 and Ar flow rates were then raised to 56 sccm and 694 sccm for a total of 750 sccm using electronic gas mass flow controllers (MKS Type 1479A). The pyridine-ferrocene solution was then injected into the first stage furnace at 1.2 mL/hr using a programmable syringe pump (New Era Pump Systems NE-1000) for a total of 60 min after which both furnaces could cool to room temperature under Ar at 200 sccm. Previous approaches yielded only ~10 mg batches[34,37], but by modifying the synthesis conditions[36] N-CNTs were collected from the deposited film on the inside of the quartz tube with a typical yield of ~100 mg or 0.728 mg/cm^2, a ten-fold increase in product over prior studies[17,37]. Undoped CNTs were prepared as above except m-xylene was used instead of pyridine, NH_3 was not used, and Ar flowed at 750 sccm during synthesis which gave a total yield of ~350 mg or 2.55 mg/cm^2.

2.2.3: $LaNiO_3$ Synthesis

LNO was prepared via a modified Pechini method[38]. Briefly, 2.5 mmol of La and Ni nitrates each were added to 50 mL of DI water containing 5 mmol of citric acid to

produce a 1:1 metal ion to citric acid molar ratio. The solution was put onto a hot plate in a fume hood, stirred and 3.33 mmol of DEG was added to the solution. A gel formed when all of the water had evaporated. The gel then combusted with a visible flame and left behind metal oxide constituents. The metal oxides were calcined in a furnace under dehumidified air (150 mL/min) at 1ºC/min from 30ºC to 700ºC, held at 700ºC for 4 hours and then allowed to cool to room temperature. The resulting LNO was washed three times with DI water and ethanol followed by ball milling for three min.

2.2.4: Materials Characterization

X-Ray Diffraction (XRD) patterns were taken on a Rigaku Spider instrument with a Cu Kα radiation (λ=1.5418 Å) source at 40 kW and 40 mA. Diffraction rings were integrated, and JADE software was used to analyze peak patterns. Samples were analyzed with XPS using a Kratos AXIS Ultra DLD (Al α radiation, λ=1.4866 eV) with high resolution spectra taken at 0.1 eV steps with 1 s, 1.5 s, 2.5 s, 2.5 s dwell time for C 1s, N 1s, O 1s, and Fe 2p regions, respectively. Raman spectra were taken of the N-CNTs and CNTs using a Renishaw inVia system with an Ar laser (λ=514.5nm, 3mW/cm^2 and 50x aperture (NA=0.75) calibrated using a silicon crystal standard. Sample diameter cross section is approximately 2 μm and spectra were taken with a single 120 s long scan. Iron content was found using thermogravimetric analysis (TGA) with a TA Instruments Q500 with 1-5 mg sample sizes in alumina crucibles. The temperature was ramped from 25ºC to 900ºC at 20ºC/min under flowing air (Praxair 99.998%) at 50 mL/min to the sample. The N-CNT TEM specimen was prepared by crushing the sample in an agate mortar

under ethanol and depositing a few drops of suspension on a porous carbon grid on a Cu support. High resolution transmission electron microscopy (TEM) images, high angle annular dark field scanning TEM (HAADF-STEM) images, energy dispersive X-ray (EDX) and electron energy loss (EELS) spectra were collected with an image and probe aberration-corrected Titan G3 electron microscope equipped with EDAX detector and Quantum GIF spectrometer. The microscope was operated at 300 kV. Surface areas of samples were measured with a Quantachrome Instruments NOVA 2000 high-speed surface area BET analyzer at 77 K. Samples were degassed for 4 hours at 120^{o}C prior to analysis and a P/P_o range of 0.05 to 0.30 was used to determine the surface area. ICP-OES measurements were made in triplicate using a Varian 710 instrument with using argon gas and 2 wt% trace metal nitric acid as the sample carriers with a 1.2 kW plasma torch. Standards were made via serial dilution of a 10 mM $Fe(NO_3)_3$ solution in 2 wt% trace metal nitric acid.

2.2.5: Electrochemical Measurements

Electrochemical testing was performed on either a CH Instruments CHI832a or a Metrohm Autolab PGSTAT302N with high speed rotators from Pine Instruments. All samples were ball milled for three minutes and 30 wt% LNO was mixed with a carbon support by ball milling for three minutes as well. All RDEs were cleaned by bath sonication in a 50:50 by volume solution of EtOH and DI water followed by polishing on pad with 50 μm alumina, rinsing with DI water and finished by sonication in a fresh 50:50 EtOH: DI water solution. Catalyst inks were prepared by adding 2 mL of NaOH

neutralized 0.05 wt% Nafion in ethanol solution to 2 mg of catalyst (1 mg/ml) and sonicating the ink for 2 hours. 10 μL of the ink was then pipetted onto a 0.196 cm^2 glassy carbon (GC) rotating disk electrode (RDE) and spun dried at 700 r.p.m. to give a composite mass loading of 51 $\mu g/cm^2$ for LNO on carbon samples. This relatively low mass loading was chosen to limit mass transfer limitations in the composite film to best measure intrinsic catalyst activities[39–41]. 7 μL (35.7 $\mu g/cm^2$) of ink was used for samples with only carbon, except for rotating ring disk electrode (RRDE) measurement where 51 $\mu g/cm^2$ was loaded, to better delineate the carbon support contribution to catalytic activity. All RDEs were tested in a standard three electrode cell at 1600 r.p.m. with a Hg/HgO (1 M KOH) reference electrode a Au counter electrode, and a film of catalyst on RDE as the working electrode with a room temperature 0.1 M KOH solution saturated with research grade O_2. RRDE and CV experiments were in identical configurations on the Metrohm Autolab PGSTAT302N except the solutions were saturated with research grade Ar. The positive feedback method was used to determine electrolyte resistance (~46.8 Ω). The solution resistance was measured for each clean RDE used, an average was taken, the differences of the RDE solution resistance were calculated from the average and the iR correction (Figure A2) was adjusted to account for slight differences in RDE resistance between electrodes.

All electrochemical tests used a Hg/HgO electrode whose open circuit potential (OCP) was measured relative to the calibrated Hg/HgO electrode to ensure a potential is never applied to the calibrated electrode. The RHE calibration procedure is provided in the Supplementary Information and the RHE potential was found to be -0.8937 V versus

the calibrated Hg/HgO (Figure A3). Linear sweep voltammograms (LSV) were performed on RDEs and were scanned at 10 mV/s and 5 mV/s for the OER and ORR, respectively. The OER test window was between 1.0307 V and 1.9937 V vs RHE, while the ORR test window was between 1.0937 V and -0.0063 V vs RHE. All OER and ORR measurements were taken in triplicate. Cyclic voltammograms (CVs) were taken on static rotating ring disk electrodes (0.2472 cm^2) at 100 mV/s from 0 to 1.4 V vs RHE in 0.1 M KOH solution saturated with Ar for at least 30 minutes. RRDE tests in the OER region were performed in identical conditions to the CVs at 10 mV/s with the Pt ring (0.1859 cm^2) cycled in the ORR region to reduce surface oxides and held at 0.5V vs RHE. The ORR RRDE measurements were performed at the same conditions as the ORR RDE measurements with the Pt ring held at 1.23 V vs RHE to ensure all ring current was due to peroxide oxidation. The collection efficiency was previously measured to be 37%[19] using 0.3 mM ferrocene-methanol in 0.1 M KCl by sweeping the disk potential from 0.1 V to 0.6 V vs Hg/HgO and holding the Pt ring potential at 0.1 V vs Hg/HgO.

Samples for ICP-OES were made by taking 4.55 mL of the electrolyte before OER CVs (sample “KOH”), after one OER CV on a carbon fiber paper (CFP) electrode (sample “CFP”) and following a OER CV of 0.3 mg cm^{-2} N-CNT on a CFP electrode (sample “N-CNT”). The CFP working electrodes were attached to a copper wire using copper tape to avoid iron contamination in the solution. Before ICP-OES measurements, 0.45 mL of 12.1 M trace metal nitric acid was added to the electrolyte samples to bring the solution to 2 wt% nitric acid.

2.3: RESULTS AND DISCUSSION

2.3.1: Characterization: Carbon Nanotubes and LNO

The N-CNT and CNT samples were well characterized before mixing with LNO to more fully understand the role of the carbon support towards OER and ORR. Figure 2.1a shows a representative high resolution TEM image of N-CNTs ranging from 5 to 20 nm in diameter. Additionally, the Fe nanoparticles (NPs) shown in the TEM and HAADF-STEM images of Figure A4 are approximately 10-20 nm in diameter and are encased in graphitic shells that are ca. 3-8 atomic layers thick. EDX (Figure A5) and EELS (Figure A6) spectra show that the N-CNT sample is composed of mostly C and Fe. EELS spectra display a small nitrogen signal around 410 eV.

XRD, a bulk technique, was used to determine the size of graphitic domains using the Scherrer equation (5.3 nm and 10.4 nm for N-CNTs and CNTs, respectively) along with the crystal structure of the Fe catalyst in the N-CNT and CNT samples. Figure A7a shows normalized XRD spectra of both samples each with two peaks, the first at 26° and the second at 44.5° 2θ corresponding to graphite and iron carbide (Fe_3C), respectively. The LNO was found to be phase pure as shown in Figure A7b. the

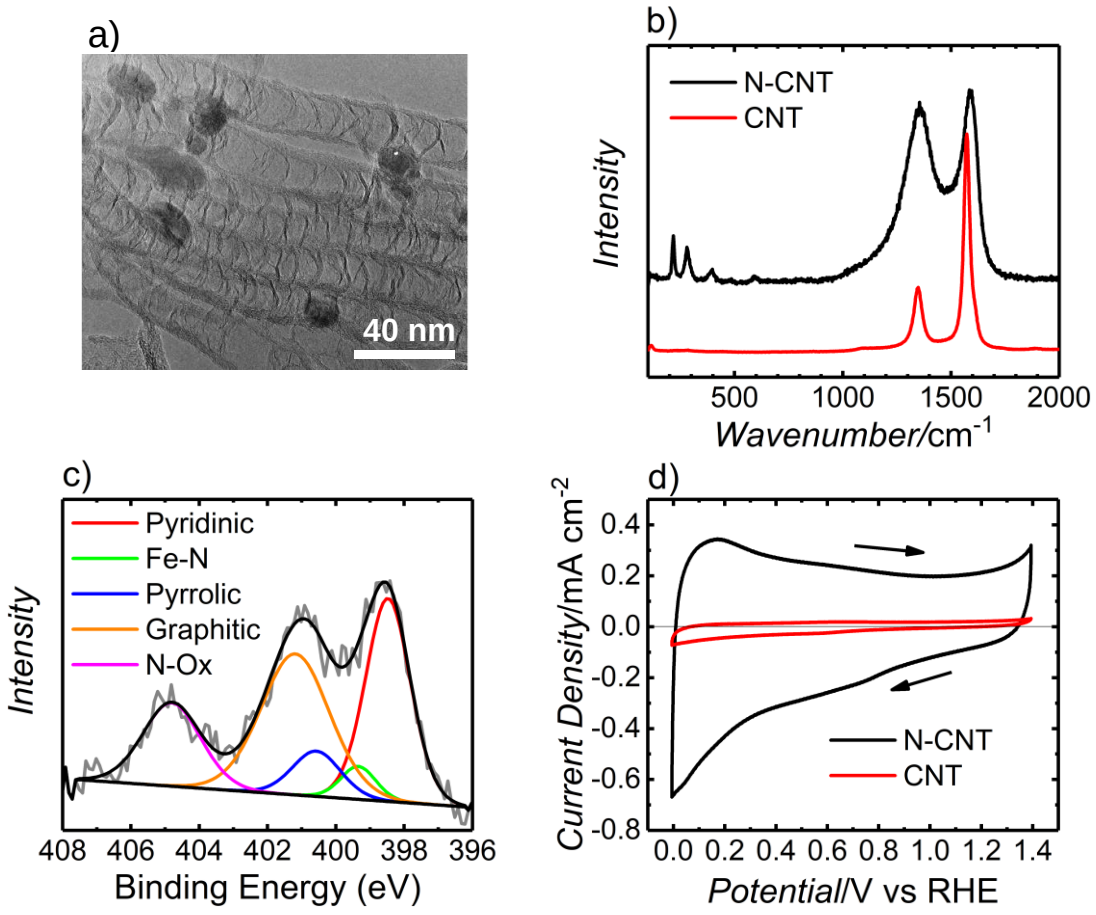

Figure 2.1 | N-CNT and CNT Characterization.

a) TEM images showing N-CNTs with encapsulated Fe nanoparticles b) Normalized Raman spectra of both N-CNTs and CNTs c) High resolution XPS spectra of N 1s of N-CNTs d) CVs of N-CNTs and CNTs in Ar saturated 0.1 M KOH at 100 mV/s with 51 μg/cm^2 total mass loading.

TGA was used to determine the total iron content in the two samples (Figure A8). The residual iron after thermal decomposition was found to be Fe_2O_3 using XRD which was weighed and its mass converted to what it would be if it were Fe_3C giving a weight percent for N-CNTs and CNTs of 20.6 wt. % and 11.9 wt. %, respectively. The N-CNT

burn off temperature appears to be 400ºC, and that of the CNTs is approximately 550ºC indicating the latter's greater thermal stability.

Raman spectra of N-CNTs in Figure 2.1b show that the N-CNTs are much more disordered than CNTs as can be seen by the relative intensities of the two peaks at approximately 1360 cm^{-1} and 1590 cm^{-1} which are commonly referred to as the D and G bands, respectively. The D band is attributed to the A_{1g} vibrational mode which is normally not Raman active, but becomes active when translational symmetry is broken in graphitic planes[42]. This broken symmetry occurs at graphite plane edges, vacancies, functionalities or any non-graphite bond[43]. The G band is assigned to the E_{2g} vibrational mode corresponding to in-plane sp^2 graphitic carbon. Tunistra *et. al.* showed[43] that the average graphite crystal size is inversely proportional to the I_D/I_G ratio which was found to be 0.91, 0.31, and 1.94[44] for the N-CNTs, CNTs and VC, respectively, giving average graphite crystallite sizes of 4.8, 10.3, 2.2 nm for the respective carbons. The smaller N-CNT graphite domain size relative to the CNTs makes intuitive sense as N-dopants would break the graphite translational symmetry and would manifest as a larger D band. The collection of peaks below 600 cm^{-1} for the N-CNTs correspond to α-Fe_2O_3 (hematite)[45,46] which is not detected in the bulk from XRD, thus suggesting that the Fe_3C particles in N-CNTs are coated in a thin α-Fe_2O_3 layer. The presence of hematite peaks in the N-CNT sample suggest that the N-CNT structure is disordered enough to allow access to oxygen from the air to oxidize the Fe_3C in the sample at ambient conditions. In contrast, CNTs do not show hematite Raman active bands thus suggesting that the iron

carbide nanoparticles are completely coated in an impermeable graphite layer since Fe_3C does not have Raman active vibrational modes[46].

XPS spectra were taken on both samples and the total nitrogen content of the N-CNTs was found to be 5.6 $\pm$ 0.5 at. %. Significant contributions are computed in Table A2 and shown in Figure 2.1c from pyridinic nitrogen (398.5 eV), nitrogen coordinated iron (399.3 eV), pyrrolic nitrogen (400.5 eV)[47], graphitic nitrogen (401.2 eV)[47], and pyridine-N-oxide (404.8 eV)[47,48]. Examining the XPS surveys of both samples in Figure A9 reveals that there is no detectable Fe in the CNT sample while there is only 1.02 at.% Fe (~4.8 wt. % Fe_3C) corresponding to roughly one quarter of that detected by TGA. The lower iron content is likely because XPS penetration depth is approximately 10 nm and each Fe NP seed appears to be coated in a ~5 nm graphitic shell. Each nanoparticle is approximately 20 nm in diameter in Figure A4 so the XPS signal would not realistically penetrate the entire sample. Both samples display a small oxygen signal as shown in Figure A10 which is mostly due to FeOOH[49] in the N-CNTs from the decomposition of adsorbed water while the undoped CNTs' spectra reveal adsorbed water and Fe_3O_4[50]. This observation agrees with the N-CNT Raman spectrum and the small size of the O 1s shoulder in the CNT spectra suggests that perhaps there is only slight oxidation of the Fe NP catalyst, possibly due to oxygen diffusion through graphitic edges and grain boundaries.

Ar saturated CVs of both samples, shown in Figure 2.1d, were taken to quantify possible redox features. N-CNT reduction current begins to increase at ~0.3 V vs RHE which corresponds to a transition of α-Fe_2O_3 to Fe_3O_4 according to the iron Pourbaix

diagram in Figure A11[51]. The capacitance of the N-CNTs and CNTs were determined to be 143 F/g and 11 F/g, respectively by using the cathodic scan as shown previously.[9] This increase is due in part to the ~5-fold increase in surface area of N-CNTs (200 m^2/g) relative to CNTs (46 m^2/g) as shown in Figure A12. Wiggins-Camacho *et.al.*[52]explained the remainder of the 13-fold increase in capacitance from nitrogen doping as a result of a higher density of states at the Fermi level that increases the capacitance per unit area. Additionally, Rice *et. al*.[53] have shown that edge plane carbon has a significantly higher capacitance per unit area than its basal plane counterpart. This observation also helps to explain the higher capacitance of N-CNTs due to their higher edge plane content according to their Raman spectra in Figure 2.1b.

2.3.2: Oxygen Reduction Reaction

Figure 2.2a shows the ORR activity of VC, CNT, and N-CNT supports with and without LNO as shown by the solid and dashed lines, respectively. All RDEs are loaded with 35.7 $\mu g/cm^2$ of carbon and an additional 15.3 $\mu g/cm^2$ of LNO. In all cases adding LNO (solid lines) raised the reduction current. For the 'carbon only' curves, the onset potential and diffusion limited current increases in the order CNT < VC < N-CNT. The low diffusion limited current of VC and the CNTs suggests that only the first two electrons are transferred to O_2 to form HO_2^- (eqn. 2) on the carbon which was confirmed by the RRDE measurements in Figure A13 where all of the measured disk current was due to peroxide generation until ~0.2V vs RHE where peroxide electroreduction (eqn. 3) begins to take place. The low CNT activity can be explained from the fact that it has

many fewer edge sites and defects according to the Raman spectra, features that are known to produce much higher electron transfer rates[54]. VC, in contrast, has more defects as well as a slight sulfur content[44] that has been shown to increase ORR activity[55]. The N-CNTs have significantly more defects, and more importantly, they have 5.6 $\pm$ 0.5 at% N dopants which are well known to catalyze the ORR while the residual Fe or its oxides can chemically disproportionate peroxide[17] thus yielding the pseudo four electron mechanistic pathway.[13,17,37,56]

There has been much debate about the nature of the active site from doping carbon with N. For example, the carbon atoms straddling both sides of edge sites containing pyridinic nitrogen atoms have been shown to be the ORR active site in both acidic[57] and neutral[17] conditions. In alkaline conditions however, carbon atoms adjacent to graphitic nitrogen are thought to act as the active site for the ORR while carbon atoms neighboring pyridinic nitrogen atoms are supposedly active toward the OER.[58]. Regardless of the identity of the ORR active site, N dopants are known to lower the ORR overpotential by donating electron density to the carbon lattice, thereby raising the Fermi level[52,59] and enhancing the affinity to donate electrons to solution according to Gerischer-Marcus theory[60]. This increase in the density of states at the Fermi level[52] also increases charge transfer rates and decreases the ORR overpotential which has been experimentally verified by Cheon *et.al*[61]. Taking Gerischer-Marcus theory into account, the finding by Yang *et.al.*[58] is somewhat unusual, because pyridinic N has a lower binding energy than graphitic N so one would expect carbons adjacent to pyridinic N to have more reducing power and thus to be more active towards the ORR. The higher

diffusion limited current, however, is likely because the residual Fe in the N-CNTs chemically disproportionates the hydroperoxide formed by the carbon as shown previously via the pseudo-four electron process [17]. The RRDE measurement performed on N-CNTs shown in Figure A13e confirms that the N-CNTs follow the pseudo-four electron process alone at lower overpotentials until ~0.5 V vs RHE, after which it is then accompanied by peroxide electroreduction. The Pt ring current magnitude rises but then falls instead of plateauing (along with the disk current) as it should if it is chemically limited by peroxide disproportionation.

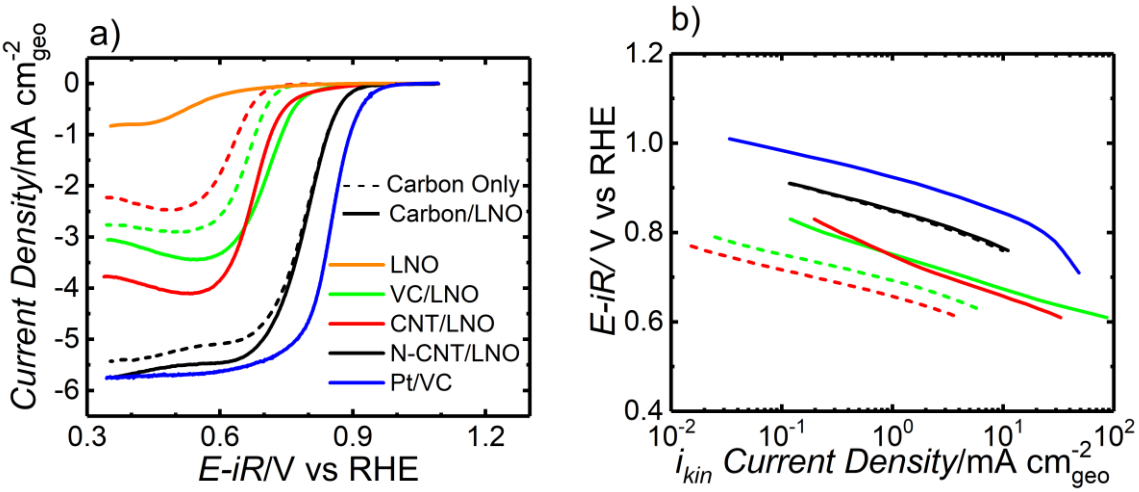

Figure 2.2 | Oxygen Reduction Activity.

ORR in O_2-saturated 0.1 M KOH at 1600 r.p.m. and a 51 μg/cm^2 mass loading a) Activity b) Tafel plot of the kinetic current obtained from the Koutecky-Levich equation (eqn. S4). The dashed lines correspond to the carbon only (35.7 μg/cm^2) and the solid lines correspond to the LNO-carbon composite while the orange 'LNO' solid line represent LNO (15.3 μg/cm^2) without carbon. Note that adding LNO and doping N into CNTs increases the diffusion limited current as well as the exchange current density indicated by the shift of the curves to higher potentials. All Tafel curves are the average of three RDE experiments.

Interestingly, supporting LNO on carbon shifts the onset potential to approximately the same potential for the VC and CNT composite, despite LNO exhibiting little ORR activity itself but does not affect the onset potential for the N-CNTs. Additionally, the order of increasing diffusion limited current with LNO changes to VC < CNT < N-CNT. These observations can be explained from the RRDE measurements in Figure A13 that show adding LNO chemically disproportionates peroxide generated on the cathodic scan which was previously rate limiting. The peroxide generation current increases on the back scan for both VC/LNO and CNT/LNO which suggests LNO peroxide chemical disproportionation activity decreases on the anodic sweep. LNO reversibility was examined by running a second scan on the two composites shown in Figure A14 which shows there is no chemical disproportionation of peroxide for VC/LNO while it is reduced by half for the CNT/LNO. By looking at the blue difference curves in Figure A14, it appears the LNO electroreduces peroxide (eqn. 3) in VC/LNO where VC did not before, and CNT/LNO has a four-fold increase in the peroxide electroreduction rate relative to CNT alone (Figure A13c). The latter observation may be explained by noting that peroxide electroreduction requires charge transfer and the CNTs will increase the electrical conductivity of the composite relative to LNO, reducing any charge transfer resistances. While, LNO peroxide chemical disproportionation is likely slower than the iron in the N-CNT, it also assists in the chemical disproportionation and electroreduction of hydroperoxide generated on N-CNTs because the composite's current increases uniformly over the entire diffusion limited regime with the LNO addition[11,17].-

Later in this paper, anodic iron leaching from the N-CNT is demonstrated at OER potentials and use RRDE measurements are used to show how the ORR activity changes before and after running an OER CV (Figure A15, S16). It appears the CNTs have enhanced peroxide electroreduction rates after an OER CV, which is likely due to oxygen functionalities formed during the OER, yet peroxide generation rates remain unchanged. In contrast, Figure A16 more clearly illustrates that the CNT/LNO composite and N-CNTs maintain their electroreduction activity while losing much of their peroxide disproportionation activity after an OER CV. LNO appears to stabilize the N-CNT ORR activity with minimal loss as shown in Figure A15g and h after much of the iron is leached from the support during the OER. A possible explanation for this is as the iron is leached from the N-CNTs, it interacts with LNO to form Ni-Fe species on the surface so there would still be iron present to catalyze the pseudo-four electron mechanism. This hypothesis is supported by the Ni redox peak anodic shift shown in Figure A17a which will be discussed in greater detail later in this paper.

Tafel plots are shown in Figure 2.2b with measured Tafel slopes reported in Table A3 that are between 60-85 mV/dec. The Tafel slope of approximately 60 mV/dec would be consistent with previous reports that the rate determining step is the protonation of superoxide (reaction S2) according to kinetic modeling studies[62]. This agrees with CV experiments in alkaline conditions at different pH values and scan rates[63], hydroperoxide decomposition measurements and modeling[37], deuterium isotope studies[64] and transfer coefficient analysis[65]. The overpotentials at 3 mA/cm^2_{geo} for N-CNT, CNT and VC composites with LNO are 0.45 V, 0.58 V and 0.59 V, respectively.

2.3.3: Oxygen Evolution Reaction

The geometric OER activity of the different composites is shown in Figure 2.3a relative to IrO_2/VC as a benchmark. While LNO on VC has a higher activity than IrO_2 on VC as shown previously[18], the activity rises significantly with the CNT and N-CNT supports. This increase can be explained by the improved electronic conductivity and the high aspect ratio of N-CNTs and CNTs that improve "wiring" of the LNO relative to VC. The conductivities of N-CNT and CNT supports were previously reported[52] to be ~300 $\pm$ 100 and 330 $\pm$ 70 S/cm, respectively, while that of VC is only ~ 5 S/cm[44]. These results explain the difference of the OER curves from VC to N-CNT and CNT supports. The change in the OER i-V curves before and after iR correction, as shown in Figure A2, is similar to the difference in the OER profiles (Figure 2.3a) between VC/LNO and CNT/LNO in that they have the same onset potential for the OER yet the CNT/LNO and N-CNT/LNO samples have a much steeper slope which suggests that the higher electronic conductivity of the catalyst-carbon composite is what enhances the LNO OER activity and not a change in the electronic structure of the catalyst. Tafel plots of the OER activities of the LNO-carbon composites are shown in Figure 2.3b. For all samples, there are distinct regions with different Tafel slopes at both low and high overpotentials along with features attributed to LNO redox reactions[9,66] around the transition between the two regimes at ~1.5 V vs RHE. The N-CNT composite appears to have an intermediate Tafel region between ~1.42-1.57 V vs RHE which can be more easily seen in Figure A18 where the Tafel slope is plotted for the four composites vs. log(mass activity).

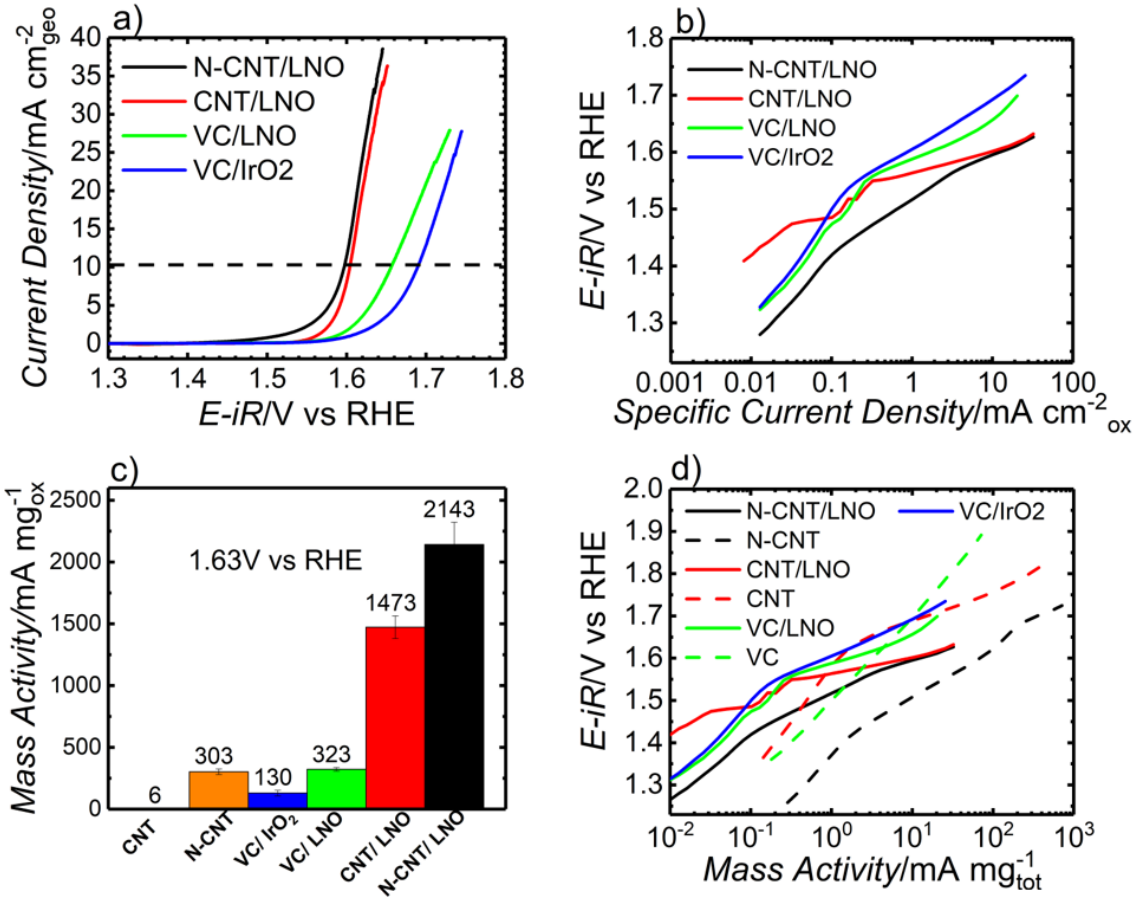

Figure 2.3 | Oxygen Evolution Activity.

a) Linear and b) log scale plots of OER activities comparing the effects of the carbon support and performance relative to 30 wt% IrO_2 on VC c) Oxide mass activity measured at 1.63 V vs. RHE in 0.1 M KOH O_2 saturated solution at 10 mV/s of LNO on different supports, the carbon supports alone, and VC/IrO_2 benchmark at 51 μg/cm^2 mass loading. The support activities are normalized to their own mass (35.7 μg/cm^2) d) Total mass activity of same samples as in c) to better compare the intrinsic role of the support.

Sample	η_{ORR} (V)	η_{OER} (V)	ΔE	Loading	Source
	-3 mA/cm$^2_{geo}$	10 mA/cm$^2_{geo}$	(V)	(μg/cm^2)	
N-CNT/LNO	0.44	0.37	0.81	51	This work
VC/LNO	0.61	0.42	1.03	51	This work
SP/ Cubic $LaNiO_3$	0.57	0.46	1.04	317	[67]
N-CNT @ $LaNiO_3$	0.46	0.51	0.97	1220	[68]
RGO/$LaNiO_3$ Nanorod	0.62	0.46	1.08	254	[69]
N-meso C /$LaNiO_3$	0.52	0.43	0.95	51	[11]
Graphene Ox./ $LaNiO_3$	0.604	0.51	1.11	51	[11]
$LaNiO_3$/NC	0.59	0.43	1.02	51	[18]
20% Ir/VC	0.54	0.38	0.92	140	1
20% Pt/VC	0.37	0.79	1.16	140	1

Table 2.1 | Comparison of Bifunctional Composites

Figure 2.3c shows the OER activity of LNO on different supports benchmarked against IrO_2/VC and our previous work[11,19] at 1.63 V vs RHE. It demonstrates that the OER activity of LNO supported on CNTs and N-CNTs is more than 10x and 16x higher, respectively, than precious metal IrO_2 supported on VC. The N-CNT and CNT support activities are normalized by the total mass of carbon on the electrode (7 μg) and are significantly less active than the metal oxides. Thus, the carbon support boosts the OER activity of LNO as opposed to catalyzing the OER itself. The total mass activities are plotted in Figure 2.3d to better compare the activities of the carbon support with and without LNO.

While the conductivity of the carbon support can be used to explain the enhanced activities of CNT/LNO and N-CNT/LNO relative to VC/LNO, one would expect CNT/LNO to be more active than N-CNT/LNO due to CNT's higher electronic conductivity. The larger activity enhancement due to N-CNT could possibly be explained

by the N-CNTs faster charge transfer rates. The N-CNTs have a higher density of states at the Fermi level[52] which should raise charge transfer rates according to Gerisher-Marcus Theory[60] and thus result in higher activities. The combination of the above effects of N-CNTs and LNO on the ORR and OER enable the LNO bifunctional window for OER and ORR to drop from 1.03 V on VC to 0.81V on N-CNTs, which is even lower than the value for the benchmark Ir/VC at three times the loading of N-CNT/LNO, as shown in Table 1. In fact, the reported N-CNTs here are the most synergistic resulting in the lowest bifunctional window compared to many other carbon-$LaNiO_3$ composites with higher mass loadings as shown in Table 1.

Additionally, the carbon's effect on the LNO redox peak is illustrated in Figure A17 by subtracting the carbon current contribution from the LNO-carbon composite's current to yield only the contribution due to LNO. Figure A17a shows that, relative to VC, CNTs as a support raises the redox peak current of LNO 7-fold, while N-CNTs approximately double the peak height and shift the peaks anodically by ~40 mV. The larger LNO redox peaks are likely due to the higher electrical conductivity of the carbon nanotubes that enable better utilization of the LNO surface.

2.3.4: RRDE Carbon Oxidation Studies

Carbon oxidation is always a concern because carbon is thermodynamically unstable[70] at OER potentials, but the kinetics may become slow enough for highly graphitic carbon to achieve acceptable catalyst stability[26,29]. A RRDE was submerged into an Ar-saturated 0.1 M KOH solution and surface oxides were reduced on the Pt ring by

cycling the ring at ORR potentials prior to the test until the CVs stabilized. The Pt ring was held at 0.5 V vs. RHE which is low enough reduce evolved oxygen, but not any carbon dioxide produced from the carbon on the disc (Figure 2.4). The onset potentials for reduction of evolved O_2 at the Pt ring are ~1.37 V and ~1.62 V vs RHE on the disk for N-CNT and CNT (without any LNO) samples, respectively, as shown in Figure 2.4. Below these potentials only Pt ring background current is detected and both N-CNTs and CNTs have a single slope on a log(i) plot indicating a Tafel region with faradaic charge transfer. Thus, the current measured in this low overpotential region *must* be due to carbon oxidation because it is the only species present that can be oxidized at this potential consistent with carbon[70] and iron[51] Pourbaix diagrams.

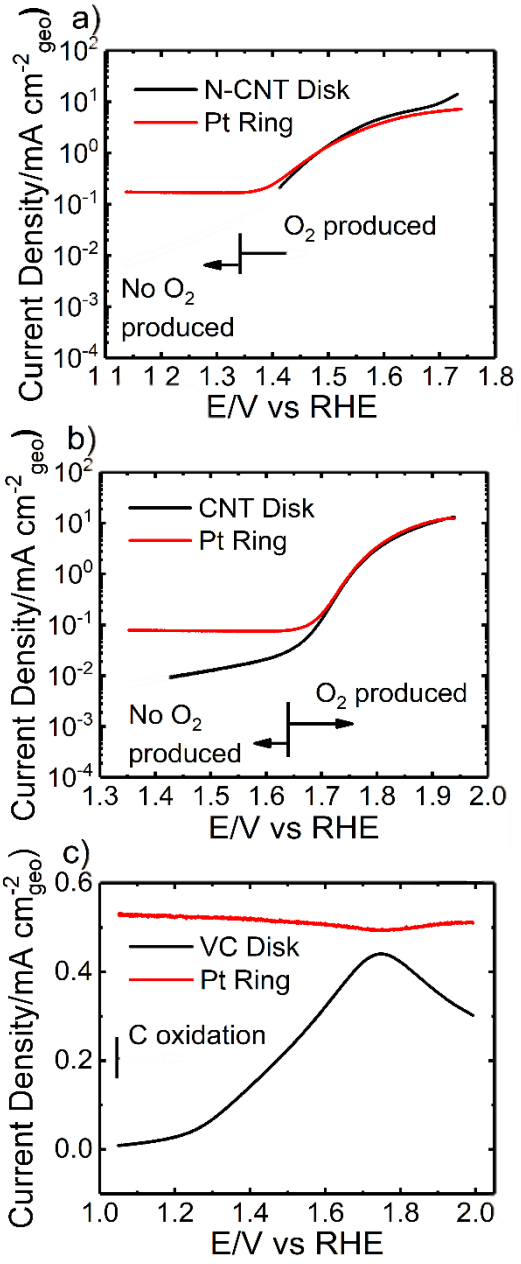

Figure 2.4 | Rotating Ring Disk Measurements.

RRDE measurements in Ar saturated 0.1 M KOH at 1600 r.p.m. with 51 μg cm^{-2} mass loading of a) N-CNT b) CNT c) VC. Note that the Pt ring reduction current begins at ~1.35 V and ~1.65V vs RHE for N-CNTs and CNTs, respectively and that the Pt ring background current is higher than the VC oxidation current. All Pt ring currents were

divided by the collection efficiency (37%) to demonstrate that anodic disk current is entirely OER as seen by curve overlap.

Speculatively, the reason for the early onset of the Pt ring current for N-CNT supports may be due to electrochemical leaching of residual Fe which occurs around 1.4 V vs RHE according to the Fe Pourbaix diagram in Figure A11[51,71]. This result agrees with the Raman and XPS data that N-CNTs contain both Fe_3C and FeOx that are accessible to the environment. Further evidence for anodic Fe leaching is seen by presence of a hysteresis loop, as shown in Figure A19 for N-CNTs in the OER, which rapidly shrinks in intensity after the first scan as the iron is removed. Additionally, ICP-OES measurements show, in Figure A20, that iron is present in the electrolyte after CVs of the N-CNT sample in the OER region to confirm Fe leaching. The RRDE experiment with VC (Figure 2.4c) shows that no oxygen was evolved and that there was so little current that the Pt ring background current was always higher than the VC disk current. This result demonstrates that VC does not catalyze the OER and that the current is predominately a result of carbon oxidation.

Whereas the role of carbon oxidation in the OER has often not been quantified in the literature, in this study we quantitatively separate the effects of carbon oxidation, the OER and anodic iron leaching. Figure A21 demonstrates that carbon oxidation rates can be extrapolated from the Tafel slopes in the low overpotential carbon oxidation region assuming the Tafel slope does not change appreciably with potential. Contributions from anodic iron leaching are quantified by comparing composites with and without LNO and it was found that iron leaching accounted for ~13% of the N-CNT/LNO OER current at

1.63 V vs RHE, while there was no sign of iron leaching for CNT/LNO or CNTs. A summary of the various current contributions for the three composites are given in Tables S5-7, respectively with Tafel slopes and exchange current densities of carbon oxidation extrapolated to 0.099V vs RHE for the various systems in Table A8. It is observed that LNO and IrO_2 change both the Tafel slope and exchange current density for carbon oxidation according to Table A8, which is, speculatively, due to metal-oxide catalyzed carbon oxidation.

2.3.5: OER Constant Current Stability Test

OER 48-hour constant current stability tests of the N-CNTs (10 A/g_{ox}; 30 μA) and CNTs (10 A/g_{tot}; 100 μA) supports with and without LNO were measured and are shown in Figure 2.5a. Of the four systems studied, all were stable for the entire 48-hour galvanostatic test, except for N-CNTs without LNO, which failed in less than two hours. The greater stability of CNTs relative to N-CNTs, without LNO, was expected considering the Raman spectra show N-CNTs with higher disorder, more edge sites and more defects with dangling bonds that would make N-CNTs more susceptible to oxidation[29,30] than the CNTs. When LNO is supported on CNTs, the overpotential decreases by approximately 50 mV, which would aid carbon stability even though the CNTs alone were already stable for 48-hours. The addition of LNO increases the N-CNT stability from two hours to up to seven days (Figure 2.5b) since LNO lowers the overpotential for the OER reaction, thereby lowering the carbon oxidation rate. Interestingly, LNO adds a small ‘potential rebound’ to CNTs (shown in Figure 2.5a inset)

and N-CNTs. The first overpotential rebound for the CNT/LNO composite is probably due to the LNO redox peak from the incorporation of solution phase hydroxide[9]. The N-CNT/LNO composite's overpotential kept increasing until after eight hours when it decreased and stabilized, which is likely due to a combination of the LNO redox peak and electrochemical Fe leaching from N-CNTs to a soluble FeO_4^{2-} as described previously[72]. So far, it is unknown why there exists a second potential rebound at approximately seven days for the N-CNT/LNO composite. The majority of the galvanostatic current is likely from the OER catalyzed by LNO because estimates of the carbon oxidation rate indicate that if all the N-CNT/LNO current were carbon oxidation then it should have failed after two hours. This estimate is consistent with the stability measurement of N-CNTs without LNO. Thus, adding an active OER catalyst such as LNO can significantly suppress carbon oxidation processes via reducing the OER overpotential and therefore the carbon oxidation overpotential as well.

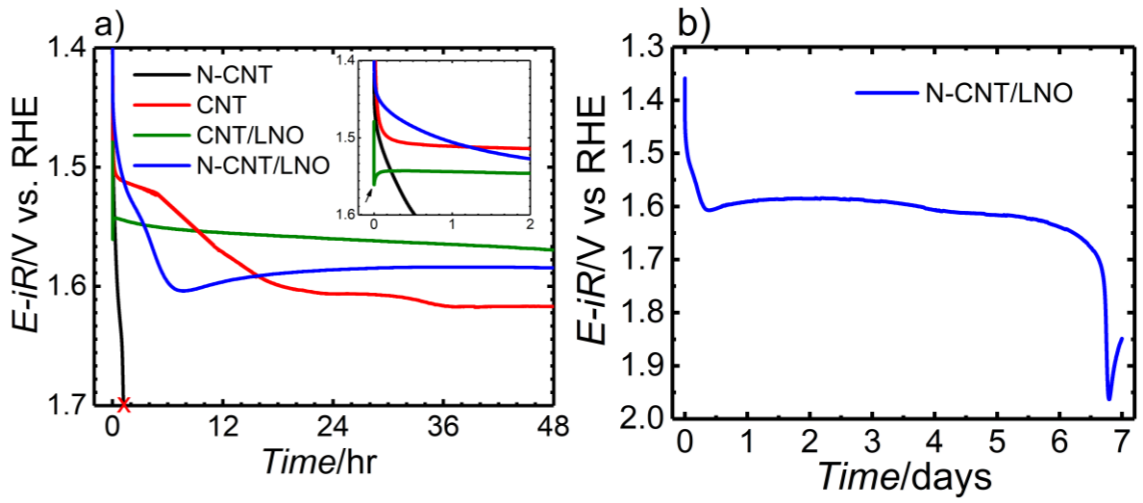

Figure 2.5 | Constant Current OER Stability.

a) 48-hour OER constant current stability test of N-CNTs and CNTs with and without LNO. N-CNT and N-CNT/LNO are tested at 10 A/g_{ox} (30 μA). CNT and CNT/LNO are tested at $10A/g_{tot}$ (100 μA). b) N-CNT/LNO seven-day stability test at same conditions as in a).

2.4: Conclusions

In summary, CNTs with high nitrogen content are synthesized using a high yield synthesis, the product of which is the best carbon support to the knowledge of the authors for perovskite oxides as a bifunctional catalyst towards the oxygen evolution and reduction reaction. The N-CNTs are compared with undoped CNTs and Vulcan Carbon to investigate chemical and morphological differences on the impact of activity and stability. The bifunctional window of the N-CNT/LNO composite was measured to be 0.81 V with a mass loading of only 51 μg cm^{-2} that survived over seven days at a constant oxidizing current of 10 A g_{ox}^{-1}, which is a much lower mass loading (Table 1) and much longer stability test relative to one-day galvanostatic tests commonly done in the literature. The N-CNT stability was increased from two hours to over seven days by

adding LNO which lowered the overpotential and thus rate of carbon oxidation. The high aspect ratio of the more conductive nanotubes enhances electrical wiring between the carbon and catalyst to boost the nanoscale LNO OER activity, while the N-dopants on the carbon along with residual iron catalyze the ORR using "pseudo"-four-electron pathway[17]. A method is demonstrated to easily use RRDE combined with ICP-OES and Tafel slope analysis to quantitatively identify carbon and iron corrosion *in-situ* to more accurately measure OER activities. This will allow the scientific community to better compare OER catalyst activities and avoid erroneous results from corrosion or comparing catalysts at overpotentials that are too low. The above results demonstrate that the carbon nanotube and LNO systems were rigorously characterized and show promise, upon further optimization, towards being bifunctional composites for metal-air batteries and regenerative fuel cell applications in the future.

2.5: ADDITIONAL INFORMATION

More details regarding the ORR mechanism, experimental procedure, sample characterization, stability, RRDE ORR results and electrochemical characterization can be found in Appendix 1.

2.6: REFERENCES

(1) Vazquez, S.; Lukic, S. M.; Galvan, E.; Franquelo, L. G.; Carrasco, J. M. Energy Storage Systems for Transport and Grid Applications. *IEEE Trans. Ind. Electron.* **2010**, *57* (12), 3881–3895. https://doi.org/10.1109/TIE.2010.2076414.

(2) Christensen, J.; Albertus, P.; Sanchez-Carrera, R. S.; Lohmann, T.; Kozinsky, B.; Liedtke, R.; Ahmed, J.; Kojic, A. A Critical Review of Li/Air Batteries. *J. Electrochem. Soc.* **2011**, *159* (2), R1–R30. https://doi.org/10.1149/2.086202jes.

(3) Rahman, M. A.; Wang, X.; Wen, C. High Energy Density Metal-Air Batteries: A Review. *J. Electrochem. Soc.* **2013**, *160* (10), A1759–A1771. https://doi.org/10.1149/2.062310jes.
(4) Gorlin, Y.; Jaramillo, T. F. A Bifunctional Nonprecious Metal Catalyst for Oxygen Reduction and Water Oxidation. *J. Am. Chem. Soc.* **2010**, *132* (39), 13612–13614. https://doi.org/10.1021/ja104587v.
(5) Hwang, J.; Rao, R. R.; Giordano, L.; Katayama, Y.; Yu, Y.; Shao-Horn, Y. Perovskites in Catalysis and Electrocatalysis. *Science* **2017**, *358* (6364), 751–756.
(6) Chen, D.; Chen, C.; Baiyee, Z. M.; Shao, Z.; Ciucci, F. Nonstoichiometric Oxides as Low-Cost and Highly-Efficient Oxygen Reduction/Evolution Catalysts for Low-Temperature Electrochemical Devices. *Chem. Rev.* **2015**, *115* (18), 9869–9921. https://doi.org/10.1021/acs.chemrev.5b00073.
(7) Suntivich, J.; May, K. J.; Gasteiger, H. A.; Goodenough, J. B.; Shao-Horn, Y. A Perovskite Oxide Optimized for Oxygen Evolution Catalysis from Molecular Orbital Principles. *Science* **2011**, *334* (6061), 1383–1385. https://doi.org/10.1126/science.1212858.
(8) Bockris, J. O.; Otagawa, T. The Electrocatalysis of Oxygen Evolution on Perovskites. *J. Electrochem. Soc.* **1984**, *131* (2), 290–302. https://doi.org/10.1149/1.2115565.
(9) Mefford, J. T.; Hardin, W. G.; Dai, S.; Johnston, K. P.; Stevenson, K. J. Anion Charge Storage through Oxygen Intercalation in LaMnO3 Perovskite Pseudocapacitor Electrodes. *Nat. Mater.* **2014**, *13* (7), 726–732. https://doi.org/10.1038/nmat4000.
(10) Nemudry, A.; Rudolf, P.; Schöllhorn, R. Topotactic Electrochemical Redox Reactions of the Defect Perovskite SrCoO2.5+x. *Chem. Mater.* **1996**, *8* (9), 2232–2238. https://doi.org/10.1021/cm950504+.
(11) Hardin, W. G.; Mefford, J. T.; Slanac, D. A.; Patel, B. B.; Wang, X.; Dai, S.; Zhao, X.; Ruoff, R. S.; Johnston, K. P.; Stevenson, K. J. Tuning the Electrocatalytic Activity of Perovskites through Active Site Variation and Support Interactions. *Chem. Mater.* **2014**, *26* (11), 3368–3376. https://doi.org/10.1021/cm403785q.
(12) Suntivich, J.; Gasteiger, H. A.; Yabuuchi, N.; Nakanishi, H.; Goodenough, J. B.; Shao-Horn, Y. Design Principles for Oxygen-Reduction Activity on Perovskite Oxide Catalysts for Fuel Cells and Metal–air Batteries. *Nat. Chem.* **2011**, *3* (7), 546–550. https://doi.org/10.1038/nchem.1069.
(13) Gong, K.; Du, F.; Xia, Z.; Durstock, M.; Dai, L. Nitrogen-Doped Carbon Nanotube Arrays with High Electrocatalytic Activity for Oxygen Reduction. *Science* **2009**, *323* (5915), 760–764. https://doi.org/10.1126/science.1168049.
(14) Zhou, M.; Wang, H.-L.; Guo, S. Towards High-Efficiency Nanoelectrocatalysts for Oxygen Reduction through Engineering Advanced Carbon Nanomaterials. *Chem. Soc. Rev.* **2016**, *45* (5), 1273–1307. https://doi.org/10.1039/C5CS00414D.
(15) Yeager, E. Electrocatalysts for O2 Reduction. *Electrochimica Acta* **1984**, *29* (11), 1527–1537. https://doi.org/10.1016/0013-4686(84)85006-9.

(16) Poux, T.; Napolskiy, F. S.; Dintzer, T.; Kéranguéven, G.; Istomin, S. Y.; Tsirlina, G. A.; Antipov, E. V.; Savinova, E. R. Dual Role of Carbon in the Catalytic Layers of Perovskite/carbon Composites for the Electrocatalytic Oxygen Reduction Reaction. *Catal. Today* **2012**, *189* (1), 83–92. https://doi.org/10.1016/j.cattod.2012.04.046.
(17) Wiggins-Camacho, J. D.; Stevenson, K. J. Mechanistic Discussion of the Oxygen Reduction Reaction at Nitrogen-Doped Carbon Nanotubes. *J. Phys. Chem. C* **2011**, *115* (40), 20002–20010. https://doi.org/10.1021/jp205336w.
(18) Hardin, W. G.; Slanac, D. A.; Wang, X.; Dai, S.; Johnston, K. P.; Stevenson, K. J. Highly Active, Nonprecious Metal Perovskite Electrocatalysts for Bifunctional Metal–Air Battery Electrodes. *J. Phys. Chem. Lett.* **2013**, *4* (8), 1254–1259. https://doi.org/10.1021/jz400595z.
(19) Mefford, J. T.; Rong, X.; Abakumov, A. M.; Hardin, W. G.; Dai, S.; Kolpak, A. M.; Johnston, K. P.; Stevenson, K. J. Water Electrolysis on La1-xSrxCoO3-δ Perovskite Electrocatalysts. *Nat. Commun.* **2016**, *7*, 11053. https://doi.org/10.1038/ncomms11053.
(20) Seitz, L. C.; Dickens, C. F.; Nishio, K.; Hikita, Y.; Montoya, J.; Doyle, A.; Kirk, C.; Vojvodic, A.; Hwang, H. Y.; Norskov, J. K.; et al. A Highly Active and Stable IrOx/SrIrO3 Catalyst for the Oxygen Evolution Reaction. *Science* **2016**, *353* (6303), 1011–1014. https://doi.org/10.1126/science.aaf5050.
(21) Rong, X.; Parolin, J.; Kolpak, A. M. A Fundamental Relationship between Reaction Mechanism and Stability in Metal Oxide Catalysts for Oxygen Evolution. *ACS Catal.* **2016**, *6* (2), 1153–1158. https://doi.org/10.1021/acscatal.5b02432.
(22) Grimaud, A.; Diaz-Morales, O.; Han, B.; Hong, W. T.; Lee, Y.-L.; Giordano, L.; Stoerzinger, K. A.; Koper, M. T. M.; Shao-Horn, Y. Activating Lattice Oxygen Redox Reactions in Metal Oxides to Catalyse Oxygen Evolution. *Nat. Chem.* **2017**, *9*, 457. https://doi.org/10.1038/nchem.2695.
(23) Jung, J.-I.; Risch, M.; Park, S.; Kim, M. G.; Nam, G.; Jeong, H.-Y.; Shao-Horn, Y.; Cho, J. Optimizing Nanoparticle Perovskite for Bifunctional Oxygen Electrocatalysis. *Energy Env. Sci* **2016**. https://doi.org/10.1039/C5EE03124A.
(24) Lee, D. U.; Park, M. G.; Park, H. W.; Seo, M. H.; Ismayilov, V.; Ahmed, R.; Chen, Z. Highly Active Co-Doped LaMnO 3 Perovskite Oxide and N-Doped Carbon Nanotube Hybrid Bi-Functional Catalyst for Rechargeable Zinc–air Batteries. *Electrochem. Commun.* **2015**, *60*, 38–41. https://doi.org/10.1016/j.elecom.2015.08.001.
(25) Elumeeva, K.; Masa, J.; Sierau, J.; Tietz, F.; Muhler, M.; Schuhmann, W. Perovskite-Based Bifunctional Electrocatalysts for Oxygen Evolution and Oxygen Reduction in Alkaline Electrolytes. *Electrochimica Acta* **2016**, *208*, 25–32. https://doi.org/10.1016/j.electacta.2016.05.010.
(26) Elumeeva, K.; Masa, J.; Tietz, F.; Yang, F.; Xia, W.; Muhler, M.; Schuhmann, W. A Simple Approach towards High-Performance Perovskite-Based Bifunctional Oxygen Electrocatalysts. *ChemElectroChem* **2016**, *3* (1), 138–143. https://doi.org/10.1002/celc.201500353.

(24) Zhu, Y.; Zhou, W.; Shao, Z. Perovskite/Carbon Composites: Applications in Oxygen Electrocatalysis. *small* **2017,** 13 (12)n/a-n/a.
(28) Liu, J.; Jin, X.; Song, W.; Wang, F.; Wang, N.; Song, Y. Facile Preparation of Modified Carbon Black-LaMnO3 Hybrids and the Effect of Covalent Coupling on the Catalytic Activity for Oxygen Reduction Reaction. *Chin. J. Catal.* **2014**, *35* (7), 1173–1188. https://doi.org/10.1016/S1872-2067(14)60066-8.
(29) Yu, P. T.; Gu, W.; Makharia, R.; Wagner, F. T.; Gasteiger, H. A. The Impact of Carbon Stability on PEM Fuel Cell Startup and Shutdown Voltage Degradation. *ECS Trans.* **2006**, *3* (1), 797–809. https://doi.org/10.1149/1.2356199.
(30) Datsyuk, V.; Kalyva, M.; Papagelis, K.; Parthenios, J.; Tasis, D.; Siokou, A.; Kallitsis, I.; Galiotis, C. Chemical Oxidation of Multiwalled Carbon Nanotubes. *Carbon* **2008**, *46* (6), 833–840. https://doi.org/10.1016/j.carbon.2008.02.012.
(31) Soares, C. O.; Silva, R. A.; Carvalho, M. D.; Jorge, M. E. M.; Gomes, A.; Rangel, C. M.; da Silva Pereira, M. I. Oxide Loading Effect on the Electrochemical Performance of LaNiO3 Coatings in Alkaline Media. *Electrochimica Acta* **2013**, *89*, 106–113. https://doi.org/10.1016/j.electacta.2012.11.040.
(32) Bauer, A.; Song, C.; Ignaszak, A.; Hui, R.; Zhang, J.; Chevallier, L.; Jones, D.; Rozière, J. Improved Stability of Mesoporous Carbon Fuel Cell Catalyst Support through Incorporation of TiO2. *Electrochimica Acta* **2010**, *55* (28), 8365–8370. https://doi.org/10.1016/j.electacta.2010.07.025.
(33) Kim, H. J.; Jackson, D. H. K.; Lee, J.; Guan, Y.; Kuech, T. F.; Huber, G. W. Enhanced Activity and Stability of TiO2-Coated Cobalt/Carbon Catalysts for Electrochemical Water Oxidation. *ACS Catal.* **2015**, *5* (6), 3463–3469. https://doi.org/10.1021/acscatal.5b00173.
(34) Maldonado, S.; Morin, S.; Stevenson, K. J. Structure, Composition, and Chemical Reactivity of Carbon Nanotubes by Selective Nitrogen Doping. *Carbon* **2006**, *44* (8), 1429–1437. https://doi.org/10.1016/j.carbon.2005.11.027.
(35) McCrory, C. C. L.; Jung, S.; Peters, J. C.; Jaramillo, T. F. Benchmarking Heterogeneous Electrocatalysts for the Oxygen Evolution Reaction. *J. Am. Chem. Soc.* **2013**, *135* (45), 16977–16987. https://doi.org/10.1021/ja407115p.
(36) Singh, C.; Shaffer, M. S.; Windle, A. H. Production of Controlled Architectures of Aligned Carbon Nanotubes by an Injection Chemical Vapour Deposition Method. *Carbon* **2003**, *41* (2), 359–368.
(37) Maldonado, S.; Stevenson, K. J. Influence of Nitrogen Doping on Oxygen Reduction Electrocatalysis at Carbon Nanofiber Electrodes. *J. Phys. Chem. B* **2005**, *109* (10), 4707–4716. https://doi.org/10.1021/jp044442z.
(38) Cushing, B. L.; Kolesnichenko, V. L.; O'Connor, C. J. Recent Advances in the Liquid-Phase Syntheses of Inorganic Nanoparticles. *Chem. Rev.* **2004**, *104* (9), 3893–3946. https://doi.org/10.1021/cr030027b.
(39) Garsany, Y.; Singer, I. L.; Swider-Lyons, K. E. Impact of Film Drying Procedures on RDE Characterization of Pt/VC Electrocatalysts. *J. Electroanal. Chem.* **2011**, *662* (2), 396–406. https://doi.org/10.1016/j.jelechem.2011.09.016.

(40) Wiberg, G. K. H.; Mayrhofer, K. J. J.; Arenz, M. Investigation of the Oxygen Reduction Activity on Silver – A Rotating Disc Electrode Study. *Fuel Cells* **2010**, *10* (4), 575–581. https://doi.org/10.1002/fuce.200900136.
(41) Schmidt, T. J.; Gasteiger, H. A.; Stäb, G. D.; Urban, P. M.; Kolb, D. M.; Behm, R. J. Characterization of High-Surface-Area Electrocatalysts Using a Rotating Disk Electrode Configuration. *J. Electrochem. Soc.* **1998**, *145* (7), 2354–2358. https://doi.org/10.1149/1.1838642.
(42) Wang, Y.; Alsmeyer, D. C.; McCreery, R. L. Raman Spectroscopy of Carbon Materials: Structural Basis of Observed Spectra. *Chem. Mater.* **1990**, *2* (5), 557–563. https://doi.org/10.1021/cm00011a018.
(43) Tuinstra, F.; Koenig, J. L. Characterization of Graphite Fiber Surfaces with Raman Spectroscopy. *J. Compos. Mater.* **1970**, *4* (4), 492–499. https://doi.org/10.1177/002199837000400405.
(44) Pantea, D.; Darmstadt, H.; Kaliaguine, S.; Sümmchen, L.; Roy, C. Electrical Conductivity of Thermal Carbon Blacks: Influence of Surface Chemistry. *Carbon* **2001**, *39* (8), 1147–1158. https://doi.org/10.1016/S0008-6223(00)00239-6.
(45) Baratto, C.; Lottici, P. P.; Bersani, D.; Antonioli, G.; Gnappi, G.; Montenero, A. Sol-Gel Preparation of α-Fe2O3 Thin Films: Structural Characterization by XAFS and Raman. *J. Sol-Gel Sci. Technol. 13* (1–3), 667–671. https://doi.org/10.1023/A:1008694519106.
(46) Park, E.; Ostrovski, O.; Zhang, J.; Thomson, S.; Howe, R. Characterization of Phases Formed in the Iron Carbide Process by X-Ray Diffraction, Mossbauer, X-Ray Photoelectron Spectroscopy, and Raman Spectroscopy Analyses. *Metall. Mater. Trans. B 32* (5), 839–845. https://doi.org/10.1007/s11663-001-0071-1.
(47) Pels, J. R.; Kapteijn, F.; Moulijn, J. A.; Zhu, Q.; Thomas, K. M. Evolution of Nitrogen Functionalities in Carbonaceous Materials during Pyrolysis. *Carbon* **1995**, *33* (11), 1641–1653. https://doi.org/10.1016/0008-6223(95)00154-6.
(48) Biniak, S.; Szymański, G.; Siedlewski, J.; Świtkowski, A. The Characterization of Activated Carbons with Oxygen and Nitrogen Surface Groups. *Carbon* **1997**, *35* (12), 1799–1810. https://doi.org/10.1016/S0008-6223(97)00096-1.
(49) Allen, G. C.; Curtis, M. T.; Hooper, A. J.; Tucker, P. M. X-Ray Photoelectron Spectroscopy of Iron–oxygen Systems. *J. Chem. Soc. Dalton Trans.* **1974**, *0* (14), 1525–1530. https://doi.org/10.1039/DT9740001525.
(50) Marcus, P.; Grimal, J. M. The Anodic Dissolution and Passivation of NiCrFe Alloys Studied by ESCA. *Corros. Sci.* **1992**, *33* (5), 805–814.
(51) Jain, A.; Ong, S. P.; Hautier, G.; Chen, W.; Richards, W. D.; Dacek, S.; Cholia, S.; Gunter, D.; Skinner, D.; Ceder, G.; Persson, K. A. Commentary: The Materials Project: A Materials Genome Approach to Accelerating Materials Innovation. *APL Mater.* **2013**, *1* (1), 011002.
(52) Wiggins-Camacho, J. D.; Stevenson, K. J. Effect of Nitrogen Concentration on Capacitance, Density of States, Electronic Conductivity, and Morphology of N-Doped Carbon Nanotube Electrodes. *J. Phys. Chem. C* **2009**, *113* (44), 19082–19090. https://doi.org/10.1021/jp907160v.

(53) Rice, R. J.; McCreery, R. L. Quantitative Relationship between Electron Transfer Rate and Surface Microstructure of Laser-Modified Graphite Electrodes. *Anal. Chem.* **1989**, *61* (15), 1637–1641. https://doi.org/10.1021/ac00190a010.
(54) Cline, K. K.; McDermott, M. T.; McCreery, R. L. Anomalously Slow Electron Transfer at Ordered Graphite Electrodes: Influence of Electronic Factors and Reactive Sites. *J. Phys. Chem.* **1994**, *98* (20), 5314–5319. https://doi.org/10.1021/j100071a023.
(55) Yang, Z.; Yao, Z.; Li, G.; Fang, G.; Nie, H.; Liu, Z.; Zhou, X.; Chen, X.; Huang, S. Sulfur-Doped Graphene as an Efficient Metal-Free Cathode Catalyst for Oxygen Reduction. *ACS Nano* **2012**, *6* (1), 205–211. https://doi.org/10.1021/nn203393d.
(56) Dai, L.; Xue, Y.; Qu, L.; Choi, H.-J.; Baek, J.-B. Metal-Free Catalysts for Oxygen Reduction Reaction. *Chem. Rev.* **2015**, *115* (11), 4823–4892. https://doi.org/10.1021/cr5003563.
(57) Guo, D.; Shibuya, R.; Akiba, C.; Saji, S.; Kondo, T.; Nakamura, J. Active Sites of Nitrogen-Doped Carbon Materials for Oxygen Reduction Reaction Clarified Using Model Catalysts. *Science* **2016**, *351* (6271), 361–365. https://doi.org/10.1126/science.aad0832.
(58) Yang, H. B.; Miao, J.; Hung, S.-F.; Chen, J.; Tao, H. B.; Wang, X.; Zhang, L.; Chen, R.; Gao, J.; Chen, H. M.; et al. Identification of Catalytic Sites for Oxygen Reduction and Oxygen Evolution in N-Doped Graphene Materials: Development of Highly Efficient Metal-Free Bifunctional Electrocatalyst. *Sci. Adv.* **2016**, *2* (4), e1501122. https://doi.org/10.1126/sciadv.1501122.
(59) Terrones, M.; Ajayan, P. M.; Banhart, F.; Blase, X.; Carroll, D. L.; Charlier, J. C.; Czerw, R.; Foley, B.; Grobert, N.; Kamalakaran, R.; et al. N-Doping and Coalescence of Carbon Nanotubes: Synthesis and Electronic Properties. *Appl. Phys. A* **2002**, *74* (3), 355–361. https://doi.org/10.1007/s003390201278.
(60) Bard, A. J. *Electroanalytical Chemistry: A Series of Advances:*; CRC Press, 1990.
(61) Cheon, J. Y.; Kim, J. H.; Kim, J. H.; Goddeti, K. C.; Park, J. Y.; Joo, S. H. Intrinsic Relationship between Enhanced Oxygen Reduction Reaction Activity and Nanoscale Work Function of Doped Carbons. *J. Am. Chem. Soc.* **2014**, *136* (25), 8875–8878. https://doi.org/10.1021/ja503557x.
(62) Shinagawa, T.; Garcia-Esparza, A. T.; Takanabe, K. Insight on Tafel Slopes from a Microkinetic Analysis of Aqueous Electrocatalysis for Energy Conversion. *Sci. Rep.* **2015**, *5*, 13801. https://doi.org/10.1038/srep13801.
(63) Yang, H.-H.; McCreery, R. L. Elucidation of the Mechanism of Dioxygen Reduction on Metal-Free Carbon Electrodes. *J. Electrochem. Soc.* **2000**, *147* (9), 3420–3428. https://doi.org/10.1149/1.1393915.
(64) Xu, J.; Huang, W.; McCreery, R. L. Isotope and Surface Preparation Effects on Alkaline Dioxygen Reduction at Carbon Electrodes. *J. Electroanal. Chem.* **1996**, *410* (2), 235–242. https://doi.org/10.1016/0022-0728(96)04545-7.
(65) Maldonado, S.; Stevenson, K. J. Direct Preparation of Carbon Nanofiber Electrodes via Pyrolysis of Iron(II) Phthalocyanine: Electrocatalytic Aspects for Oxygen

Reduction. *J. Phys. Chem. B* **2004**, *108* (31), 11375–11383. https://doi.org/10.1021/jp0496553.
(66) Forslund, R. P.; Mefford, J. T.; Hardin, W. G.; Alexander, C. T.; Johnston, K. P.; Stevenson, K. J. Nanostructured LaNiO3 Perovskite Electrocatalyst for Enhanced Urea Oxidation. *ACS Catal.* **2016**, *6* (8), 5044–5051. https://doi.org/10.1021/acscatal.6b00487.
(67) Zhou, W.; Sunarso, J. Enhancing Bi-Functional Electrocatalytic Activity of Perovskite by Temperature Shock: A Case Study of LaNiO3−δ. *J. Phys. Chem. Lett.* **2013**, *4* (17), 2982–2988. https://doi.org/10.1021/jz401169n.
(68) Lee, D. U.; Park, H. W.; Park, M. G.; Ismayilov, V.; Chen, Z. Synergistic Bifunctional Catalyst Design Based on Perovskite Oxide Nanoparticles and Intertwined Carbon Nanotubes for Rechargeable Zinc–Air Battery Applications. *ACS Appl. Mater. Interfaces* **2015**, *7* (1), 902–910. https://doi.org/10.1021/am507470f.
(69) Hu, J.; Liu, Q.; Shi, Z.; Zhang, L.; Huang, H. LaNiO 3 -Nanorod/graphene Composite as an Efficient Bi-Functional Catalyst for Zinc–air Batteries. *RSC Adv.* **2016**, *6* (89), 86386–86394. https://doi.org/10.1039/C6RA16610E.
(70) Materials Project https://materialsproject.org/#apps/pourbaixdiagram/{“chemsys”%3A[“C”]} (accessed Nov 20, 2016).
(71) Persson, K. A.; Waldwick, B.; Lazic, P.; Ceder, G. Prediction of Solid-Aqueous Equilibria: Scheme to Combine First-Principles Calculations of Solids with Experimental Aqueous States. *Phys. Rev. B* **2012**, *85* (23), 235438.
(72) Lyon, J. L.; Stevenson, K. J. Anomalous Electrochemical Dissolution and Passivation of Iron Growth Catalysts in Carbon Nanotubes. *Langmuir* **2007**, *23* (22), 11311–11318. https://doi.org/10.1021/la7019186.

Chapter 3: Anion-Based Redox Pseudocapacitance of the Perovskite Library $La_{1-x}Sr_xBO_{3-\delta}$ (B = Fe, Mn, Co)[2]

3.1 INTRODUCTION

Humanity is heading toward a more sustainable future that utilizes renewables by humanity adopting cost effective solar and wind power in addition to electric vehicles. These technologies are creating greater demand for next generation energy storage with low cost and rapid charging capabilities. Lithium ion batteries have gained the most notoriety regarding energy storage due to relatively long charging times. With this in mind, applications that require fast charging rates such as electric vehicles or high power like grid-scale electric frequency regulation could be addressed by high power electrochemical pseudocapacitors.[1]

Electric double-layer capacitors (EDLCs) or supercapacitors that store charge electrostatically (e.g. non-faradaically) in the double layer at the surface-electrolyte interface can charge and discharge on the order of milliseconds to seconds. This accumulated charge can be thought of as a surface capacitance (dQ/dE) that results in a capacitor's energy density given by equation 1:

$$E = \frac{1}{2} C V_{cell}^2 \quad (1)$$

[2] Adapted with permission from C.T. Alexander, J. T. Mefford, J. Saunders, R. P. Forslund, K. P. Johnston and K. J. Stevenson. Anion-Based Pseudocapacitance of the Perovskite Library $La_{1-x}Sr_xBO_{3-\delta}$ (B = Fe, Mn, Co). ACS Appl. Mater. Interfaces 2019, 11, 5084−5094. Copyright © 2019 American Chemical Society. C.T. Alexander synthesized the Sr-rich composites, did iodometric titrations of the iron series, made and tested the asymmetric pseudocapacitors and wrote the manuscript. J. Saunders synthesized most of the samples. J. T. Mefford performed CVs on the single perovskite materials and assisted intellectually. R. P. Forslund made the $LaFeO_3$ sample. K. P. Johnston and K. J. Stevenson assisted in writing the manuscript.

where E is the energy density (Wh kg^{-1}), C is the specific capacitance (F g^{-1}) of the electroactive material, and V_{cell} is the applied cell voltage. Unfortunately, because EDLCs only store charge non-faradaically at the material's surface, the bulk material is effectively wasted mass and volume. If charge could be stored faradaically similar to a battery, then the bulk material could be much more efficiently utilized.

Pseudocapacitors are a promising energy storage technology because they store charge faradaically like a battery, but the charge is stored near the surface which allows for faster charging and discharging. Pseudocapacitors faradaic charge transfer occurs via one of three different mechanisms such as underpotential deposition, redox pseudocapacitance, or cation intercalation pseudocapacitance[2]. For the curious reader, we advise seeing Conway[2] and Augustyn[3] to find more detailed explanations about these electrochemical mechanisms. Pseudocapacitive behavior is indicated by current-voltage curves with redox peak currents that are linearly proportional to the scan rate (ν) superimposed onto the general rectangular shape in an EDLC's profile.[2] This means the capacitance is not always constant over the potential window and the material is thus said to exhibit pseudocapacitance.

The breadth of pseudocapacitive materials that have been studied is vast and includes high surface area and functionalized carbons, RuO_2,[2] MnO_2,[2] IrO_2, $NiO/Ni(OH)_2$, $Co_3O_4/Co(OH)_2$, SnO_2, V_2O_5, etc. as reviewed elsewhere.[3,5,10,12] Our group previously reported the first example of hydroxide anion-based pseudocapacitance in an oxygen vacancy rich $LaMnO_3$ perovskite material to be an excellent pseudocapacitor.[15] In follow on work our group demonstrated that the redox potential of the B-site can be

shifted by substituting higher oxidation state elements with lower ones such as replacing La^{3+} with Sr^{2+} in the A-site. Because electroneutrality is required, this lower oxidation state substitution must be compensated for by either the B-site oxidizing or oxygen vacancies forming.[16,17] Our group showed that the anion intercalation mechanism in $LaMnO_3$ is affected by the oxygen vacancy content (δ) and can be described in a perovskite for a given transition metal B as:

$$La_{1-x}Sr_x\left[B_{2\delta}^{z+};B_{2\delta}^{(z+1)+}\right]O_{3-\delta}+2\delta e^-+\delta H_2O \leftrightarrow La_{1-x}Sr_x\left[B_{2\delta}^{z+};B_{(1-2\delta)}^{(z+1)+}\right]O_{3-\delta}+2\delta OH^- \quad (2)$$

Recently, others have also demonstrated anion-based pseudocapacitance in BSCF,[18] $SrCo_{0.9}Nb_{0.1}O_{3-\delta}$,[19] $LaNiO_3$,[20] and $La_{1-x}Sr_xMnO_3$ (x = 0-0.5).[21] For instance, Liu[18] studied BSCF and hexagonal-$SrCoO_3$ pseudocapacitance and found that cation leaching during cycling increases the perovskite surface area and the resulting pseudocapacitance. Additionally, our group has previously noted oxygen ion mobility in electrocatalytic applications in the $La_{1-x}Sr_xCoO_{3-\delta}$ (x = 0-1) series as well.[16] Perovskite oxides are a robust platform to tune their electrochemical properties via elemental substitution in their A and B-sites.

Herein, we report the synthesis and characterization of the structural and electrochemical properties of a library of perovskites with the composition $La_{1-x}Sr_xBO_{3-\delta}$ (x = 0-1; B = Fe, Mn, Co) to better understand the phase space for designing asymmetric anion-based pseudocapacitors with wide voltage windows. Moreover, we show that the iron, manganese and cobalt series' surface area-normalized capacities increase linearly

with oxygen vacancy content and that the B-site controls the standard redox potential. The material with the highest measured pseudocapacitance was $La_{0.2}Sr_{0.8}MnO_{2.7}$ yielding 492 F g_{ox}^{-1} at 5 mV s^{-1}, and because each B-site element has its own characteristic redox potential, two perovskites could be chosen to produce a larger voltage window with high pseudocapacitance which will be discussed further in Chapter 4.

3.2 EXPERIMENTAL

3.2.1: Chemicals

$La(NO_3)_3*6H_2O$ (99.995%), $Sr(NO_3)_2$ (99+%), $Fe(NO_3)_3*9H_2O$ (99.995%), $Mn(NO_3)_2*4H_2O$ (99.999%), $Co(NO_3)_2*6H_2O$ (98%), tetramethylammonium hydroxide (TMAOH, 99%), tetrapropylammonium bromide (TPAB, 98%), citric acid, ethylenediaminetetraacetic acid (EDTA), sodium hydroxide, potassium hydroxide, and anhydrous ethanol (Absolute 200 proof) were purchased from Fisher Scientific. These chemicals and diethylene glycol (DEG), hydrochloric acid (HCl), potassium iodide (KI), standard potassium iodate (KIO_3) solution, corn starch, sodium thiosulfate ($Na_2S_2O_3$), XC-72 Vulcan carbon (VC), nitric acid (HNO_3), Nafion (5 wt.% in ethanol), and deionized water (18 MΩ cm) were all used as received without further purification.

3.2.2: Synthesis of $La_{1-x}Sr_xBO_{3-\delta}$ (B = Fe, Mn, Co; 0<x<1)

The perovskite materials in this paper were made via a co-precipitation synthesis[22] similar to our previous work.[15,16,23] For brevity, the materials $La_{1-x}Sr_xBO_{3-\delta}$ (B=Fe, Mn or Co) will be referred to as LSBOX(1-X) (for example, $La_{0.2}Sr_{0.8}MnO_{3-\delta}$ will

be referred to as LSMO28). Briefly, 50 mL of an aqueous 0.5 M metal nitrate solution with the appropriate cation ratios to make the target material was slowly titrated (~1 drop every 3 seconds) into 200 mL of a 10 wt.% TMAOH solution containing 1349 mg TPAB. A light brown precipitate formed with each drop and the solutions were stirred for at least three days, but the $SrCoO_{3-\delta}$ and $SrFeO_{3-\delta}$ samples were stirred for 5 days and 10 days, respectively. The samples with more Sr^{2+} added would form a white film on the solution surface and the light brown precipitates would turn dark brown in color that was almost black after a day of stirring. The key to promote intimate precursor mixing is to slow the drip rate for samples with more Sr^{2+} content to allow for more ambient CO_2 to dissolve in solution to form CO_3^{2-} ions and precipitate $SrCO_3$. Additionally, we realized this after the samples were made and the same compositions could be more easily synthesized if Na_2CO_3 were added to the TMAOH solution as the carbonate source. The precipitates were collected using two 50 mL centrifuge tubes per sample, centrifuged at 8000 r.p.m. for four minutes and the supernatant was decanted off. The precipitates were washed and vortexed with ~35 mL of deionized (DI) water per centrifuge tube three times and collected by centrifugation each time using the above conditions. The precipitate was resuspended with DI water and probe sonicated for three minutes. The suspension was frozen as a thin film by spraying it from a squirt bottle held about three feet high onto a rotating drum at cryogenic temperatures using dry ice. The ice encasing the precipitate was lyophilized away at -10^{o}C and ~25 mTorr for at least 24 hours.[24]

The remaining powder was calcined using a tube furnace with a quartz tube and alumina calcination boat to hold the samples. Samples were heated in air from room

temperature to 120°C in 35 minutes, held at 120°C for one hour, heated to 950°C in 45 minutes and held at 950°C for 4 hours for the iron and manganese samples and 5 hours for the cobalt series before the materials cooled naturally to room temperature. $LaMnO_3$ was heated to 700°C instead of 950°C and LSMO28 was reduced at 400°C for 4 hours in a 7% H_2/Ar atmosphere to form the perovskite phase. Rapidly quenching[25–27] SCO with liquid N_2 and with air cooled cryogenically with acetone and dry ice yielded $Sr_2Co_2O_5$ (BM-SCO) while using an O_2 atmosphere yielded the phase pure SCO perovskite phase. The perovskite SFO phase was reduced to $Sr_2Fe_2O_5$ (BM-SFO) by heating the SFO to 350°C in a 7% H_2/Ar atmosphere for 4 hours followed by cooling naturally to room temperature. A summary of relevant experimental parameters is given in Table A9.

3.3.3: Citric Acid Synthesis of $LaFeO_3$

LFO was difficult to make phase pure via the co-precipitation synthesis so a citric acid route, also known as the Pechini synthesis, was used.[22] In short, the metal nitrates were mixed in deionized water with citric acid, EDTA, DEG in a 1:1:1:0.66 molar ratio based on a total metal cation concentration. The pH was raised to 7 using a 10 wt% TMAOH solution and the water was magnetically stirred and heated to evaporate the water and form a gel that was subsequently burned to a char on a hotplate in a closed fume hood followed by calcination in air at 700°C for 4 hours as described above and in Table A9.

3.3.4: Materials Characterization.

The materials' lattice structure was determined using wide-angle X-ray diffraction on a Rigaku Spider instrument with Cu Kα radiation (λ = 1.5406 Å) source at 40 mA and 40 kW. The data was analyzed using JADE software to identify phases. A Brunauer-Emmett-Teller (BET) instrument (Quantachrome Instruments NOVA 2000 high-speed surface area analyzer) was used to degas the samples overnight under vacuum and measure sample surface areas at 77 K using N_2 adsorption. Data points from the 0.05 to 0.3 P/P_o range were used to extract the surface area from the adsorption data as shown in Figure A22. B-site oxidation state and oxygen vacancy content was measured using iodometric titrations as reported previously[16,28] using solutions made from preboiled deionized water. Approximately 15-20 mg of sample was added to a sealed 3-neck round bottom flask and dissolved in Ar-saturated 6 M HCl. It was noted that the LSFO x = 0-0.8 samples required at least 20 minutes to dissolve completely. 3 mL of 2 M KI was added to the cell and was immediately titrated with 25 mM $Na_2S_2O_3$ solution that had been standardized against a 0.1 M KIO_3 standard solution. When the solution had been titrated to a faint yellow color, 1 mL of starch indicator made from the supernatant of a boiled 1 wt.% corn starch solution was added. The solution was then titrated until its color changed from deep purple to clear. All iodometric titrations were made in triplicate.

3.3.5: Three-electrode cell preparation.

Electrodes were prepared the same way as described earlier,[15,29,30] but with modifications made to the perovskite to carbon weight ratio. Briefly, all carbon and perovskite powders were washed with deionized water three times and ethanol three

times using vacuum filtration followed by ball milling for three minutes in a Wig-L-Bug ball mill. All powders were supported onto activated Vulcan carbon (VC^A) in an 85:15 perovskite: carbon weight ratio by ball milling for three minutes. The VC was activated by soaking it in 1 M HNO_3 overnight at 80°C. The composite materials were sonicated in 1 mg mL^{-1} solution of ethanol with 0.05 wt% Na-substituted Nafion for two hours before being pipetted and spun-cast at 700 r.p.m. onto the rotating disk electrode's (RDE's) glassy carbon disk (diameter = 0.5 cm, area = 0.196 cm^2) at a 51.0 μg cm^{-2} (10 μg) total mass loading. The RDEs used to measure the carbon capacitance had a 7.65 μg cm^{-2} mass loading (1.5 μg). RDEs were prepared by sonicating the disk in a 1:1 ethanol: deionized water solution, followed by polishing using 50 nm alumina, rinsing and sonicating in a fresh 1:1 ethanol: deionized water solution.

3.3.6: Electrochemical Measurements.

Three-electrode electrochemical testing was performed on a Metrohm Autolab PGSTAT302N and CH Instruments CHI832a with high speed rotators from Pine instruments. A Hg/HgO (1 M KOH) reference electrode and Au wire counter electrode were used for the 3-electrode measurements and all tests were conducted in Ar-saturated 1 M KOH. The cyclic voltammograms (CVs) on the $La_{1-x}Sr_xFeO_{3-\delta}$ (-1.2 V to 0.2 V vs Hg/HgO), $La_{1-x}Sr_xMnO_{3-\delta}$ (-0.6 V to 0.4 V vs Hg/HgO) and $La_{1-x}Sr_xCoO_{3-\delta}$ (-0.4 V vs 0.5 V vs Hg/HgO) materials were cycled for at most 10 cycles at 100 mV s^{-1} or until the CV stabilized to measure the specific capacitance (F g^{-1}) measurement according to equation 3:[2]

$$C_s = \frac{1}{2m\nu|V_c - V_a|} \oint_{V_a}^{V_c} i\,(V)dV \quad (3)$$

Where *m* is the mass loading of electroactive material on the electrode (g), ν is the scan rate of the CV (V s^{-1}) while V_c and V_a are the cathodic and anodic limits of the CV window. The integral represents the entire area within the CV loop over the cathodic and anodic sweeps which is divided by 2 to yield the average capacitance for a single sweep. Every sample was tested using five electrodes with each electrode's capacitance measured in triplicate at one scan rate (100, 50, 25, 10, 5 mV s^{-1}) per electrode to get an average and standard deviation. The carbon contribution (in Figure A23) was removed to clearly delineate the role of the perovskites.

3.3: RESULTS AND DISCUSSION

3.3.1: Perovskite crystal structure and surface area trends

For simplicity, the perovskite samples will be referred to as LSBO(1-X)X (e.g. $La_{0.2}Sr_{0.8}FeO_{3-\delta}$ as LSFO28) and brownmillerite phases will be labeled with 'BM' (e.g. $Sr_2Co_2O_5$ as BM-SCO). The materials from this study were synthesized phase pure using our previously developed coprecipitation synthetic method[24,30] as confirmed by XRD in Figure 3.1. Materials were calcined at 950°C to decompose the $SrCO_3$ precursor[32] and crystallize the correct phase for all Sr^{2+}-containing compositions.[26,27] The x = 0-0.2 LSFO samples in Figure 3.1a formed the orthorhombic *Pbnm* structure while the higher Sr-content (x = 0.4-0.8) samples formed the rhombohedral *R-3c* lattice structure as their Goldschmidt tolerance factor increased which is in agreement with crystal system trends observed in the literature.[17] Complete Sr^{2+} substitution into La^{3+} sites yielded the cubic

Pm-3m perovskite phase (SFO) while the brownmillerite BM-SFO assembled into the orthorhombic *Ibm2* lattice structure. Our results, summarized in Table A10, mostly agree with the LSFO phase diagram[33] with the differences in LSFO28 being attributed to its high oxygen vacancy concentration. The orthorhombic phase formations in the x = 0-0.2 and BM-SFO compositions likely result from the predominance[33,34] of Fe^{3+} and Fe^{5+} that do not cause the Jahn-Teller distortion elongation of the c-axis. However, the ionic radii of these ions in the B-site yields a Goldschmidt tolerance factor less than 0.9 which causes significant octahedral tilting and distortion of a would-be cubic lattice into an orthorhombic lattice.[35,36] Upon further Sr^{2+} substitution, as Dann *et. al.* showed,[33] Fe^{5+} is replaced by Fe^{4+} as the predominate higher oxidation state which causes Jahn-Teller distortions that elongate the c-axis that would favor a tetragonal crystal system, but a tolerance factor less than 1 causes slight octahedral tilting that leads to the rhombohedral structure.[36] The peaks at approximately 32º and 57º 2θ in Figure 3.1b-c correspond to the (200) and (300) planes which are oxygen rich. These peaks shift to higher 2θ which indicates the oxygen planes get closer together with increasing Sr^{2+} content. The BM-SFO phase is an exception whose peaks shift to lower 2θ similar to the lower Sr^{2+} LSFO orthorhombic phases, except the peak splits indicating ordering in the (200), (141) and (002) planes.

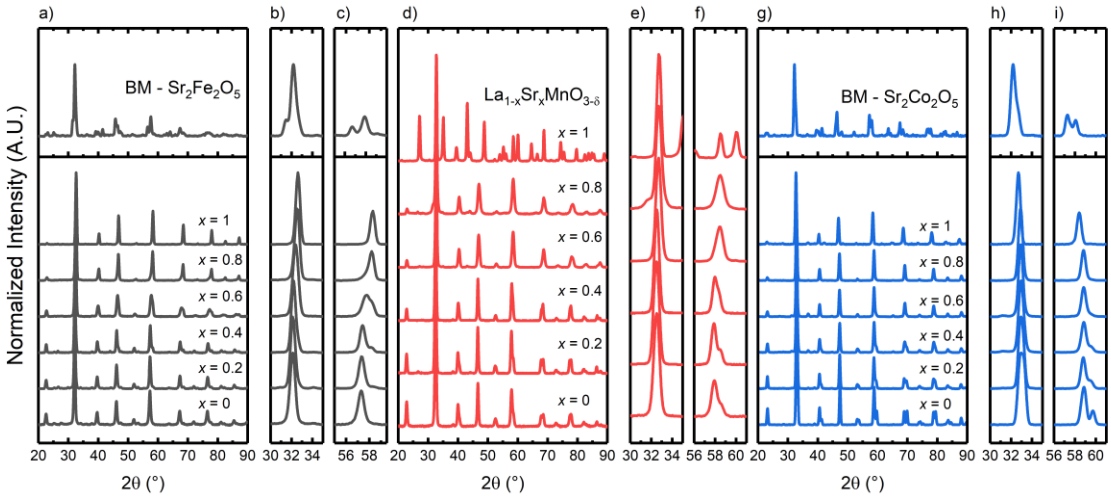

Figure 3.1 | PXRD patterns of $La_{1-x}Sr_xBO_{3-\delta}$ (B = Fe, Mn, Co).

(a-c) $La_{1-x}Sr_xFeO_{3-\delta}$ series, (d-f) $La_{1-x}Sr_xMnO_{3-\delta}$ series and (g-i) $La_{1-x}Sr_xCoO_{3-\delta}$ series with the peaks at ~32° 2θ and ~57° 2θ respectively magnified for clarity.

In contrast to the LSFO series, the LSMO sample with x = 0-0.4 crystallized into the rhombohedral *R-3c* lattice followed by the tetragonal *I4/mcm* structure for the x = 0.6-0.8 compositions in agreement with the LSMO phase diagram under our calcination conditions.[37,38] The predominance of Mn^{3+} as shown in Figure 3.2a explains the elongated c-axis for all LSMO samples due to Jahn-Teller distortions caused by Mn^{3+}. Substituting all of the La^{3+} for Sr^{2+} in the A-site gives a Goldschmidt-tolerance factor greater than one yielding the hexagonal *P6₃/mmc* phase[17] as seen in Figure 3.1d for x = 1 with results summarized in Table A11. The purpose of this paper is to elucidate trends in perovskite-based pseudocapacitance so the hexagonal SMO phase was not utilized in electrochemical experiments. Examining Figures 3.1e and 1f shows the (200) plane spacing does not shift within the sensitivity of our instrument while the lattice appears to

contract slightly with increasing Sr^{2+} content as shown by the shift to higher 2θ for the peak at ~58° 2θ.

Figure 3.1g shows that LSCO with x = 0-0.4 formed the rhombohedral *R-3c* structure while the higher Sr^{2+} content at x = 0.6 and at x = 0.8 formed the cubic *Pm-3m* and tetragonal *P4/mmm* phases, respectively. At x = 1 the perovskite SCO crystallized into the tetragonal *I4/mmm* lattice if calcined under an oxygen atmosphere while the brownmillerite BM-SCO formed the orthorhombic *Imma* structure during calcination in air. Unlike LSFO and LSMO, the peaks at ~33° and ~59° 2θ in Figures 3.1h and 3.1i do not shift within the sensitivity of our instrument except for the SCO and BM-SCO compositions where peaks shifted to lower 2θ indicating a slight unit cell expansion. These crystal structure transformations at increasing Sr^{2+} content are summarized in Table A12 and show agreement with the LSCO phase diagram.[39] Greater detail on the LSCO series' crystal structure can be found in our previous work.[16]

Brunauer-Emmett-Teller N_2 adsorption was used to measure the sample surface areas which were approximately 3-5 $m^2\ g^{-1}$ for LSFO and LSCO while LSMO had a range of 6-11 $m^2\ g^{-1}$ with values summarized in Table A13. Most of these surface areas are lower than what was reported in our previous work (~10 $m^2\ g^{-1}$)[15,24,30] because most of the materials were calcined at 950°C as opposed to 700°C which caused increased sintering. Additionally, difficulties synthesizing LFO using the coprecipitation synthesis and instead prompted the use of a Pechini-type synthesis utilizing citric acid as a chelating agent that intimately mixes metal oxide precursor particles instead of metal

hydroxides. Using this synthesis allowed for calcination at 700°C which yielded a higher surface area (11 m^2 g^{-1}) due to reduced sintering at the lower temperatures.

3.3.2: Sr^{2+} content affects oxygen vacancy concentration and B-site oxidation state

Replacing La^{3+} with Sr^{2+} in the perovskite A-site adds an extra electron per formula unit which has to be compensated for by either forming oxygen vacancies or through further oxidation of the B-site.[16,17,40] Oxygen vacancy content and B-site oxidation state were determined by performing iodometric titrations in triplicate with data plotted in Figure 3.2 and values summarized in Table A14. The overarching trend for the three series in Figure 3.2b is a systematic increase in oxygen vacancy concentration with further Sr^{2+}-substitution, but the magnitudes of the trends vary considerably depending on the Sr^{2+} content. Examining the LSFO series in Figure 3.2 shows that iron in the B-site causes the perovskite to preferentially form oxygen vacancies (δ) rather than oxidizing the iron center because of the difficulty in oxidizing Fe^{3+} except for the SFO perovskite phase denoted by the grey star.

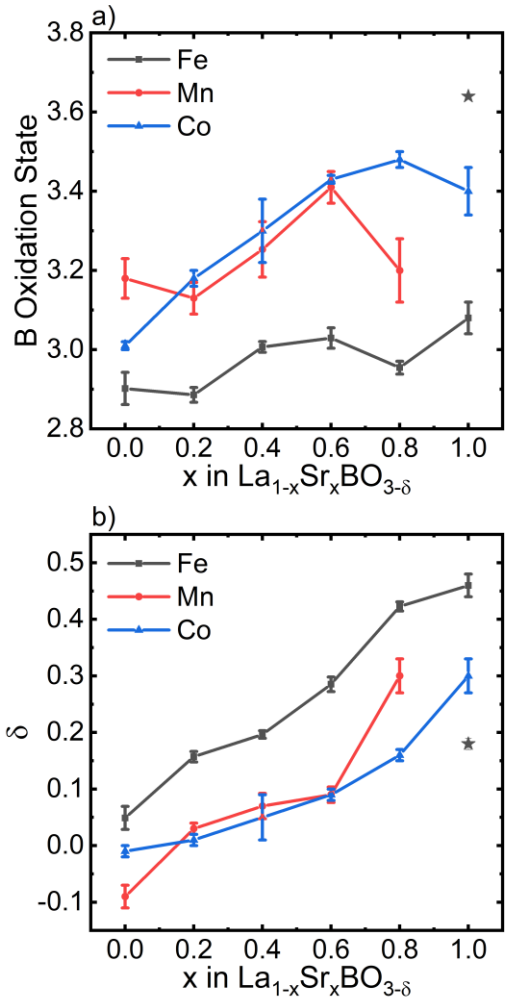

Figure 3.2 | B site oxidation state and oxygen vacancy characterization.

(a) B-site oxidation state (z^{+}) of $La_{1-x}Sr_xBO_{3-\delta}$ (B = Fe, Mn, Co) and (b) oxygen vacancy content (δ) versus Sr^{2+} content (x). The * is the perovskite $SrFeO_{3-\delta}$.

Unlike LSFO, LSMO preferentially oxidizes Mn^{3+} to Mn^{4+} rather than form oxygen vacancies after removing super-stoichiometric lattice oxygen (x = 0). To convert the partially hexagonal LSMO28 phase into the tetragonal perovskite phase, the sample was reduced in a 7% H_2/Ar atmosphere at 400°C that converted Mn^{4+} into the larger

Mn^{3+}. This reduction treatment is responsible for the uptick in the LSMO28 oxygen vacancy concentration to $\delta = 0.3 \pm 0.03$.

The LSCO iodometric titration trends agree with our previous results[16] that demonstrate preferential Co^{3+} oxidation to Co^{4+} until approximately $Co^{3.5+}$ at which point the oxygen vacancy concentration increases significantly with a constant $Co^{3.5+}$ oxidation state because of Fermi edge pinning the O_{2p} band.[41] The reason the SCO oxidation state decreased relative to LSCO28 in Figure 3.2a is because at high temperatures metal oxides become thermally reduced and emit O_2 from the lattice, and quenching the SCO from 950^{o}C to room temperature would not give the perovskite time to reincorporate oxygen into its lattice structure while cooling to room temperature.

3.3.3: Sr^{2+} effect on pseudocapacitance and redox potentials for $La_{1-x}Sr_xBO_{3-\delta}$ (B = Fe, Mn, Co)

The CVs in Figure 3.3a-c were used to calculate the perovskites' gravimetric capacitance (Figure 3.3d-f) and demonstrate a consistent increase in capacitance with increasing Sr^{2+} content for all three series. Capacitance at various scan rates is plotted in Figure A24 with the activated Vulcan carbon (VC^A) contribution (shown in Figure A23) removed for clarity as well. As shown in Figure A25, OH^- anion-based pseudocapacitance is the dominant charge storage mechanism, in agreement with our previous work.[15] K^+ ion intercalation is ruled out by the significant decrease in the CV area of the most capacitive materials (BM-SFO, LSMO28, SCO) when the electrolyte was changed from alkaline 1 M KOH to the neutral 1 N K_2SO_4 despite the K^+ electrolyte concentration being held constant.

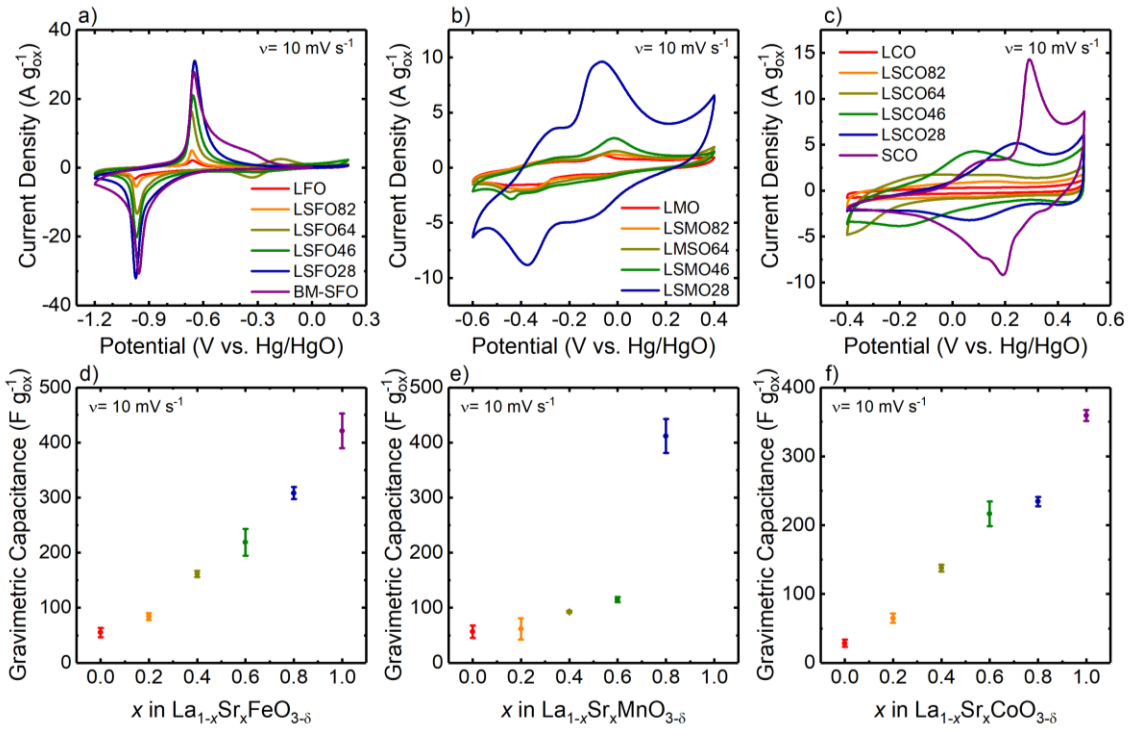

Figure 3.3 | Electrochemical characterization of $La_{1-x}Sr_xBO_{3-d}$ (B = Fe, Mn, Co).

Cyclic Voltammograms at 10 mV s^{-1} of (a) $La_{1-x}Sr_xFeO_{3-\delta}$ (b) $La_{1-x}Sr_xMnO_{3-\delta}$ (c) $La_{1-x}Sr_xCoO_{3-\delta}$ with the corresponding pseudocapacitance trends with Sr^{2+} content at 10 mV s^{-1} in Ar-saturated 1 M KOH for the (d) Fe, (e) Mn, (f) Co series with 51 µg cm^{-2} mass loadings on RDEs.

It is surprising at first that the LSFO series' $E_{1/2}$ redox potential lies at a more negative (i.e. higher energy) potential than the more electropositive LSMO series, but this is explained by the extra electron in Fe^{2+} with higher energy due to electron-pair repulsions in the t_{2g} band shown schematically in Figure 3.4i. This observation is further supported by the relative oxidation state trends between series shown in Figure 3.2a with a trend of increasing oxidation state in the order $Fe^{2+/3+} < Mn^{3+/4+} < Co^{3+/4+}$ that matches well with the observed peak positions. Comparing the three B-site series, the LSFO

samples have the highest peak currents that suggest fast lattice oxygen diffusion rates which is supported by the LSFO series' high oxygen vacancy concentrations. The redox peaks centered at $E_{1/2}$ ~ -0.8 V vs Hg/HgO are attributed to OH^- anion intercalation induced by $Fe^{2+/3+}$ and possibly $Fe^{3+/5+}$ transitions through Fe^{4+} disproportionation as described by Dann et.al.[33] for x = 0, 0.2[33] and BM-SFO,[34] but LSFO64 shows the presence of a reversible redox peak centered at ~ -0.3 V vs Hg/HgO which is attributed to be the $Fe^{3+/4+}$ transition.

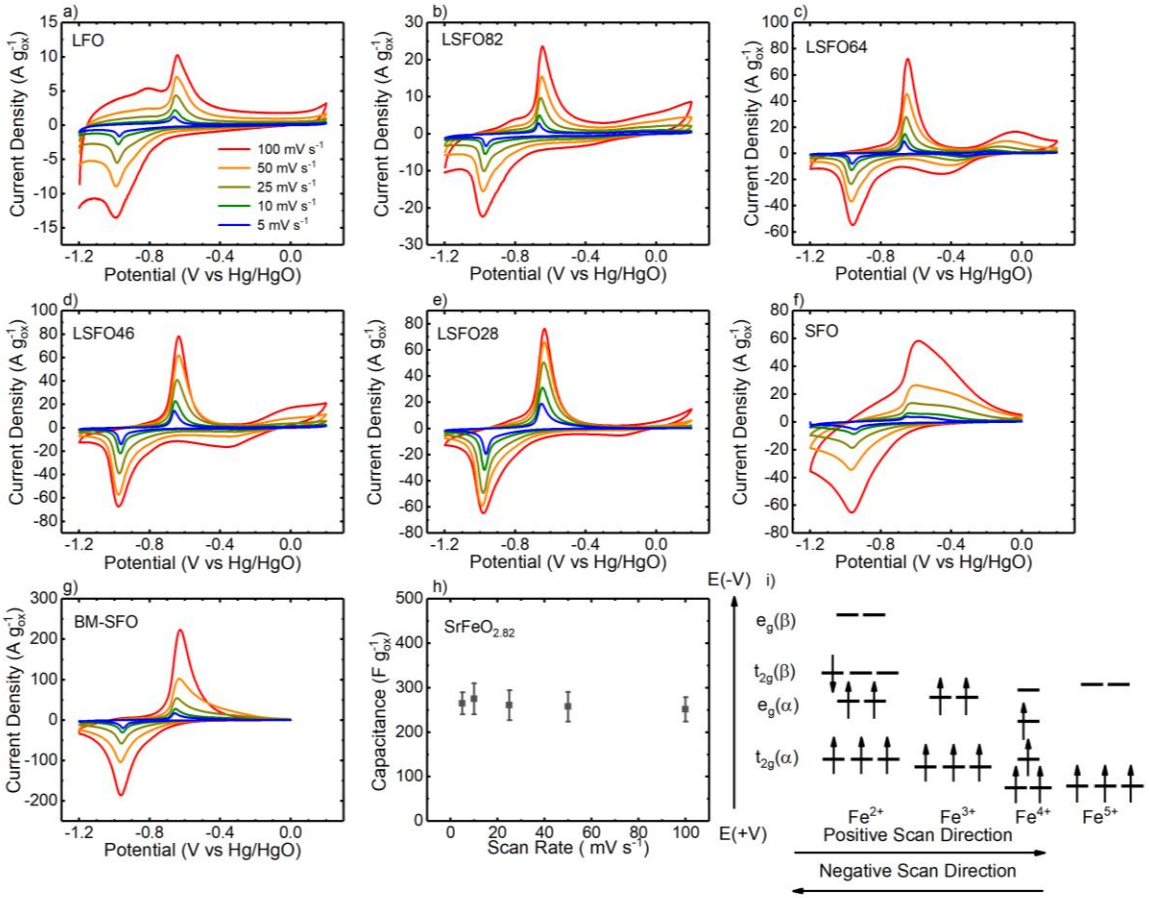

Figure 3.4 | $La_{1-x}Sr_xFeO_{3-\delta}$ series cyclic voltammetry scan rate dependence.

Cyclic voltammograms at 100, 50, 25, 10, 5 mV s^{-1} scan rates in Ar-saturated 1M KOH with 51 μg cm^{-2} loadings are given for (a) LFO, (b) LSFO82, (c) LSFO64, (d) LSFO46, (e) LSFO28, (f) SFO, (g)BM-SFO. The anodic redox peak at ~-0.8 V vs Hg/HgO and capacitive current at lower potentials for all samples is likely due to hydrogen adsorption/desorption in alkaline conditions as reported previously.[3] Measured capacitance values at different scan rates with carbon contributions subtracted out are shown for (h) $SrFeO_{2.82}$ and a scheme (i) depicting the electronic configuration of Fe^{2+}, Fe^{3+}, Fe^{4+}, and Fe^{5+} is presented to rationalize LSFO peak positions. The down spin (β) energy levels are omitted for $Fe^{3+/4+/5+}$ for simplicity because they are unoccupied.

Upon studying the redox peaks centered at -0.8 V vs Hg/HgO in Figure 3.4 in comparison with Figure 3.2, it is apparent that increasing oxygen vacancy content caused by Sr^{2+} substitution (Figure 3.2b) is responsible for the peaks' growth as the iron oxidation state remained relatively constant. In contrast, the higher potential redox peaks at ~ -0.3 V vs Hg/HgO are more apparent at higher scan rates in $La_{1-x}Sr_xFeO_{3-\delta}$ for x = 0.2-0.8 and its size trends with iron's oxidation state in Figure 3.2a. The oxidation state dependence gives credence to the idea that these higher-potential peaks result from $Fe^{3+/4+}$ transitions through OH^- anion (de)intercalation. Interestingly, the $Fe^{3+/4+}$ redox peaks shift ~100 mV more positive indicating the materials' decreasing Fermi energy with increasing Sr^{2+} content. The SFO redox peak broadening shown in Figure 3.4f is likely caused by a much larger $Fe^{3+/4+}$ couple that merges with the $Fe^{2+/3+}$ peak due to its much higher oxidization state (z+ ~ 3.6+) relative to the other LSFO compositions (z+ ~ +2.9) plotted in Figure 3.2a. Figure 3.3a reveals at lower scan rates that the BM-SFO has a lower peak current than LSFO28 which implies slower lattice oxygen diffusion than LSFO28. Additionally, BM-SFO has a broad shoulder on the anodic scan that is attributed to a two phase transition from BM-SFO to $SrFeO_{2.75}$ as the oxide ion intercalation reaction progresses.[34]

Figure 3.3b shows the LSMO series has two pairs of redox peaks centered at -0.3 V and -0.1 V vs Hg/HgO that are attributed to $Mn^{2+/3+}$ and $Mn^{3+/4+}$ transitions respectively, caused by OH^- anion based intercalation in agreement with our previous results.[15] It is noted that the LMO capacitance is lower than what our group reported previously[15] because VC^A is used as a conductive support instead of a N-doped mesoporous carbon. Additionally, the carbon content has been decreased from 70 wt.% to 15 wt.% to better emulate practical devices that use 80-85 wt.% electroactive material.[19,42] Additionally, LSMO28 demonstrates significantly higher capacitance than the other LSMO samples due to the H_2 reduction heat treatment that significantly increased the oxygen vacancy content (Figure 3.2b) allowing for more charge storage as lattice oxygen.

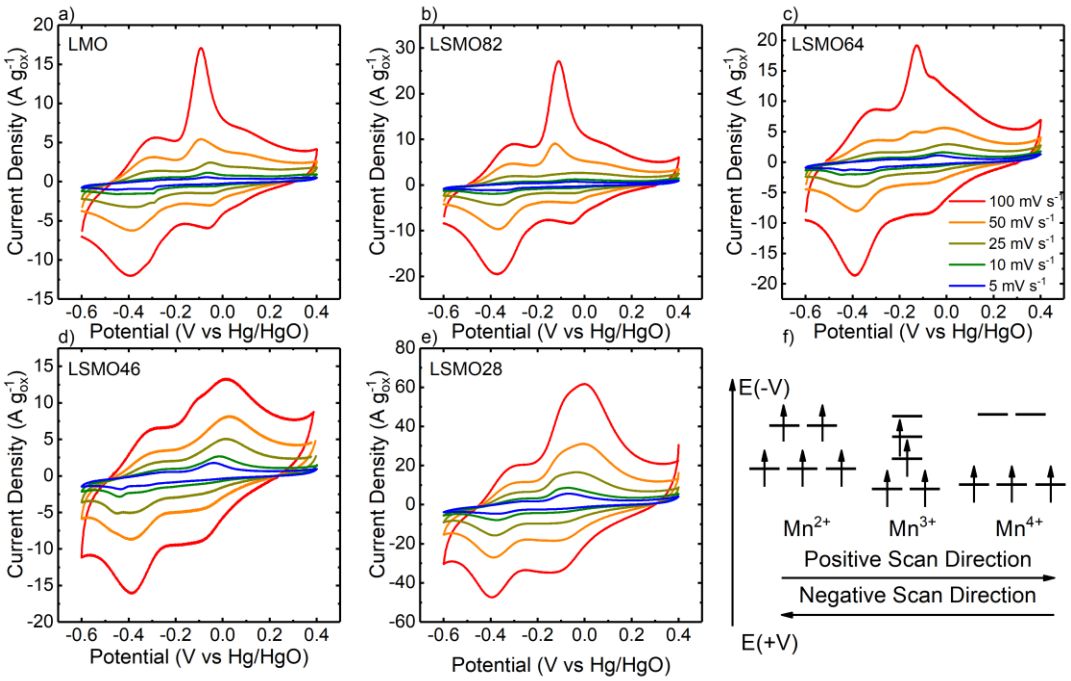

Figure 3.5 | $La_{1-x}Sr_xMnO_{3-\delta}$ series cyclic voltammetry scan rate dependence.
Cyclic voltammograms at 100, 50, 25, 10, 5 mV s^{-1} scan rates are given for (a) LMO, (b) LSMO82, (c) LSMO64, (d) LSMO46 and (e) LSMO28. A scheme (f) of the electronic configuration of Mn^{2+}, Mn^{3+} and Mn^{4+} is given as well.

Examining the LSMO series in Figure 3.5 shows there are actually three redox peaks in the positive scan direction, but only two on the back scan with the more negative of the two being approximately twice as tall as the other. Comparing the LSMO series' peaks in Figure 3.5a-e shows the middle anodic peak at -0.1 V vs Hg/HgO shrinks relative to the growing peak at 0 V vs Hg/HgO. The peak at 0 V grows consistently with oxygen vacancy concentration caused by Sr^{2+} substitution and hydrogen reduction which further supports that this feature is due to the $Mn^{3+/4+}$ redox couple from anion intercalation. In contrast, the anodic peaks at -0.3 V and -0.1 V vs Hg/HgO grow inversely to the manganese oxidation state, or, more simply, as Mn^{2+} replaces Mn^{3+} the $Mn^{2+/3+}$ redox peaks grow. The separate peak positions (-0.3 V and -0.1 V) for the $Mn^{2+/3+}$ transition is attributed to changes in oxygen energy sites when cubic Mn^{2+} converts to tetragonal Mn^{3+} resulting from Mn^{3+} Jahn-Teller distortions as depicted in Figure 3.5f, and their cathodic peaks merge to form the larger peak at ~ -0.4 V vs Hg/HgO on the negative potential sweep.

The LSCO series shows the largest redox peak shift towards higher potentials (Figure 3.3c) caused by increasing Sr^{2+} content and these peaks become more obvious when $x \geq 0.6$, due to their significant oxygen vacancy content (Figure 3.2b). The redox potential shift can be explained by the oxygen vacancy solid solution behavior that was

demonstrated previously[25,43] by galvanostatically oxidizing BM-SCO which lowers the material's Fermi level.

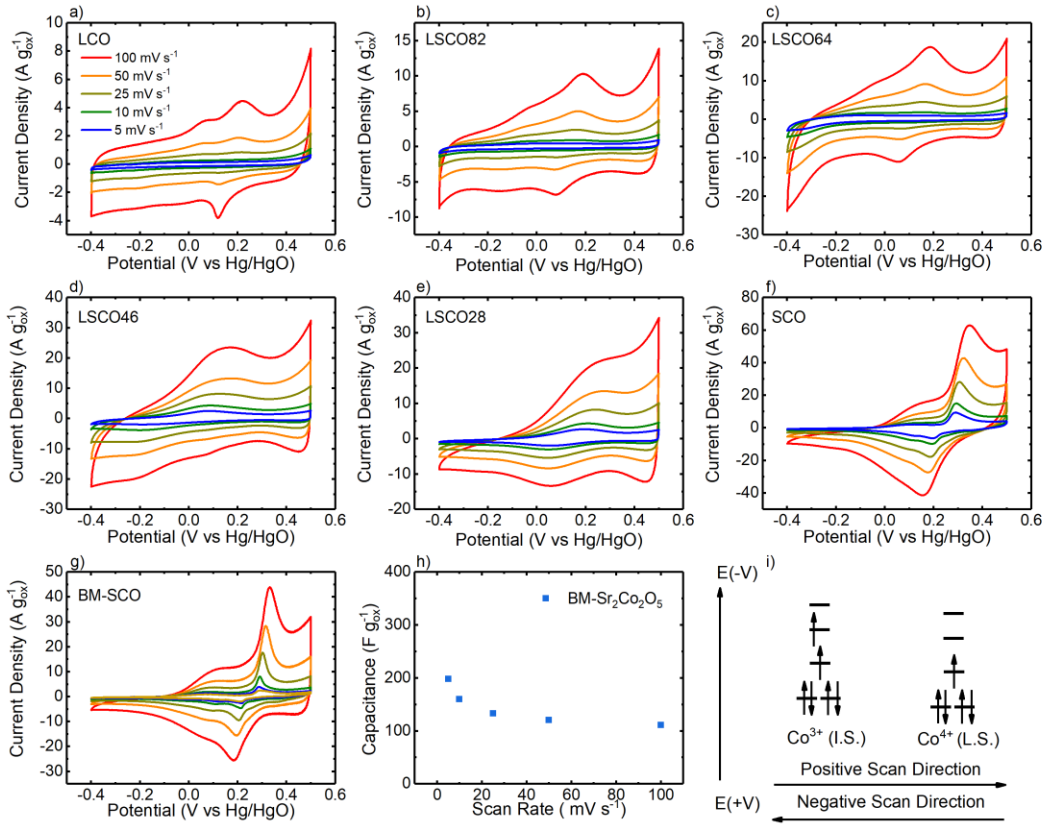

Figure 3.6 | $La_{1-x}Sr_xCoO_{3-\delta}$ series cyclic voltammetry scan rate dependence.

Cyclic voltammograms at 100, 50, 25, 10, 5 mV s^{-1} scan rates are given for (a) LCO, (b) LSCO82, (c) LSCO64, (d) LSCO46, (e) LSCO28, (f) SCO and (g)BM-SCO. Additionally, the (h) capacitance of BM-$Sr_2Co_2O_5$ and a scheme (i) of the electronic configuration of Co^{3+} and Co^{4+} is given as well. 'I.S.' and 'L.S.' are acronyms for 'Intermediate Spin' and 'Low Spin' which describe the electronic spin states of the cobalt ions.

Further examining the peak shape evolution with increasing Sr^{2+} content in Figure 3.6 shows that all LSCO compositions demonstrate redox behavior but that the x = 0-0.4 compositions have two peaks on the positive sweep. In contrast, there is only one peak on

the negative sweep and is not easily explained by the LSCO electronic configuration in Figure 3.6i. One explanation could be that the anodic peak at ~0.2 V vs Hg/HgO corresponds to the $Co^{3+\rightarrow4+}$ transition and the cathodic peak (~0.1 V vs Hg/HgO) is the $Co^{4+\rightarrow3+}$ reduction while the unpaired, anodic peak at ~0.05 V vs Hg/HgO could be due to surface restructuring causing a distribution of oxygen lattice site energies. Interestingly, the sharp redox features in the x = 0-0.4 compositions seem to combine with higher Sr^{2+}-content to form a single pair of broad, gently sloping redox peaks centered at ~0.1 V vs Hg/HgO for x = 0.6-1 suggesting these peaks have more facile anion intercalation into oxygen vacancies because there are significantly more oxygen vacancies present for these compositions according to Figure 3.2b. These $E_{1/2}$ potential appears to trend (Figure A2.5) with the samples' oxidation states (Figure 3.2a) thus suggesting that these features mark the individual compositions' Fermi energy. Additionally, the x = 1 compositions have a large, sharp pair of redox peaks centered at 0.25 V vs Hg/HgO which is attributed to a transition from cubic $SrCoO_{2.75}$ to tetragonal $SrCoO_{2.875}$ and back to cubic $SrCoO_{2.75}$ at the surface.[25] BM-SCO CVs are shown for comparison in Figure 3.6g, but interestingly its redox peaks centered around 0.25V vs Hg/HgO are much sharper relative to SCO (Figure 3.6f) indicating slower lattice oxygen diffusion which could be caused by lattice strain from brownmillerite to cubic to tetragonal transitions during oxygen intercalation.[25] A lower lattice oxygen diffusion rate means less bulk material would be utilized for charge storage and would explain why the BM-SCO capacitance, shown in Figure 3.6h, is less than half that of SCO.

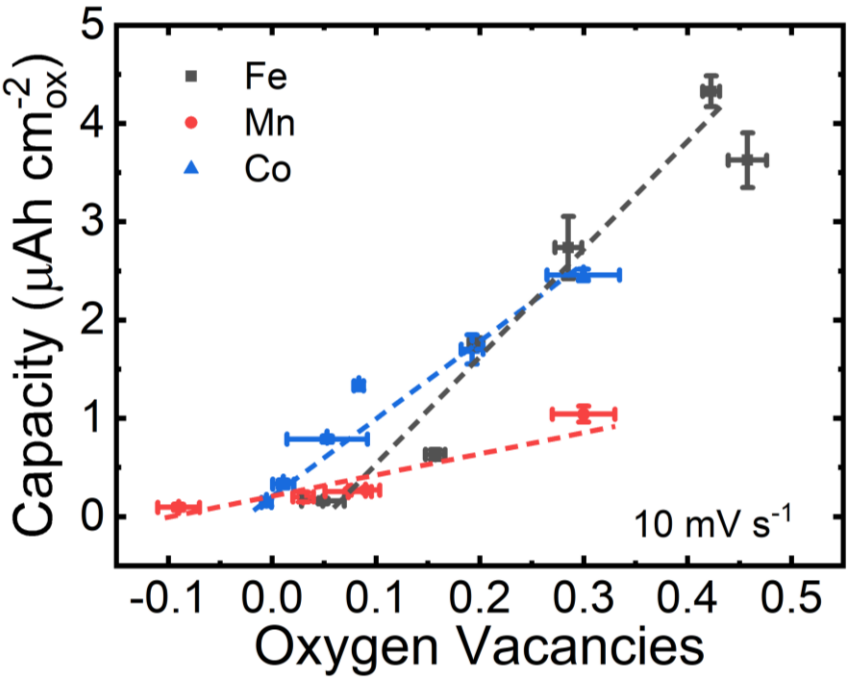

Figure 3.7 | Surface charge density versus perovskite oxygen vacancy content.

Normalizing the materials' measured charge capacity at 10 mV s^{-1} by their surface area yields linear trends versus their oxygen vacancy content. Using charge capacity rather than pseudocapacitance accounts for the different voltage window sizes between the B-site elements.

The surface area-normalized charge capacity at 10 mV s^{-1} (Figure 3.7) was found to trend linearly with perovskite oxygen vacancy concentration in Figure 3.7 for the LSFO, LSMO and LSCO series. This result agrees with previous observations[15,19] and supports the oxide anion intercalation pseudocapacitive mechanism (equation 2) where oxygen vacancies in the bulk can be utilized for charge storage despite differences in charge transfer limitations being kinetic or diffusive in nature. Interestingly, the charge capacity slope with oxygen vacancy content was different depending on the element in the perovskite B-site. If lattice oxygen diffusion is fast- meaning charge transfer is

kinetically limited like for the LSFO series-one would expect the measured capacitance to fall less substantially with increasing scan rate (Figure A24a), which further corroborates the redox peak analysis above. This observation lies in contrast to LSMO28 and SCO in Figure A24 b,c respectively, which show the LSMO28 gravimetric capacitance to remain steady only above a 25 mV s^{-1} scan rate while the SCO pseudocapacitance consistently falls with increasing scan rate. These observations suggest that LSMO28 is diffusion limited at scan rates below 25 mV s^{-1} and can more easily access the bulk structure while SCO is constantly diffusion limited at the relevant time scale because at slower scan rates it will have more time to utilize the bulk material for charge storage.

In summary, we have synthesized a phase pure perovskite library with compositions $La_{1-x}Sr_xBO_{3-\delta}$ (B = Fe, Mn, Co; x = 0-1) and have measured the materials' anion-intercalation pseudocapacitance as a function of oxygen vacancy content. The perovskites' pseudocapacitance was found to increase linearly with oxygen vacancy concentration via Sr-substitution into the A-site. Additionally, the redox potential was found to depend on the transition metal in the B-site and the transition metal's oxidation state. Thus, we have explored the perovskite phase space that will allow better future design for perovskite asymmetric pseudocapacitors.

3.4: CONCLUSIONS

We have synthesized three series of perovskite oxides with increasing Sr^{2+} content ($La_{1-x}Sr_xBO_{3-\delta}$, x = 0-1, B = Fe, Mn, Co) to better understand pseudocapacitor

design parameters and demonstrate the first all-perovskite asymmetric pseudocapacitors. Upon carefully selecting the A and B site perovskite compositions, the voltage window and redox peak currents may be manipulated to raise energy and power densities to levels on par with leading pseudocapacitors. Results showed that oxygen vacancies caused by Sr^{2+} substitution linearly increases the area-normalized charge capacity with the slope dependent on the B-site element. While oxide vacancies affect the pseudocapacitance, it was found that the B-site element and its oxidation state control the redox peak positions, with a higher oxidation state leading to a more positive redox potential. These descriptors will enable the future design of high energy density asymmetric pseudocapacitors.

3.5 ADDITIONAL INFORMATION

More details can be found in Appendix 2 regarding synthesis conditions, sample characterization, carbon capacitance contributions, sample crystallographic parameters, sample capacitance values at multiple scan rates and their electrochemical characterization in addition.

3.6 REFERENCES

(1) Miller, J. R.; Simon, P. MATERIALS SCIENCE: Electrochemical Capacitors for Energy Management. *Science* **2008**, *321* (5889), 651–652. https://doi.org/10.1126/science.1158736.

(2) Conway, B. E. *Electrochemical Supercapacitors: Scientific Fundamentals and Technological Applications*; Springer Science & Business Media, 2013.

(3) Augustyn, V.; Simon, P.; Dunn, B. Pseudocapacitive Oxide Materials for High-Rate Electrochemical Energy Storage. *Energy Environ. Sci.* **2014**, *7* (5), 1597. https://doi.org/10.1039/c3ee44164d.

(4) Simon, P.; Gogotsi, Y. Materials for Electrochemical Capacitors. *Nat. Mater.* **2008**, *7* (11), 845–854. https://doi.org/10.1038/nmat2297.

(5) Wang, G.; Zhang, L.; Zhang, J. A Review of Electrode Materials for Electrochemical Supercapacitors. *Chem Soc Rev* **2012**, *41* (2), 797–828. https://doi.org/10.1039/C1CS15060J.

(6) Wang, F.; Xiao, S.; Hou, Y.; Hu, C.; Liu, L.; Wu, Y. Electrode Materials for Aqueous Asymmetric Supercapacitors. *RSC Adv.* **2013**, *3* (32), 13059. https://doi.org/10.1039/c3ra23466e.
(7) Mefford, J. T.; Hardin, W. G.; Dai, S.; Johnston, K. P.; Stevenson, K. J. Anion Charge Storage through Oxygen Intercalation in LaMnO3 Perovskite Pseudocapacitor Electrodes. *Nat. Mater.* **2014**, *13* (7), 726–732. https://doi.org/10.1038/nmat4000.
(8) Mefford, J. T.; Rong, X.; Abakumov, A. M.; Hardin, W. G.; Dai, S.; Kolpak, A. M.; Johnston, K. P.; Stevenson, K. J. Water Electrolysis on La1-xSrxCoO3-δ Perovskite Electrocatalysts. *Nat. Commun.* **2016**, *7*, 11053. https://doi.org/10.1038/ncomms11053.
(9) Richter, J.; Holtappels, P.; Graule, T.; Nakamura, T.; Gauckler, L. J. Materials Design for Perovskite SOFC Cathodes. *Monatshefte Für Chem. - Chem. Mon.* **2009**, *140* (9), 985–999. https://doi.org/10.1007/s00706-009-0153-3.
(10) Liu, Y.; Dinh, J.; Tade, M. O.; Shao, Z. Design of Perovskite Oxides as Anion-Intercalation-Type Electrodes for Supercapacitors: Cation Leaching Effect. *ACS Appl. Mater. Interfaces* **2016**, *8* (36), 23774–23783. https://doi.org/10.1021/acsami.6b08634.
(11) Zhu, L.; Liu, Y.; Su, C.; Zhou, W.; Liu, M.; Shao, Z. Perovskite SrCo0.9Nb0.1O3−δ as an Anion-Intercalated Electrode Material for Supercapacitors with Ultrahigh Volumetric Energy Density. *Angew. Chem.* **2016**, *128* (33), 9728–9731. https://doi.org/10.1002/ange.201603601.
(12) Che, W.; Wei, M.; Sang, Z.; Ou, Y.; Liu, Y.; Liu, J. Perovskite LaNiO 3-δ Oxide as an Anion-Intercalated Pseudocapacitor Electrode. *J. Alloys Compd.* **2018**, *731*, 381–388. https://doi.org/10.1016/j.jallcom.2017.10.027.
(13) Lang, X.; Mo, H.; Hu, X.; Tian, H. Supercapacitor Performance of Perovskite La $_{1-x}$ Sr $_{x}$ MnO $_{3}$. *Dalton Trans* **2017**, *46* (40), 13720–13730. https://doi.org/10.1039/C7DT03134C.
(14) Cushing, B. L.; Kolesnichenko, V. L.; O'Connor, C. J. Recent Advances in the Liquid-Phase Syntheses of Inorganic Nanoparticles. *Chem. Rev.* **2004**, *104* (9), 3893–3946. https://doi.org/10.1021/cr030027b.
(15) Kuznetsov, D. A.; Han, B.; Yu, Y.; Rao, R. R.; Hwang, J.; Román-Leshkov, Y.; Shao-Horn, Y. Tuning Redox Transitions via Inductive Effect in Metal Oxides and Complexes, and Implications in Oxygen Electrocatalysis. *Joule* **2017**. https://doi.org/10.1016/j.joule.2017.11.014.
(16) Hardin, W. G.; Slanac, D. A.; Wang, X.; Dai, S.; Johnston, K. P.; Stevenson, K. J. Highly Active, Nonprecious Metal Perovskite Electrocatalysts for Bifunctional Metal–Air Battery Electrodes. *J. Phys. Chem. Lett.* **2013**, *4* (8), 1254–1259. https://doi.org/10.1021/jz400595z.
(17) Nemudry, A.; Rudolf, P.; Schöllhorn, R. Topotactic Electrochemical Redox Reactions of the Defect Perovskite SrCoO2.5+x. *Chem. Mater.* **1996**, *8* (9), 2232–2238. https://doi.org/10.1021/cm950504+.

(18) Grenier, J.-C.; Ghodbane, S.; Demazeau, G.; Pouchard, M.; Hagenmuller, P. Le Cobaltite de Strontium Sr2Co2O5 : Caracterisation et Proprietes Magnetiques. *Mater. Res. Bull.* **1979**, *14* (6), 831–839. https://doi.org/10.1016/0025-5408(79)90145-4.
(19) Qiu, L.; Lee, T. H.; Liu, L.-M.; Yang, Y. L.; Jacobson, A. J. Oxygen Permeation Studies of SrCo0.8Fe0.2O3 − δ. *Solid State Ion.* **1995**, *76* (3), 321–329. https://doi.org/10.1016/0167-2738(94)00296-5.
(20) Laiho, R.; Lisunov, K. G.; Lähderanta, E.; Petrenko, P. A.; Salminen, J.; Stamov, V. N.; Stepanov, Y. P.; Zakhvalinskii, V. S. Low-Field Magnetic Properties of LaMnO3+δ with 0.065≤δ≤0.154. *J. Phys. Chem. Solids* **2003**, *64* (12), 2313–2319. https://doi.org/10.1016/S0022-3697(03)00266-X.
(21) Alexander, C. T.; Abakumov, A. M.; Forslund, R. P.; Johnston, K. P.; Stevenson, K. J. Role of the Carbon Support on the Oxygen Reduction and Evolution Activities in LaNiO3 Composite Electrodes in Alkaline Solution. *ACS Appl. Energy Mater.* **2018**, *1* (4), 1549–1558. https://doi.org/10.1021/acsaem.7b00339.
(22) Hardin, W. G.; Mefford, J. T.; Slanac, D. A.; Patel, B. B.; Wang, X.; Dai, S.; Zhao, X.; Ruoff, R. S.; Johnston, K. P.; Stevenson, K. J. Tuning the Electrocatalytic Activity of Perovskites through Active Site Variation and Support Interactions. *Chem. Mater.* **2014**, *26* (11), 3368–3376. https://doi.org/10.1021/cm403785q.
(23) L'vov, B. V.; Ugolkov, V. L. Peculiarities of CaCO3, SrCO3 and BaCO3 Decomposition in CO2 as a Proof of Their Primary Dissociative Evaporation. *Thermochim. Acta* **2004**, *410* (1–2), 47–55. https://doi.org/10.1016/S0040-6031(03)00372-1.
(24) Dann, S. E.; Currie, D. B.; Weller, M. T.; Thomas, M. F.; Al-Rawwas, A. D. The Effect of Oxygen Stoichiometry on Phase Relations and Structure in the System La1-xSrxFeO3-δ ($0 \leq X \leq 1$, $0 \leq \delta \leq 0.5$). *J. Solid State Chem.* **1994**, *109* (1), 134–144. https://doi.org/10.1006/jssc.1994.1083.
(25) Nemudry, A.; Weiss, M.; Gainutdinov, I.; Boldyrev, V.; Schöllhorn, R. Room Temperature Electrochemical Redox Reactions of the Defect Perovskite SrFeO2.5+x. *Chem. Mater.* **1998**, *10* (9), 2403–2411. https://doi.org/10.1021/cm980090v.
(26) Cook, R.; Sammells, A. On the Systematic Selection of Perovskite Solid Electrolytes for Intermediate Temperature Fuel Cells. *Solid State Ion.* **1991**, *45* (3–4), 311–321. https://doi.org/10.1016/0167-2738(91)90167-A.
(27) Woodward, P. M. Octahedral Tilting in Perovskites. II. Structure Stabilizing Forces. *Acta Crystallogr. B* **1997**, *53* (1), 44–66. https://doi.org/10.1107/S0108768196012050.
(28) Mitchell, J. F.; Argyriou, D. N.; Potter, C. D.; Hinks, D. G.; Jorgensen, J. D.; Bader, S. D. Structural Phase Diagram of La1-xSrxMnO3: Relationship to Magnetic and Transport Properties. *Phys. Rev. B* **1996**, *54* (9), 6172–6183. https://doi.org/10.1103/PhysRevB.54.6172.

(29) Chmaissem, O.; Dabrowski, B.; Kolesnik, S.; Mais, J.; Jorgensen, J. D.; Short, S. Structural and Magnetic Phase Diagrams of La 1 − X Sr X MnO 3 and Pr 1 − Y Sr Y MnO 3. *Phys. Rev. B* **2003**, *67* (9). https://doi.org/10.1103/PhysRevB.67.094431.
(30) James, M.; Avdeev, M.; Barnes, P.; Morales, L.; Wallwork, K.; Withers, R. Orthorhombic Superstructures within the Rare Earth Strontium-Doped Cobaltate Perovskites: Ln1−xSrxCoO3−δ (Ln=Y3+, Dy3+–Yb3+; 0.750⩽x⩽0.875). *J. Solid State Chem.* **2007**, *180* (8), 2233–2247. https://doi.org/10.1016/j.jssc.2007.04.029.
(31) Inoue, I. H. Electrostatic Carrier Doping to Perovskite Transition-Metal Oxides. *Semicond. Sci. Technol.* **2005**, *20* (4), S112–S120. https://doi.org/10.1088/0268-1242/20/4/013.
(32) Armstrong, A. R.; Holzapfel, M.; Novák, P.; Johnson, C. S.; Kang, S.-H.; Thackeray, M. M.; Bruce, P. G. Demonstrating Oxygen Loss and Associated Structural Reorganization in the Lithium Battery Cathode Li[Ni0.2Li0.2Mn0.6]O2. *J. Am. Chem. Soc.* **2006**, *128* (26), 8694–8698. https://doi.org/10.1021/ja062027+.
(33) Tripkovic, A. V.; Popovi, K. D.; MomEilovic', J. D.; DraEi, D. M. Kinetic and Mechanistic Study of Methanol Oxidation on a Pd 111) Surface in Alkaline Media. 12.
(34) Brousse, T.; Taberna, P.-L.; Crosnier, O.; Dugas, R.; Guillemet, P.; Scudeller, Y.; Zhou, Y.; Favier, F.; Bélanger, D.; Simon, P. Long-Term Cycling Behavior of Asymmetric Activated carbon/MnO2 Aqueous Electrochemical Supercapacitor. *J. Power Sources* **2007**, *173* (1), 633–641. https://doi.org/10.1016/j.jpowsour.2007.04.074.
(35) Lankhorst, M. H. R.; Bouwmeester, H. J. M.; Verweij, H. High-Temperature Coulometric Titration of La1−xSrxCoO3−δ: Evidence for the Effect of Electronic Band Structure on Nonstoichiometry Behavior. *J. Solid State Chem.* **1997**, *133* (2), 555–567. https://doi.org/10.1006/jssc.1997.7531.

Chapter 4: Sr-Rich Perovskites for Energy Dense Asymmetric Anion-Based Pseudocapacitors[3]

4.1 INTRODUCTION

The need for low-cost, fast charging and discharge energy storage increases every year as more and more wind and solar power gets added to the grid.[1]Applications that require fast charging or discharging include electric vehicle acceleration and regenerative breaking.[1] Additionally, uninterruptable power supplies and high frequency power regulation are high power applications for a more sustainable and resilient electric grid. Chapter 3 discussed pseudocapacitors as being a promising energy storage technology for these high power applications.[2]

A capacitor's energy density is given by equation 1:

$$E = \frac{1}{2} C V_{cell}^2 \quad (1)$$

where E is the energy density (Wh kg^{-1}), C is the specific capacitance (F g^{-1}) of the electroactive material, and V_{cell} is the applied cell voltage. Because of the square-power dependence on V_{cell}, non-aqueous pseudocapacitor materials such as high surface area carbons,[3,4] V_2O_5,[5] α-MoO_3,[6] T-Nb_2O_5,[7] TiO_2 nanotubes,[8] etc. have been explored as possible solutions due to the organic electrolytes' larger electrochemical potential stability window.[9,4,10] Industry has already commercialized early non-aqueous carbon

[3] Adapted with permission from C.T. Alexander, J. T. Mefford, J. Saunders, R. P. Forslund, K. P. Johnston and K. J. Stevenson. Anion-Based Pseudocapacitance of the Perovskite Library $La_{1-x}Sr_xBO_{3-\delta}$ (B = Fe, Mn, Co). ACS Appl. Mater. Interfaces 2019, 11, 5084−5094. Copyright © 2019 American Chemical Society. C.T. Alexander synthesized the Sr-rich composites, did iodometric titrations of the iron series, made and tested the asymmetric pseudocapacitors and wrote the manuscript. J. Saunders synthesized most of the samples. J. T. Mefford performed CVs on the single perovskite materials and assisted intellectually. R. P. Forslund made the $LaFeO_3$ sample. K. P. Johnston and K. J. Stevenson assisted in writing the manuscript.

based supercapacitors capable of storing 4 Wh kg^{-1} when charging at 400 W kg^{-1} but these devices do have disadvantages such as the high cost of the electroactive materials and organic electrolytes, lower power and capacitance relative to aqueous electrolytes, safety concerns, and low water impurity requirements (3-5 ppm) for proper performance. [10,11]

Aqueous electrolytes, on the other hand, afford lower material costs, higher power (due to increased electrolyte concentration), increased safety, increased environmentally friendliness and offer a wider operating temperature range than their non-aqueous counterparts.[10,12] Aqueous electrolytes span the entire pH range with acidic, neutral, and alkaline solutions commonly containing ~ 5 M H_2SO_4, 0.5 M Na_2SO_4 and 1 M or 6 M KOH respectively.[12] Scientists have studied vast a fast number of pseudocapacitor materials that include high surface area and functionalized carbons, RuO_2,[13] MnO_2,[13] IrO_2, $NiO/Ni(OH)_2$, $Co_3O_4/Co(OH)_2$, SnO_2, V_2O_5, etc. as reviewed elsewhere.[9,4,10,12] One strategy to increase the pseudocapacitor energy density has been to expand the working voltage window with an asymmetric design. The approach has been to use a pseudocapacitive material as the positive electrode coupled with a negative electrode-typically a high surface area carbon relying on non-Faradaic double layers (ion-adsorption)[12]-which has led to complex combinations such as TiO_2/MnO_2[14] and MnO_2-SWCNT/In_2O_3-SWCNT[15] asymmetric pseudocapacitors to name a couple. The shear breadth in pseudocapacitor type, structure, composition, and testing procedure reported in the literature makes it difficult to make rational asymmetric pseudocapacitor design decisions.

Chapter 3 discussed our group's discovery of an oxygen vacancy rich $LaMnO_3$ perovskite material to be an excellent pseudocapacitor based on a hydroxide anion intercalation mechanism .[16] It was shown in Chapter 3 that the anion intercalation mechanism is affected by the oxygen vacancy content (δ) and can be described in a perovskite for a given transition metal B as:

$$La_{1-x}Sr_x\left[B_{2\delta}^{z+};B_{(1-2\delta)}^{(z+1)+}\right]O_{3-\delta}+2\delta OH^- \leftrightarrow La_{1-x}Sr_x\left[B_{2\delta}^{z+};B_{2\delta}^{(z+1)+}\right]O_{3-\delta}+2\delta e^-+\delta H_2O \quad (2)$$

Recently, others have demonstrated anion-based pseudocapacitance in BSCF,[17] $SrCo_{0.9}Nb_{0.1}O_{3-\delta,}$[18] $LaNiO_{3,}$[19] $La_{1-x}Sr_xMnO_3$ (x = 0-0.5)[20] some of which have made either symmetric or asymmetric pseudocapacitors with activated carbon as the anode. For instance, Liu[17] studied BSCF and hexagonal $SrCoO_3$ pseudocapacitance and found that cation leaching during cycling increases the perovskite surface area and the resulting pseudocapacitance. Additionally, our group has previously noted oxygen ion mobility in electrocatalytic applications in the $La_{1-x}Sr_xCoO_{3-\delta}$ (x = 0-1) series as well.[21] In Chapter 3, it was demonstrated that the redox potential is controlled by the B-site. Additionally, the redox potential could be shifted by substituting higher oxidation state elements with lower ones into the A-site such as replacing La^{3+} with Sr^{2+} which must be compensated for by either oxidizing the B-site or introducing oxygen vacancies to maintain charge neutrality.[21,22] The Brownmillerite $SrFeO_{2.5}$ (BM-SFO), $La_{0.2}Sr_{0.8}MnO_{3-\delta}$ (LSMO28) and

$SrCoO_{3-\delta}$ (SCO) were found to have the highest pseudocapacitance for each of their respective transition metal series.[23]

Herein, we report using BM-SFO, LSMO28 and SCO perovskites to both widen the voltage window for cell operation and increase the charge stored per unit area via Sr-substitution into the A-site. We made three perovskite pairs, each with a high pseudocapacitance, with different B-site permutations to produce a larger voltage window because different B-site elements have their own characteristic redox potential. Thus, we constructed the first all-perovskite asymmetric pseudocapacitors using the most pseudocapacitive materials from each transition metal perovskite series to increase the device's cell voltage and produce a large energy density of 31 Wh kg^{-1} at 450 W kg^{-1} where Brownmillerite $SrFeO_{2.5}$ was employed as the anode and $SrCoO_{2.7}$ as the cathode.

4.2 EXPERIMENTAL

4.2.1: Chemicals

$La(NO_3)_3*6H_2O$ (99.995%), $Sr(NO_3)_2$ (99+%), $Fe(NO_3)_3*9H_2O$ (99.995%), $Mn(NO_3)_2*4H_2O$ (99.999%), $Co(NO_3)_2*6H_2O$ (98%), tetramethylammonium hydroxide (TMAOH, 99%), tetrapropylammonium bromide (TPAB, 98%), citric acid, ethylenediaminetetraacetic acid (EDTA), sodium hydroxide, potassium hydroxide, and anhydrous ethanol (Absolute 200 proof) were purchased from Fisher Scientific. These chemicals and diethylene glycol (DEG), hydrochloric acid (HCl), potassium iodide (KI), standard potassium iodate (KIO_3) solution, corn starch, sodium thiosulfate ($Na_2S_2O_3$),

XC-72 Vulcan carbon (VC), nitric acid (HNO_3), Nafion (5 wt.% in ethanol), and deionized water (18 MΩ cm) were all used as received without further purification.

4.2.2: Synthesis of BM-$SrFeO_{2.5}$ and $SrCoO_{3-\delta}$

The BM-$SrFeO_{2.5}$ and $SrCoO_{3-\delta}$ perovskite were made via a co-precipitation synthesis[24] similar to our previous work.[16,21,25] For brevity, BM-$SrFeO_{2.5}$ and $SrCoO_{3-\delta}$ will be referred to as BM-SFO and SCO respectively. Briefly, 50 mL of an aqueous 0.5 M metal nitrate solution with the appropriate cation ratios to make the target material was slowly titrated (~1 drop every 3 seconds using a burette) into 200 mL of a 10 wt.% TMAOH solution containing 321.17 mg of Na_2CO_3 for the BM-SFO synthesis and 1 wt.% TMAOH solution without Na_2CO_3 for the SCO synthesis with each containing 1358.6 mg of TPAB. It was helpful to have a slight (1-2 mol%) Co^{2+} excess in the SCO synthesis.

Before the metal nitrate solution began dripping for the SCO synthesis, the TMAOH solution pH was measured to be 13.01 followed by bubbling CO_2 into the solution for a few minutes which lowered the pH down to 10.18 to increase the CO_3^{2-} concentration and encourage $SrCO_3$ precipitation. A light brown precipitate formed with each drop for BM-SFO and a cyan color for the SCO synthesis while the solutions stirred overnight. The following morning, the burette containing the SCO metal nitrate solution had ~2 mL left to drip and the solution was a pale blue color (suggesting α-$Co(OH)_2$ formed). Bubbling oxygen gas into the solution appeared to have no effect on the precipitate color so 0.484 mL of 30 wt.% H_2O_2 in 0.242 mL increments was added to

oxidize the cobalt ions and hydroxides which turned the solution an olive green and brown color with the pH at 9.98. Oxygen gas was then bubbled into the SCO+TMAOH solution for 26 hours while stirring and caused the solution color to turn brown thus indicating $Co(OH)_3$ had formed. The SCO solution was magnetically stirred under ambient conditions for one more day thus yielding a 3-day total to stir.

The precipitates were collected using two 50 mL centrifuge tubes per sample, centrifuged at 8000 r.p.m. for four minutes and the supernatant was decanted off. The precipitates were washed and vortexed with ~35 mL of deionized (DI) water per centrifuge tube three times and collected by centrifugation each time using the above conditions. The precipitate was resuspended with DI water and probe sonicated for three minutes. The suspension was then sprayed from a squirt bottle held about three feet high onto a rotating drum cooled to cryogenic temperatures using dry ice to freeze the solution into a thin film. The ice encasing the precipitate was lyophilized away at -10^{o}C and ~25 mTorr for at least 24 hours.[26]

The remaining powder was calcined using a tube furnace with a quartz tube and alumina calcination boat to hold the samples. The alumina boats were pre-washed with 3 M HNO_3, ethanol and dried in an oven at 80^{o}C. Samples were heated in air from room temperature to 120^{o}C in 5 minutes, held at 120^{o}C for one hour, heated to 950^{o}C in 45 minutes and held at 950^{o}C for 5 hours for SCO with 200 mL min^{-1} of oxygen flowing and 150 mL min^{-1} of air for BM-SFO before cooling naturally to room temperature. Rapidly quenching[27–29] SCO with liquid N_2 and cryogenically cooled (via acetone and dry ice) oxygen gas at maximum flow rate yielded the phase pure SCO perovskite phase. The

perovskite SFO phase was reduced to $Sr_2Fe_2O_5$ (BM-SFO) by heating the SFO to 350^{o}C in a 7% H_2/Ar atmosphere for 4 hours followed by cooling naturally to room temperature.

4.2.3: Citric Acid Synthesis of $La_{0.2}Sr_{0.8}MnO_{3-\delta}$

$La_{0.2}Sr_{0.8}MnO_{3-\delta}$ (LSMO28) was more straightforward to make using the Pechini synthesis.[24] In short, the metal nitrates were mixed in deionized water with citric acid, EDTA, DEG in a 1:1:1:0.66 molar ratio based on a total metal cation concentration-with a total of 5 mmol of the metals ions used. The pH was raised to 7.17 using a 5 wt% TMAOH solution with DI water added to have a 50 mL total solution volume. The solution was then magnetically stirred at 100 r.p.m. on a hot plate at 140^{o}C to evaporate the water and form a gel that was subsequently burned to a char on a hotplate in a closed fume hood.

The char was then loaded into a furnace as described above, but in an alumina tube. The temperature was raised to 120^{o}C in 35 minutes, followed by a 1-hour hold, followed by a 45-minute ramp to 950^{o}C and the LSMO28 was calcined at 950^{o}C for 5 hours under 220 mL min^{-1} flowing air. The furnace was then allowed to naturally cool to room temperature. The LSMO28 was then ramped to 400^{o}C in 35 minutes and reduced at 400^{o}C for 4 hours in a 7% H_2/N_2 atmosphere (150 mL min^{-1}) to form the phase pure perovskite structure.

4.2.3: Materials Characterization.

The materials' lattice structure was determined using wide-angle X-ray diffraction on a Rigaku Spider instrument with Cu Kα radiation (λ = 1.5406 Å) source at 40 mA and

40 kW. The data was analyzed using JADE software to identify phases. A Brunauer-Emmett-Teller (BET) instrument (Quantachrome Instruments NOVA 2000 high-speed surface area analyzer) was used to degas the samples overnight under vacuum and measure sample surface areas at 77 K using N_2 adsorption. Data points from the 0.05 to 0.3 P/P_o range were used to extract the surface area from the adsorption data as shown in Figure A26. B-site oxidation state and oxygen vacancy content were measured using iodometric titrations as reported previously[21,30] using solutions made from preboiled deionized water. Approximately 15-20 mg of sample was added to a sealed 3-neck round bottom flask and dissolved in Ar-saturated 6 M HCl. 3 mL of 2 M KI was added to the cell and was immediately titrated with 25 mM $Na_2S_2O_3$ solution that had been standardized against a 0.1 M KIO_3 standard solution. When the solution had been titrated to a faint yellow color, 1 mL of starch indicator made from the supernatant of a boiled 1 wt.% corn starch solution was added. The solution was then titrated until its color changed from deep purple to clear. All iodometric titrations were made in triplicate.

4.24: Three-electrode cell preparation.

Electrodes were prepared the same way as described earlier[16,31,32], but with modifications made to the perovskite to carbon weight ratio. Briefly, all carbon and perovskite powders were washed with deionized water three times and ethanol three times using vacuum filtration followed by ball milling for three minutes in a Wig-L-Bug ball mill. All powders were supported onto activated Vulcan carbon (VC^A) in an 85:15 perovskite: carbon weight ratio by ball milling for three minutes. The VC was activated

by soaking it in 1 M HNO_3 overnight at 80°C. The composite materials were sonicated in 1 mg mL^{-1} solution of ethanol with 0.05 wt% Na-substituted Nafion for two hours before being pipetted and spun-cast at 700 r.p.m. onto the rotating disk electrode's (RDE's) glassy carbon disk (diameter = 0.5 cm, area = 0.196 cm^2) at a 51.0 μg cm^{-2} (10 μg) total mass loading. The RDEs used to measure the carbon capacitance had a 7.65 μg cm^{-2} mass loading (1.5 μg). RDEs were prepared by sonicating the disk in a 1:1 ethanol: deionized water solution, followed by polishing using 50 nm alumina, rinsing and sonicating in a fresh 1:1 ethanol: deionized water solution.

4.2.5: Carbon Fiber Paper, Ni Foam and Two-electrode cell preparation.

The same ink prepared as described in the 3-electrode cell section was pipetted onto Ni foam (2 mm thick, 100 ppi, 95% porosity, Marketech) in 100 μL increments or a 5 mg mL^{-1} ink onto carbon fiber paper (CFP, AvCarb MGL 190 from Fuel Cell Store) in 25 μL increments on a hot plate at 140°C to yield a 1 mg cm^{-2} mass loading. Prior to depositing the active materials, the CFP electrodes were soaked in acetone at 80°C for at least 30 minutes and the 1 cm^2 electrode square was soaked in 3 M HNO_3 for 30 seconds, followed by neutralization in a saturated $NaHCO_3$ solution and rinsing in DI water and ethanol. The composites' mass loading was designed to give the two electrodes equal total capacitance based on the perovskite-carbon composite gravimetric capacitance values from the three-electrode cell. Electrodes were dried overnight under ambient conditions and the Ni foam electrodes were pressed between two pieces of weigh paper to ~0.1 mm using an Arbor Press. The electrodes were wetted with a droplet of 1 M KOH

and 7 µL of isopropanol followed by rinsing with 1 mL of 1 M KOH to allow the electrolyte to penetrate pores. Ni foam electrodes were sandwiched between two glass slides separated by a glass fiber membrane shown in Figure A27, while the CFP electrodes were held 1 cm apart due to their fragility.

4.2.6: Electrochemical Measurements.

Three-electrode electrochemical testing was performed on a Metrohm Autolab PGSTAT302N and CH Instruments CHI832a with high speed rotators from Pine instruments. A Hg/HgO (1 M KOH) reference electrode and Au wire counter electrode were used for the 3-electrode measurements and all tests were conducted in Ar-saturated 1 M KOH. The cyclic voltammograms (CVs) on the BM-SFO (-1.2 V to 0.2 V vs Hg/HgO), LSMO28 (-0.6 V to 0.4 V vs Hg/HgO) and SCO (-0.4 V vs 0.5 V vs Hg/HgO) materials were cycled for at most 10 cycles at 100 mV s^{-1} or until the CV stabilized to measure the specific capacitance (F g^{-1}) measurement according to equation 3:[13]

$$C_s = \frac{1}{2mv|V_c - V_a|} \oint_{V_a}^{V_c} i\,(V) dV \qquad (3)$$

Where m is the mass loading of electroactive material on the electrode (g), ν is the scan rate of the CV (V s^{-1}) while V_c and V_a are the cathodic and anodic limits of the CV window. The integral represents the entire area within the CV loop over the cathodic and anodic sweeps which is divided by 2 to yield the average capacitance for a single sweep. Every sample was tested using five electrodes with each electrode's capacitance measured in triplicate at one scan rate (100, 50, 25, 10, 5 mV s^{-1}) per electrode to get an average and standard deviation. Two-electrode electrochemical testing was performed

using an Arbin Instruments battery cycler. The BM-SFO, LSMO28 and SCO used (from Chapter 3) for the Ni foam two-electrode measurements were recalcined at 950°C to eliminate small $SrCO_3$ impurities that had grown in over the course of the study while another batch of materials (as described above in Chapter 4) for the CFP electrodes needed to be made due to insufficient material. Galvanostatic charge-discharge (GCD) measurements were made to calculate the two-electrode capacitance[33]:

$$C = \frac{(V_{max} - \Delta V_{iR})I}{t_{dis}} \quad (4)$$

where V_{max} is the electrolyte window [V], ΔV_{iR} is the iR drop [V] due to electrode resistance on discharge, I is the constant applied current [A g_{ox}^{-1}] and t_{dis} is the total time for the two-electrode cell to discharge to 0 V. The energy density of the composite was calculated according to:

$$U = \frac{1}{2} C V_{max}^2 \quad (5)$$

4.3: RESULTS AND DISCUSSION

4.3.1: Perovskite Lattice Characterization

The perovskites used to construct the asymmetric pseudocapacitors were made phase pure via a co-precipitation method followed by calcining the materials at 950°C. The brownmillerite-$SrFeO_{2.5}$ (BM-SFO) crystallized into an orthorhombic structure belonging to the Icmm space group shown in Figure 4.1a which is slightly different from what was found in Chapter 3 (Appendix A2). The $La_{0.2}Sr_{0.8}MnO_{3-\delta}$ (LSMO28) arranged into a rhombohedral structure in the R-3c space group as reported previously[23] while the $SrCoO_{3-\delta}$ (SCO) formed a cubic lattice in the Pm-3m space group. The cubic SCO

structure contrasts with the tetragonal structure as previously observed[21,23] which suggests that this SCO sample has higher oxidation state cobalt with fewer oxygen vacancies[27] thus agreeing with results in Figure 4.1b,c.

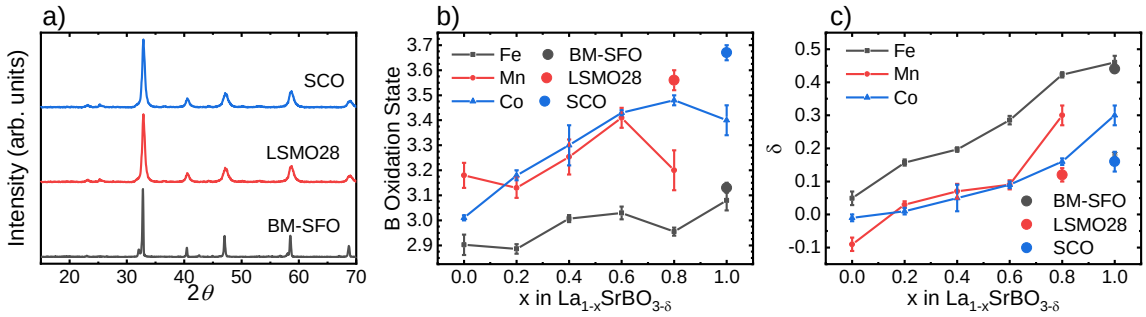

Figure 4.1 | Perovskite Crystallographic and Chemical Characterization.

(a) X-ray Diffraction (XRD) patterns indicating $SrCoO_{3-\delta}$, $La_{0.2}Sr_{0.8}MnO_{3-d}$ and BM-$Sr_2Fe_2O_5$ phase purity with the perovskites' (b) B-site oxidation states and (c) oxygen vacancy content shown and determined from performing iodometric titrations in triplicate. The lines in Figure 4.1b,c are from the perovskite library in Chapter 3 with the solid circles being the oxidation state and oxygen vacancy values for the materials in this chapter.

The perovskites' B-site oxidation state and oxygen vacancy content was measured in triplicate using iodometric titrations as shown in Figure 4.1 b,c with the perovskites from Chapter 3 shown as a comparison. The BM-SFO has a similar but slightly higher oxidation state ($z^+ \sim 3.1+$) and lower oxygen vacancy content ($\delta \sim 0.43$) than that of the BM-SFO synthesized in Chapter 3. The LSMO28 made here, however, has an oxidation state ($z^+ \sim 3.6+$) and oxygen vacancy content ($\delta \sim 0.12$) that trends with the rest of the LSMO series in Figure 4.1 b,c that suggests it was not as reduced as the LSMO28 sample in Chapter 3. The higher oxidation state Mn could possibly be a side effect of the Pechini synthesis. The SCO quench resulted in a higher oxidation state ($z^+ \sim 3.7+$) with lower oxygen vacancy content ($\delta \sim 0.15$) than the SCO measured in Chapter 3 which could be

the result from adding H_2O_2 to the solution synthesis. The sample surface areas were measured to be ~ 3, 14 and 2 m^2 g^{-1} for BM-SFO, LSMO28 and SCO with more precise values given in Table A15. The most likely reason for LSMO28's higher surface area than the other samples is the Pechini synthesis which would agree with previous surface area results.[23]

4.3.2: Oxygen kinetic, diffusion and vacancy contributions to pseudocapacitance

The redox peaks' scan rate dependence for these pseudocapacitor materials can be used to determine if the materials are limited by charge transfer kinetics or instead by lattice oxygen diffusion rates. A material that exhibits purely capacitive behavior will have a current-potential profile that is proportional to the scan rate ($i \sim \nu$) while a material that is diffusion limited will exhibit current with square root scan rate dependence ($i \sim \nu^{1/2}$).[34] The most capacitive samples' peak current density trends are plotted in Figure 4.2 which shows that BM-SFO (Figure 4.2a-c) and LSMO28 (Figure 4.2d-f) are kinetically limited-meaning they exhibit mostly capacitive behavior due to fast lattice oxygen diffusion kinetics. This contrasts with SCO (Figure 4.2g-i) whose redox peaks more closely resemble diffusion limited behavior and further supports the idea that the redox peaks correspond to a phase transformation.

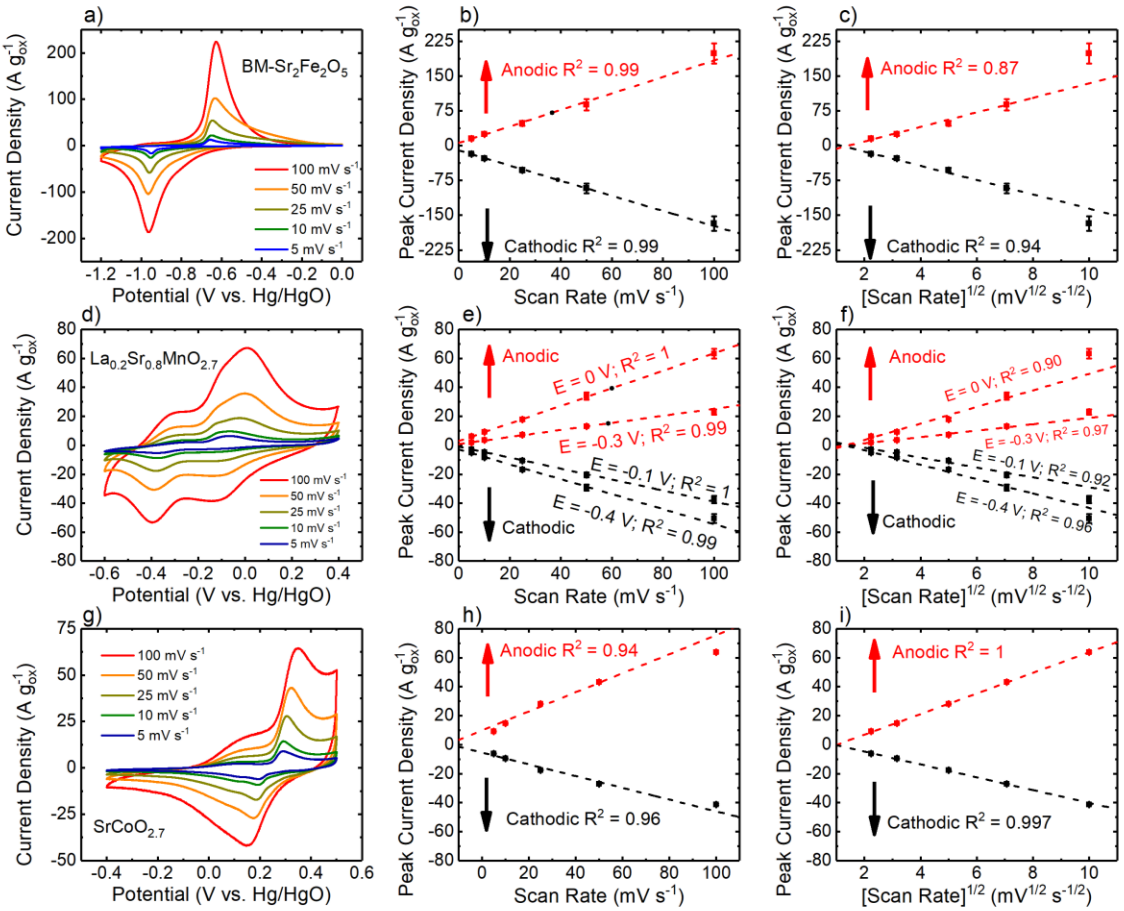

Figure 4.2 | Power law analysis of the Sr^{2+}-rich materials' redox peaks.

CVs and their corresponding scan rate dependence to determine if charge transfer processes are kinetically limited or diffusion limited for (a-c) BM-$Sr_2Fe_2O_5$, (d-f) $La_{0.2}Sr_{0.8}MnO_{3-\delta}$ and (g-i) $SrCoO_{3-\delta}$. If the peak current density is proportional to the scan rate (ν) then the material is kinetically limited as opposed to diffusion limited if it is proportional to the square root of the scan rate ($\nu^{1/2}$).[34]

Applying this analysis over the entire potential range (discussed further in Appendix 3) allows the purely capacitive current component to be plotted as a shaded envelope in Figure 4.3a-c. The BM-SFO exhibits almost entirely pseudocapacitive behavior over the entire voltage window in Figure 4.3a and shows two peaks within the

cathodic peak at ~ -0.95V vs Hg/HgO which could be the $Fe^{5+\rightarrow 3+}$ and $Fe^{3+\rightarrow 2+}$ transitions in agreement with the Fe^{z+} electronic configuration shown in Figure 3.4i. The LSMO28 CV in Figure 4.3b is composed of approximately half capacitive current while SCO is almost entirely diffusion controlled in Figure 4.3c. The LSMO28 capacitive envelope has three peaks on the positive scan (at ~ -0.35 V, -0.2 V, and 0.05 V vs Hg/HgO) and two on the back scan (at -0.45 V and -0.1 V vs Hg/HgO) which could also correspond to the Mn^{z+} electronic energy levels shown in Figure 3.5f. Figure 4.3c shows SCO capacitive current disappearing completely around the redox peak $E_{1/2}$ at ~ 0.3 V vs Hg/HgO which further supports the diffusion limited nature of SCO.

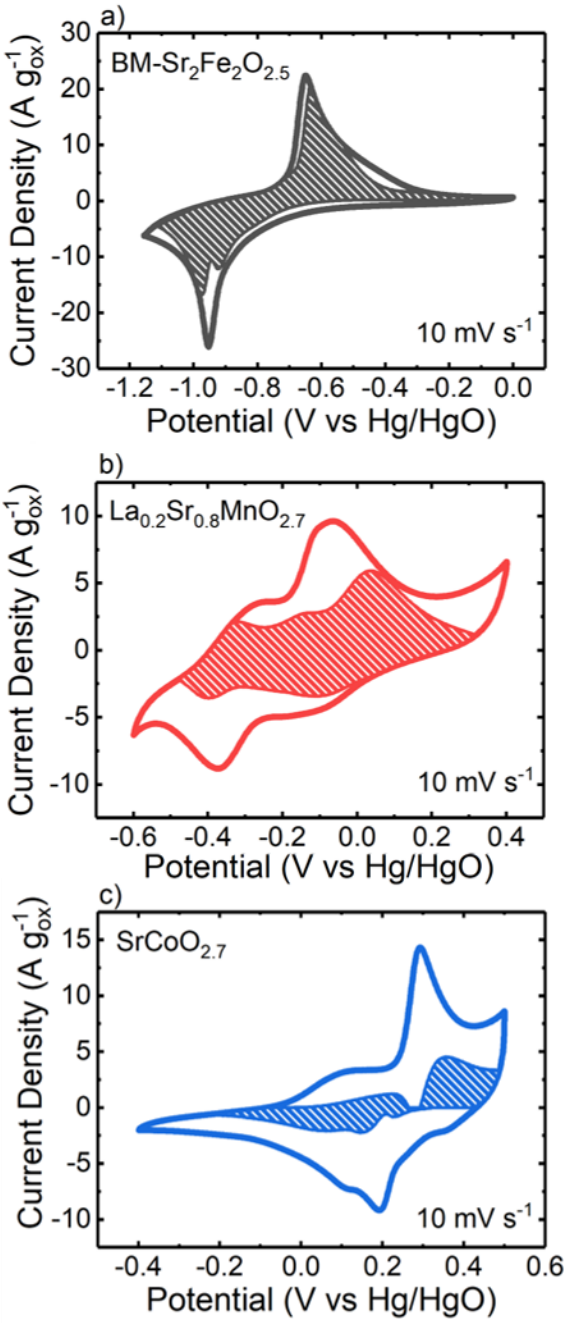

Figure 4.3 | Capacitive components and oxygen vacancy trends.

Cyclic voltammograms in Ar-saturated 1 M KOH at 10 mV s^{-1} with the capacitive current contributions in a shaded envelope are shown for (a) BM-$Sr_2Fe_2O_5$, (b) $La_{0.2}Mn_{0.8}MnO_{3-\delta}$ and (c) $SrCoO_{3-\delta}$.

4.3.3 Carbon Fiber Paper vs. Ni foam Current Collector Performance

Before constructing an asymmetric pseudocapacitor, it is important to first study the background currents and material interactions from the carbon fiber paper (CFP) and Ni foam current collectors. CFP and Ni foam cyclic voltammograms are shown in Figure 4.4 which demonstrate CFP's background current being approximately one hundred times smaller than Ni foam's. Ni foam has a large redox peak that begins just above 0.4 V vs Hg/HgO so future three electrode measurements on Ni foam were not conducted above this potential to avoid this high background current.

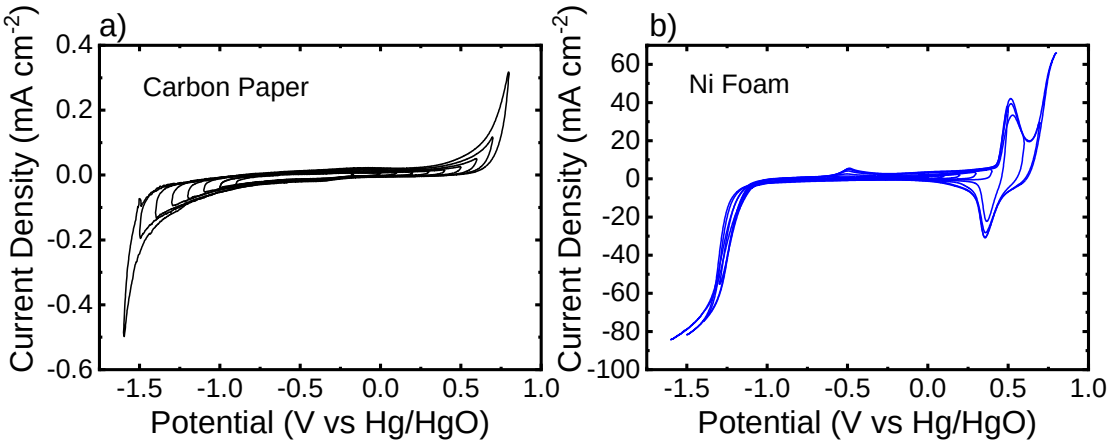

Figure 4.4 | Determining the Carbon Fiber Paper and Ni Foam voltage window and background current.

Cyclic voltammograms of (a) carbon fiber paper and (b) Ni foam were run at 100 mV s^{-1} in Ar-saturated 1 M KOH.

Current collector-perovskite interactions were then studied in a three-electrode cell setup. By using cyclic voltammetry, it is apparent in Figure 4.5 that the samples

supported on CFP have a higher performance than those on Ni foam possibly due to NiO coating the current collector surface that could limit charge transfer rates. Interestingly, these materials' CVs on Ni foam is similar in shape to their CVs in neutral 1 N K_2SO_4 (Figure A2.5) which could mean that OH^- is severely mass transfer limited within the Ni foam electrodes. In fact, the SCO on Ni foam CV in Figure 4.5f could be mostly due to the Ni foam redox peaks centered at ~0.4 V vs Hg/HgO in agreement with the literature.[35] These results combined with the poor asymmetric GCD curves in Figure A29 and the CVs in Figure A30 suggest that CFP is the more ideal current collector for making an asymmetric pseudocapacitor.

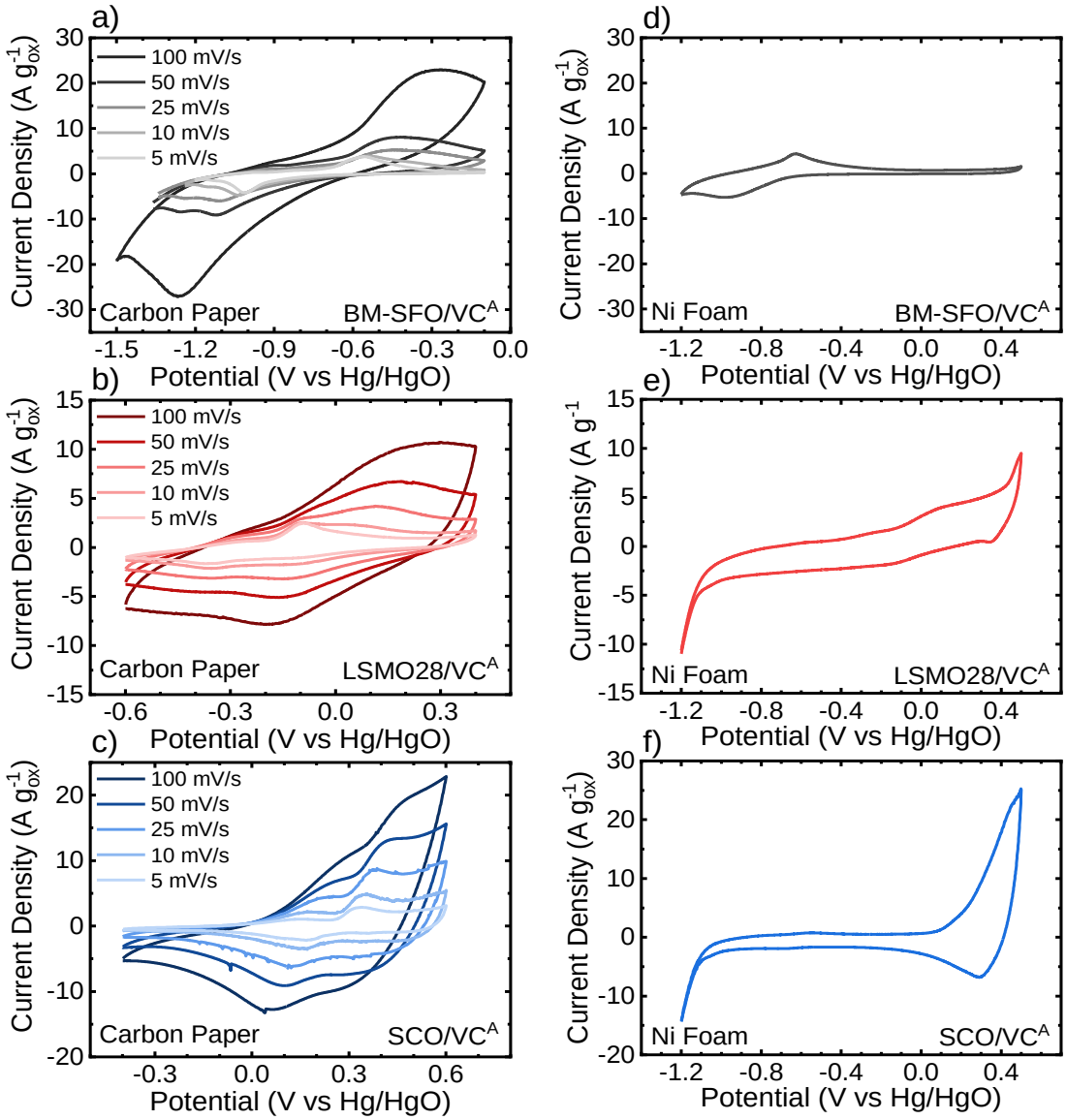

Figure 4.5 | B-site end member three electrode cyclic voltammetry on Carbon Fiber Paper versus Ni foam.

Cyclic voltammogram measurements made in Ar-saturated 1 M KOH at various scan rates on (a-c) Carbon Fiber Paper and at 100 mV s^{-1} on (d-f) Ni foam. The Carbon Fiber Paper electrodes were cycled at multiple scan rates because the perovskite CVs were like those on the RDEs.

These perovskite's mass-normalized capacitance measured on RDEs (51 μg cm^{-2}) and CFP (1 mg cm^{-2}) are shown for comparison in Figure A28 with the corresponding samples in Chapter 3 to better understand the changes caused by batch-to-batch variation and those caused by higher mass loadings on CFP electrodes. The BM-SFO's capacitance here trends higher with a steeper slope below 25 mV s^{-1} indicating new diffusion limitations while the LSMO28 capacitance in this chapter remains relatively constant with scan rate in contrast to the more-reduced LSMO28 in Chapter 3. The results indicate a lower mass-normalized capacitance on RDEs for the three materials, but when the measured charge capacity is normalized by the materials' BET surface area, the samples' charge capacity agrees well with their series' trends as shown in Figure 4.6, except for the new BM-SFO. This could be due to its slightly higher oxidation state-shown in Figure 4.1b and emphasized by the relatively larger anodic shoulder in Figure 4.6b at ~ -0.4 V vs Hg/HgO which could prevent Fe^{5+} from being stable.[36] Additionally, all materials demonstrated the diffusion limited capacitance increase with lower scan rates when supported on the CFP at high mass loading. These results emphasize the importance of comparing materials via their surface area-normalized charge capacity in the same cell configuration and designing pseudocapacitors with high vacancy content and high surface area.

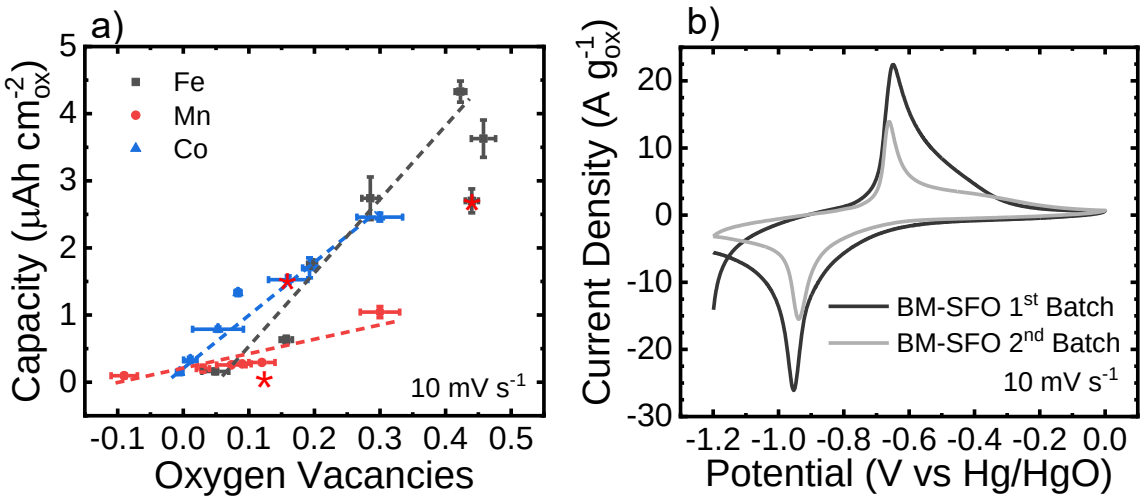

Figure 4.6 | Surface area-normalized capacity comparison of the materials tested on CFP electrodes.

(a) The data marked with a red star (*) are the freshly made samples. The SCO and LSMO28 samples follow the same trend as their respective samples while the BM-SFO seems to be have approximately 20% lower surface area-normalized capacity than expected from the LSFO series. This could be due to the (b) BM-SFO 2nd batch (Chapter 4) having more Fe^{4+} being stable present and stable than Fe^{5+} due the sample's slightly higher oxidation state shown in Figure 4.6a. The 1st batch corresponds to the BM-SFO sample and CV from Chapter 3.

4.3.4: Asymmetric Pseudocapacitors

Previous work by our group[16] as well as others[17–19] has demonstrated the practicality of anion-intercalation symmetric pseudocapacitors or asymmetric pseudocapacitors with activated carbon as the anode but there are no reports, to the best of our knowledge, of all-perovskite asymmetric anion-intercalation pseudocapacitors in the literature. Figure 4.7a shows CVs of the compositions with the highest capacitance at 10 mV s^{-1} for each series. Given the large difference in redox potentials between the samples, carefully selecting two perovskite oxide compositions allows us to tune the charge and discharge potentials of an all-perovskite pseudocapacitor device. Our cell notation will be written as anode//cathode to identify the asymmetric pseudocapacitor of interest (e.g. BM-SFO//SCO represents BM-SFO as the anode material and SCO as the cathode material). Based on the redox peaks' positions for each material, one would expect the asymmetric pseudocapacitor energy density to trend as BM-SFO//SCO > BM-SFO//LSMO28 > LSMO28//SCO caused by the differences between redox $E_{1/2}$ potentials. However, one would expect the power density to trend as BM-SFO//LSMO28 > BM-SFO//SCO > LSMO28//SCO because SCO is diffusion limited while LSMO28 is only kinetically limited based on Figure 4.2.

The above hypotheses with the Sr-rich perovskites were tested by pipetting an ink of 85:15 perovskite: VC^A weight ratio composite onto carbon fiber paper (CFP) electrodes with a 1 mg cm^{-2} mass loading. Three-electrode CVs of these materials supported on CFP are shown in Figure 4.7b-d and have notably altered redox peak shapes.

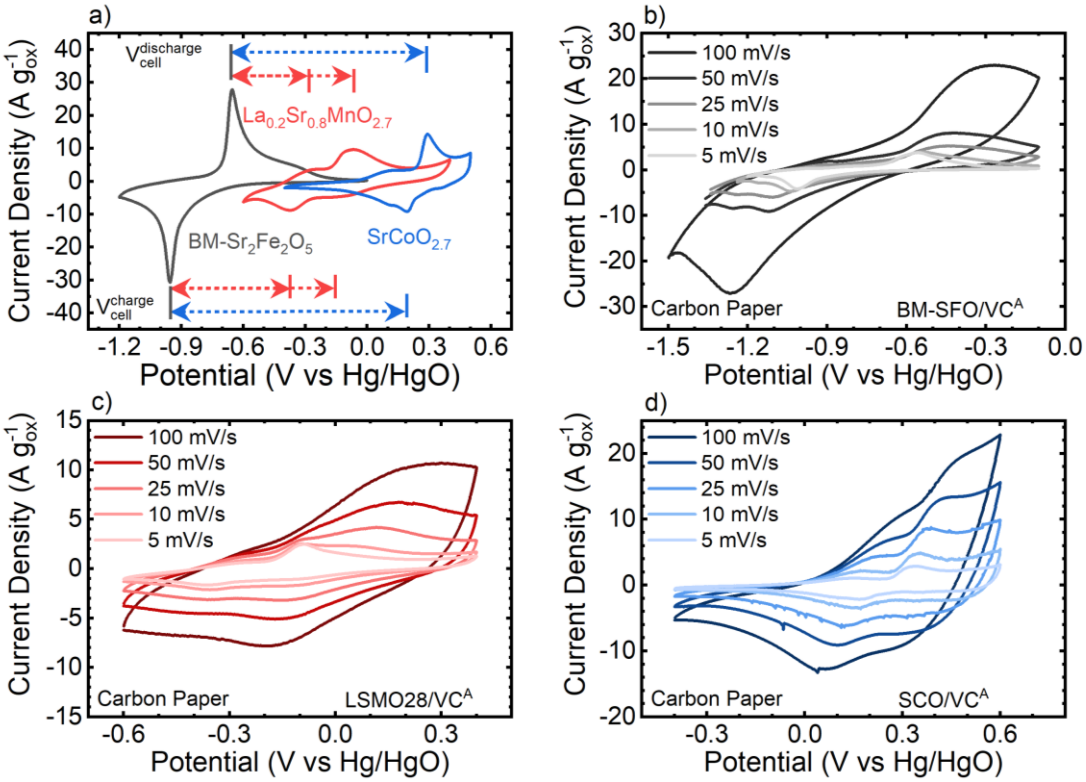

Figure 4.7 | Sr^{2+}-rich material comparison for pseudocapacitor design.

(a) BM-SFO, LSMO28, and SCO CVs at 10 mV s^{-1} scan rate measured using RDEs with charge and discharge peak couples identified for an asymmetric pseudocapacitor. CVs at multiple scan rates on carbon fiber paper with 1 mg cm^{-2} loadings of (b) BM-SFO/VC^A, (c) LSMO28/VC^A, (d) SCO/VC^A are shown and all measurements here were conducted in Ar-saturated 1 M KOH.

The BM-SFO CVs on CFP (Figure 4.7b) show redox peaks that separate further with increasing scan rate that indicates diffusion limitations likely due to OH^- mass transport resistance within the thicker electrode film. Additionally, sweeping the potential more slowly shows two BM-SFO peaks on the cathodic scan similar to the capacitive contribution in Figure 4.3a. LSMO28 and SCO show broader features in Figure 4.7c,d

with their main feature in the positive scan direction above 0.1 V vs Hg/HgO and then in the entire negative scan direction growing with the scan rate.

The asymmetric pseudocapacitor voltage windows were determined by expanding the CV voltage window on the electrodes (shown in Figure A31) and assigning the voltage window to be the potential that gave an positive 0.5 A g_{ox}^{-1} (i.e. 0.5 mA cm^{-2}) on the back scan to ensure the galvanostatic charge-discharge (GCD) tests would not be significantly affected by electrolyte breakdown at low constant currents and high potentials. For clarity, positive (i.e. anodic) and negative (i.e. cathodic) currents correspond to the device charging and discharging respectively. The different asymmetric pseudocapacitors' CV profiles in Figure 4.8a-c demonstrate 1.8 V to 2.0 V voltage windows and show different peak shape and positions on charge and discharge that can be rationalized by examining the 3-electrode CV measurements shown in Figure A32. The charging peak at 1.4 V in Figure 4.8a corresponds to the voltage difference between the BM-SFO peak at -1.05 V and SCO peak at 0.35 V vs Hg/HgO in Figure A32. Additionally, its discharge peak (Figure 4.8a) at 0.95 V and shoulder result from the voltage difference between the positive BM-SFO peak at -0.55 V vs Hg/HgO and the negative SCO peaks at 0.4 V and 0.15 V vs Hg/HgO. A similar analysis for the BM-SFO//LSMO28 and LSMO28//SCO pseudocapacitors explains their peak positions as well. For example, the LSMO28//SCO pseudocapacitor exhibits two pairs of sharper redox peaks on charge and discharge that correspond to each materials' two redox features.

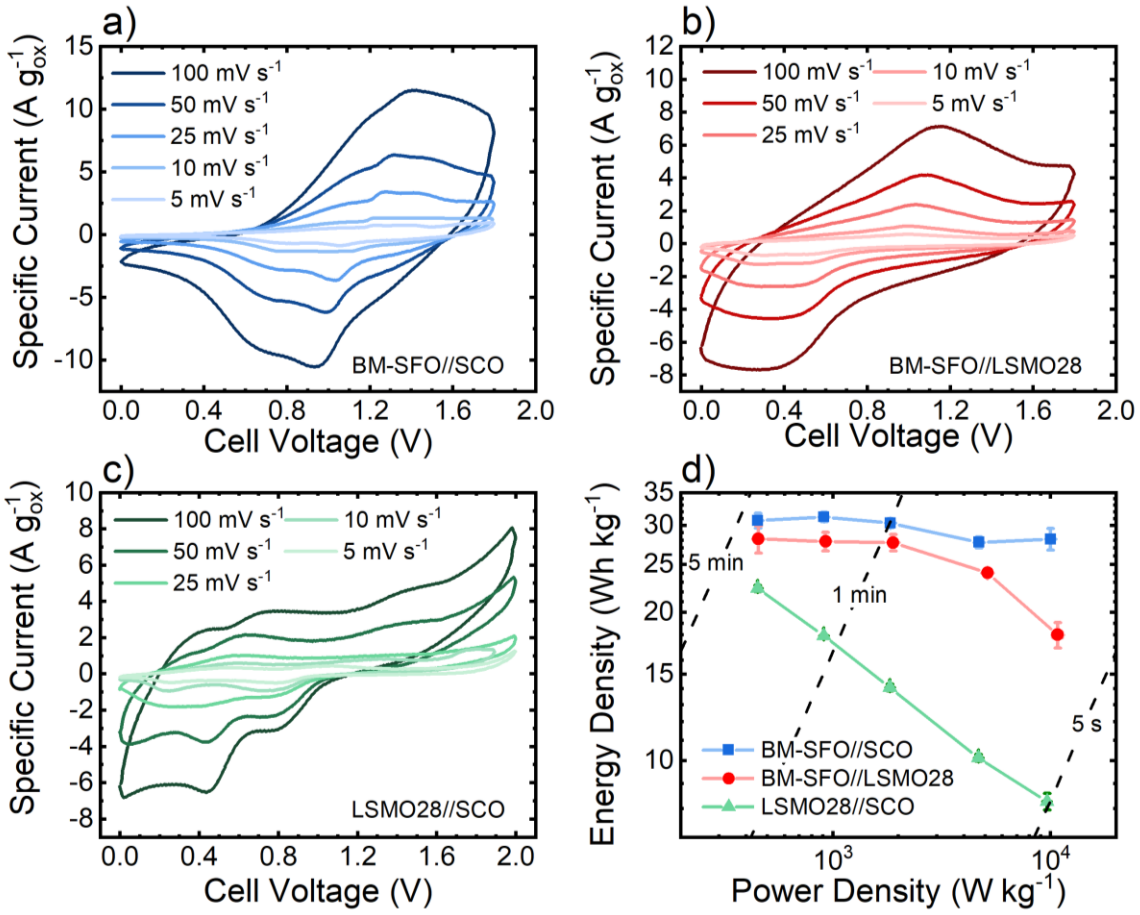

Figure 4.8 | Asymmetric pseudocapacitor cyclic voltammetry of $SrCoO_{3-\delta}$, $La_{0.2}Sr_{0.8}MnO_{3-\delta}$, BM-$Sr_2Fe_2O_5$ permutations.

CVs at various scan rates taken in Ar-saturated 1 M KOH on carbon fiber paper with 1 mg cm^{-2} mass loading of (a) BM-SFO//SCO, (b) LSMO28//SCO and (c) BM-SFO//LSMO28 with the notation given as anode//cathode. A (d) Ragone plot is given to compare energy and power density characteristics between the devices with dashed lines to indicate approximate charging and discharging times. All perovskite samples were prepared using an 85:15 perovskite: VC^A weight ratio.

The Ragone plot in Figure 4.8d shows the three asymmetric pseudocapacitors' energy and power densities from galvanostatic measurements (Figure A29a-c) with the BM-SFO//SCO device being the most energy dense, as expected, with it reaching an

energy density of 31 Wh kg^{-1} energy at low power density (450 W kg^{-1}) and retains most of its energy density (28 Wh kg^{-1}) at high power density (10,000 W kg^{-1}). Interestingly, BM-SFO//LSMO28 maintains a similar energy density up to ~2,000 W kg^{-1} but falls at higher power densities suggesting diffusion limitations which disagrees with our earlier hypothesis of power density trends. This occurs because the wider voltage window SCO allows more energy to be stored and discharged per unit time despite SCO being more diffusion limited than LSMO28. The LSMO28//SCO asymmetric pseudocapacitor appears to be diffusion limited over the whole examined power density range due to the decrease in energy stored as the power is increased which agrees with what one would expect from these materials having larger diffusion limitations than BM-SFO. Overall, these results indicate a promising new avenue for increasing the pseudocapacitor cell voltage by utilizing differences in perovskite redox potentials and consequently the performance of these devices. In time, they may become a viable, commercializable energy storage technology with further optimization of both the perovskite compositions and surface area as well as cell design parameters such as mass loading and the perovskite: carbon ratio.

4.4: CONCLUSIONS

In summary, we studied the current-potential scan rate dependence of BM-SFO, LSMO28 and SCO in 1 M KOH and found that the BM-SFO's and LSMO28' pseudocapacitance is charge transfer limited while SCO's is oxide-ion diffusion limited in nature. The asymmetric pseudocapacitor design was studied by comparing the current

collector performance of carbon fiber paper (CFP) and Ni foam and CFP was found to be the better support. Additionally, the first all-perovskite asymmetric pseudocapacitors were made to the best of our knowledge by choosing pairs of Sr-rich perovskites with large differences between their redox potentials to store charge at high potentials up to 2.0 V to increase their energy density. The BM-SFO//SCO high energy density of 31 Wh kg^{-1} at 450 W kg^{-1} is much higher than the 1.8 Wh kg^{-1} for the symmetric LSMO15//LSMO15@CFP,[20] 4 Wh kg^{-1} for industrial non-aqueous supercapacitors[10,11] and is on par with the VC^{A}//$SrCo_{0.9}Nb_{0.1}O_{3-\delta}$@Ni foam (37.6 Wh kg^{-1}).[18] Further work to increase the perovskite redox voltage window, increase electroactive material surface area and electrode support optimization could lead to longer lasting, faster charging energy storage in the future.

4.5 ADDITIONAL INFORMATION

More details regarding calculating the capacitive contribution to the cyclic voltammograms, synthesis conditions, sample characterization, electrode design, carbon capacitance contributions, sample crystallographic parameters, sample capacitance values at multiple scan rates and their electrochemical characterization in addition to asymmetric pseudocapacitor design and current collectors can be found in Appendix 3.

4.6 REFERENCES

(1) Vazquez, S.; Lukic, S. M.; Galvan, E.; Franquelo, L. G.; Carrasco, J. M. Energy Storage Systems for Transport and Grid Applications. *IEEE Trans. Ind. Electron.* **2010**, *57* (12), 3881–3895. https://doi.org/10.1109/TIE.2010.2076414.

(2) Miller, J. R.; Simon, P. MATERIALS SCIENCE: Electrochemical Capacitors for Energy Management. *Science* **2008**, *321* (5889), 651–652. https://doi.org/10.1126/science.1158736.

(3) Frackowiak, E.; Béguin, F. Carbon Materials for the Electrochemical Storage of Energy in Capacitors. *Carbon* **2001**, *39* (6), 937–950. https://doi.org/10.1016/S0008-6223(00)00183-4.
(4) Simon, P.; Gogotsi, Y. Materials for Electrochemical Capacitors. *Nat. Mater.* **2008**, *7* (11), 845–854. https://doi.org/10.1038/nmat2297.
(5) Chernova, N. A.; Roppolo, M.; Dillon, A. C.; Whittingham, M. S. Layered Vanadium and Molybdenum Oxides: Batteries and Electrochromics. *J. Mater. Chem.* **2009**, *19* (17), 2526. https://doi.org/10.1039/b819629j.
(6) Brezesinski, T.; Wang, J.; Tolbert, S. H.; Dunn, B. Ordered Mesoporous α-MoO3 with Iso-Oriented Nanocrystalline Walls for Thin-Film Pseudocapacitors. *Nat. Mater.* **2010**, *9* (2), 146–151. https://doi.org/10.1038/nmat2612.
(7) Brezesinski, K.; Wang, J.; Haetge, J.; Reitz, C.; Steinmueller, S. O.; Tolbert, S. H.; Smarsly, B. M.; Dunn, B.; Brezesinski, T. Pseudocapacitive Contributions to Charge Storage in Highly Ordered Mesoporous Group V Transition Metal Oxides with Iso-Oriented Layered Nanocrystalline Domains. *J. Am. Chem. Soc.* **2010**, *132* (20), 6982–6990. https://doi.org/10.1021/ja9106385.
(8) Xiong, H.; Yildirim, H.; Shevchenko, E. V.; Prakapenka, V. B.; Koo, B.; Slater, M. D.; Balasubramanian, M.; Sankaranarayanan, S. K. R. S.; Greeley, J. P.; Tepavcevic, S.; et al. Self-Improving Anode for Lithium-Ion Batteries Based on Amorphous to Cubic Phase Transition in TiO2 Nanotubes. *J. Phys. Chem. C* **2012**, *116* (4), 3181–3187. https://doi.org/10.1021/jp210793u.
(9) Augustyn, V.; Simon, P.; Dunn, B. Pseudocapacitive Oxide Materials for High-Rate Electrochemical Energy Storage. *Energy Environ. Sci.* **2014**, *7* (5), 1597. https://doi.org/10.1039/c3ee44164d.
(10) Wang, G.; Zhang, L.; Zhang, J. A Review of Electrode Materials for Electrochemical Supercapacitors. *Chem Soc Rev* **2012**, *41* (2), 797–828. https://doi.org/10.1039/C1CS15060J.
(11) Supercapacitor carbons http://dx.doi.org/10.1016/j.mattod.2013.09.005 (accessed May 16, 2018).
(12) Wang, F.; Xiao, S.; Hou, Y.; Hu, C.; Liu, L.; Wu, Y. Electrode Materials for Aqueous Asymmetric Supercapacitors. *RSC Adv.* **2013**, *3* (32), 13059. https://doi.org/10.1039/c3ra23466e.
(13) Conway, B. E. *Electrochemical Supercapacitors: Scientific Fundamentals and Technological Applications*; Springer Science & Business Media, 2013.
(14) Gu, J.; Jin, C.; Bian, Z.; Liu, X.; Li, S.; Tang, S.; Yuan, D. Asymmetric Capacitors Based on TiO<Subscript>2</Subscript> and Mesoporous MnO<Subscript>2</Subscript> Electrodes Using Neutral Aqueous Electrolyte. *J. Nanoparticle Res.* **2017**, *19* (9), 322. https://doi.org/10.1007/s11051-017-4015-3.
(15) Chen, P.-C.; Shen, G.; Shi, Y.; Chen, H.; Zhou, C. Preparation and Characterization of Flexible Asymmetric Supercapacitors Based on Transition-Metal-Oxide Nanowire/Single-Walled Carbon Nanotube Hybrid Thin-Film Electrodes. *ACS Nano* **2010**, *4* (8), 4403–4411. https://doi.org/10.1021/nn100856y.

(16) Mefford, J. T.; Hardin, W. G.; Dai, S.; Johnston, K. P.; Stevenson, K. J. Anion Charge Storage through Oxygen Intercalation in LaMnO3 Perovskite Pseudocapacitor Electrodes. *Nat. Mater.* **2014**, *13* (7), 726–732. https://doi.org/10.1038/nmat4000.
(17) Liu, Y.; Dinh, J.; Tade, M. O.; Shao, Z. Design of Perovskite Oxides as Anion-Intercalation-Type Electrodes for Supercapacitors: Cation Leaching Effect. *ACS Appl. Mater. Interfaces* **2016**, *8* (36), 23774–23783. https://doi.org/10.1021/acsami.6b08634.
(18) Zhu, L.; Liu, Y.; Su, C.; Zhou, W.; Liu, M.; Shao, Z. Perovskite SrCo0.9Nb0.1O3−δ as an Anion-Intercalated Electrode Material for Supercapacitors with Ultrahigh Volumetric Energy Density. *Angew. Chem.* **2016**, *128* (33), 9728–9731. https://doi.org/10.1002/ange.201603601.
(19) Che, W.; Wei, M.; Sang, Z.; Ou, Y.; Liu, Y.; Liu, J. Perovskite LaNiO 3-δ Oxide as an Anion-Intercalated Pseudocapacitor Electrode. *J. Alloys Compd.* **2018**, *731*, 381–388. https://doi.org/10.1016/j.jallcom.2017.10.027.
(20) Lang, X.; Mo, H.; Hu, X.; Tian, H. Supercapacitor Performance of Perovskite La $_{1-x}$ Sr $_{x}$ MnO $_{3}$. *Dalton Trans* **2017**, *46* (40), 13720–13730. https://doi.org/10.1039/C7DT03134C.
(21) Mefford, J. T.; Rong, X.; Abakumov, A. M.; Hardin, W. G.; Dai, S.; Kolpak, A. M.; Johnston, K. P.; Stevenson, K. J. Water Electrolysis on La1-xSrxCoO3-δ Perovskite Electrocatalysts. *Nat. Commun.* **2016**, *7*, 11053. https://doi.org/10.1038/ncomms11053.
(22) Richter, J.; Holtappels, P.; Graule, T.; Nakamura, T.; Gauckler, L. J. Materials Design for Perovskite SOFC Cathodes. *Monatshefte Für Chem. - Chem. Mon.* **2009**, *140* (9), 985–999. https://doi.org/10.1007/s00706-009-0153-3.
(23) Alexander, C. T.; Mefford, J. T.; Saunders, J.; Forslund, R. P.; Johnston, K. P.; Stevenson, K. J. Anion-Based Pseudocapacitance of the Perovskite Library La1–xSrxBO3−δ (B = Fe, Mn, Co). *ACS Appl. Mater. Interfaces* **2019**. https://doi.org/10.1021/acsami.8b19592.
(24) Cushing, B. L.; Kolesnichenko, V. L.; O'Connor, C. J. Recent Advances in the Liquid-Phase Syntheses of Inorganic Nanoparticles. *Chem. Rev.* **2004**, *104* (9), 3893–3946. https://doi.org/10.1021/cr030027b.
(25) Kuznetsov, D. A.; Han, B.; Yu, Y.; Rao, R. R.; Hwang, J.; Román-Leshkov, Y.; Shao-Horn, Y. Tuning Redox Transitions via Inductive Effect in Metal Oxides and Complexes, and Implications in Oxygen Electrocatalysis. *Joule* **2017**. https://doi.org/10.1016/j.joule.2017.11.014.
(26) Hardin, W. G.; Slanac, D. A.; Wang, X.; Dai, S.; Johnston, K. P.; Stevenson, K. J. Highly Active, Nonprecious Metal Perovskite Electrocatalysts for Bifunctional Metal–Air Battery Electrodes. *J. Phys. Chem. Lett.* **2013**, *4* (8), 1254–1259. https://doi.org/10.1021/jz400595z.
(27) Nemudry, A.; Rudolf, P.; Schöllhorn, R. Topotactic Electrochemical Redox Reactions of the Defect Perovskite SrCoO2.5+x. *Chem. Mater.* **1996**, *8* (9), 2232–2238. https://doi.org/10.1021/cm950504+.

(28) Grenier, J.-C.; Ghodbane, S.; Demazeau, G.; Pouchard, M.; Hagenmuller, P. Le Cobaltite de Strontium Sr2Co2O5 : Caracterisation et Proprietes Magnetiques. *Mater. Res. Bull.* **1979**, *14* (6), 831–839. https://doi.org/10.1016/0025-5408(79)90145-4.
(29) Qiu, L.; Lee, T. H.; Liu, L.-M.; Yang, Y. L.; Jacobson, A. J. Oxygen Permeation Studies of SrCo0.8Fe0.2O3 − δ. *Solid State Ion.* **1995**, *76* (3), 321–329. https://doi.org/10.1016/0167-2738(94)00296-5.
(30) Laiho, R.; Lisunov, K. G.; Lähderanta, E.; Petrenko, P. A.; Salminen, J.; Stamov, V. N.; Stepanov, Y. P.; Zakhvalinskii, V. S. Low-Field Magnetic Properties of LaMnO3+δ with 0.065≤δ≤0.154. *J. Phys. Chem. Solids* **2003**, *64* (12), 2313–2319. https://doi.org/10.1016/S0022-3697(03)00266-X.
(31) Alexander, C. T.; Abakumov, A. M.; Forslund, R. P.; Johnston, K. P.; Stevenson, K. J. Role of the Carbon Support on the Oxygen Reduction and Evolution Activities in LaNiO3 Composite Electrodes in Alkaline Solution. *ACS Appl. Energy Mater.* **2018**, *1* (4), 1549–1558. https://doi.org/10.1021/acsaem.7b00339.
(32) Hardin, W. G.; Mefford, J. T.; Slanac, D. A.; Patel, B. B.; Wang, X.; Dai, S.; Zhao, X.; Ruoff, R. S.; Johnston, K. P.; Stevenson, K. J. Tuning the Electrocatalytic Activity of Perovskites through Active Site Variation and Support Interactions. *Chem. Mater.* **2014**, *26* (11), 3368–3376. https://doi.org/10.1021/cm403785q.
(33) Zhang, S.; Pan, N. Supercapacitors Performance Evaluation. *Adv. Energy Mater.* **2015**, *5* (6), 1401401. https://doi.org/10.1002/aenm.201401401.
(34) Bard, A. J. *Electroanalytical Chemistry: A Series of Advances:*; CRC Press, 1990.
(35) Xing, W.; Qiao, S.; Wu, X.; Gao, X.; Zhou, J.; Zhuo, S.; Hartono, S. B.; Hulicova-Jurcakova, D. Exaggerated Capacitance Using Electrochemically Active Nickel Foam as Current Collector in Electrochemical Measurement. *J. Power Sources* **2011**, *196* (8), 4123–4127. https://doi.org/10.1016/j.jpowsour.2010.12.003.
(36) Nemudry, A.; Weiss, M.; Gainutdinov, I.; Boldyrev, V.; Schöllhorn, R. Room Temperature Electrochemical Redox Reactions of the Defect Perovskite SrFeO2.5+x. *Chem. Mater.* **1998**, *10* (9), 2403–2411. https://doi.org/10.1021/cm980090v.

Chapter 5: $LaNi_{1-x}Fe_xO_{3-\delta}$ and $SrFeO_{2.5}$ Perovskites For High Power Asymmetric and Symmetric Pseudocapacitors

5.1: Introduction

Safe, inexpensive and high power energy storage is increasing in importance as the world pushes to decarbonize the world economy by implementing sustainable, though intermittent, solar and wind energy resources.[1] A promising technology to meet this need are pseudocapacitors which can store charge faradaically at or near its surface which grants them higher charge storage capacity than electrochemical double layer capacitors (EDLCs) while yielding faster charge/discharge rates than a battery.[1–3] EDLCs store charge non-faradaically, meaning they store charge based on the electric field created between the electrode and ions in the electrolyte double layer with no charge crossing the electrode-double layer interface. In contrast, a faradaic charge transfer process involves a charge transfer across the double layer, and pseudocapacitance is one such process.

Conway explained several pseudocapacitive mechanisms that include underpotential deposition, redox pseudocapacitance and intercalation pseudocapacitance.[4,5] Pseudocapacitive materials like metal oxides have been studied extensively for energy storage, predominately with cation redox or cation intercalation pseudocapacitance mechanisms.[2,6] Our group was the first to demonstrate anion-

intercalation pseudocapacitance using a $LaMnO_3$ perovskite.[7] Perovskite oxides have the unit cell formula ABO_3 where the A-site is either an alkali or lanthanide element while the B-site is a transition metal element. By strategically selecting the A-site elemental composition, one can easily control the B-site element's oxidation state or the overall oxygen vacancy content via charge compensation.[8,9] For example, substituting La^{3+} for Sr^{2+} in the A-site will cause oxygen vacancy formation, B-site oxidation, or both. The $LaMnO_{3-\delta}$ anion-intercalation mechanism works via hydroxide ions filling oxygen vacancies to become lattice oxide ions that can then further diffuse into the bulk structure mediated by oxygen vacancies according to:

$$\mathrm{La}[\mathrm{Mn}^{2+}_{2\delta};\mathrm{Mn}^{3+}_{1-2\delta}]\mathrm{O}_{3-\delta} + 2\delta\mathrm{OH}^- \leftrightarrow La\mathrm{Mn}^{3+}\mathrm{O}_3 + 2\delta\mathrm{e}^- + \delta\mathrm{H}_2\mathrm{O} \qquad (1)$$

Since first demonstrating perovskites' anion-intercalation pseudocapacitance, researchers have studied many anion-based pseudocapacitive materials such as $La_{1-x}Sr_xMnO_3$,[7,8,10] $La_{1-x}Ca_xMnO_3$,[11] $SrCo_{0.9}Nb_{0.1}O_3$, [12] $La_{1-x}Sr_xFeO_3$,[8,13,14] $LaNiO_3$,[15,16] $Zn_xCo_{1-x}O$ nano-rods,[17] etc. and tested a variety as symmetric pseudocapacitors. The energy stored (E) for a capacitor is given by equation 2:

$$E = \frac{1}{2}CV_{cell}^2 \qquad (2)$$

where C is the electrodes' specific capacitance (F g^{-1}) and V_{cell} is the device's cell voltage. Equation 2 suggests that increasing the cell voltage is a good strategy to further increase a device's energy density which can be done by constructing an asymmetric pseudocapacitor. The material combinations for developing high voltage asymmetric pseudocapacitors have typically involved a high surface area carbon as the negative

electrode with materials like $LaNiO_3$ nanosheets,[18] $BiFeO_3$-reduced graphene oxide composite,[19] $Ba_2Bi_{0.1}Sc_{0.2}Co_{1.7}O_{6-\delta}$,[20] and $ZnCo_{1.5}(OH)_{4.5}Cl_{0.5}$[21] as the positive electrode. Recently, our group made a perovskite oxide materials library with $La_{1-x}Sr_xBO_{3-\delta}$ (B= Fe, Mn, Co) and demonstrated oxide ion intercalation generality in oxygen deficient perovskites.[8] In that work, it was shown that increasing oxygen vacancy content raised the material's pseudocapacitance while changing the B-site element altered the perovskites' intercalation redox potential. The possible device voltage window was then expanded by making an all perovskite asymmetric pseudocapacitor that took advantage of the large redox potential difference between $Fe^{2+/3+}$ and $Co^{3+/4+}$ redox in brownmillerite-$SrFeO_{2.5}$ (BM-SFO) and $SrCoO_{2.7}$ (SCO). The maximum voltage window achieved in this cell was 1.8 V with a maximum discharge potential at 0.95 V to yield a high energy density of 31 Wh kg^{-1} at 450 W kg^{-1}.[8] This was on par with other asymmetric pseudocapacitors like AC//$SrCo_{0.9}Nb_{0.1}O_3$ on Ni foam with a 1.5 V cell voltage and a 1.05 V discharge peak to yield 38 Wh kg^{-1} at 430 W kg^{-1}.[12] The cell voltage is limited by negative and positive electrode activity towards the hydrogen evolution and oxygen evolution reaction respectively in alkaline electrolyte. However, the device's power and energy density could be further enhanced if the transition metal redox potential difference is increased between the high voltage cathode and low voltage anode.

BM-SFO's low $Fe^{2+/3+}$ redox potential and low activity towards the HER makes it an ideal candidate as an anode for an asymmetric device.[8] Since SCO was previously used as the cathode,[8] a more electronegative B-site element like $Ni^{2+/3+}$ was chosen for the B-site because its redox behavior occurs at higher potentials than the $Co^{3+/4+}$ couple.[22]

Thus $LaNiO_{3-\delta}$ was selected due to reports indicating intercalation pseudocapacitance at high oxygen vacancy content.[15,20] Furthermore, our hypothesis is that its redox potential could be increased further by using the inductive effect[23] caused by interactions between dissimilar transition metals like Ni and Fe that is observed in $La_{0.5}Sr_{1.5}Ni_{1-x}Fe_xO_{4+\delta}$ (RP-LSNF) Ruddlesden-Popper,[24] NiO with iron impurities,[25] and $Ni(OH)_2$/NiOOH.[26] Similar to how bonding energy levels shift up and down according to molecular orbital theory, the inductive effect results in the more electronegative element's electronic energy bands to lower in energy (resulting in a higher redox potential) while causing the more electropositive element's electronic energy bands to increase in energy (shown as a lower redox potential). Thus, a series of $LaNi_{1-x}Fe_xO_{3-\delta}$ (x=0, 0.15, 0.55) perovskite materials was synthesized to be the cathode. These Ni-Fe compositions were chosen to maximize stored charge and potential based on the RP-LSNF materials.[24] For simplicity, these materials will be referred to as LNFXX where "XX" is the iron percent in the B-site (for example, $LaNi_{0.85}Fe_{0.15}O_{3-\delta}$ is represented as LNF15). The samples were further reduced in a H_2 environment at elevated temperatures to form oxygen vacancies to increase the amount of charge stored[7] instead of through the more difficult Sr A-site substitution with Ni in the B-site.[24,27]

In this work, we demonstrate the largest discharge potential (1.1 V) for an asymmetric anion-based pseudocapacitor to the best of our knowledge using BM-SFO//LNF55 as the electrodes with a total cell voltage of 1.8 V and 11.4 Wh kg^{-1} of energy stored at 453 W kg^{-1} power density. The 1.1 V discharge potential was achieved by using the inductive effect between Ni-O-Fe bonding interactions to push the $Ni^{2+/3+}$

redox potential higher. Additionally, a LNF55 symmetric pseudocapacitor was demonstrated for the first time with the largest discharge capacity reported for an anion-based symmetric pseudocapacitor at 0.95 V difference between the $Fe^{3+/4+}$ and $Ni^{2+/3+}$ redox reactions. The LNF materials were found to not have an intercalation pseudocapacitance mechanism, but instead followed a surface redox mechanism that enabled the LNF55//LNF55 pseudocapacitor to deliver a significant power density of 250,000 W kg^{-1} with 4.3 Wh kg^{-1} energy stored. This work shows an avenue to achieve higher voltage pseudocapacitors in the future by taking advantage of this inductive effect between different transition metals.

5.2: EXPERIMENTAL METHODS

5.2.1: Chemicals

$La(NO_3)_3*6H_2O$ (99.995%), $Sr(NO_3)_2$ (>99%), $Ni(NO_3)_2*6H_2O$ (99%), $Fe(NO_3)_3*9H_2O$ (99.995%) were purchased from ARCOS Organics and were used as received. Citric acid (100%), ethylenediaminetetraacetic acid (EDTA), potassium hydroxide, tetramethylammonium hydroxide (TMAOH), potato starch, hydrochloric acid (HCl), potassium iodide (KI), sodium thiosulfate ($Na_2S_2O_3$) and standard potassium iodate (KIO_3) were purchased from Fischer Scientific and 7% hydrogen gas with balance nitrogen was purchased from Praxair. The deionized (DI) water used was produced via ultrafiltration and had an 18 MΩ cm resistivity.

5.2.2: Perovskite synthesis

Perovskites were made using a Pechini synthesis[28] similar to that reported previously.[22] Briefly, 2.5 mmol of lanthanum nitrate or strontium nitrate and 2.5 mmol total of nickel nitrate and/or iron nitrate, at the appropriate ratios, were added to 50 mL of DI (deionized) water containing 5 mmol of citric acid and EDTA each. The solution was then neutralized using 30 mL of 1 M TMAOH to encourage ligand-metal chelation. This mixture was magnetically stirred at 100 r.p.m. on a hot plate at 140^{o}C to evaporate the water in solution thus leaving a thick gel behind. The gel in the glassware was then heated to 200-300^{o}C in a closed fume hood until it combusted to leave behind a dry ash. The ash was then placed into an alumina calcination boat in an alumina tube and calcined in a tube furnace under flowing air at 150 mL min^{-1}. The LNF samples were ramped to 700^{o}C in two hours and calcined at 700^{o}C for four hours before cooling to room temperature. The SFO was heated to 120^{o}C in 35 minutes, held at 120^{o}C for an hour and was then raised to 950^{o}C in 45 minutes to calcine at 950^{o}C for 5 hours followed by natural cooling to room temperature. The LNF samples were gently reduced in a 7% H_2/N_2 atmosphere flowing at 25 ml min^{-1} with a 2^{o}C min^{-1} ramp to 300^{o}C and held at 300^{o}C for 4 hours to avoid over reduction[29–32] while the SFO was reduced to BM-SFO by heating to 350^{o}C in 30 minutes and holding it at 350^{o}C for 4 hours. Both reductions were followed by natural cooling to room temperature.

5.2.3: Material characterization

The samples' phase purity and crystal structure were confirmed using x-ray diffraction (XRD) patterns taken on a Rigaku Miniflex 600 Diffractometer II with a Cu

Kα radiation (λ=1.5406 Å) source at 15 mA and 40 kW. JADE software was used to analyze and identify the sample phases. The samples' surface area was measured using a Brunauer-Emmett-Teller (BET) instrument (Quantachrome Instruments NOVA 2000 high-speed surface area analyzer) to first degas the samples overnight under mechanical vacuum and surface area measurements were taken at 77 K using N_2 adsorption. The linear P/P_o range used to measure the surface area was from 0.05 to 0.3 on the adsorption curve. The samples' oxygen vacancy content and B-site oxidation state was measured in triplicate via iodometric titrations as described previously except with corn starch replaced by potato starch for a sharper endpoint titration.[8] The LNF surface was characterized via x-ray photoelectron spectroscopy (XPS) using a Kratos axis Ultra DLD (Al α radiation, λ=1.4866 eV) instrument with high resolution spectra taken in 0.1 eV steps for the Ni 3p and Fe 2p regions. XPS spectra were calibrated relative to the adventitious carbon peak at 284.8 eV.

5.2.4: Three-Electrode Cell Preparation

The working electrode was an 85:15 perovskite: activated Vulcan carbon (VC^A) weight ratio composite. 51 μg cm^{-2} of the composites were loaded onto a 0.5 cm diameter (area= 0.196 cm^2) glassy carbon electrode (GCE) sheathed in polyether ether ketone (PEEK) in a rotating disk electrode (RDE) configuration. The composite was prepared using several steps. First, the perovskites taken from the furnace were washed using DI water followed by ethanol three times each via vacuum filtration with a nylon filter and were dried in a vacuum oven at 80°C. VC^A was prepared by ball milling XC-72 Vulcan

carbon from Cabot Corp. in a Wig-L-Bug ball mill for three minutes followed by soaking it in a 1 M HNO_3 solution at 80ºC overnight to increase its wettability by adding oxygen functionality to the surface. The VC^A was then collected and washed similarly to the perovskites as described above. The perovskites and VC^A were then separately ball milled for three minutes to break up agglomerates and then ball milled together into 85:15 perovskite: VC^A weight ratio composites.

The composites were loaded onto the GCEs by sonicating them in a 1 mg mL^{-1} solution of ethanol with 0.05 wt.% Na-substituted Nafion for two hours and pipetting them in 3.5, 3.5, 3 µL increments onto the GCE followed by rotation at ~185 r.p.m. until the ink completely dried to get a uniform film of 10 µg total loading. The electrodes used to measure the VC^A cyclic voltammograms (CVs) were loaded with 1.5 µg VC^A (7.65 µg cm^{-2}) which is the amount of carbon in the composites. The GCEs were cleaned by sonicating in a 1:1 DI water: ethanol volume ratio solution for thirty seconds followed by polishing in an alternating figure eight pattern using 50 nm alumina on a micro cloth polishing pad from CH Instruments. The electrodes were then rinsed with DI water, sonicated in a fresh 1:1 ethanol: DI water solution and rinsed again with DI water from a squirt bottle. The GCE was repolished and rinsed if the water from the final rinse did not seem to completely wet the electrode.

5.2.5: Two-Electrode Cell Preparation

The same ink as described above was used except it contained 10 mg mL^{-1} of composite material. 100 µL of this ink was pipetted in 10 to 20 µL increments onto both

sides of a 1 cm^2 square carbon fiber paper electrode (CFP, AvCarb MGL 190 from Fuel Cell Store) suspended just above a hot plate at 140^oC to get a 1 mg cm^{-2} total composite mass loading. Before the composite was added, the CFP electrodes were sonicated in acetone for 30 seconds and then sat in an oven at 80^oC for 30 minutes. Then only the 1 cm^2 electrode square (not the arm attached to it) was soaked in a 1 M HNO_3 for 30 seconds, followed by neutralization in a saturated $NaHCO_3$ solution, rinsing in DI water and then ethanol to dry. The composites' mass loading was designed to give each electrode the same stored charge based on the perovskite/carbon composite charge in the 3-electrode cell. The drop cast electrodes were dried overnight under ambient conditions. Before testing, a 1 M KOH drop was added to the CFP electrode square followed by 7 µL of isopropanol (IPA) and then rinsed the electrode with 1 mL of 1 M KOH to enable electrolyte penetration into the CFP pores. The electrodes were then allowed to soak in 1 M KOH for at least an hour before testing. Cu tape was attached to the CFP arm due to its fragility which was then wrapped with parafilm as illustrated previously[8] to prevent Cu-electrolyte contact to Cu from participating.

5.2.6: Electrochemical Characterization

Electrochemical measurements were made using a Metrohm Autolab PGSTAT302N with Pine Instrument high-speed rotators for a three-electrode set up while an Arbin Instruments battery cycler was used for two-electrode measurements. Three-electrode measurements were conducted in a European five-neck flask filled with Ar-saturated 1 M KOH with a 1 M KOH Hg/HgO reference electrode and gold wire

counter electrode contained behind a glass frit. CVs were cycled for BM-SFO between -1.2 V to 0.2 V vs Hg/HgO with the cathodic LNF peak cycled between -1.1 V to 0.4 V vs Hg/HgO and the anodic LNF peak cycled between 0.2 V to 0.6 V vs Hg/HgO at 100, 50, 25, 10 and 5 mV s^{-1} scan rates with one electrode per scan rate cycled three times. The electrode conditioning was performed by cycling over the entire voltage window ten times at 100 mV s^{-1} before each test. The capacitance per mass was calculated according to equation 3:

$$C_s = \frac{1}{2m\upsilon|V_C - V_A|}\oint_{V_C}^{V_A} i(V)dV \quad (3)$$

where m is the mass loading on the electrode [g], υ is the scan rate in the CV [V s^{-1}], i is the current [A], V is the applied potential and V_C and V_A are the lower (cathodic) and upper (anodic) voltage limited of the potential window [V]. Two electrode testing was performed by first identifying the voltage window via CVs with increasing voltage potentials swept at 100 mV s^{-1} in Ar-saturated 1 M KOH and choosing the potential that gave positive 0.5 A $g^{-1}_{composite}$ current on the back scan. Galvanostatic charge-discharge (GCD) tests were then run at 100, 50, 10, 5, 2, 1, 0.5 A $g^{-1}_{composite}$ currents to measure the devices' energy density vs. power density performance with the capacitance measured according to equation 4:

$$C = \frac{(V_{max} - \Delta V_{iR})I}{t_{dis}} \quad (4)$$

where V_{max} is the electrolyte window [V], ΔV_{iR} is the potential iR drop [V] due to current flowing through the resistance within the electrode, I is the constant applied current [A g^{-1}] and t_{dis} is the time [s] it takes the two-electrode cell to completely discharge to zero

volts. The two-electrode energy density (U [Wh kg^{-1}]) is then calculated according to equation 5:

$$U = \frac{1}{2} C V_{max}^2 \tag{5}$$

and the power density (P [W kg^{-1}]) is given by equation 6:

$$P = \frac{U}{t_{dis}} \tag{6}$$

5.3: Results and Discussion

5.3.1: Perovskite Physical Characterization

The brownmillerite-$SrFeO_{2.5}$ (BM-SFO) and $LaNi_{1-x}Fe_xO_{3-\delta}$ (LNF) perovskites were made phase pure as shown in Figure 5.1a. The samples were reduced in a hydrogen atmosphere to increase their oxygen vacancy content and thereby create more oxide storage sites.[7,8,20] The LNF perovskites will be referred to as LNFXX where "XX" is the iron content percent in the B-site (for example, LNF15 represents $LaNi_{0.85}Fe_{0.15}O_{3-\delta}$). LNF00 has a rhombohedral structure belonging to the R-3c space group and its peak at 32° 2θ has a tail at higher 2θ that corresponds to monoclinic $LaNiO_{2.5}$[30] in the C2/c space group. $LaNiO_{2.5}$ contains a mixture of Ni^{3+} in octahedral coordination and Ni^{+} in square-planar coordination which was confirmed by Moriga *et.al*[29] via XRD and XPS measurements. The $Ni^{1+/3+}$ oxidation states both have Jahn-Teller distortions that elongate their c-axis, while Ni^{2+} does not.[29] As a result, lattice strain would arise in the $LaNiO_{2.5}$ structure at Ni^{2+}-O-Ni^{3+} bonds , thus leading to Ni^{1+} being more stable than Ni^{2+}.[29] LNF15 was found to be orthorhombic in the Pbnm space group while LNF55 had a cubic crystal structure in the Pm-3m space group. Additionally, BM-SFO had an orthorhombic

lattice structure in the Ibm2 space group in agreement with prior work.[8] Table A16 summarizes these XRD results and crystal lattice parameters.

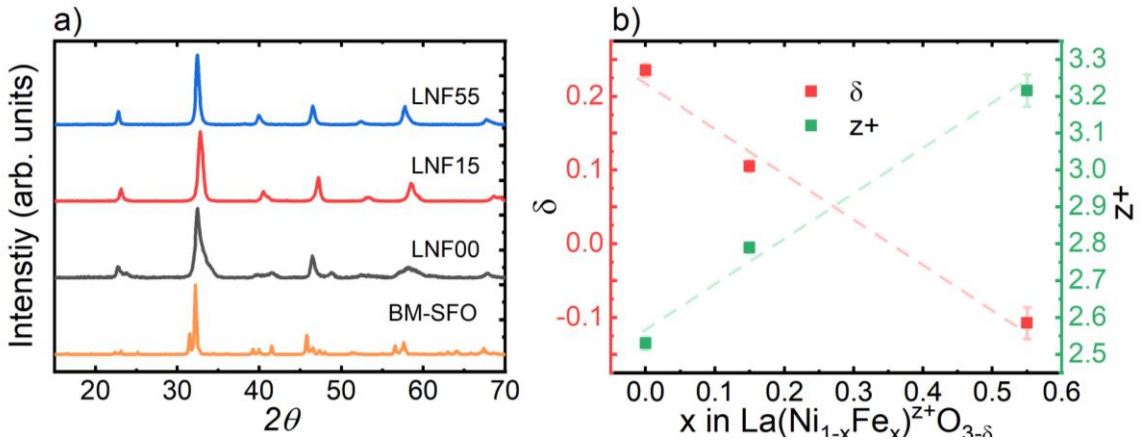

Figure 5.1 | Lattice Characterization.

(a) Phase pure XRD patterns of $LaNi_{1-x}Fe_xO_{3-d}$ and BM-$SrFeO_{2.5}$ samples. The samples' (b) oxygen vacancy content and (c) B-site oxidation state in triplicate via iodometric titration.

The LNF perovskites' BET surface areas were approximately 10 m^2 g^{-1} while BM-SFO had a 3 m^2 g^{-1} area with the precise values summarized in Table A17. The variation between the two is due to the higher calcination conditions for BM-SFO (950°C) compared to LNF (700°C) that would cause particle sintering and thus lower the exposed surface area. The perovskites' oxygen vacancy content and oxidation state were measured using iodometric titrations. The oxygen vacancy content of LNF00 is d = 0.235 and it decreases monotonically, shown in Figure 5.1b, as Fe is substituted into Ni sites to the point where LNF55 is actually super-stoichiometric in oxygen, which can be better interpreted as the presence of cation vacancies instead.[7] The consistent increase in perovskite oxygen content trending with the iron content is also translated to higher

oxidation states from 2.53+ for LNF00 all the way to 3.22+ for LNF55 in Figure 5.1b. These results are summarized in Table A18 along with the BM-SFO oxygen vacancy content (δ= 0.45) and iron oxidation state (z^{+}=3.09).

XPS was used to characterize the LNF surface, and the results show that increasing the iron content lowered the Ni surface content from ~11 at% to ~4 at% as shown in Figure A33a,c. The iron surface composition increased with iron content from ~3 at% to ~8 at% from LNF00 to LNF55 in Figure A33c. Interestingly, the lanthanum content stayed constant at 20 at% as expected, but the oxygen content was fixed at approximately 66 at% (which was greater than the expected 60 at%) and by mass-balance suggested that the total B-site content (shown in Figure A33c) was 13 at% (lower than the expected 20 at%). This means that the surface area for all the LNF perovskites' is cation deficient in Ni and Fe. This was an unexpected result considering that LNF00 and LNF15 were measured to have oxygen vacancies in their bulk.

5.3.2: Electrochemical Characterization

The BM-SFO redox activity displays large redox peak current densities over 100 A g_{ox}^{-1} with an $E_{1/2}$ centered at approximately -0.8 V vs Hg/HgO in Figure 5.2a in agreement with our prior report.[8] The BM-SFO peak current densities are approximately half that of what our group measured previously[8] due to the surface area being approximately half as well. The redox pseudocapacitance behavior and charge capacity in Figure 5.2d indicate that the BM-SFO bulk is being utilized for charge storage. The large redox peak separation suggests that the material exhibits battery-like behavior

(diffusional control) but its current-potential profile increases linearly with the scan rate[8] like a pseudocapacitor.[4] This scan rate dependence was previously attributed[8] to extrinsic pseudocapacitance caused by the perovskite's nano-size (L~ 64 nm based on BET surface area and perovskite density) being much smaller than the diffusion length ($(D_{ox}t)^{1/2}$) that leads to rapid diffusion rates and thus high current.

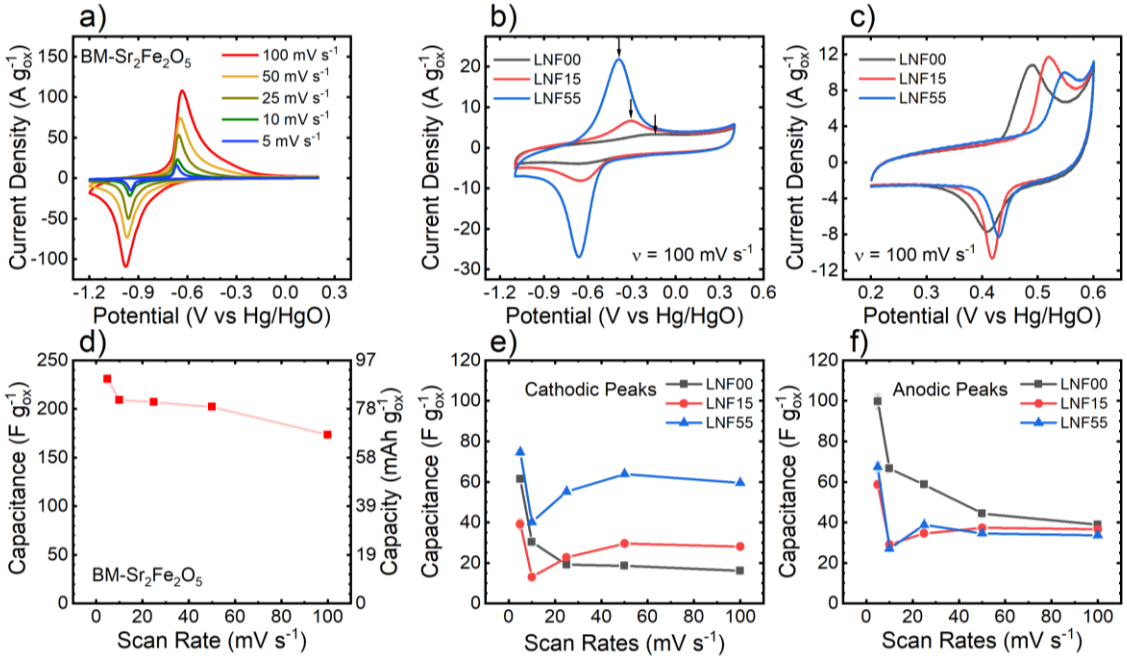

Figure 5.2 | Electrochemical Characterization.

Cyclic voltammograms of (a) BM-SFO and the (b) cathodic and (c) anodic redox peaks of $LaNi_{1-x}Fe_xO_{3-\delta}$ with their capacitance values given for each (d-f). CVs were taken in Ar-saturated 1 M KOH with 51 µg cm^{-2} 85:15 perovskite:VC^A composite loading and the carbon contribution to capacitance was subtracted from the perovskite-carbon composite capacitance.

There has been much debate in the literature[3,33] [3,33] about the meaning of pseudocapacitance and distinguishing it from battery-like behavior because both are faradaic in nature, but have different current-potential characteristics as described above.

To address whether BM-SFO is pseudocapacitive or battery-like, a constant current test at 16 mA g^{-1}_{ox} was performed on BM-SFO in Ar-saturated 1 M KOH to extract and insert oxide ions into the structure. BM-$SrFeO_x$ shows three rough plateau-like features during extraction with oxide solid solution behavior between the plateaus in Figure A34 indicating a two-phase transformation at x=2.55, 2.49 and 2.45, while the anion insertion shows two distinct plateaus at -0.65 V and -0.35 V vs Hg/HgO.

Nucleation energy barriers to these multiple phase transitions would slow charge transfer kinetics,[34] thus requiring a large overpotential in both directions towards intercalation and thus explain the large observed peak separation in BM-SFO.[4] Other work by Nemudry, *et. al.*[35] has identified the slow phase transformation of $SrFeO_{2.5}$ to $SrFeO_3$ occurring at approximately 0.2 V vs Hg/HgO at a 1.5 mA g_{ox}^{-1} current density. A small hump at x = 2.50 is observed during insertion occurring at approximately 0.4 V vs Hg/HgO which agrees with Nemudry[35] considering the iR drop and polarization resistance resulting from the ~10x higher applied current. The insertion plateaus at -0.65 V and -0.35 V vs Hg/HgO are possibly due to phase transitions involving the square planar $SrFeO_2$.[36,37] [36,37] These phase transformations would have no Jahn-Teller distortion differences between Fe^{2+} and Fe^{3+} that could cause strain during phase transformation and limit oxide diffusion[4,8] which would explain the high currents from BM-SFO and small capacitance/charge capacity increase with decreasing scan rate observed in Figure 5.2d. The BM-SFO large redox peak splitting combined with the constant current results in Figure A34 suggests that BM-SFO behaves as an oxide ion battery, however, the peak current density's linear trend with scan rate ($i \sim \upsilon$) suggests it is an extrinsic

pseudocapacitor. By combining these ideas together, BM-SFO could be considered a 'super-battery' material, but BM-SFO acts more as a high rate battery.

The LNF series' CVs show two pairs of redox peaks in Figure 5.2b,c. The peaks in Figure 5.2c are attributed to the $Ni^{2+/3+}$ redox couple and shift positively with increasing iron content. It was initially surprising to see the second pair of redox peaks, shown in Figure 5.2b, that increased in size and decreased in $E_{1/2}$ potential (marked with arrows to guide the eye) with increasing iron content. A previous report[8] showed that the $La_{1-x}Sr_xFeO_{3-\delta}$ series had redox peaks centered at approximately -0.8V ($Fe^{2+/3+}$) and -0.2V ($Fe^{3+/4+}$) vs Hg/HgO so it was surprising to find a pair of redox peaks between these two Fe redox potentials. These results can be explained by the inductive effect for tuning redox potentials as discussed by Kuznetsov, *et.al.*[23] for electrocatalysis applications where the more positive redox potential gets shifted higher and the more negative redox potential gets shifted lower when multiple redox reactions occur within the same material. The inductive effect can be thought of the same way the orbital energies shift in molecular orbital theory, in that the more electronegative orbital shifts to lower energy (or higher potentials) while the more electropositive orbital rises in energy (or lower potentials). Instead of discrete orbital energies shifting in MO theory, however, the inductive effect causes electronic energy bands within a solid material to shift up and down in energy for the more electropositive and more electronegative element respectively.[23] The redox peaks centered at approximately -0.5 V vs Hg/HgO shift to lower potentials with increasing iron content so they would therefore correspond to the shifted $Fe^{3+/4+}$ couple resulting from inductive coupling.

The VC^A capacitance was measured (Figure A35) and subtracted from the LNF series CVs' capacitance at various scan rates shown in Figure A36 with the corresponding LNF capacitance values shown in Figure 5.2e,f. The dip in capacitance at 10 mV s^{-1} was due to the VC^A capacitance subtraction, but despite this, it is easily seen in Figure 5.2e that the $Fe^{3+/4+}$ cathodic peak capacitance increases with iron content despite the oxygen vacancy content decrease. This result could be explained by the formation of cation vacancies in the bulk by Fe atoms diffusing to iron "surface vacancy" sites to participate in Fe-O redox similar to $Mn^{3+/4+}$ in $LaMnO_{3-\delta}$.[7] This trend runs counter to the anodic $Ni^{2+/3+}$ peak capacitance that initially decreases and then stays constant with increasing iron content, shown in Figure 5.2f. These capacitance values were lower than expected based on previous reports of $LaNiO_{3-\delta}$[15,18] which reported capacitances of approximately 290 F g^{-1} at 5 mV s^{-1} despite a similarly high oxygen vacancy content (δ = 0.235 for LNF00). One possibility is that the Ni foam current collector in previous studies contributed to a large background current leading to misleadingly high capacitance values.[38] To avoid confusion in the future, researchers should test pseudocapacitive materials on either a carbon substrate or another substrate with low background current.

5.3.3: Kinetic vs. Diffusion Limitations in LNF

The possibility of diffusion limitations for these redox reactions was evaluated by determining what fraction of the measured LNF current was capacitive in nature or involved a diffusion limited process. This can be done by recognizing that current resulting from capacitive processes will have a linear scan rate dependence ($i \sim \upsilon^1$) while

diffusion limited current will have a square root scan rate dependence ($i \sim \upsilon^{1/2}$).[39] The current-scan rate dependence in CVs at all potentials can be used to calculate[8,40] and plot the capacitive contributions shown as the shaded regions in Figure 5.3.

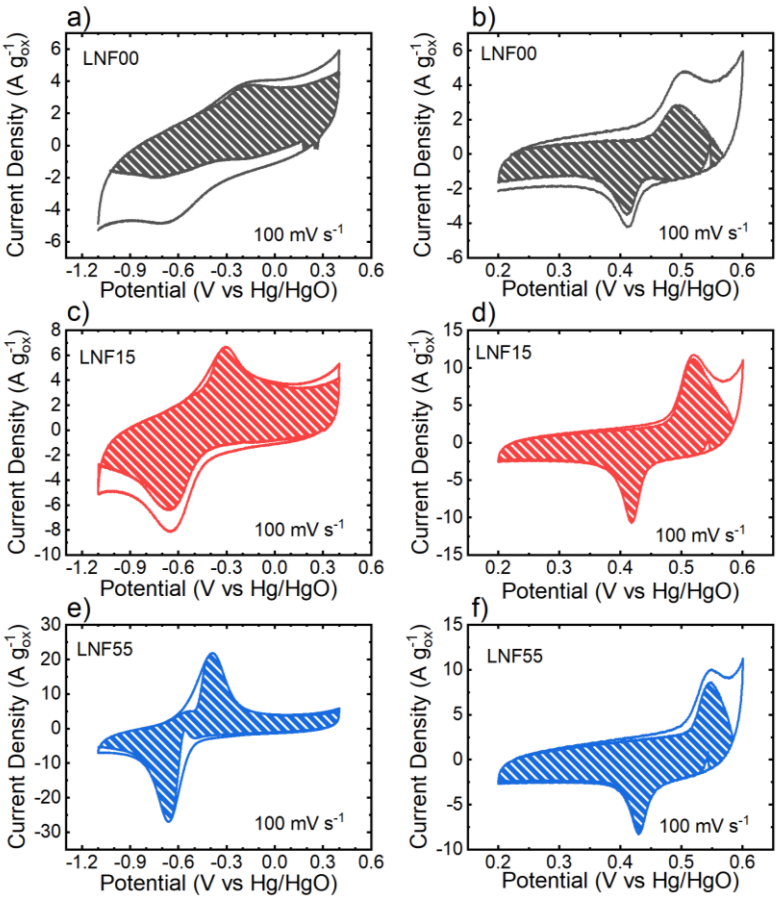

Figure 5.3 | Capacitive Contribution Determination.

CVs for (a-b) LNF00, (c-d) LNF15 and (e-f) LNF55 split into columns for the (a, c, e) cathodic peaks and (b, d, f) anodic peaks. The unshaded area for the anodic peaks near 0.6 V vs Hg/HgO is due to the oxygen evolution reaction (OER) onset. The shaded areas under the CVs represent contributions to redox pseudocapacitive currents.

The results show the samples' capacitive current contribution increasing with rising iron content for both redox peaks in Figure 5.3. The LNF00 oxide $Ni^{2+\rightarrow 3+}$ peak on

the positive sweep in Figure 5.3b appears to have some diffusion limitations that adding iron eliminates. The unshaded diffusive area appearing around the LNF55 $E_{1/2}$ value at ~-0.5 V vs Hg/HgO in Figure 5.3e is just a capacitive envelope calculation artifact because the peak separation decreases at slower scan rates as shown in Figure A36e. Pseudocapacitive redox peak splitting occurs for any pseudocapacitive process where the rate constant is small relative to the applied scan rate.[41]

The LNF anion-based redox was confirmed by measuring the LNF series' CVs (Figure A37) in Ar-saturated 1 N K_2SO_4 to hold the K^+ ion concentration to be the same as 1 M KOH. The $Ni^{2+/3+}$ peaks had completely disappeared in Figure A37b,d,f while the $Fe^{3+/4+}$ redox peaks shrank significantly and shifted to more positive potentials in Figure A37a,c,e that one would expect for OH^- based mechanisms. Although hydroxide was confirmed to participate in the pseudocapacitive mechanism, it did not explain the LNF series' lower-than-expected capacitance. To determine if the mechanism involved anion intercalation or anion surface redox, the moles of oxide anions was calculated by integrating the area under the $Ni^{2+/3+}$ and $Fe^{3+/4+}$ redox peaks which were then normalized by the moles of surface unit cells calculated using the BET surface area and XRD lattice parameters.

The results show that LNF00 only uses half an oxide anion or a full hydroxide ion per surface unit cell in Figure 5.4a. Instead of an anion intercalation mechanism as expected, a single hydroxide ion being used per surface unit cell suggests the $Ni^{2+/3+}$ peak involves a redox pseudocapacitive mechanism using surface NiO groups according to equation 7:

$$NiO + OH^- \rightarrow NiOOH + e^- \quad (7)$$

similar to $Ni(OH)_2$ in alkaline solution.[4,23] As the iron content increases, the fraction of $Ni^{2+/3+}$ used decreases while the $Fe^{3+/4+}$ peak increases from 1 oxide ion to 3.5 oxide anions per surface unit cell in Figure 5.4a. The iron redox peak utilizes more than just a single oxide ion as iron content increases thus suggesting it follows the more expected intercalation pseudocapacitance mechanism shown in equation 8:

$$La\mathrm{Ni}_{1-x}\left[\mathrm{Fe}^{3+}_{(1-2\delta)};\mathrm{Fe}^{4+}_{2\delta}\right]_x\mathrm{O}_{3-\delta} + 2\delta\mathrm{e}^- + \delta\mathrm{H_2O} \leftrightarrow \mathrm{LaNi}_{1-x}[\mathrm{Fe}^{3+}]_x\mathrm{O}_{3-\delta} + 2\delta\mathrm{OH}^- \quad (8)$$

despite the decrease in oxygen vacancies and oxygen superstoichiometry in LNF55. This data suggests that the intercalation mechanism would likely involve cation vacancy formation as previously described for $LaMnO_{3-\delta}$,[7] which agrees with the XPS results showing B-site vacancies at the perovskite surface in Figure A33c.

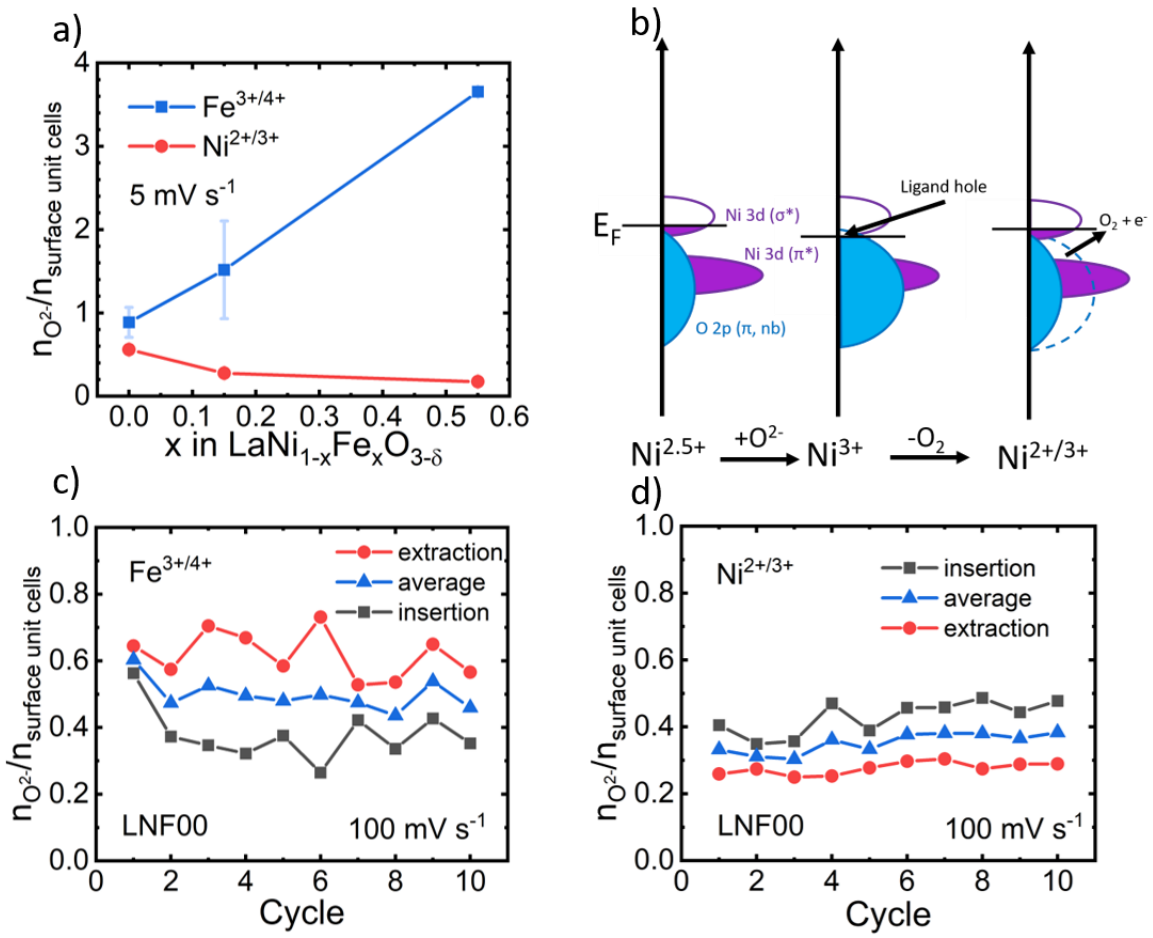

Figure 5.4 | Anion Adsorption vs. intercalation.

(a) The moles of oxide ions per mole of surface unit cells for the LNF $Fe^{3+/4+}$ and $Ni^{2+/3+}$ redox peaks versus B-site iron content with the values and error bars being the result from the forward and back scans at 5 mV s^{-1}. The moles of oxide ions were found by integrating the current to determine the charge on the forward scans and back scans together. (b) $Ni^{2+/3+}$ electronic configuration schematic during oxide insertion that shows oxide insertion causing the Fermi level to dip into the O 2p band as Ni^{2+} converts to Ni^{3+} which C causes oxide anions to be oxidized and emitted from the lattice as O_2, thus limiting oxide intercalation into the bulk. Moles of oxide ions at per mole of surface unit cells of different cycles at 100 mV s^{-1} for the (c) $Fe^{3+/4+}$ and (d) $Ni^{2+/3+}$ redox peaks.

One possible reason why anion intercalation does not occur could be due to the difference in Jahn-Teller distortions between Ni^{2+} and Ni^{3+}. As discussed above, Ni^{3+}

results in Jahn-Teller distortions unlike Ni^{2+} which causes the Ni^{3+} oxide octahedra to elongate along the unit cell c-axis that would cause strain at a Ni^{2+}-Ni^{3+} boundary and could limit oxide diffusion into the bulk for charge storage. In contrast, oxide anion diffusion was not limited by Jahn-Teller induced strain in Fe, Mn and Co perovskites as reported previously[8] as the Fe and Co electronic configurations did not pass through Jahn-Teller/non-Jahn-Teller distortion transitions and Mn^{3+} could disproportionate into Mn^{2+} and Mn^{4+} to avoid differences in Jahn-Teller distortions.[42]

Another explanation involves the $Ni^{2+/3+}$ electronic configuration during oxide insertion as illustrated in Figure 5.4b. As LNF further oxidizes Ni^{2+} to Ni^{3+}, the perovskite's Fermi level would dip into the O 2p band. Fermi level pinning[9,43] at the top of the O 2p band causes lattice O^{2-} to oxidize, release oxygen gas and donate an electron back into the Ni σ^* band thus reducing some Ni^{3+} back to Ni^{2+} as shown in Figure 5.4b as described elsewhere.[9] Therefore, not being able to insert oxide ions and utilize the bulk structure for charge storage due to complete Ni^{3+} formation would also explain the perovskites' lower capacitance.

The idea that Ni^{3+} limits anion intercalation was tested by calculating the moles of oxide ions used per mole of surface unit cells for the LNF00 conditioning cycles at 100 mV s^{-1} as shown in Figure A38. If the Ni^{3+} were limiting, it would be expected that the moles used per surface unit cell would not change with cycling because Ni^{3+} would block the surface. However, if instead the bulk oxygen vacancies were filled on the first cycle, then the number of oxide ions used per surface unit cell would be much higher on the first scan with the subsequent scans using a lower, but constant number of oxide ions.

Figure 5.4c shows there is a net drop in oxide anions used for the $Fe^{3+/4+}$ couple after the first cycle which suggests some irreversible filling of oxygen vacancies. Interestingly, at higher scan rates (100 mV s^{-1}) the $Fe^{3+/4+}$ couple only uses half an oxide ion or a full OH^- ion suggesting it is kinetically limited by surface OH^- redox like the $Ni^{2+/3+}$ couple. $Fe^{3+/4+}$ redox couple has a net extraction of ~0.2 oxide ions per cycle per unit cell which could be caused by the lower potentials reducing more Ni^{3+} to Ni^{2+} and thus lessen the extraction of oxide anions from the lattice.

Figure 5.4d shows the $Ni^{2+/3+}$ redox uses approximately 0.3 oxide ions per surface unit cell on average regardless of cycle number, thus suggesting Ni^{3+} blocks anion intercalation. Additionally, the lower number of OH^- used per surface unit cell suggests that OH^- adsorption is the rate limiting step at higher scan rates. In contrast to the $Fe^{3+/4+}$ couple, $Ni^{2+/3+}$ has a net insertion of oxide ions into the structure which could be due to a small amount of Ni^{2+} dissolving into solution as $Ni(OH)_3^-$. Figure A38b supports Ni^{2+} dissolution for only the first cycle because the LNF00 double layer capacitance decreases after the first cycle and stabilizes for the remaining scans which means surface restructuring is limited to the first cycle. The difference between the insertion and extraction charge in Figure 5.4d is likely an artifact caused the background subtraction for the cathodic scan that would not include the charge resulting from the LNF00 profile becoming more square with cycling in Figure A38b.

5.3.4: (A)symmetric Pseudocapacitors

The overall goal of this work was to increase the anion-based perovskite pseudocapacitor voltage window (V_{cell}) via substituting Fe in the B-site to utilize the inductive effect and increase the Ni redox potential because a capacitors' energy density and power density is proportional to the square of the cell voltage (eq. 5 and 6). LNF55 was selected as the cathode material because its $Ni^{2+/3+}$ redox peaks occur at the highest potential in the LNF series. The cell design nomenclature used herein is given as "anode material//cathode materials"; for example, BM-SFO//LNF55 means that BM-$SrFeO_{2.5}$ is the low voltage anode, and $LaNi_{0.45}Fe_{0.55}O_{3-\delta}$ is the high voltage cathode. Symmetric LNF55//LNF55 pseudocapacitor cells were made to utilize the large potential difference between the $Ni^{2+/3+}$ and $Fe^{3+/4+}$ redox peaks. The active material was supported onto a carbon fiber paper (CFP) electrode with 1 mg cm^{-2} mass loading of the limiting electrode material similar to our previous work.[8] CFP was used due to its much lower background current than Ni foam to minimize contributions from the current collector on the measured device performance.[38]

The voltage window was determined by cycling two-electrode cells at 100 mV s^{-1} in Ar-saturated 1 M KOH at increasing potential windows as shown in Figure A39 and choosing the upper voltage window limit as the cell voltage that yielded a positive 0.5 A g_{tot}^{-1} on the back sweep. The BM-SFO//LNF55 and LNF55//LNF55 voltage window were determined to be 1.8 V and 1.6 V respectively which suggests that LNF55 is a more active hydrogen evolution reaction (HER) catalyst than BM-SFO.

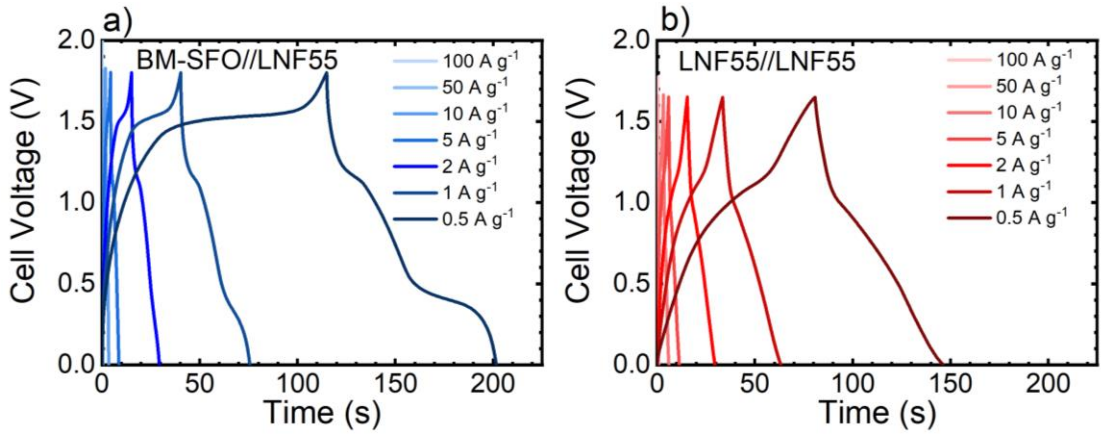

Figure 5.5 | Galvanostatic Charge Discharge (GCD) Curves for Asymmetric and Symmetric pseudocapacitors.

GCD curves for the asymmetric (a) BM-SFO//LNF55 hybrid pseudocapacitor and symmetric (b) LNF55//LNF55 pseudocapacitor taken in Ar-saturated 1 M KOH with the perovskite composite supported on carbon fiber paper.

The energy and power densities of both devices were measured using galvanostatic (e.g. constant current) charge and discharge measurements using the discharge curve for evaluating performance. Shown in Figure 5.5, the BM-SFO//LNF55 device shows a single battery-like plateau at ~1.5 V corresponding to the voltage difference between the BM-SFO cathodic peak and the LNF55 $Ni^{2+/3+}$ anodic peak. On discharge, it shows two faradaic features at 1.1 V and ~0.4 V in Figure 5.5a and Figure 5.6a. The 1.1 V feature matches the potential difference between the BM-SFO anodic peak and the LNF55 $Ni^{2+/3+}$ cathodic peak while the 0.4 V feature corresponds to the potential difference between the BM-SFO $E_{1/2}$ and the LNF55 $Fe^{3+/4+}$ $E_{1/2}$ redox peaks which makes sense from the perspective of a redox battery discharging at low (0.5 A g^{-1}) currents. Another possibility is that the 0.4 V redox feature in Figure 5.6a could be due to some residual oxygen reduction/hydrogen reduction reaction (ORR/HRR) activity from

trapped O_2 and H_2 bubbles caused by minor electrolyte breakdown when the cell is at higher potentials.

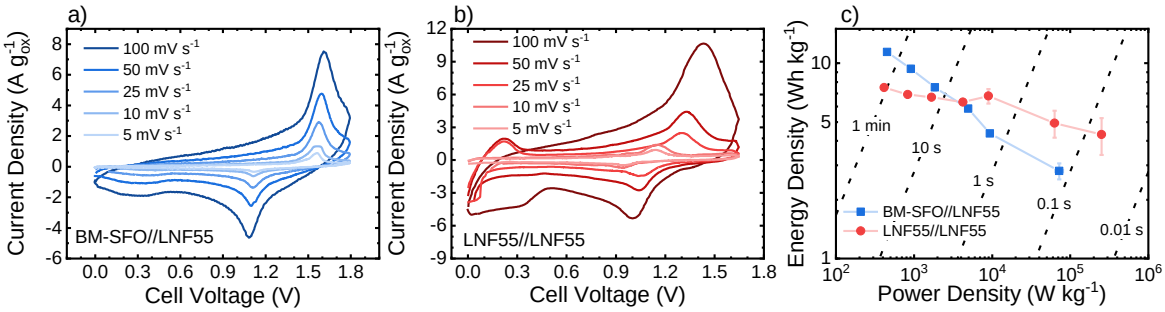

Figure 5.6 | Asymmetric and symmetric pseudocapacitor cells.

CVs of (a) BM-SFO//LNF55 and (b) LNF55//LNF55 in Ar-saturated 1 M KOH at various scan rates. (c) Ragone plot showing energy density and power density values calculated from their GCD discharge curves shown in Figure A39. The error bars are based on triplicate measurements.

In contrast, the LNF55//LNF55 symmetric pseudocapacitor does not show distinct plateaus in its GCD curves, but only a small hump at approximately 1 V in Figure 5.5b that corresponds to the potential difference between the LNF55 $Fe^{3+/4+}$ $E_{1/2}$ and $Ni^{2+/3+}$ $E_{1/2}$. Figure 5.6b, which shows CVs of both cell setups, better illustrates the discharge potential between the $Ni^{2+/3+}$ and $Fe^{3+/4+}$ redox with a discharge peak at 1 V and the charge peak between 1.2 V to 1.4 V depending on the scan rate and thus giving the LNF55//LNF55 device the largest operating potential for any anion-based symmetric pseudocapacitor reported to the best of our knowledge. The redox feature at 0-0.3 V in Figure 5.6b occurs only for faster scan rates which suggests that it could be due to ORR/HRR from trapped bubbles within the CFP pores that did not have enough time to diffuse away.

The behavior of the BM-SFO//LNF55 device can be best described as a hybrid oxide battery-pseudocapacitor. In contrast, the LNF55//LNF55 device's behavior would be best described as a symmetric pseudocapacitor.[44] Figure 5.6c shows a Ragone plot based on the discharge curves in Figure 5.5 according to equations 5 and 6. The BM-SFO//LNF55 hybrid device achieved a high 11.4 Wh kg^{-1} energy density at 453 W kg^{-1} although not quite as high as 31 Wh kg^{-1} at 450 W kg^{-1} for BM-SFO//SCO as reported previously[8] due to the LNF55's lower capacitance than $SrCoO_{3-\delta}$ (SCO). The LNF55//LNF55 symmetric pseudocapacitor achieved an exceptional 251,000 W kg^{-1} power density at 4.3 Wh kg^{-1} and maintained a 7.5 Wh kg^{-1} energy density down to 414 W kg^{-1}. The symmetric pseudocapacitor could reach such high power because LNF55 stores charge primarily at the surface and thus avoids the kinetic limitations BM-SFO would experience in the bulk. Thus, LNF55 is better suited towards high power applications like regenerative breaking and acceleration in electric vehicles and frequency regulation in the electric grid. Overall, these results showed that selective substitution of multiple transition metals into the perovskite B-site with the very electronegative Ni can inductively shift their redox peaks higher or lower to further increase the redox potential in anion-based energy storage devices. These concepts can lead to further design directions to enable safe, low cost, anion-based energy storage in the future.

5.4: CONCLUSIONS

BM-$SrFeO_{2.5}$ and a $LaNi_{1-x}Fe_xO_{3-\delta}$ perovskite series were synthesized and characterized to use Ni's higher electronegativity along with the inductive effect[23] to

achieve the largest redox potential window reported to date for an anion-based pseudocapacitor. The BM-SFO//LNF55 oxide battery-pseudocapacitor hybrid (or asymmetric pseudocapacitor for short) displayed a 1.1 V discharge voltage and 1.8 V cell voltage with the previous highest discharge voltage at 1.05 V[12] for activated carbon//$SrCo_{0.9}Nb_{0.1}O_{3-\delta}$ and 0.95 V for BM-$SrFeO_{2.5}$//$SrCoO_{2.7}$.[8] The LNF materials' pseudocapacitance involved predominately surface-based $Fe^{3+/4+}$ and $Ni^{2+/3+}$ redox processes rather than bulk intercalation that enabled the high power LNF55//LNF55 pseudocapacitor to discharge at 250,000 W kg^{-1} power density with 4.3 Wh kg^{-1} energy density. The LNF55//LNF55 pseudocapacitor has a discharge peak at 1 V thus making it the largest operating potential for any reported anion-based symmetric pseudocapacitor to date. BM-SFO was found to be a battery-like material from constant current curves, but with large currents exceeding 100 A g^{-1} at 100 mV s^{-1}. By utilizing the BM-SFO bulk, the BM-SFO//LNF55 asymmetric pseudocapacitor could achieve a high 11.4 Wh kg^{-1} energy density at 453 W kg^{-1}. Future anion pseudocapacitor development may utilize elemental substitution to take advantage of the inductive effect and further extend the voltage windows of novel devices. Additionally, future materials may be designed to manage strain caused by lattice distortions as well as bulk Fermi energy levels and lattice oxygen contents to allow for charge storage in the bulk.

5.5: Additional Information

More details regarding sample lattice parameters, BET surface areas, iodometric titration results, XPS spectra and surface compositions, BM-SFO constant current data,

VC^A CVs and capacitance values, the LNF series' CVs in 1 M KOH and 1 N K_2SO_4, device voltage window determination and GCD curves can be found in Appendix 4.

5.6: REFERENCES

(1) Nan, H.; Hu, X.; Tian, H. Recent Advances in Perovskite Oxides for Anion-Intercalation Supercapacitor: A Review. *Mater. Sci. Semicond. Process.* **2019**, *94*, 35–50. https://doi.org/10.1016/j.mssp.2019.01.033.

(2) Augustyn, V.; Simon, P.; Dunn, B. Pseudocapacitive Oxide Materials for High-Rate Electrochemical Energy Storage. *Energy Environ. Sci.* **2014**, *7* (5), 1597–1614. https://doi.org/10.1039/c3ee44164d.

(3) Simon, P.; Gogotsi, Y. Materials for Electrochemical Capacitors. *Nat. Mater.* **2008**, *7* (11), 845–854. https://doi.org/10.1038/nmat2297.

(4) Conway, B. E. *Electrochemical Supercapacitors: Scientific Fundamentals and Technological Applications*; Springer Science & Business Media, 2013.

(5) Conway, B. E. Two-Dimensional and Quasi-Two-Dimensional Isotherms for Li Intercalation and Upd Processes at Surfaces. *Electrochimica Acta* **1993**, *38* (9), 1249–1258. https://doi.org/10.1016/0013-4686(93)80055-5.

(6) Hahn, B. P.; Long, J. W.; Rolison, D. R. Something from Nothing: Enhancing Electrochemical Charge Storage with Cation Vacancies. *Acc. Chem. Res.* **2013**, *46* (5), 1181–1191. https://doi.org/10.1021/ar200238w.

(7) Mefford, J. T.; Hardin, W. G.; Dai, S.; Johnston, K. P.; Stevenson, K. J. Anion Charge Storage through Oxygen Intercalation in LaMnO3 Perovskite Pseudocapacitor Electrodes. *Nat. Mater.* **2014**, *13* (7), 726–732. https://doi.org/10.1038/nmat4000.

(8) Alexander, C. T.; Mefford, J. T.; Saunders, J.; Forslund, R. P.; Johnston, K. P.; Stevenson, K. J. Anion-Based Pseudocapacitance of the Perovskite Library La1–xSrxBO3−δ (B = Fe, Mn, Co). *ACS Appl. Mater. Interfaces* **2019**. https://doi.org/10.1021/acsami.8b19592.

(9) Mefford, J. T.; Rong, X.; Abakumov, A. M.; Hardin, W. G.; Dai, S.; Kolpak, A. M.; Johnston, K. P.; Stevenson, K. J. Water Electrolysis on La1-xSrxCoO3-δ Perovskite Electrocatalysts. *Nat. Commun.* **2016**, *7*, 11053. https://doi.org/10.1038/ncomms11053.

(10) Lang, X.; Mo, H.; Hu, X.; Tian, H. Supercapacitor Performance of Perovskite $La_{1-x}Sr_xMnO_3$. *Dalton Trans* **2017**, *46* (40), 13720–13730. https://doi.org/10.1039/C7DT03134C.

(11) Mo, H.; Nan, H.; Lang, X.; Liu, S.; Qiao, L.; Hu, X.; Tian, H. Influence of Calcium Doping on Performance of LaMnO 3 Supercapacitors. *Ceram. Int.* **2018**, *44* (8), 9733–9741. https://doi.org/10.1016/j.ceramint.2018.02.205.

(12) Zhu, L.; Liu, Y.; Su, C.; Zhou, W.; Liu, M.; Shao, Z. Perovskite SrCo0.9Nb0.1O3−δ as an Anion-Intercalated Electrode Material for Supercapacitors with Ultrahigh

Volumetric Energy Density. *Angew. Chem. Int. Ed. 55* (33), 9576–9579. https://doi.org/10.1002/anie.201603601.
(13) Wang, W.; Lin, B.; Zhang, H.; Sun, Y.; Zhang, X.; Yang, H. Synthesis, Morphology and Electrochemical Performances of Perovskite-Type Oxide LaxSr1-xFeO3 Nanofibers Prepared by Electrospinning. *J. Phys. Chem. Solids* **2019**, *124*, 144–150. https://doi.org/10.1016/j.jpcs.2018.09.011.
(14) Li, Z.; Zhang, W.; Yuan, C.; Su, Y. Controlled Synthesis of Perovskite Lanthanum Ferrite Nanotubes with Excellent Electrochemical Properties. *RSC Adv.* **2017**, *7* (21), 12931–12937. https://doi.org/10.1039/C6RA27423D.
(15) Che, W.; Wei, M.; Sang, Z.; Ou, Y.; Liu, Y.; Liu, J. Perovskite LaNiO 3-δ Oxide as an Anion-Intercalated Pseudocapacitor Electrode. *J. Alloys Compd.* **2018**, *731*, 381–388. https://doi.org/10.1016/j.jallcom.2017.10.027.
(16) Ho, K.-H.; Wang, J. Hydrazine Reduction of LaNiO3 for Active Materials in Supercapacitors. *J. Am. Ceram. Soc.* **2017**, *100* (10), 4629–4637. https://doi.org/10.1111/jace.14997.
(17) Ling, T.; Da, P.; Zheng, X.; Ge, B.; Hu, Z.; Wu, M.; Du, X.-W.; Hu, W.-B.; Jaroniec, M.; Qiao, S.-Z. Atomic-Level Structure Engineering of Metal Oxides for High-Rate Oxygen Intercalation Pseudocapacitance. *Sci. Adv.* **2018**, *4* (10), eaau6261. https://doi.org/10.1126/sciadv.aau6261.
(18) Li, Z.; Zhang, W.; Wang, H.; Yang, B. Two-Dimensional Perovskite LaNiO3 Nanosheets with Hierarchical Porous Structure for High-Rate Capacitive Energy Storage. *Electrochimica Acta* **2017**, *258*, 561–570. https://doi.org/10.1016/j.electacta.2017.11.099.
(19) Moitra, D.; Anand, C.; Ghosh, B. K.; Chandel, M.; Ghosh, N. N. One-Dimensional BiFeO3 Nanowire-Reduced Graphene Oxide Nanocomposite as Excellent Supercapacitor Electrode Material. *ACS Appl. Energy Mater.* **2018**, *1* (2), 464–474. https://doi.org/10.1021/acsaem.7b00097.
(20) Liu, Y.; Wang, Z.; Veder, J.-P. M.; Xu, Z.; Zhong, Y.; Zhou, W.; Tade, M. O.; Wang, S.; Shao, Z. Highly Defective Layered Double Perovskite Oxide for Efficient Energy Storage via Reversible Pseudocapacitive Oxygen-Anion Intercalation. *Adv. Energy Mater.* **2018**, *8* (11), 1702604. https://doi.org/10.1002/aenm.201702604.
(21) Pan, Z.; Jiang, Y.; Yang, P.; Wu, Z.; Tian, W.; Liu, L.; Song, Y.; Gu, Q.; Sun, D.; Hu, L. In Situ Growth of Layered Bimetallic ZnCo Hydroxide Nanosheets for High-Performance All-Solid-State Pseudocapacitor. *ACS Nano* **2018**, *12* (3), 2968–2979. https://doi.org/10.1021/acsnano.8b00653.
(22) Alexander, C. T.; Abakumov, A. M.; Forslund, R. P.; Johnston, K. P.; Stevenson, K. J. Role of the Carbon Support on the Oxygen Reduction and Evolution Activities in LaNiO3 Composite Electrodes in Alkaline Solution. *ACS Appl. Energy Mater.* **2018**, *1* (4), 1549–1558. https://doi.org/10.1021/acsaem.7b00339.
(23) Kuznetsov, D. A.; Han, B.; Yu, Y.; Rao, R. R.; Hwang, J.; Román-Leshkov, Y.; Shao-Horn, Y. Tuning Redox Transitions via Inductive Effect in Metal Oxides and Complexes, and Implications in Oxygen Electrocatalysis. *Joule* **2017**. https://doi.org/10.1016/j.joule.2017.11.014.

(24) Forslund, R. P.; Hardin, W. G.; Rong, X.; Abakumov, A. M.; Filimonov, D.; Alexander, C. T.; Mefford, J. T.; Iyer, H.; Kolpak, A. M.; Johnston, K. P.; et al. Exceptional Electrocatalytic Oxygen Evolution via Tunable Charge Transfer Interactions in La 0.5 Sr 1.5 Ni 1−x Fe X O 4±δ Ruddlesden-Popper Oxides. *Nat. Commun.* **2018**, *9* (1), 3150. https://doi.org/10.1038/s41467-018-05600-y.
(25) Corrigan, D. A. The Catalysis of the Oxygen Evolution Reaction by Iron Impurities in Thin Film Nickel Oxide Electrodes. *J. Electrochem. Soc.* **1987**, *134* (2), 377–384. https://doi.org/10.1149/1.2100463.
(26) Louie, M. W.; Bell, A. T. An Investigation of Thin-Film Ni–Fe Oxide Catalysts for the Electrochemical Evolution of Oxygen. *J. Am. Chem. Soc.* **2013**, *135* (33), 12329–12337. https://doi.org/10.1021/ja405351s.
(27) Cao, Y.; Lin, B.; Sun, Y.; Yang, H.; Zhang, X. Sr-Doped Lanthanum Nickelate Nanofibers for High Energy Density Supercapacitors. *Electrochimica Acta* **2015**, *174*, 41–50. https://doi.org/10.1016/j.electacta.2015.05.131.
(28) Cushing, B. L.; Kolesnichenko, V. L.; O'Connor, C. J. Recent Advances in the Liquid-Phase Syntheses of Inorganic Nanoparticles. *Chem. Rev.* **2004**, *104* (9), 3893–3946. https://doi.org/10.1021/cr030027b.
(29) Moriga, T.; Usaka, O.; Imamura, T.; Nakabayashi, I.; Matsubara, I.; Kinouchi, T.; Kikkawa, S.; Kanamaru, F. Synthesis, Crystal Structure, and Properties of Oxygen-Deficient Lanthanum Nickelate LaNiO3−x ($0 \leq X \leq 0.5$). *Bull. Chem. Soc. Jpn.* **1994**, *67* (3), 687–693. https://doi.org/10.1246/bcsj.67.687.
(30) Crespin, M.; Levitz, P.; Gatineau, L. Reduced Forms of LaNiO 3 Perovskite. Part 1.—Evidence for New Phases: La 2 Ni 2 O 5 and LaNiO 2. *J. Chem. Soc. Faraday Trans. 2 Mol. Chem. Phys.* **1983**, *79* (8), 1181–1194.
(31) Hayward, M. A.; Green, M. A.; Rosseinsky, M. J.; Sloan, J. Sodium Hydride as a Powerful Reducing Agent for Topotactic Oxide Deintercalation: Synthesis and Characterization of the Nickel(I) Oxide LaNiO2. *J. Am. Chem. Soc.* **1999**, *121* (38), 8843–8854. https://doi.org/10.1021/ja991573i.
(32) Alonso, J. A.; Martínez-Lope, M. J. Preparation and Crystal Structure of the Deficient Perovskite LaNiO 2.5, Solved from Neutron Powder Diffraction Data. *J. Chem. Soc. Dalton Trans.* **1995**, No. 17, 2819–2824.
(33) Brousse, T.; Bélanger, D.; Long, J. W. To Be or Not To Be Pseudocapacitive? *J. Electrochem. Soc.* **2015**, *162* (5), A5185–A5189. https://doi.org/10.1149/2.0201505jes.
(34) Bazant, M. Z. Theory of Chemical Kinetics and Charge Transfer Based on Nonequilibrium Thermodynamics. *Acc. Chem. Res.* **2013**, *46* (5), 1144–1160. https://doi.org/10.1021/ar300145c.
(35) Nemudry, A.; Weiss, M.; Gainutdinov, I.; Boldyrev, V.; Schöllhorn, R. Room Temperature Electrochemical Redox Reactions of the Defect Perovskite SrFeO2.5+x. *Chem. Mater.* **1998**, *10* (9), 2403–2411. https://doi.org/10.1021/cm980090v.
(36) Tassel, C.; Kageyama, H. Square Planar Coordinate Iron Oxides. *Chem. Soc. Rev.* **2012**, *41* (6), 2025–2035. https://doi.org/10.1039/C1CS15218A.

(37) Tsujimoto, Y.; Tassel, C.; Hayashi, N.; Watanabe, T.; Kageyama, H.; Yoshimura, K.; Takano, M.; Ceretti, M.; Ritter, C.; Paulus, W. Infinite-Layer Iron Oxide with a Square-Planar Coordination. *Nature* **2007**, *450* (7172), 1062–1065. https://doi.org/10.1038/nature06382.
(38) Xing, W.; Qiao, S.; Wu, X.; Gao, X.; Zhou, J.; Zhuo, S.; Hartono, S. B.; Hulicova-Jurcakova, D. Exaggerated Capacitance Using Electrochemically Active Nickel Foam as Current Collector in Electrochemical Measurement. *J. Power Sources* **2011**, *196* (8), 4123–4127. https://doi.org/10.1016/j.jpowsour.2010.12.003.
(39) Bard, A. J. *Electroanalytical Chemistry: A Series of Advances:*; CRC Press, 1990.
(40) Liu, T.-C.; Pell, W. G.; Conway, B. E.; Roberson, S. L. Behavior of Molybdenum Nitrides as Materials for Electrochemical Capacitors Comparison with Ruthenium Oxide. *J. Electrochem. Soc.* **1998**, *145* (6), 1882–1888. https://doi.org/10.1149/1.1838571.
(41) Conway, B. E. Transition from "Supercapacitor" to "Battery" Behavior in Electrochemical Energy Storage. *J. Electrochem. Soc.* **1991**, *138* (6), 1539–1548. https://doi.org/10.1149/1.2085829.
(42) Hunter, J. C. Preparation of a New Crystal Form of Manganese Dioxide: λ-MnO2. *J. Solid State Chem.* **1981**, *39* (2), 142–147.
(43) Maiyalagan, T.; Jarvis, K. A.; Therese, S.; Ferreira, P. J.; Manthiram, A. Spinel-Type Lithium Cobalt Oxide as a Bifunctional Electrocatalyst for the Oxygen Evolution and Oxygen Reduction Reactions. *Nat. Commun.* **2014**, *5*, 3949. https://doi.org/10.1038/ncomms4949.
(44) Gogotsi, Y.; Penner, R. M. Energy Storage in Nanomaterials – Capacitive, Pseudocapacitive, or Battery-Like? *ACS Nano* **2018**, *12* (3), 2081–2083. https://doi.org/10.1021/acsnano.8b01914.

Appendices

APPENDIX 1: ROLE OF THE CARBON SUPPORT ON THE OXYGEN REDUCTION AND EVOLUTION ACTIVITIES IN $LaNiO_3$ COMPOSITE ELECTRODES IN ALKALINE SOLUTION

A1.1 Brief Description of Reaction 2.2

Cline and Bielski showed[1–3] that reaction 2 proceeds by first reducing adsorbed oxygen to superoxide:

$$O_{2(ads)} + e^- \rightarrow O_2^- \quad \text{(S1)}$$

which is protonated to form a peroxide radical

$$O_2^- + H_2O \rightarrow HO_2^{\cdot} + OH^- \quad \text{(S2)}$$

that reacts with superoxide to form hydroperoxide and molecular oxygen

$$O_2^- + HO_2^{\cdot} \rightarrow HO_2^- + O_2 \quad \text{(S3)}$$

A1.2 RHE Measurement

All potentials are reported relative to RHE which was measured by first polishing and cycling a Pt disk RDE in H_2 saturated 0.5 M H_2SO_4 between 0.8 V and -0.63 V vs Ag/AgCl at 100 mV/s until the profile stabilized indicating complete reduction of surface oxides to Pt metal. Then the Pt RDE was rinsed with DI water and cycled in a H_2 saturated 0.1 M KOH solution from 0.7 V to -0.7 V vs Hg/HgO at 100 mV/s until the profile stabilized. The actual RHE CVs were run at 1 mV/s in the H_2 saturated 0.1 M KOH and RHE was taken to be the average potential of the forward and backward scans at zero current (Figure A3).

A1.3. ORR Raw Data to Tafel Plot Conversion

When an electrochemical reaction is mass transfer limited on an RDE the current can be described by the Koutecký-Levich equation[4]:

$$\frac{1}{i} = \frac{1}{i_{kin}} + \frac{1}{i_{l,c}} \quad \text{(S4)}$$

where i is the raw current, i_{kin} is the kinetic current in the absence of mass transfer resistance and $i_{l,c}$ is the diffusion limited current. Equation (S4) can be rearranged and solved for i_{kin} to yield:

$$i_{kin} = \frac{i * i_{l,c}}{i_{l,c} - i} \quad \text{(S5)}$$

Plotting this kinetic current versus the iR corrected potential allows one to measure Tafel slopes and better understand the kinetics of the reaction.

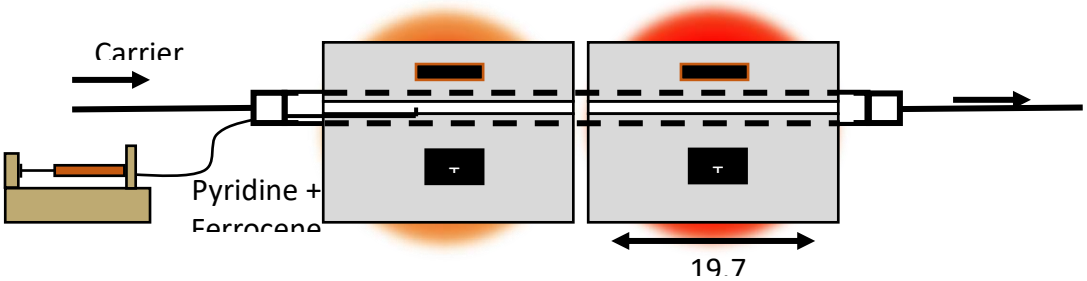

Figure A1 | CVD furnace schematic.

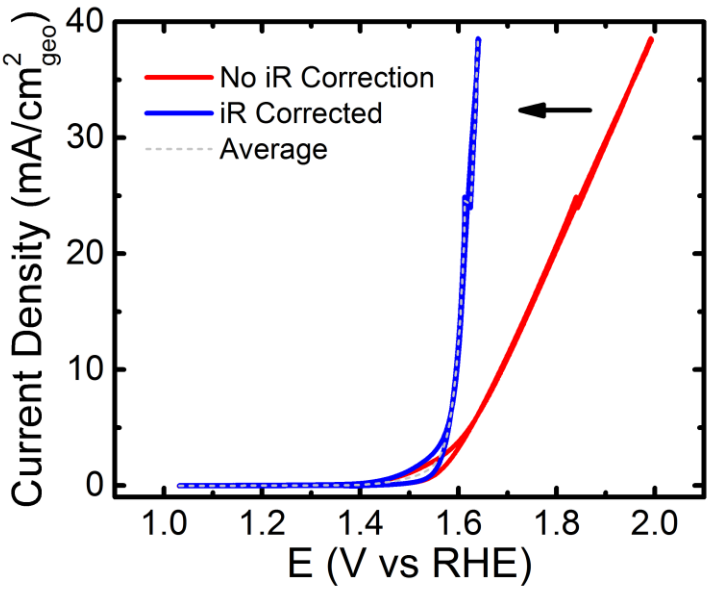

Figure A2 | iR correction example.

OER polarization curves for both iR corrected and uncorrected N-CNT/LNO at 10 mV/s in O_2 saturated 0.1 M KOH rotating at 1600 rpm. The discontinuity at ~25 mA/cm$^2_{geo}$ is due to an oxygen bubble dislodging from the electrode surface. Solution resistance was measured to be 46.8 Ω on average.

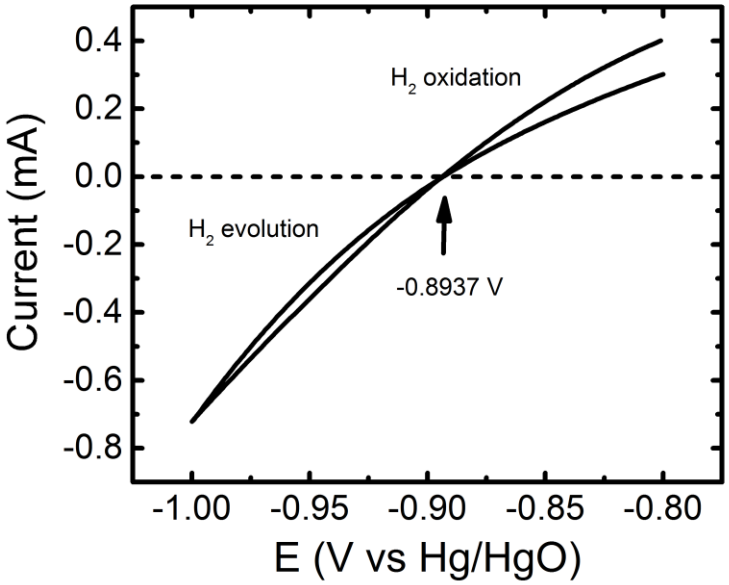

Figure A3 | RHE calibration.

We calibrated a mercury/mercury oxide (Hg/HgO) standard reference electrode to RHE in a saturated a solution of 0.1M KOH with ultra-high purity hydrogen gas to measure. A Pt RDE (0.196 cm^2) was used as the working electrode and a gold wire as the counter electrode.

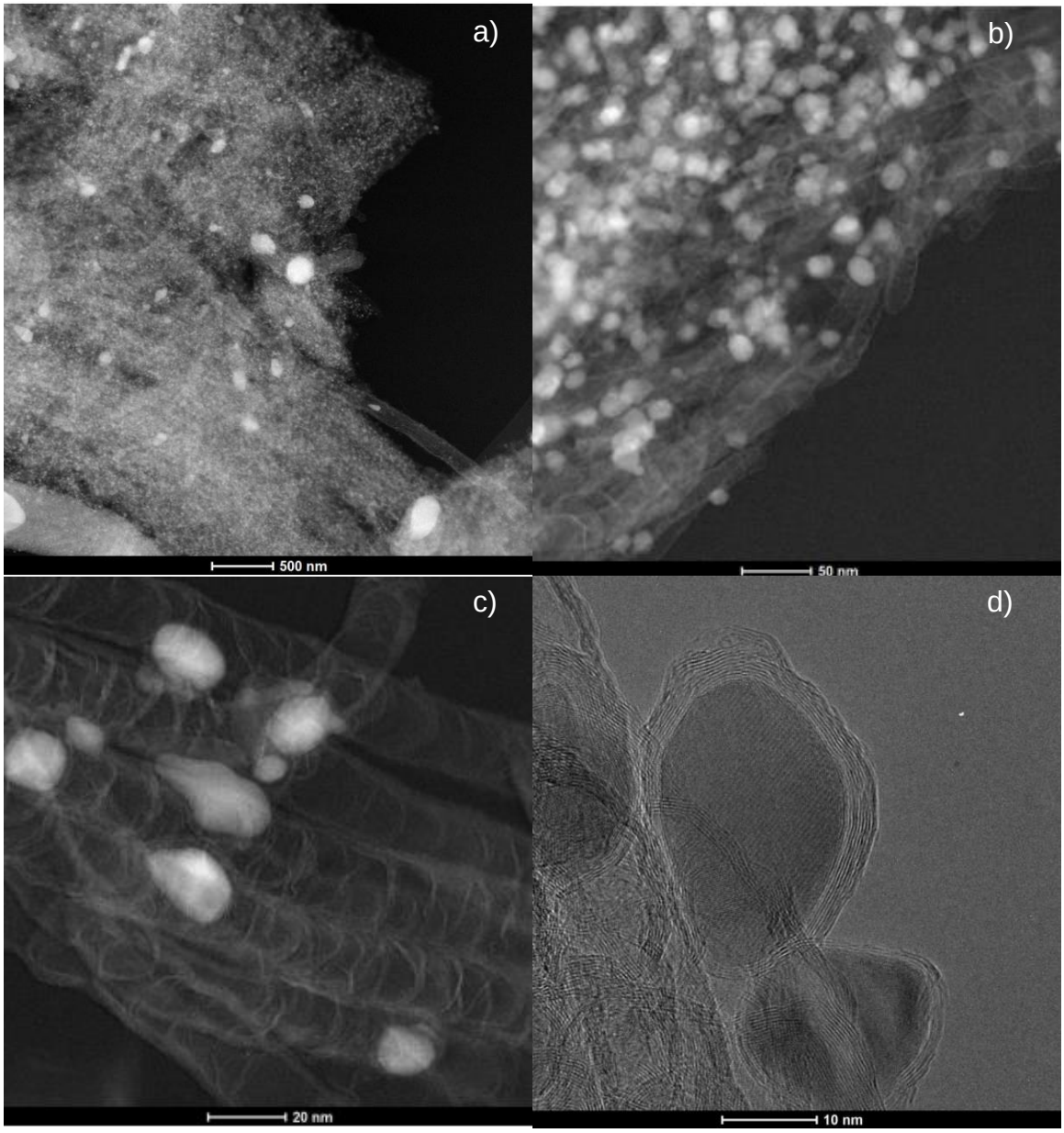

Figure A4 | TEM and HAADF-STEM images of N-doped carbon nanotubes.

a) Low magnification HAADF-STEM image showing N-CNTs decorated with numerous nanoparticles b) and c) HAADF-STEM image showing N-CNTs with attached nanoparticles d) HRTEM images showing crystalline nanoparticles with graphitic shell.

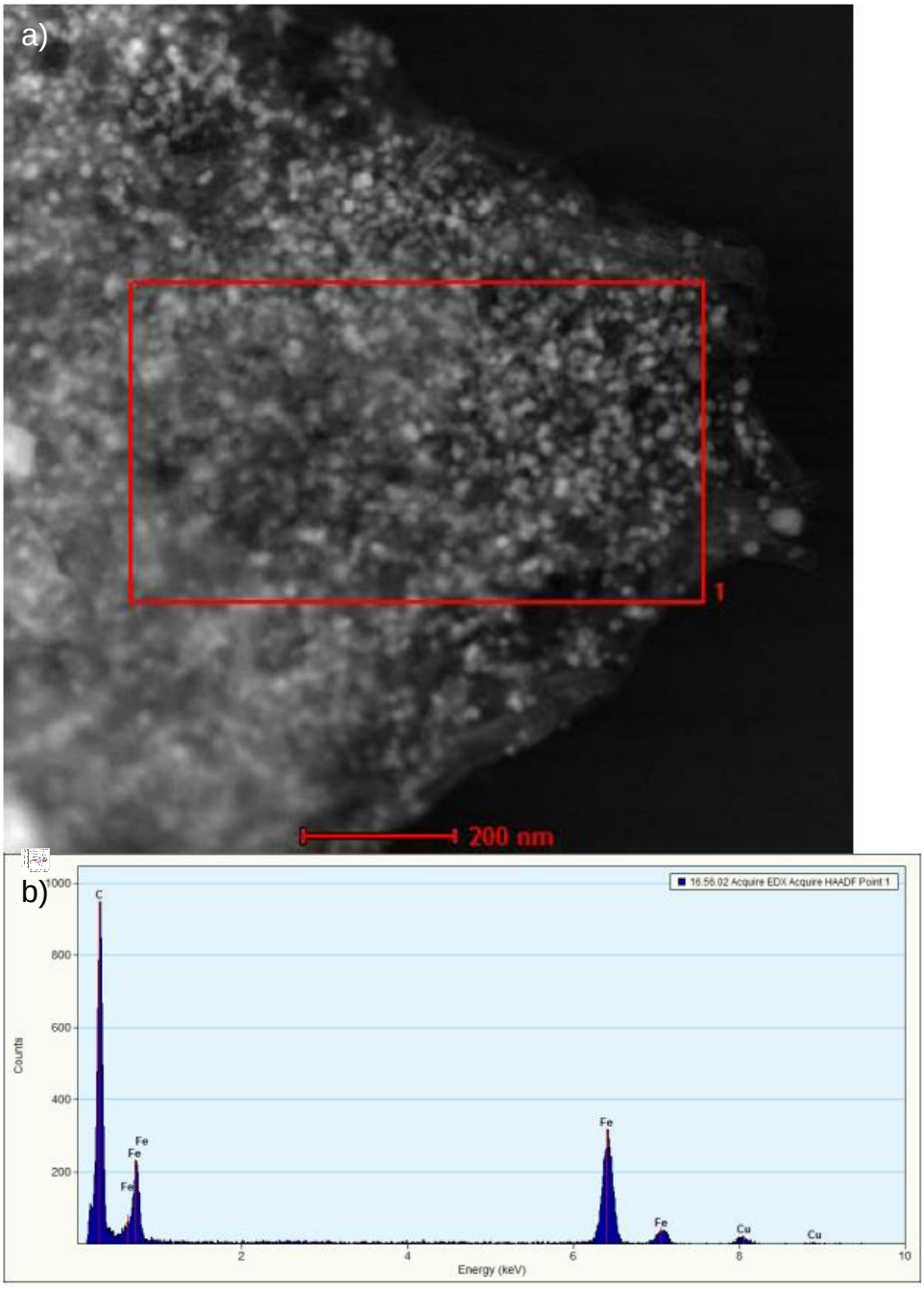

Figure A5 | HAADF-STEM and EDX.

a) HAADF-STEM image with the area selected for EDX analysis. b) The corresponding EDX spectrum showing presence of carbon and iron.
The Cu signal originates from the specimen support.

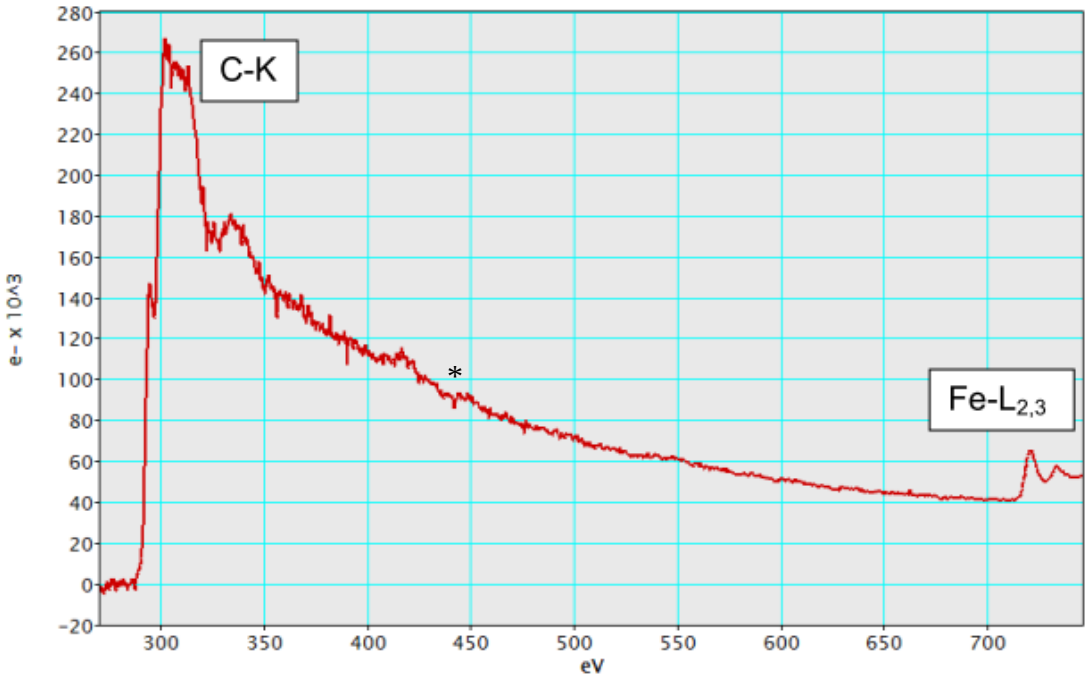

Figure A6 | EELS spectrum showing the C-K and Fe- L 2,3 edges.

*Nitrogen X edge

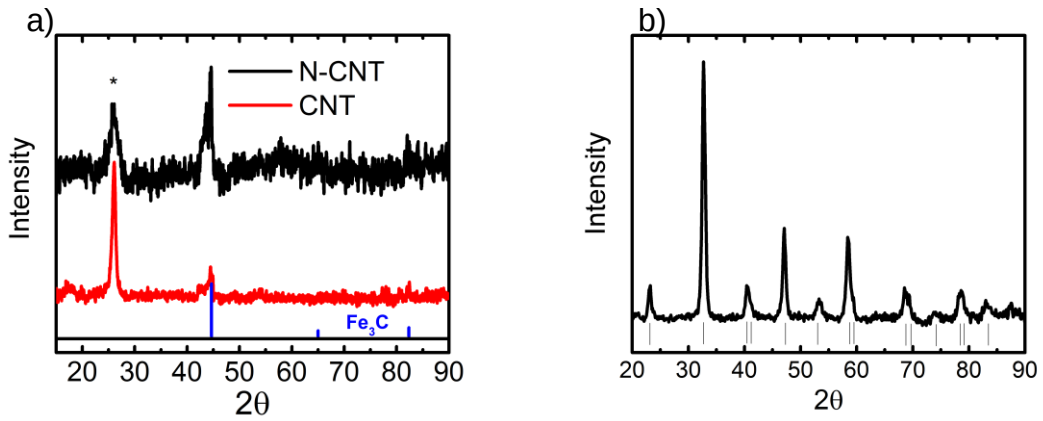

Figure A7 | XRD spectra.

a) N-CNT and CNT with the * indicating the graphitic peak b) $LaNiO_3$.

N-CNT FWHM graphite: 1.7003 2theta @26.03° iron carbide: 1.74879 2θ @ 44.05°
CNT FWHM graphite: 0.86974 2theta @26.03° iron carbide: 1.10623 2θ @ 44.41°

wavelength= 1.5418 Å

Tau=0.93 Å

N-CNT: 53.3 Å or 5.33nm
CNT: 104.2 Å or 10.42nm

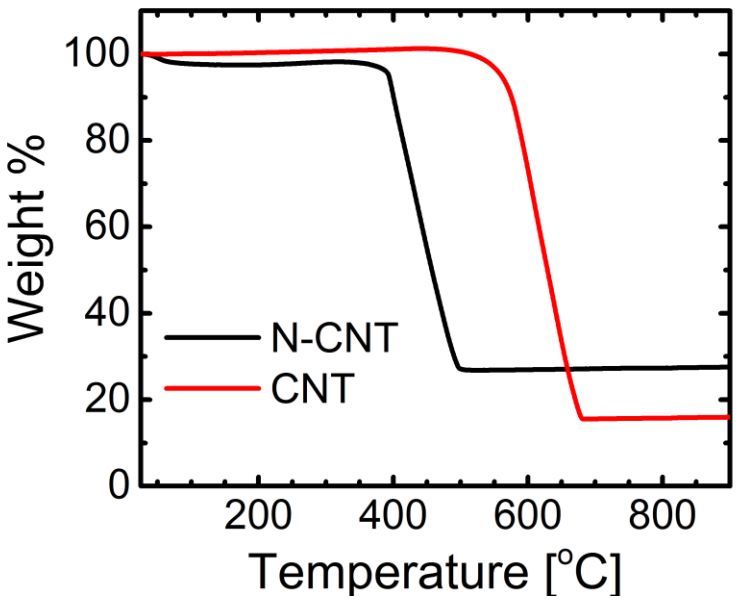

Figure A8 | TGA of N-CNT and CNT at 20°C/min with air flowing at 50 mL/min.

The residual mass was found to be Fe_2O_3 hematite and when its mass is converted to Fe_3C as found in XRD the Fe_3C wt% was found to be 20.6 wt% and 11.9 wt% for N-CNT and CNT, respectively.

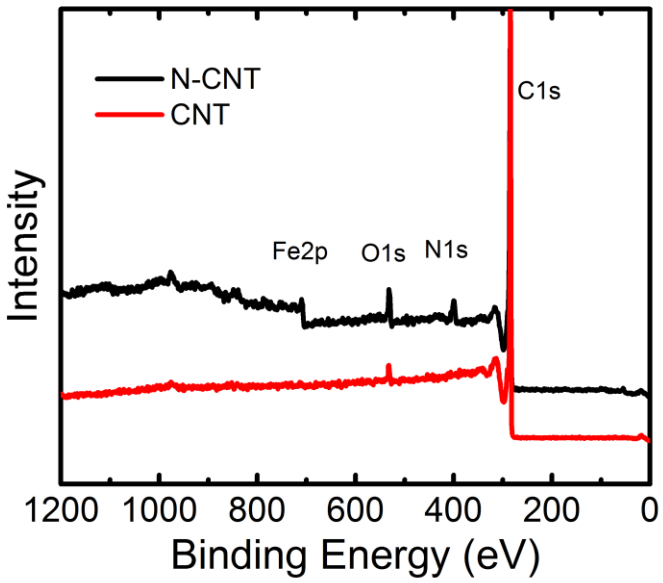

Figure A9 | XPS survey of CNTs and N-CNTs.

No sign of nitrogen or iron in CNT.

Sample	C 1s	O 1s	N 1s	Fe 2p
	at. %	at. %	at. %	at. %
N-CNT	90.1	3.19	5.68	1.02
CNT	98.36	1.64	0	0

Table A1 | XPS Results

Name	Position (eV)	FWHM (eV)	at. %
Pyridinic	398.5	1.542	33.8
Pyrrolic	400.6	1.654	8.1
Graphitic	401.2	2.355	35.8
Oxidized N	404.8	1.994	18.0
Fe-N	399.3	1.207	4.3

Table A2 | N-CNT XPS Results. N 1s composition

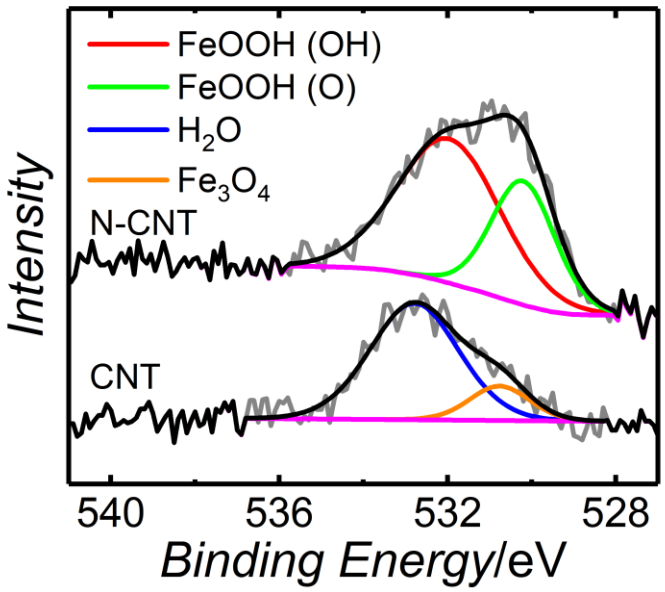

Figure A10 | O 1s XPS spectra of CNTs and N-CNTs.

The N-CNT O 1s spectra shows two peaks corresponding to the OH group (531.9 eV) and oxide group (530.2 eV) of FeOOH that comes from the decomposition of water[5]. The larger area of the hydroxide component suggests that the iron seed is heavily hydroxylated. In contrast, the CNT exhibits peaks corresponding to adsorbed water (532.8 eV) and Fe_3O_4 (530.8 eV)[6] which suggests that the water cannot reach the iron oxide surface due to the impermeable graphite layer in the CNT.

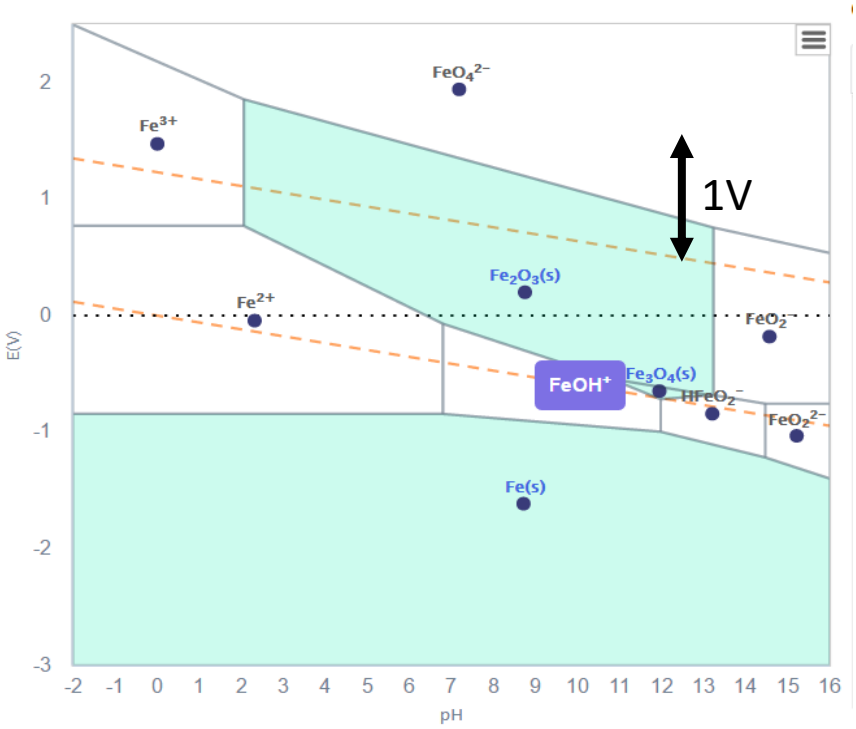

Figure A11 | Fe Pourbaix Diagram.

Note that the iron anion species becomes thermodynamically stable at ~1.3-1.4V vs RHE[7,8] in agreement with the RRDE Pt ring current. This figure was used with permission from https://materialsproject.org/#apps/pourbaixdiagram
the vertical double arrow line and '1V' text was added for clarity.

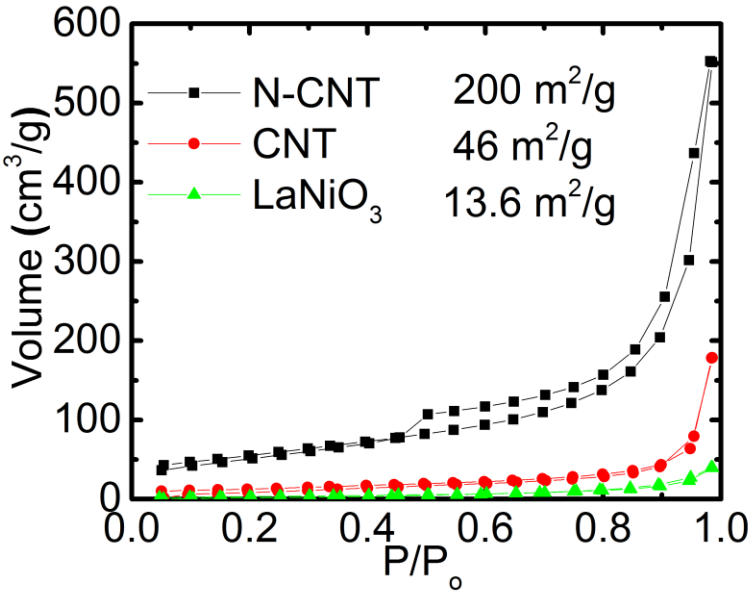

Figure A12 | BET plot of N-CNT, CNT, and $LaNiO_3$.

Sample	Tafel Slopes (mV/dec)	i_{ex} (mA/cm^2_{geo})
N-CNT/LNO	65	1.52E-6
N-CNT	69.1	2.83E-6
CNT/LNO	86.9	2.58E-6
CNT	61.2	4.2E-10
VC/LNO	77.2	6.35E-7
VC	61.4	1.67E-9
20 wt% Pt/VC	59	6.24E-6

Table A3 | Tafel slopes and i_{ex} for ORR

Sample	C_{ox}	Fe_{leach}	OER
	(mV/dec)	(mV/dec)	(mV/dec)
N-CNT	211±1	112.5±0.4	80±2
CNT	260±3	-	63.8±0.3
VC	198±0.4	-	-
N-CNT/LNO	161±2	92.5±0.4	56±0.4
CNT/LNO	108±1	-	37.5±0.4
VC/LNO	197±6	-	56.6±0.4
VC/IrO_2	209±4	-	81.5±0.7

Table A4 | $LaNiO_3$ increases carbon oxidation rate of Carbon Nanotubes

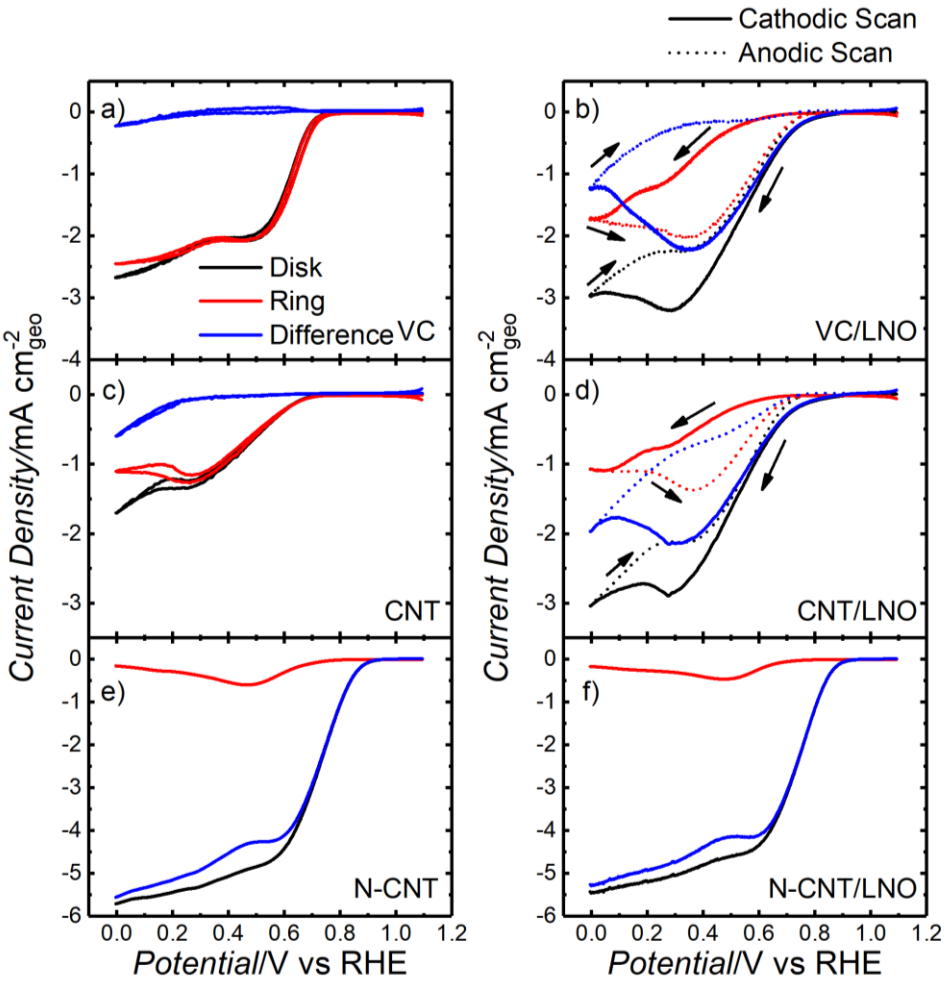

Figure A13 | RRDE measurements of each carbon and its composite.

The reported measurements are CVs of the first scan in O_2 saturated, 0.1 M KOH with a 1 M KOH Hg/HgO reference electrode at 5 mV s^{-1} and 1600 r.p.m. for a) VC b) VC/LNO c) CNT d) CNT/LNO e) N-CNT f) N-CNT/LNO with the Pt ring held at 1.23V vs RHE to avoid OER and make all ring current due to peroxide oxidation. Mass loadings for the carbon only samples are 35.7 μg/cm^2 while the composite mass loadings are 51 μg/cm^2 to easily distinguish the effect of adding LNO. The Pt Ring currents (red lines) were normalized by the ring area (0.1859 cm^2) and the RRDE collection efficiency (37 %) that was reported in the SI of our previous work[9]. The backs scans (dashed lines) of VC/LNO and CNT/LNO show the increased activity towards peroxide generation and lowered activity towards peroxide electrochemical reduction. The way to think about the 'Difference' curve (blue lines) is that they are the Disk current (black lines) that is *not* peroxide generation like peroxide electroreduction and/or the pseudo four electron process.

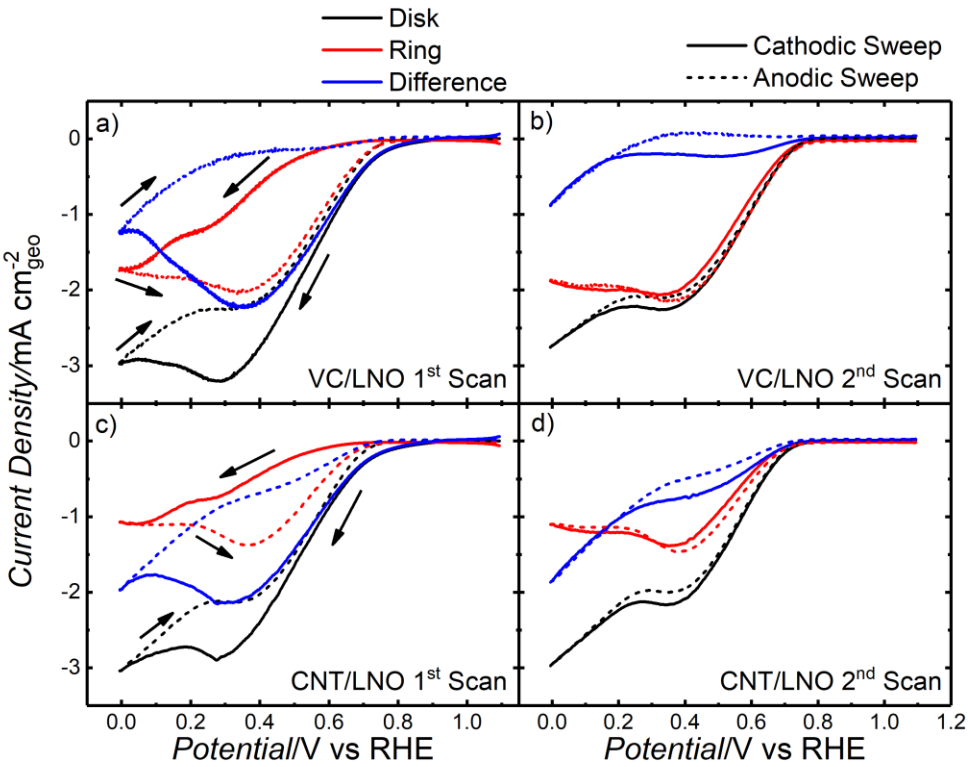

Figure A14 | RRDE measurements 1st and 2nd Scan.

Measurements taken in oxygen saturated 0.1 M KOH at 1600 r.p.m. and 5 mV s^{-1} with 51 μg/cm^2 mass loading and the Pt ring held at 1.23 V vs RHE. The Pt ring current was normalized by its collection efficiency (37 %). The a) VC/LNO 1st scan and b) VC/LNO 2nd scan show similar trends to c) CNT/LNO 1st scan and d) CNT/LNO 2nd scan respectively that the LNO chemical disproportionation rate decreases significantly after the first ORR CV, but then follows the peroxide electroreduction step as seen by the boost in the 'Difference' current which is the difference in current between the Disk and Ring.

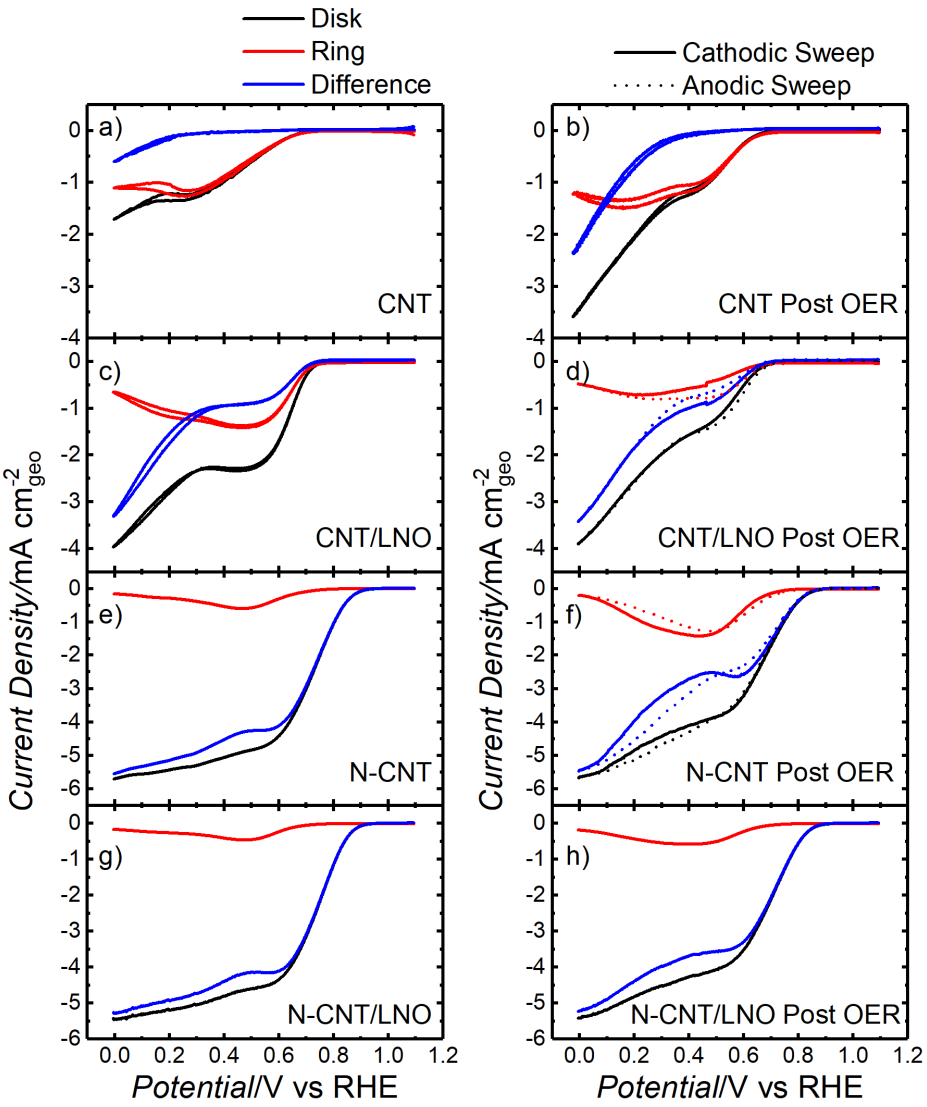

Figure A15 | ORR activity before and after OER CV.

CNT and N-CNT and their composites were tested using an RRDE in ORR conditions before and after running an OER CV. The samples looked at were a) CNT b) CNT Post OER c) CNT/LNO d) CNT/LNO Post OER e) N-CNT f) N-CNT Post OER g) N-CNT/LNO h) N-CNT/LNO Post OER. After the OER, CNT is actually *more* active toward peroxide electroreduction, likely due to oxygen functionalities added at OER potentials. It appears CNT/LNO loses its peroxide disproportionation activity after the OER, but maintains the most of the N-CNT composite ORR activity after cycling relative to the N-CNT only sample. The N-CNT/LNO composite forward and back scans overlapped which is by it does not look like the anodic sweep is shown.

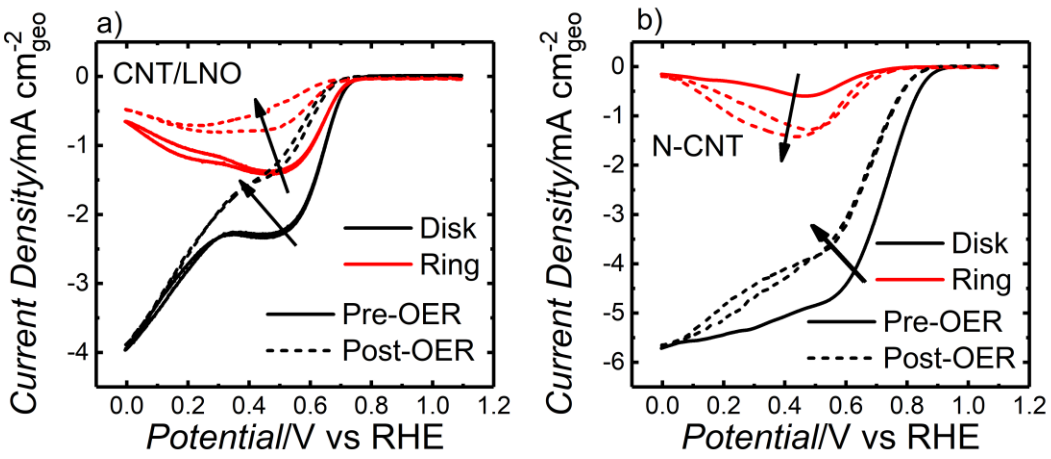

Figure A16 | CNT/LNO and N-CNT pre and post OER CV comparison.

The ORR CVs before and after an OER CV of a) CNT/LNO and b) N-CNT are overlaid to better illustrate the changes in activity. The peroxide disproportionation ability appears to have diminished significantly for both samples while the peroxide electroreduction to OH- has not changed.

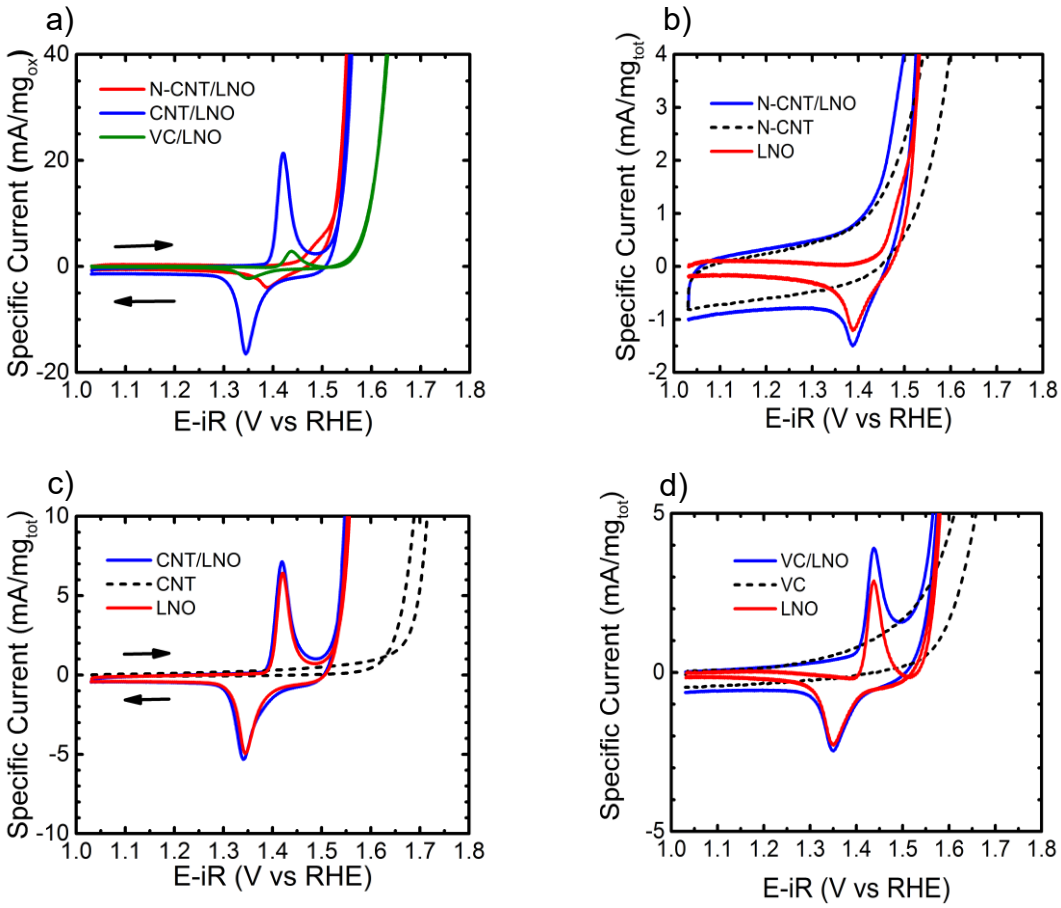

Figure A17 | Ni redox peak on different carbon supports.

a) Plot of $LaNiO_3$ anodic and cathodic peaks with the carbon contribution to current subtracted out. b-d) OER curves of $LaNiO_3$ supported on carbon, the carbon curves used to subtract the carbon current contribution and the resulting $LaNiO_3$ curve from the difference. Note that these curves were taken after the first cycle to present a stable peak shape. The peak current and position is dependent on the carbon support. Peak potentials increase for $LaNiO_3$ on different supports in the order of CNT < VC < N-CNT, but peak current increase in the order N-CNT < VC < CNT.

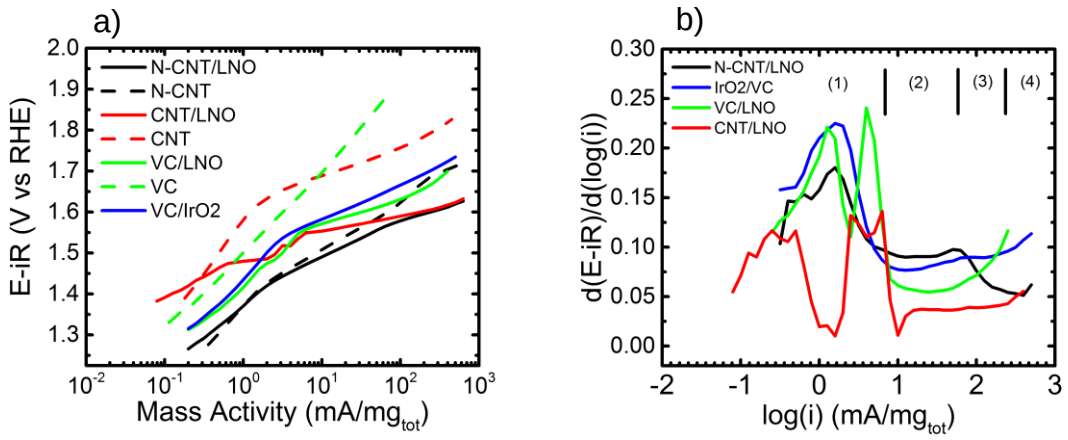

Figure A18 | Tafel region analysis.

a) Potential vs mass activity plot and b) derivative plot showing various regions: (1) Carbon oxidation and LNO redox peaks; (2) Iron dissolution in N-CNT, but OER for LNO supported on VC and CNT; (3) OER for all samples and (4) Bubble formation begins to block the electrode surface and Tafel slopes increase.

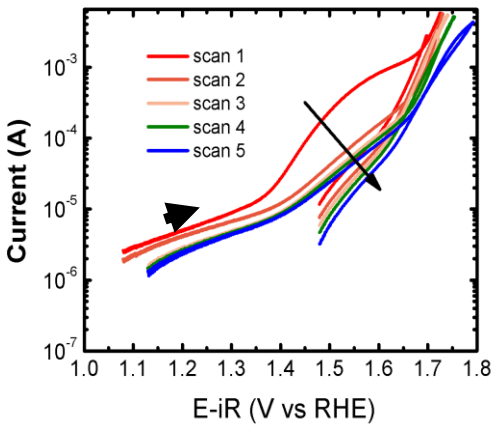

Figure A19 | Multiple scans of N-CNT to illustrate the anodic iron leaching hump decreasing with each cycle as the iron content decreases.

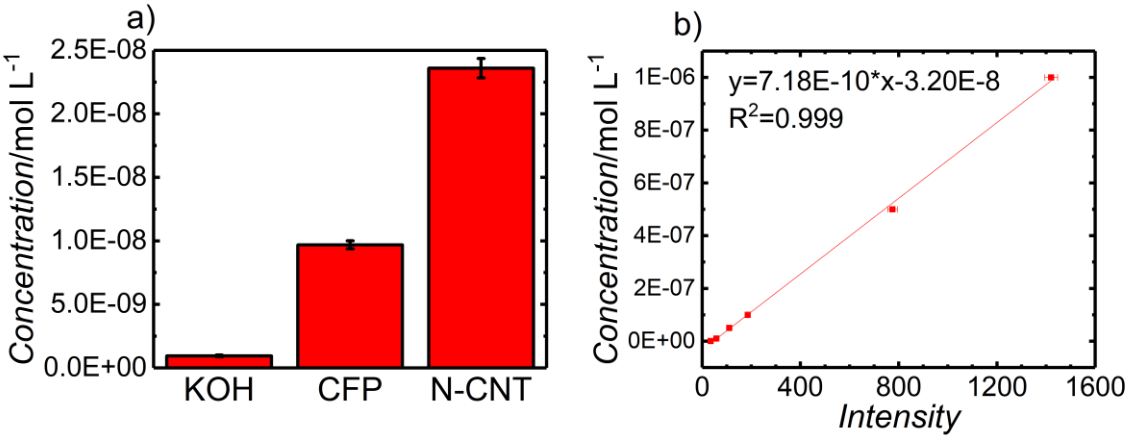

Figure A20 | Fe leaching determination via ICP-OES.

a) Concentration of iron present in 0.1 M KOH control group, in solution after carbon fiber paper (CFP) OER CV and in solution after 0.3 mg cm^{-2} N-CNT on CFP OER CV b) iron calibration curve for iron concentration determination

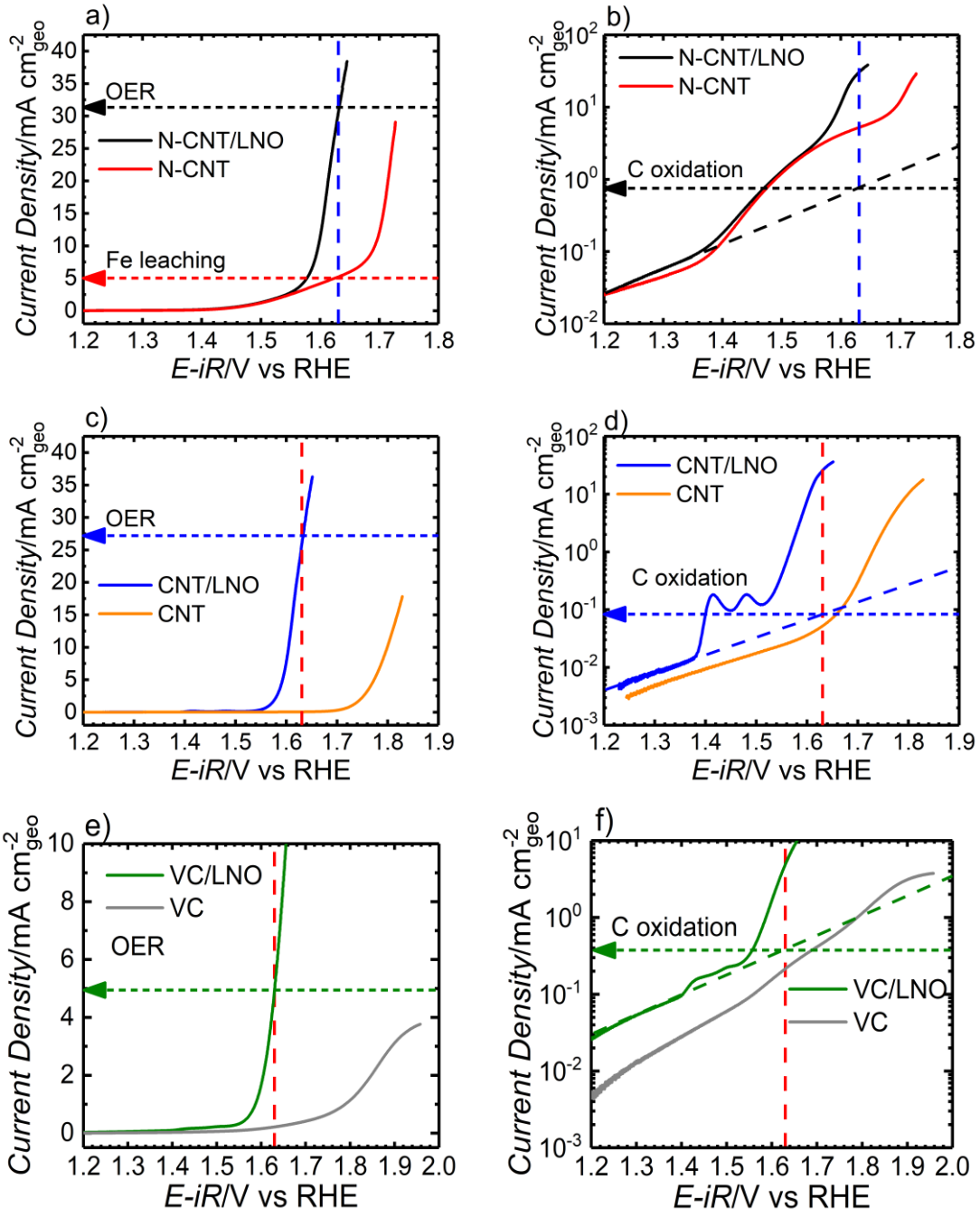

Figure A21 | Faradaic multi-reaction quantification of a) N-CNT/LNO, c) CNT/LNO and e) VC/LNO on a linear scale and b) N-CNT/LNO, d) CNT/LNO and f) VC/LNO on a semilog scale.

Reaction	Measured Current Density	Current Contribution	Current Contribution
	(mA/cm_{geo}^2)	(mA/cm_{geo}^2)	%
Carbon Oxidation	0.7	0.7	2.2%
Iron Leaching	5	4.3	13.6%
OER	31.5	26.5	84.2%

Table A5 | N-CNT/LNO Current Contributions at 1.63V vs RHE

Reaction	Measured Current Density	Current Contribution	Current Contribution
	(mA/cm_{geo}^2)	(mA/cm_{geo}^2)	%
Carbon Oxidation	0.08	0.08	0.2%
OER	27.4	27.32	99.8%

Table A6 | CNT/LNO Current Contributions at 1.63V vs RHE

Reaction	Measured Current Density	Current Contribution	Current Contribution
	(mA/cm_{geo}^2)	(mA/cm_{geo}^2)	%
Carbon Oxidation	0.38	0.38	7.6%
OER	5.0	4.62	92.4%

Table A7 | VC/LNO Current Contributions at 1.63V vs RHE

Sample	Tafel slope	$Log_{10}(i_{ex})$
	(mV/dec)	(mA/cm^2_{carbon})
N-CNT/LNO	**271**	**-7.5**
CNT/LNO	**333**	**-6.9**
VC/LNO	**358**	**-6.6**
N-CNT	403	-6.2
CNT	350	-6.9
VC	300	-8.5
VC/IrO2	**351**	**-6.8**

Table A8 | Carbon Oxidation Kinetics

A1.4 References

(1) Cline, K. K.; McDermott, M. T.; McCreery, R. L. Anomalously Slow Electron Transfer at Ordered Graphite Electrodes: Influence of Electronic Factors and Reactive Sites. *J. Phys. Chem.* **1994**, *98* (20), 5314–5319. https://doi.org/10.1021/j100071a023.

(2) Yang, H.-H.; McCreery, R. L. Elucidation of the Mechanism of Dioxygen Reduction on Metal-Free Carbon Electrodes. *J. Electrochem. Soc.* **2000**, *147* (9), 3420–3428. https://doi.org/10.1149/1.1393915.

(3) Bielski, B. H. J.; Allen, A. O. Mechanism of the Disproportionation of Superoxide Radicals. *J. Phys. Chem.* **1977**, *81* (11), 1048–1050. https://doi.org/10.1021/j100526a005.

(4) Bard, A. J. *Electroanalytical Chemistry: A Series of Advances:*; CRC Press, 1990.

(5) Allen, G. C.; Curtis, M. T.; Hooper, A. J.; Tucker, P. M. X-Ray Photoelectron Spectroscopy of Iron–oxygen Systems. *J. Chem. Soc. Dalton Trans.* **1974**, *0* (14), 1525–1530. https://doi.org/10.1039/DT9740001525.

(6) Marcus, P.; Grimal, J. M. The Anodic Dissolution and Passivation of NiCrFe Alloys Studied by ESCA. *Corros. Sci.* **1992**, *33* (5), 805–814.

(7) Jain, A.; Ong, S. P.; Hautier, G.; Chen, W.; Richards, W. D.; Dacek, S.; Cholia, S.; Gunter, D.; Skinner, D.; Ceder, G.; et al. Commentary: The Materials Project: A Materials Genome Approach to Accelerating Materials Innovation. *APL Mater.* **2013**, *1* (1), 11002. https://doi.org/10.1063/1.4812323.

(8) Lee, Y.-L.; Kleis, J.; Rossmeisl, J.; Shao-Horn, Y.; Morgan, D. Prediction of Solid Oxide Fuel Cell Cathode Activity with First-Principles Descriptors. *Energy Environ. Sci.* **2011**, *4* (10), 3966. https://doi.org/10.1039/c1ee02032c.

APPENDIX 2: ANION-BASED REDOX PSEUDOCAPACITANCE OF THE PEROVSKITE LIBRARY $La_{1-x}Sr_xBO_{3-\Delta}$ (B = FE, MN, CO)

Series	x	mMol La	mMol Sr	mMol B	wt% TMAOH	Approx. Drip time	Stir Time (days)	Furnace Condition	Gas	Reduction Treatment
LSFO	0**	2.50	0	2.50	N/A	N/A	N/A	(3)	air	-
	0.2	1.99	0.51	2.49	10	2 hr 15 min	3	(1)	air	-
	0.4	1.49	1.00	2.48	10	2 hr 15 min	3	(1)	air	-
	0.6	1.00	1.50	2.49	10	2 hr 15 min	3	(1)	air	-
	0.8	0.50	2.00	2.48	10	2 hr 15 min	5	(1)	air	-
	1	0.00	2.50	2.48	10	*	10	(1)	air	-
	BM	0.00	2.50	2.48	10	*	10	(1)	air	(2)
LSMO	0	2.48	0.00	2.49	1	*	2	(3)	air	-
	0.2	2.00	0.51	2.50	10	*	1	(1)	air	-
	0.4	1.50	1.01	2.51	10	*	1	(1)	air	-
	0.6	0.99	1.50	2.48	10	*	1	(1)	air	-
	0.8	0.49	2.01	2.50	10	*	1^+	$(1)^+$	air	(5)
LSCO	0	2.478	0	2.538	1	4 hr 30 min	3	(4)	air	-
	0.2	1.985	0.494	2.432	1	4 hr 30 min	3	(4)	air	-
	0.4	1.491	0.988	2.423	1	4 hr 30 min	3	(4)	air	-
	0.6	0.995	1.476	2.44	1	4 hr 30 min	3	(4)	air	-
	0.8	0.497	1.963	2.439	1	4 hr 30 min	3	(4)	air	-
	1	0	2.498	2.502	1	4 hr 30 min	5	(4)	O_2	-
	BM	0	2.517	2.499	1	4 hr 30 min	5	(6)	air	-

(1) 25C->(30min)->120C(1hr)->(45min)->950C(4hr)->Cool to RT Naturally

(2) 25C->(30min)->350C(4hr)->Cool to RT Naturally in 7%H_2/Ar

(3) 25C->(30min)->120C(1hr)->(45min)->700C(4hr)->Cool to RT Naturally

(4) 25C->(30min)->120C(1hr)->(45min)->950C(5hr)->Cool to RT Naturally

(5) 25C->(30min)->400C(1hr)->Cool to RT Naturally in 7%H_2/Ar

(6) 25C->(30min)->120C(1hr)->(45min)->950C(5hr)->Liq. N_2 Quench

* Not recorded, but the dripping occurred over several hours

** Synthesized using a citric acid synthesis

\+ LSMO28 had a significant La_2O_3 impurity after calcination, which disappeared upon reduction.

Table A9 | $La_{1-x}Sr_xBO_{3-\delta}$ (B = Fe, Mn, Co) Synthesis Conditions

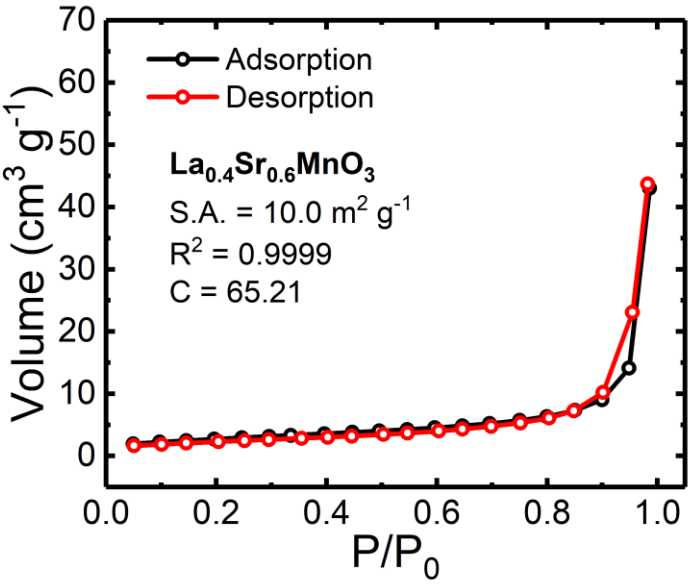

Figure A22 | Sample BET curve of perovskite sample.

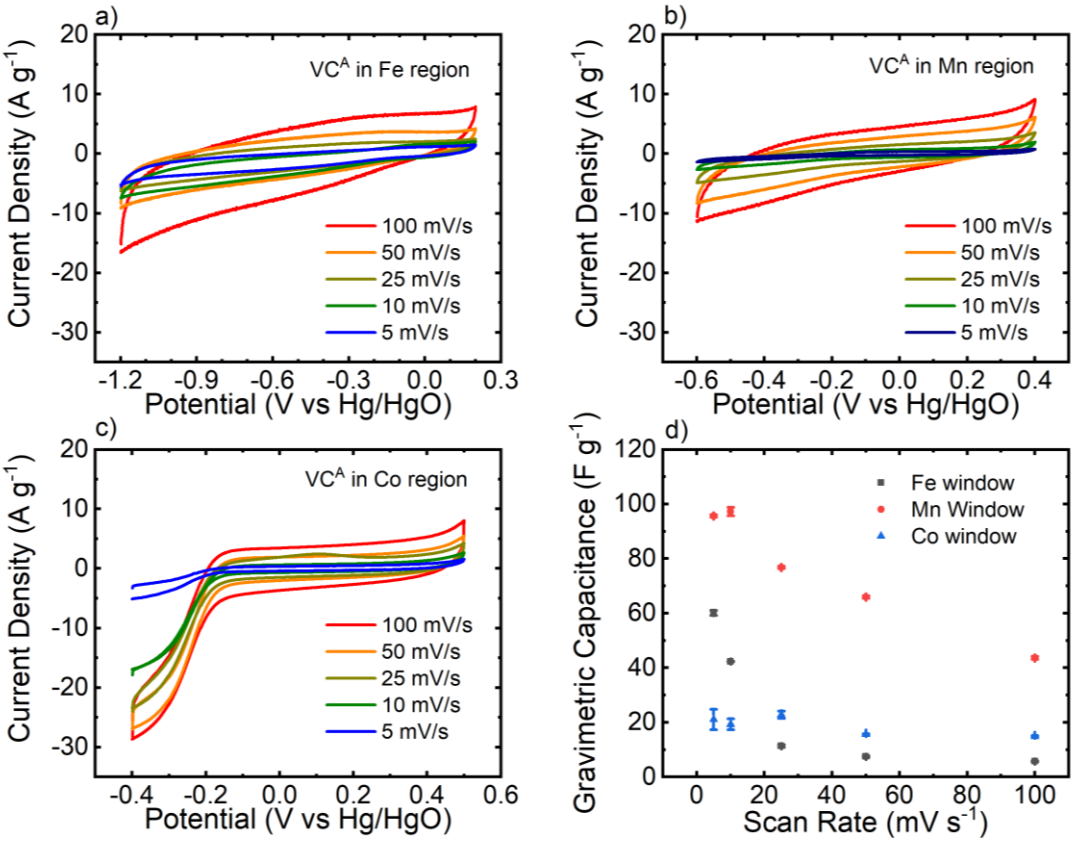

Figure A23 | Activated Vulcan carbon (VC^A) capacitance contribution.

CVs of VC^A in the (a) Fe, (b) Mn, (c) Co potential regions with a 7.65 µg cm^{-2} mass loading in Ar-saturated 1M KOH with (d) capacitance values shown. The Co potential region below ~0.2V was not included in the capacitance calculation due to that region being predominately ORR current due to slight amount of oxygen produced at potentials above 0.4 V vs Hg/HgO.

x in $La_{1-x}Sr_xFeO_{3-\delta}$	Space Group	Crystal System	a (Å)	b(Å)	c (Å)
0	Pbnm	Orthorhombic	5.552	5.563	7.843
0.2	Pbnm	Orthorhombic	5.550	5.508	7.844
0.4	R-3c	Rhombohedral	5.4784	-	13.3928
0.6	R-3c	Rhombohedral	5.51107	-	13.41578
0.8	R-3c	Rhombohedral	5.51107	-	13.41578
1	Pm-3m	Cubic	3.827(1)	-	-
BM-SFO	Ibm2	Orthorhombic	5.5298(4)	15.598	5.6687(4)

(Values were taken from PDF cards)

Table A10 | $La_{1-x}Sr_xFeO_{3-\delta}$ X-Ray Crystallography Parameters

x in $La_{1-x}Sr_xMnO_{3-\delta}$	Space Group	Crystal System	a (Å)	c (Å)
0	R-3c	Rhombohedral	5.531	13.363
0.2	R-3c	Rhombohedral	5.5288	13.3666
0.4	R-3c	Rhombohedral	5.493	13.361
0.6	I4/mcm	Tetragonal	5.4697	7.7391
0.8	I4/mcm*	Tetragonal	-	-
1	$P6_3/mmc$	Hexagonal	5.449	9.0804

(Values were taken from PDF cards; * x = 0.8 PDF card matched to x = 0.55)

Table A11 | $La_{1-x}Sr_xMnO_{3-\delta}$ X-Ray Crystallography Parameters

x in $La_{1-x}Sr_xCoO_{3-\delta}$	Space Group	Crystal System	a (Å)	c (Å)
0	R-3c	Rhombohedral	5.4418(1)	13.0922(3)
0.2	R-3c	Rhombohedral	5.4436(1)	13.1567(5)
0.4	R-3c	Rhombohedral	5.4389(1)	13.1826(6)
0.6	Pm-3m	Cubic	3.8374(1)	-
0.8	P4/mmm	Tetragonal	3.83864(8)	2a
1	I4/mmm	Tetragonal	7.7220(7)	15.519(2)
BM-SCO	Imma	Orthorhombic	5.4579(3)	5.5643(3)

(Values were reported previously[2])

Table A12 | $La_{1-x}Sr_xCoO_{3-\delta}$ X-Ray Crystallography Parameters

x in $La_{1-x}Sr_xBO_{3-\delta}$	B		
	Fe	Mn	Co
0	11.6*	11.4	4
0.2	4.7	6.1	4.5
0.4	3.4	8.2	4.2
0.6	3	10	4.3
0.8	2.7	10.5	3.1
1	4.4	N/A	3.6
Brownmillerite	3.8	N/A	3.2
* Made using citric acid synthesis			

Table A13 | BET Surface Areas ($m^2 g^{-1}$)

x in $La_{1-x}Sr_xB^{z+}O_{3-\delta}$	B:	δ		
		Mn	Fe	Co
0		-0.09 ± 0.02	0.05 ± 0.02	-0.01 ± 0.01
0.2		0.03 ± 0.01	0.157 ± 0.009	0.01 ± 0.01
0.4		0.07 ± 0.02	0.197 ± 0.007	0.05 ± 0.04
0.6		0.09 ± 0.01	0.29 ± 0.01	0.09 ± 0.01
0.8		0.30 ± 0.03*	0.423 ± 0.008	0.16 ± 0.01
1		N/A	0.18 ± 0.01	0.30 ± 0.03
Brownmillerite		N/A	0.46 ± 0.02**	-
x in $La_{1-x}Sr_xB^{z+}O_{3-\delta}$	B:	z^+		
		Mn	Fe	Co
0		3.18 ± 0.05	2.90 ± 0.04	3.01 ± 0.01
0.2		3.13 ± 0.04	2.89 ± 0.02	3.18 ± 0.02
0.4		3.25 ± 0.07	3.01 ± 0.01	3.30 ± 0.08
0.6		3.41 ± 0.04	3.03 ± 0.03	3.43 ± 0.01
0.8		3.2 ± 0.08*	2.95 ± 0.02	3.48 ± 0.02
1		N/A	3.64 ± 0.04	3.40 ± 0.06
Brownmillerite		N/A	3.08 ± 0.04**	-

* Reduced in 7% H_2/Ar at 400°C for 4 hours to get phase pure
**Reduced in 7% H_2/Ar at 350°C for 4 hours to get phase pure
Error is based on the st. dev. of triplicate measurements

Table A14 | Oxygen Vacancy Concentration, δ, and B site oxidation state, z+

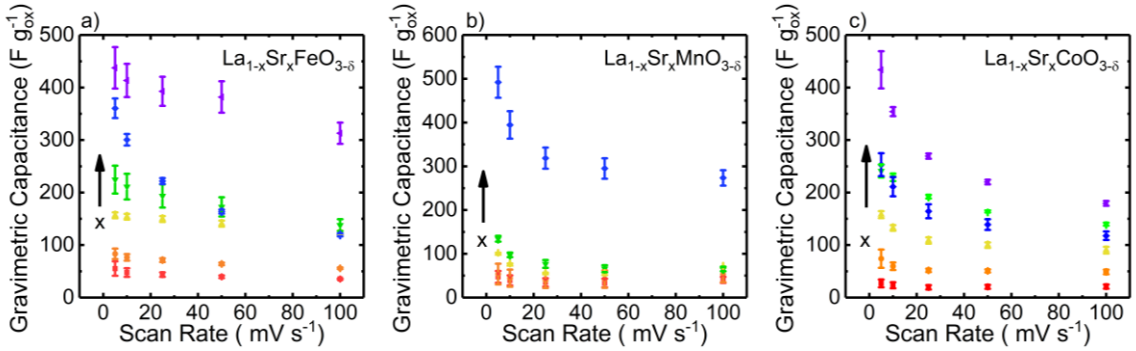

Figure A24 | Capacitance vs scan rate for $La_{1-x}Sr_xBO_{3-\delta}$ (B = Fe, Mn, Co) series.

Capacitance of (a) $La_{1-x}Sr_xFeO_{3-\delta}$ (b) $La_{1-x}Sr_xMnO_{3-\delta}$ (c) $La_{1-x}Sr_xCoO_{3-\delta}$ at 100, 50, 25, 10, 5 mV s^{-1} in Ar-saturated 1M KOH with the carbon contribution removed

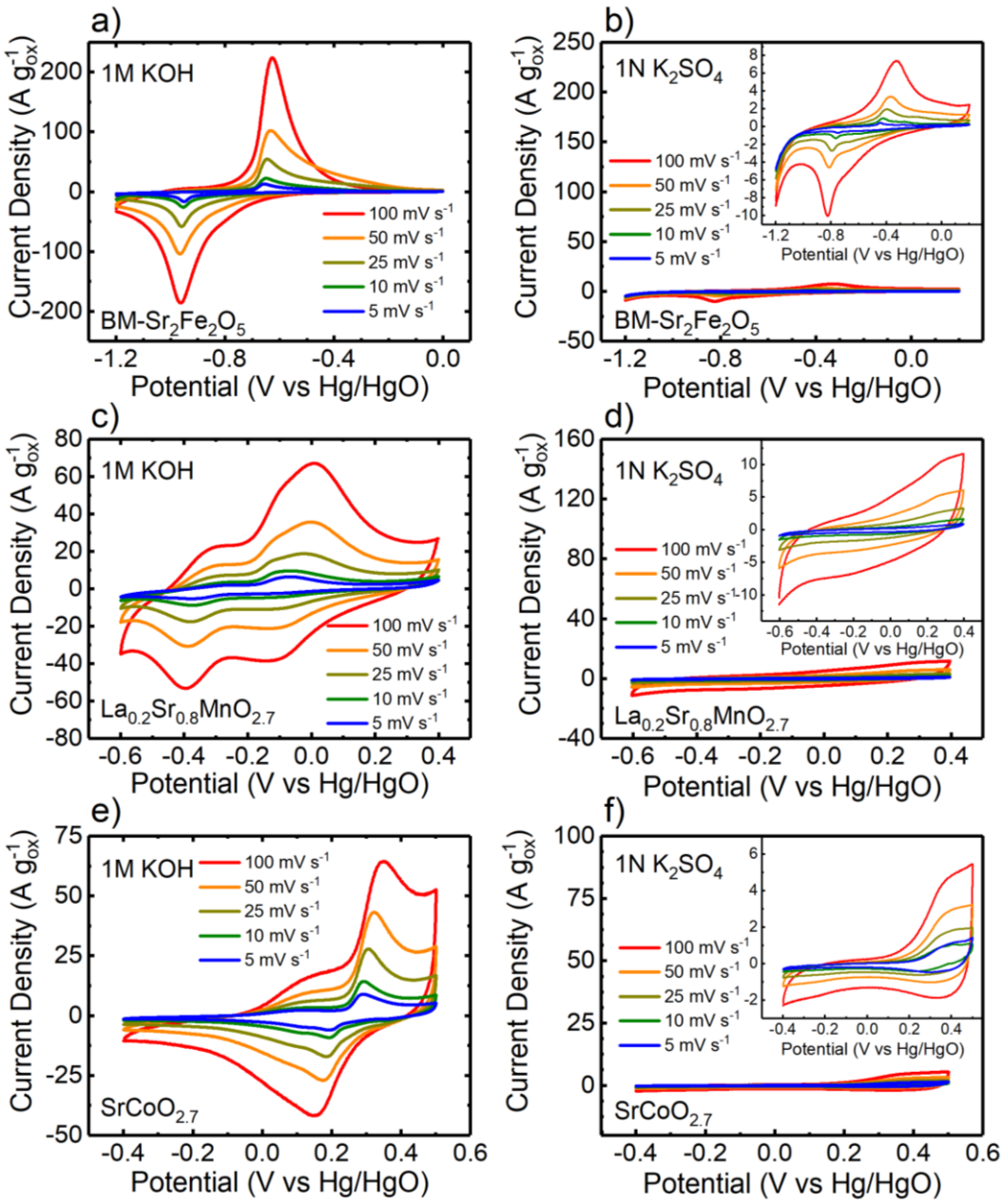

Figure A25 | Alkaline vs neutral electrolyte cyclic voltammetry comparison.

CVs of BM-SFO in (a) 1 M KOH and (b) 1 N K_2SO_4, LSMO28 in (c) 1 M KOH and (d) 1 N K_2SO_4 and SCO in (e) 1 M KOH and (f) 1 N K_2SO_4 showing that the pseudocapacitance is due to hydroxide anion intercalation. The sharp decrease in CV area illustrates the decrease in capacitance from alkaline to neutral solutions despite holding the K^+ concentration constant.

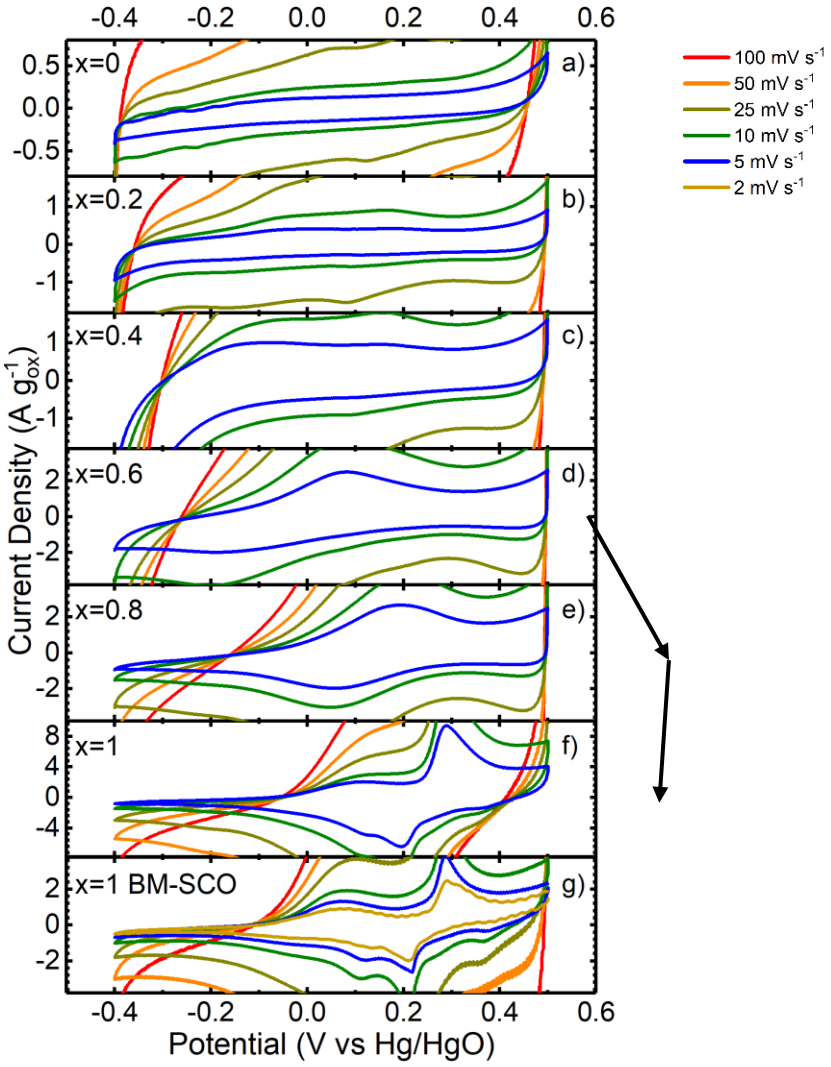

Figure A2.5 | $La_{1-x}Sr_xCoO_{3-\delta}$ series cyclic voltammetry slow scans.

Cyclic voltammograms from Figure A2.7 zoomed in at low scan rates are given for (a) LCO, (b) LSCO82, (c) LSCO64, (d) LSCO46, (e) LSCO28, (f) SCO and (g)BM-SCO.

A2.1: References

(1) Mefford, J. T.; Rong, X.; Abakumov, A. M.; Hardin, W. G.; Dai, S.; Kolpak, A. M.; Johnston, K. P.; Stevenson, K. J. Water Electrolysis on La1-xSrxCoO3-δ Perovskite Electrocatalysts. *Nat. Commun.* **2016**, *7*, 11053. https://doi.org/10.1038/ncomms11053.

APPENDIX 3: SR-RICH PEROVSKITES FOR ENERGY DENSE ASYMMETRIC ANION-BASED PSEUDOCAPACITORS

A3.1: Capacitance Envelope Calculation

Current (i) due to capacitance is proportional to the scan rate (ν) while that due to diffusion limited faradaic current is proportional to the square root of the scan rate ($\nu^{1/2}$). An electrochemical system with both capacitive and diffusive components can be said to have a current that is proportional to the scan rate raised to the power 'b' ($i = c*\nu^b$ with c being a constant) where b is between 0.5 and 1. This mixture of capacitive current and diffusion-limited current can be expressed as a weighted fraction between the two component contributions:

$$xv + (1-x)v^{0.5} = v^b \tag{A3.1}$$

where *x* is the fraction of the total current that is capacitive in nature. Solving for x as follows yields:

$$xv + v^{0.5} - xv^{0.5} = v^b \tag{A3.2}$$

$$xv^{0.5} + 1 - x = v^{b-0.5} \tag{A3.3}$$

$$x(v^{0.5} - 1) = v^{b-0.5} - 1 \tag{A3.4}$$

$$x = \frac{v^{b-0.5}-1}{v^{0.5}-1} \tag{A3.5}$$

and b can be found by rearranging:

$$i = c * v^b \tag{A3.6}$$

$$\log(i) = b * \log(v) + \log(c) \tag{A3.7}$$

with the slope of log(i) vs log(v) being equal to *b*. By calculating *b* at all potentials and plugging them into equation A3.5 the capacitive current contribution can be plotted as done in Figure 4.3a-c.[1]

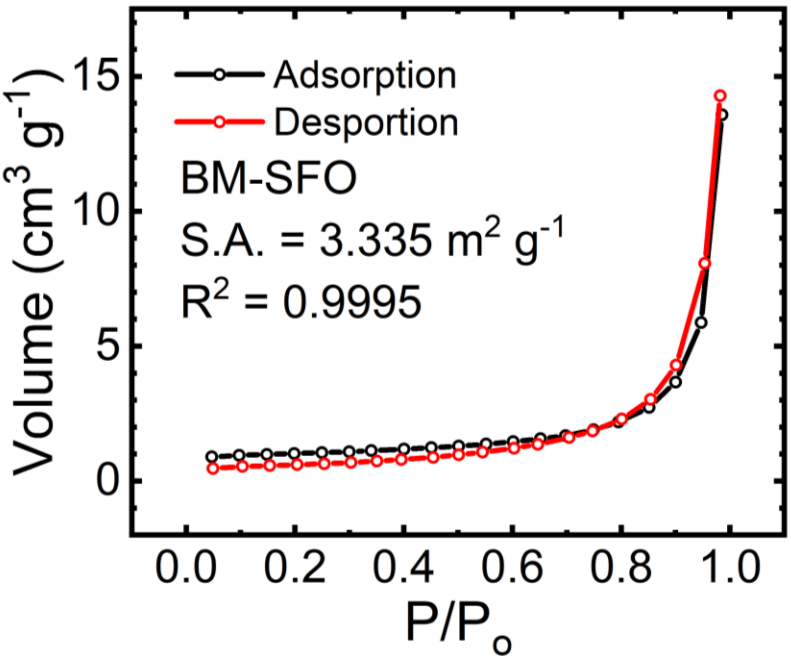

Figure A26 | Sample BET curve of perovskite sample.

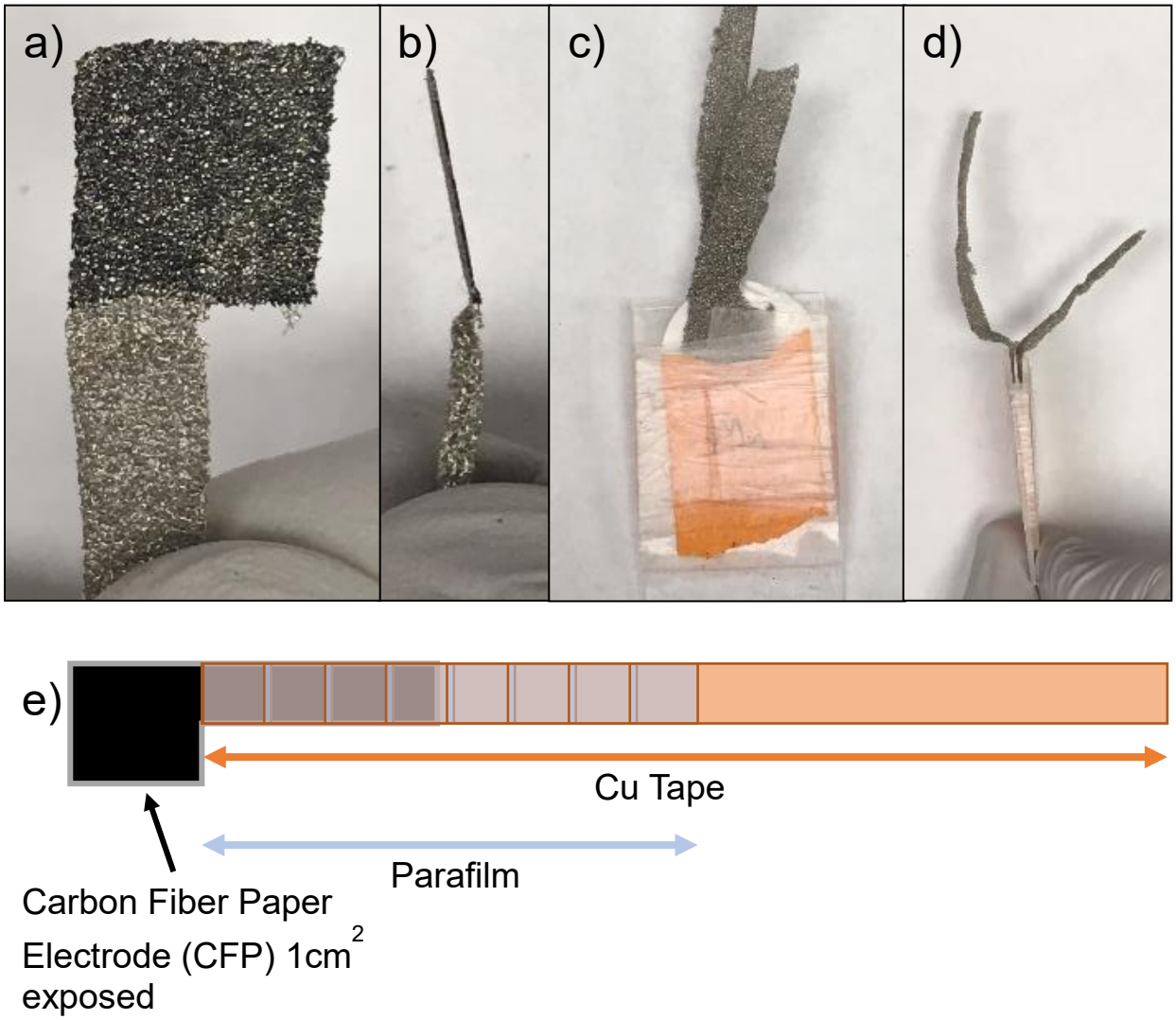

Figure A27 | Ni Foam and Carbon Fiber Paper electrode setup for two-electrode measurements.

(a) Front and (b) side view of pressed Ni foam electrode with 1 mg cm^{-2} of perovskite-carbon composite on the 1 cm^2 square pressed to ~0.1 mm thickness. (c) Front and (d) side view of two Ni foam electrodes sandwiched between two glass slides held together by Parafilm with a glass fiber separator between the Ni foam electrodes to prevent a short-circuit. (e) Schematic of Carbon Fiber Paper cut to have a 1 cm^2 square with a 2 cm long arm stuck onto copper tape followed by wrapping the arm and copper tape with Parafilm to ensure only the square material contacted the electrolyte.

Sample	Surface Area [$m^2 g^{-1}$]
BM-SFO	3.3
LSMO28	14.3
SCO	1.9

Table A15 | BET Surface Areas of Asymmetric Pseudocapacitor Materials

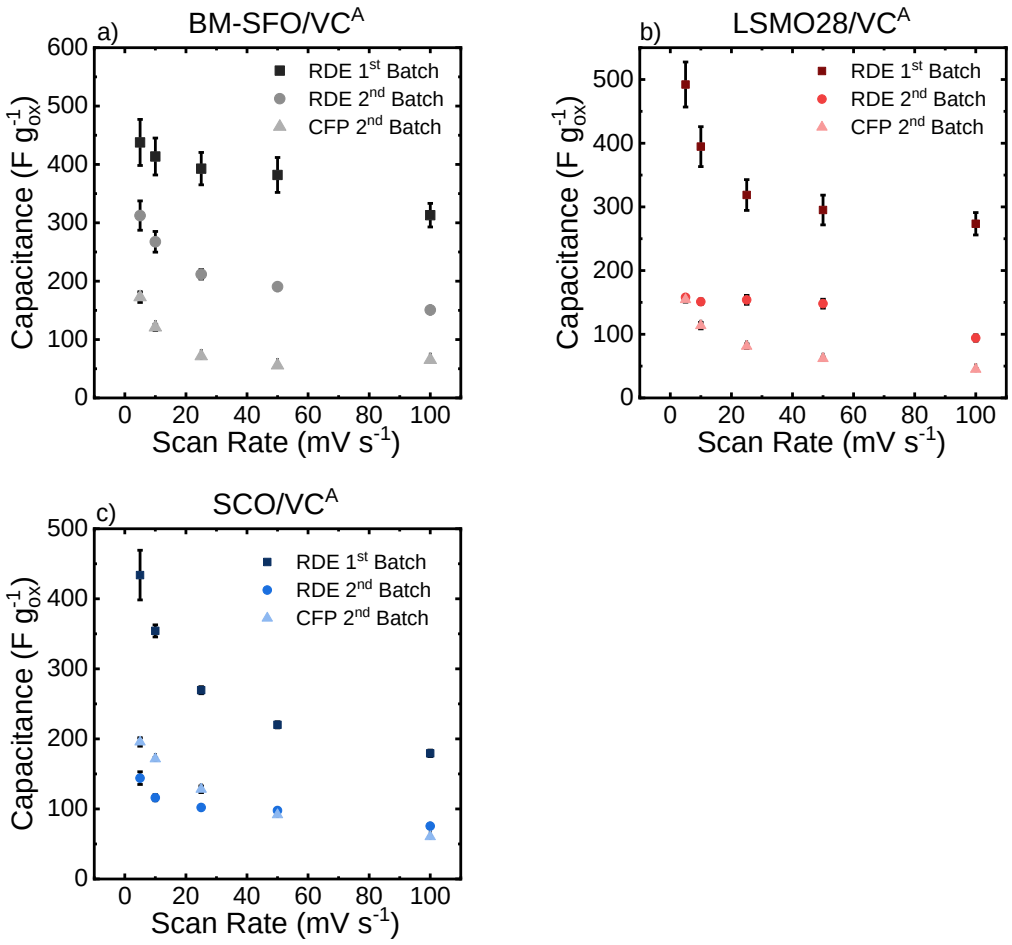

Figure A28 | Comparing CFP materials pseudocapacitance.

The three-electrode pseudocapacitance of (a) BM-SFO, (b) LSMO28 and (c) SCO is compared between the materials presented in the discussion earlier (squares) with a second batch of materials with the same A and B-site composition, but different surface areas (circles) at 0.051 mg cm^{-2} loading on RDEs and their performance on carbon fiber paper at 1 mg cm^{-2} loading (triangles).

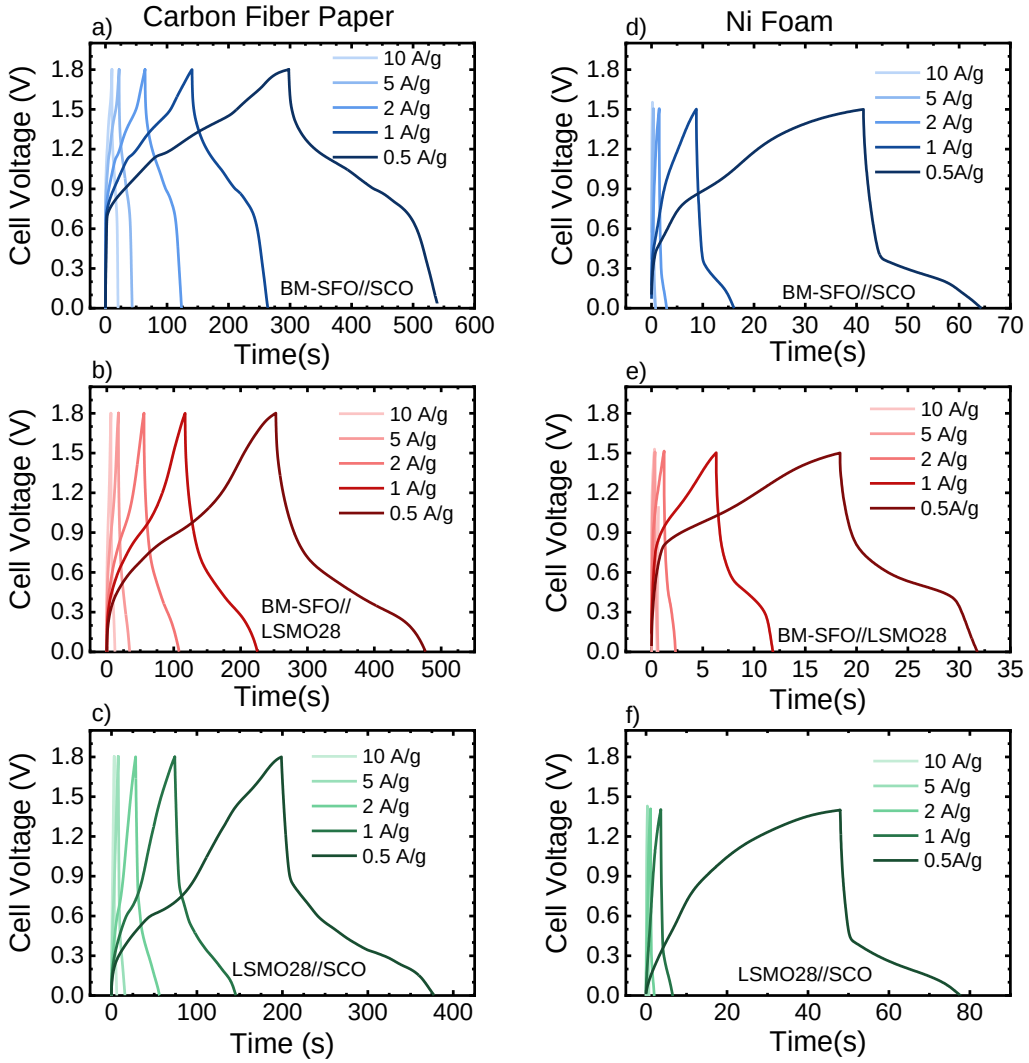

Figure A29 | Galvanostatic charge-discharge curves of asymmetric pseudocapacitors.

Constant current charge-discharge curves of (a,d) BM-SFO//SCO, (b,e) LSMO28//SCO (c,f) BM-SFO//LSMO28 asymmetric pseudocapacitors on (a-c) carbon fiber paper (CFP) and (d-f) Ni foam with the nomenclature represented as 'anode material//cathode material'. The asymmetric pseudocapacitors were made from either CFP or Ni foam electrodes with 1 mg cm^{-2} mass loading of 85:15 perovskite:carbon weight ratio composite tested in Ar-saturated 1 M KOH solution.

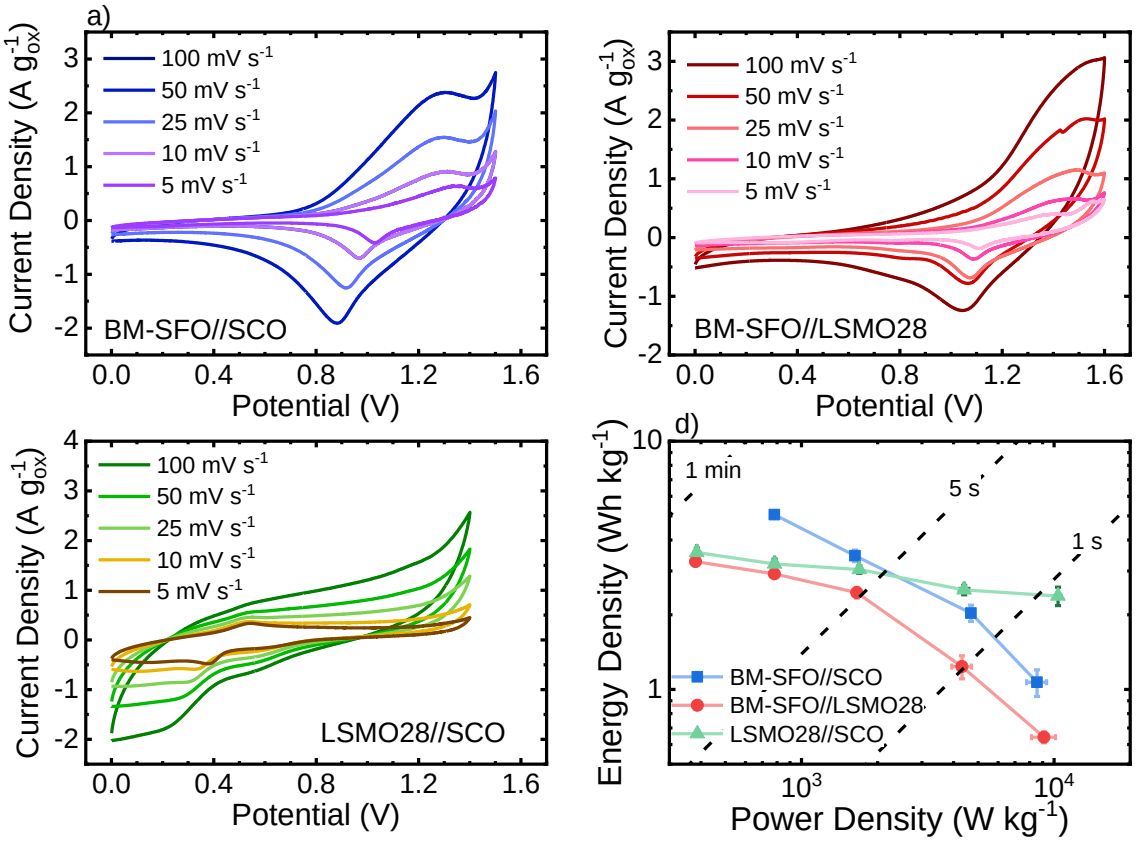

Figure A30 | Asymmetric pseudocapacitor cyclic voltammetry of $SrCoO_{2.7}$, $La_{0.2}Sr_{0.8}MnO_{2.7}$, BM-$Sr_2Fe_2O_5$ permutations on Ni Foam.

CVs at various scan rates taken in Ar-saturated 1 M KOH on Ni foam with 1 mg cm^{-2} mass loading of (a) BM-SFO//SCO, (b) LSMO28//SCO and (c) BM-SFO//LSMO28 with the notation given as Anode//Cathode. A (d) Ragone plot is given to compare energy and power density characteristics between the devices.

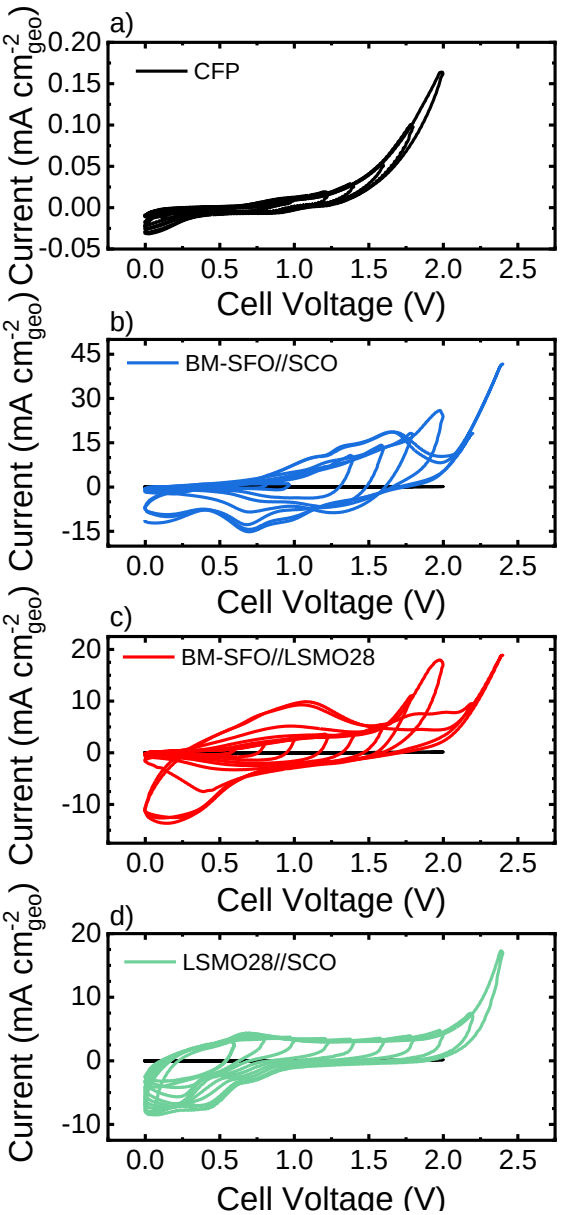

Figure A31 | Voltage Window Determination of CFP Asymmetric Pseudocapacitors.

Cyclic Voltammograms of (a) CFP, (b) BM-SFO//SCO, (c) BM-SFO//LSMO28 and (d) LSMO28//SCO asymmetric pseudocapacitors were run in Ar-saturated 1 M KOH at 100 mV s^{-1} with 1 mg cm^{-2} mass loading to determine the devices' voltage window by increasing the window width by 200 mV every cycle. The voltage window was chosen by identifying the potential on the back scan that gave 0.5 A g^{-1} anodic current.

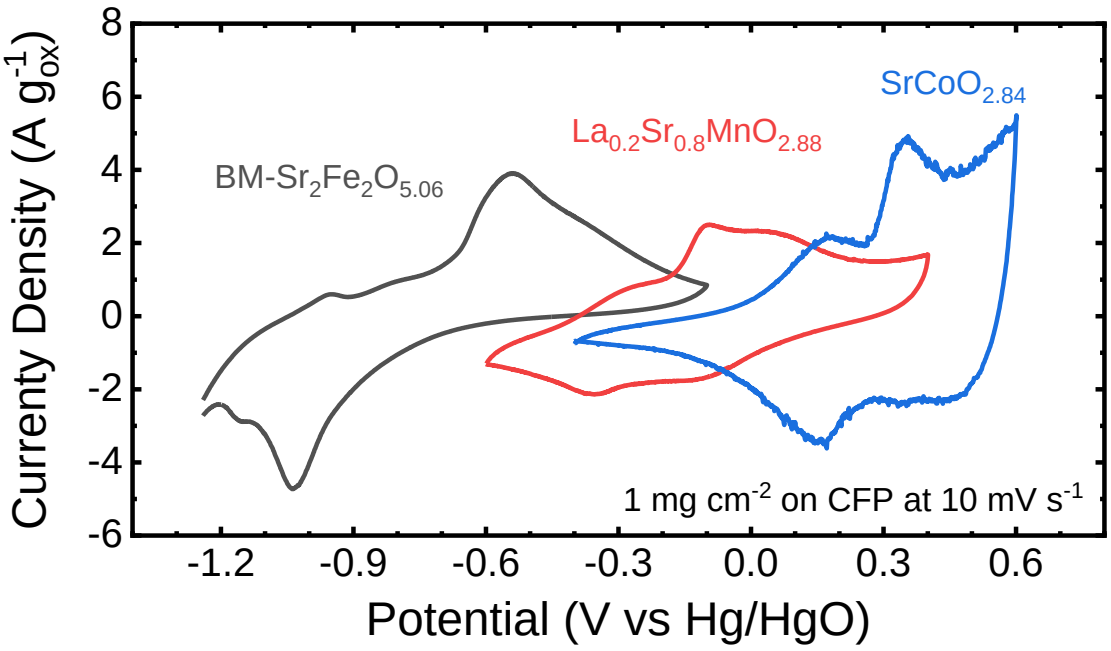

Figure A32 | Electrochemical Comparison of BM-SFO, LSMO28 and SCO on Carbon Fiber Paper in Ar-saturated 1 M KOH.

A3.2: Carbon Fiber Paper Current Collector Suggestions for improvement

While the reported energy densities for the asymmetric pseudocapacitors are high, they are lower than we expected based on our previous results for $LaMnO_3$.[2] This can be partially accounted for by the lower voltage window due to the higher catalytic activity towards the OER as a result of increasing oxygen vacancies from Sr^{2+} doping,[3] but it is most likely due to a combination of (1) the lower carbon loading in this work relative to our previous paper (15 wt.% VC^A vs. 70 wt.% N-doped carbon),[2] (2) CFP having much lower pore volume than Ni foam and (3) bubble formation on the CFP electrodes as the electrodes were cycled.

Less carbon present in the electrode would mean less perovskite that is electrically connected to the system to be utilized for charge storage. Lower pore volume in the CFP relative to Ni foam means the electroactive material has less current collector area and less electrolyte surface area to contact thus leading to mass transfer resistances and poor material utilization. Lastly, small bubbles that form and do not readily leave the electrode surface will block electrolyte from contacting the electroactive material and hinder material utilization. Despite these challenges, we have demonstrated three different all-perovskite asymmetric pseudocapacitors with a high 31 Wh kg^{-1} energy density which can be improved further by solving these issues and additionally increasing the perovskite oxygen vacancy content and surface area in the future.

A3.3: References

(1) Liu, T.-C.; Pell, W. G.; Conway, B. E.; Roberson, S. L. Behavior of Molybdenum Nitrides as Materials for Electrochemical Capacitors Comparison with Ruthenium Oxide. *J. Electrochem. Soc.* **1998**, *145* (6), 1882–1888. https://doi.org/10.1149/1.1838571.

(2) Mefford, J. T.; Hardin, W. G.; Dai, S.; Johnston, K. P.; Stevenson, K. J. Anion Charge Storage through Oxygen Intercalation in LaMnO3 Perovskite Pseudocapacitor Electrodes. *Nat. Mater.* **2014**, *13* (7), 726–732. https://doi.org/10.1038/nmat4000.

(3) Mefford, J. T.; Rong, X.; Abakumov, A. M.; Hardin, W. G.; Dai, S.; Kolpak, A. M.; Johnston, K. P.; Stevenson, K. J. Water Electrolysis on La1-xSrxCoO3-δ Perovskite Electrocatalysts. *Nat. Commun.* **2016**, *7*, 11053. https://doi.org/10.1038/ncomms11053.

APPENDIX 4: $LaNi_{1-x}Fe_xO_{3-\Delta}$ AND $SrFeO_{2.5}$ PEROVSKITES FOR HIGH POWER ASYMMETRIC AND SYMMETRIC PSEUDOCAPACITORS

Sample	Space Group	Crystal System	a(Å)	b(Å)	c(Å)
LNF00	R-3c	Rhombohedral	5.4524	-	13.1572
LNF15	Pbnm	Orthorhombic	5.526	5.495	7.786
LNF55	Pm-3m	Cubic	3.89	-	-
BM-SFO	Icmm	Orthorhombic	5.6727	15.582	5.5303

Table A16 | Perovskite X-Ray Crystallography parameters

Samples	BET Area (m2/g)
$LaNiO_3$	9.323
$LaNi_{0.85}Fe_{0.15}O_3$	10.19
$LaNi_{0.45}Fe_{0.55}O_3$	12.49
BM-$SrFeO_{2.5}$	2.904

Table A17 | BET Surface Areas

Sample	δ			z+		
LNF00	0.235	±	0.009	2.53	±	0.02
LNF15	0.105	±	0.008	2.79	±	0.02
LNF55	-0.11	±	0.02	3.22	±	0.04
BM-SFO	0.45	±	0.05	3.09	±	0.09

Table A18 | Iodometric Titration Results

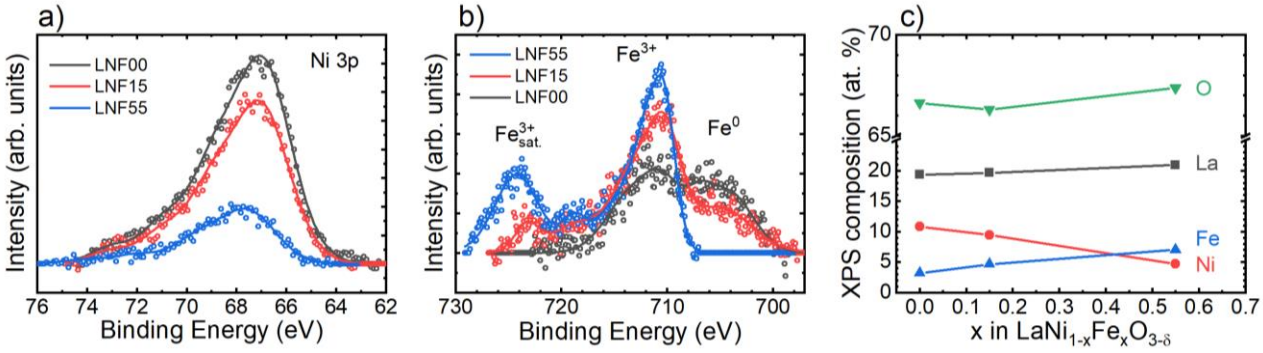

Figure A33 | X-Ray Photoelectron Spectroscopy Characterization.

The high resolution XPS spectra of the LNF series' (a) Ni 3p and (b) Fe 2p regions are shown in addition to (c) the surface atomic composition.

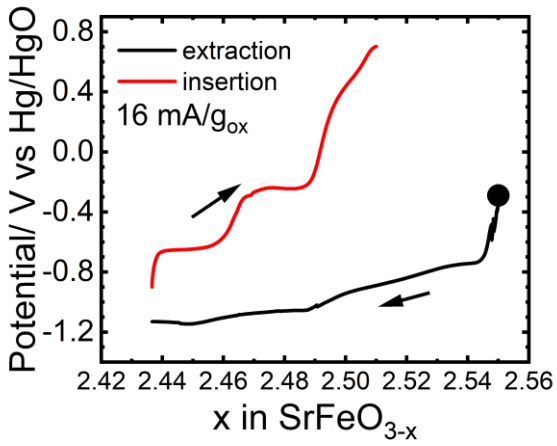

Figure A34 | BM-$SrFeO_{2.5}$ constant current test.

A 16 mg g_{ox}^{-1} constant current was applied to BM-SFO/VC^{A} supported on a glassy carbon rotating disc electrode (51 µg cm^{-2} loading) in an Ar-saturated 1 M KOH solution.

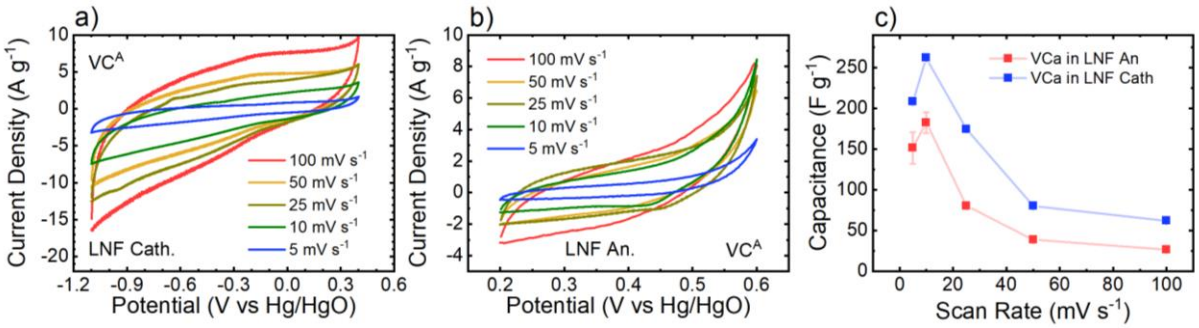

Figure A35 | Cyclic Voltammograms of activated Vulcan Carbon (VC^A).

CVs of VC^A in the (a) cathodic and (b) anodic regions are shown at various scan rates in Ar-saturated 1 M KOH at 7.65 µg cm^{-2} mass loading-the same carbon mass in the perovskite-carbon composite- with the (c) corresponding capacitance values shown.

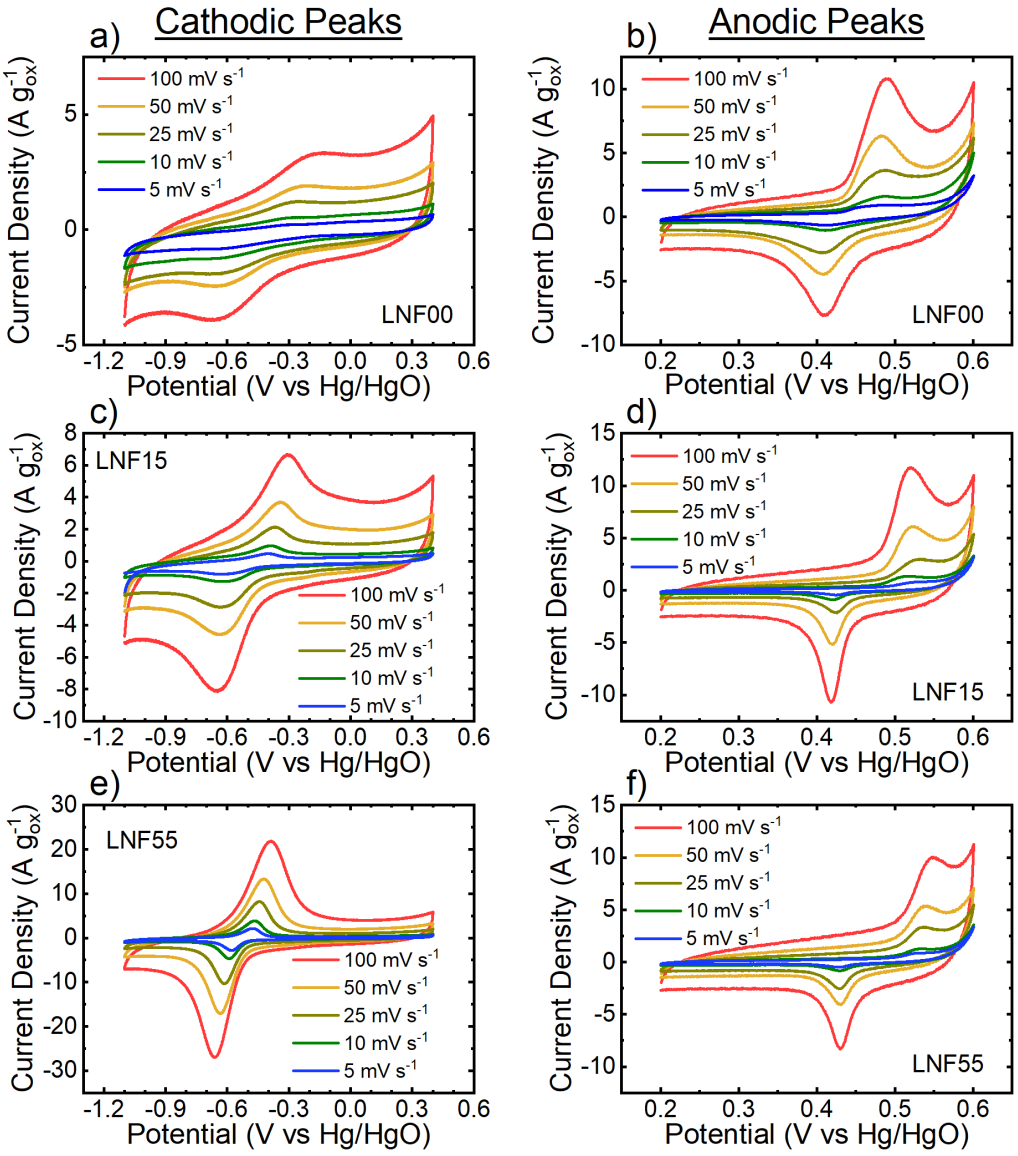

Figure A36 | Cyclic Voltammograms of $LaNi_{1-x}Fe_xO_{3-\delta}$ series.

CVs were taken in Ar-saturated 1 M KOH at 100, 50, 25, 10 and 5 mV s^{-1} scan rates of (a,b) LNF00, (c,d) LNF15 and (e,f) LNF55 which were in an 85:15 perovskite: VC^A weight ratio at 51 µg cm^{-2} mass loading.

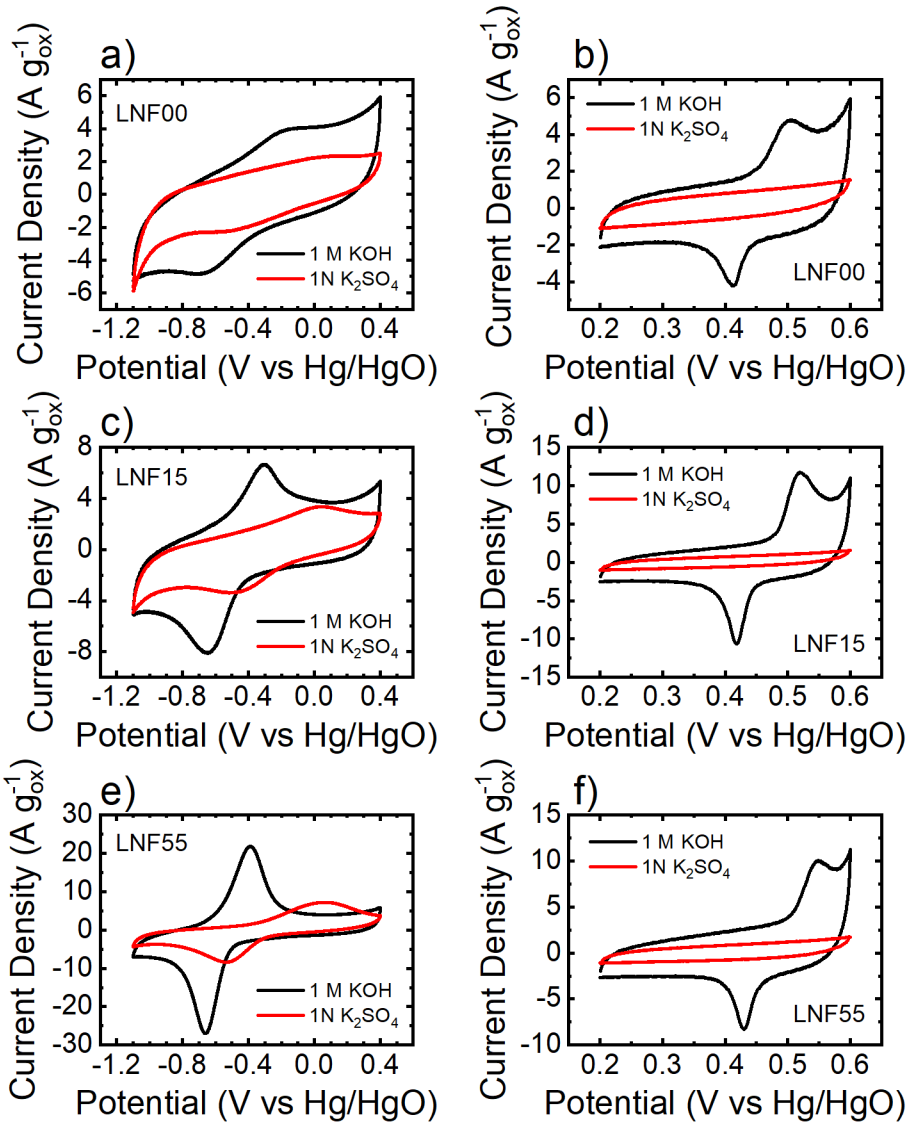

Figure A37 | Anion Intercalation determination.

Cyclic voltammograms are shown of (a, b) LNF00, (c, d) LNF15 and (e, f) LNF55 in 1 M KOH and 1 N K_2SO_4 cycled at 100 mV s^{-1}. The perovskites' redox peaks are significantly diminished, and the cathodic peaks are shifted to higher potentials which indicates a OH^- participation in these redox reactions.

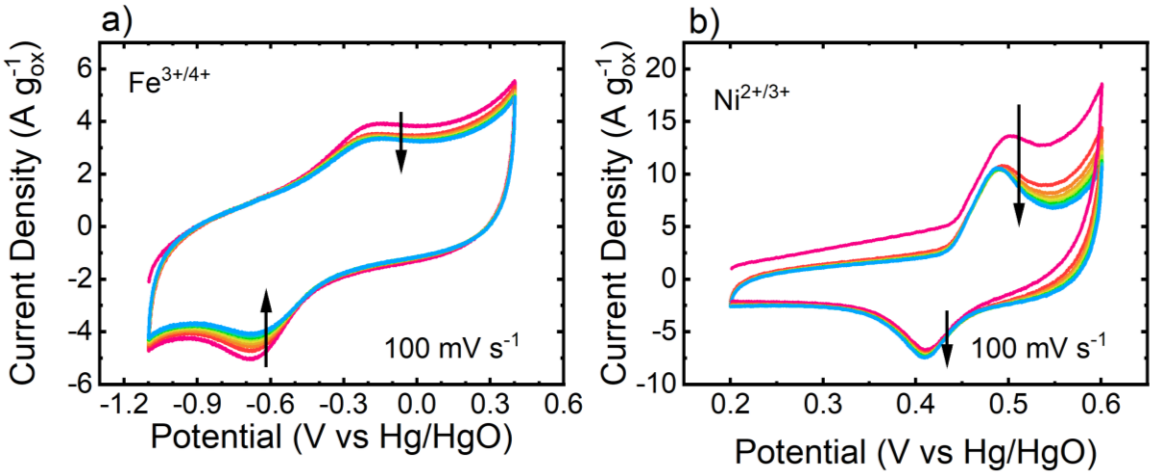

Figure A38 | LNF00 cycling.

Cyclic voltammograms of the LNF00 (a) $Fe^{3+/4+}$ and (b) $Ni^{2+/3+}$ redox peaks at 100 mV s^{-1} in Ar-saturated 1 M KOH for 10 cycles.

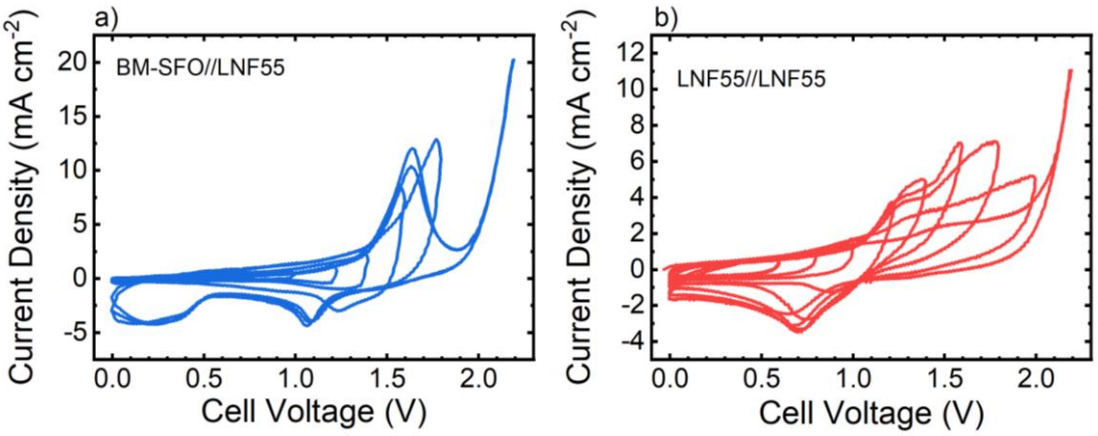

Figure A39 | Voltage Window Determination of Asymmetric and Symmetric Pseudocapacitors.

CVs with increasing potential window size were taken for the (a) BM-SFO//LNF55 asymmetric pseudocapacitor and the (b) LNF55//LNF55 symmetric pseudocapacitor. Active material was loaded onto carbon fiber paper at 1 mg_{tot} cm^{-2} loading and the potential was swept at 100 mV s^{-1} in Ar-saturated 1 M KOH.

Bibliography

(1) Intergovernmental Panel on Climate Change. *Global Warming of 1.5°C*; 2018.
(2) EIA - International Energy Outlook 2017 https://www.eia.gov/outlooks/archive/ieo17/ (accessed Apr 11, 2019).
(3) Ritchie, H.; Roser, M. Renewable Energy. *Our World Data* **2017**.
(4) O'Hayre, R. P.; Cha, S.-W.; Colella, W. G.; Prinz, F. B. *Fuel Cell Fundamentals*, Third edition.; Wiley: Hoboken, New Jersey, 2016.
(5) Bard, A. J. *Electroanalytical Chemistry: A Series of Advances:*; CRC Press, 1990.
(6) Smith, T. J.; Stevenson, K. J. Reference Electrodes. In *Handbook of Electrochemistry*; Elsevier, 2007; pp 73–110.
(7) Conway, B. E. *Electrochemical Supercapacitors: Scientific Fundamentals and Technological Applications*; Springer Science & Business Media, 2013.
(8) Conway, B. E. Two-Dimensional and Quasi-Two-Dimensional Isotherms for Li Intercalation and Upd Processes at Surfaces. *Electrochimica Acta* **1993**, *38* (9), 1249–1258. https://doi.org/10.1016/0013-4686(93)80055-5.
(9) Frackowiak, E.; Béguin, F. Carbon Materials for the Electrochemical Storage of Energy in Capacitors. *Carbon* **2001**, *39* (6), 937–950. https://doi.org/10.1016/S0008-6223(00)00183-4.
(10) Simon, P.; Gogotsi, Y. Materials for Electrochemical Capacitors. *Nat. Mater.* **2008**, *7* (11), 845–854. https://doi.org/10.1038/nmat2297.
(11) Engelsmann, K.; Lorenz, W. J.; Schmidt, E. Underpotential Deposition of Lead on Polycrystalline and Single-Crystal Gold Surfaces: Part I. Thermodynamics. *J. Electroanal. Chem. Interfacial Electrochem.* **1980**, *114* (1), 1–10. https://doi.org/10.1016/S0022-0728(80)80431-1.
(12) Gloaguen, F.; Léger, J.-M.; Lamy, C. An Electrochemical Quartz Crystal Microbalance Study of the Hydrogen Underpotential Deposition at a Pt Electrode. *J. Electroanal. Chem.* **1999**, *467* (1), 186–192. https://doi.org/10.1016/S0022-0728(98)00448-3.
(13) Tripković, A. V.; Popović, K. D.; Momčilović, J. D.; Dražić, D. M. Kinetic and Mechanistic Study of Methanol Oxidation on a Pt(100) Surface in Alkaline media1Dedicated to Professor Aleksandar R. Despić on the Occasion of His 70th birthday.1. *J. Electroanal. Chem.* **1998**, *448* (2), 173–181. https://doi.org/10.1016/S0022-0728(97)00141-1.
(14) Conway, B. E. Transition from "Supercapacitor" to "Battery" Behavior in Electrochemical Energy Storage. *J. Electrochem. Soc.* **1991**, *138* (6), 1539–1548. https://doi.org/10.1149/1.2085829.
(15) Brousse, T.; Bélanger, D.; Long, J. W. To Be or Not To Be Pseudocapacitive? *J. Electrochem. Soc.* **2015**, *162* (5), A5185–A5189. https://doi.org/10.1149/2.0201505jes.
(16) Conway, B. E.; Birss, V.; Wojtowicz, J. The Role and Utilization of Pseudocapacitance for Energy Storage by Supercapacitors. *J. Power Sources* **1997**, *66* (1–2), 1–14.

(17) Mefford, J. T.; Hardin, W. G.; Dai, S.; Johnston, K. P.; Stevenson, K. J. Anion Charge Storage through Oxygen Intercalation in LaMnO3 Perovskite Pseudocapacitor Electrodes. *Nat. Mater.* **2014**, *13* (7), 726–732. https://doi.org/10.1038/nmat4000.
(18) Christensen, J.; Albertus, P.; Sanchez-Carrera, R. S.; Lohmann, T.; Kozinsky, B.; Liedtke, R.; Ahmed, J.; Kojic, A. A Critical Review of Li/Air Batteries. *J. Electrochem. Soc.* **2011**, *159* (2), R1–R30. https://doi.org/10.1149/2.086202jes.
(19) Rahman, M. A.; Wang, X.; Wen, C. High Energy Density Metal-Air Batteries: A Review. *J. Electrochem. Soc.* **2013**, *160* (10), A1759–A1771. https://doi.org/10.1149/2.062310jes.
(20) Chen, Z.; Higgins, D.; Yu, A.; Zhang, L.; Zhang, J. A Review on Non-Precious Metal Electrocatalysts for PEM Fuel Cells. *Energy Environ. Sci.* **2011**, *4* (9), 3167. https://doi.org/10.1039/c0ee00558d.
(21) Hardin, W. G.; Slanac, D. A.; Wang, X.; Dai, S.; Johnston, K. P.; Stevenson, K. J. Highly Active, Nonprecious Metal Perovskite Electrocatalysts for Bifunctional Metal–Air Battery Electrodes. *J. Phys. Chem. Lett.* **2013**, *4* (8), 1254–1259. https://doi.org/10.1021/jz400595z.
(22) Hardin, W. G.; Mefford, J. T.; Slanac, D. A.; Patel, B. B.; Wang, X.; Dai, S.; Zhao, X.; Ruoff, R. S.; Johnston, K. P.; Stevenson, K. J. Tuning the Electrocatalytic Activity of Perovskites through Active Site Variation and Support Interactions. *Chem. Mater.* **2014**, *26* (11), 3368–3376. https://doi.org/10.1021/cm403785q.
(23) Mefford, J. T.; Rong, X.; Abakumov, A. M.; Hardin, W. G.; Dai, S.; Kolpak, A. M.; Johnston, K. P.; Stevenson, K. J. Water Electrolysis on La1-xSrxCoO3-δ Perovskite Electrocatalysts. *Nat. Commun.* **2016**, *7*, 11053. https://doi.org/10.1038/ncomms11053.
(24) Rong, X.; Parolin, J.; Kolpak, A. M. A Fundamental Relationship between Reaction Mechanism and Stability in Metal Oxide Catalysts for Oxygen Evolution. *ACS Catal.* **2016**, *6* (2), 1153–1158. https://doi.org/10.1021/acscatal.5b02432.
(25) Grimaud, A.; Diaz-Morales, O.; Han, B.; Hong, W. T.; Lee, Y.-L.; Giordano, L.; Stoerzinger, K. A.; Koper, M. T. M.; Shao-Horn, Y. Activating Lattice Oxygen Redox Reactions in Metal Oxides to Catalyse Oxygen Evolution. *Nat. Chem.* **2017**, *9*, 457. https://doi.org/10.1038/nchem.2695.
(26) Maiyalagan, T.; Jarvis, K. A.; Therese, S.; Ferreira, P. J.; Manthiram, A. Spinel-Type Lithium Cobalt Oxide as a Bifunctional Electrocatalyst for the Oxygen Evolution and Oxygen Reduction Reactions. *Nat. Commun.* **2014**, *5*, 3949. https://doi.org/10.1038/ncomms4949.
(27) Lovreček, B.; Batinic, M.; Čaja, J. The Electrochemical Oxygen Reduction on the Graphite Electrode. *Electrochimica Acta* **1983**, *28* (5), 685–690. https://doi.org/10.1016/0013-4686(83)85065-8.
(28) Maldonado, S.; Stevenson, K. J. Influence of Nitrogen Doping on Oxygen Reduction Electrocatalysis at Carbon Nanofiber Electrodes. *J. Phys. Chem. B* **2005**, *109* (10), 4707–4716. https://doi.org/10.1021/jp044442z.

(29) Wiggins-Camacho, J. D.; Stevenson, K. J. Mechanistic Discussion of the Oxygen Reduction Reaction at Nitrogen-Doped Carbon Nanotubes. *J. Phys. Chem. C* **2011**, *115* (40), 20002–20010. https://doi.org/10.1021/jp205336w.
(30) Yeager, E. Electrocatalysts for O2 Reduction. *Electrochimica Acta* **1984**, *29* (11), 1527–1537. https://doi.org/10.1016/0013-4686(84)85006-9.
(31) Poux, T.; Napolskiy, F. S.; Dintzer, T.; Kéranguéven, G.; Istomin, S. Y.; Tsirlina, G. A.; Antipov, E. V.; Savinova, E. R. Dual Role of Carbon in the Catalytic Layers of Perovskite/carbon Composites for the Electrocatalytic Oxygen Reduction Reaction. *Catal. Today* **2012**, *189* (1), 83–92. https://doi.org/10.1016/j.cattod.2012.04.046.
(32) Matsumoto, Y.; Sato, E. Electrocatalytic Properties of Transition Metal Oxides for Oxygen Evolution Reaction. *Mater. Chem. Phys.* **1986**, *14* (5), 397–426.
(33) Bockris, J. O.; Otagawa, T. The Electrocatalysis of Oxygen Evolution on Perovskites. *J. Electrochem. Soc.* **1984**, *131* (2), 290–302. https://doi.org/10.1149/1.2115565.
(34) Richter, J.; Holtappels, P.; Graule, T.; Nakamura, T.; Gauckler, L. J. Materials Design for Perovskite SOFC Cathodes. *Monatshefte Für Chem. - Chem. Mon.* **2009**, *140* (9), 985–999. https://doi.org/10.1007/s00706-009-0153-3.
(35) Vazquez, S.; Lukic, S. M.; Galvan, E.; Franquelo, L. G.; Carrasco, J. M. Energy Storage Systems for Transport and Grid Applications. *IEEE Trans. Ind. Electron.* **2010**, *57* (12), 3881–3895. https://doi.org/10.1109/TIE.2010.2076414.
(36) Gorlin, Y.; Jaramillo, T. F. A Bifunctional Nonprecious Metal Catalyst for Oxygen Reduction and Water Oxidation. *J. Am. Chem. Soc.* **2010**, *132* (39), 13612–13614. https://doi.org/10.1021/ja104587v.
(37) Hwang, J.; Rao, R. R.; Giordano, L.; Katayama, Y.; Yu, Y.; Shao-Horn, Y. Perovskites in Catalysis and Electrocatalysis. *Science* **2017**, *358* (6364), 751–756.
(38) Chen, D.; Chen, C.; Baiyee, Z. M.; Shao, Z.; Ciucci, F. Nonstoichiometric Oxides as Low-Cost and Highly-Efficient Oxygen Reduction/Evolution Catalysts for Low-Temperature Electrochemical Devices. *Chem. Rev.* **2015**, *115* (18), 9869–9921. https://doi.org/10.1021/acs.chemrev.5b00073.
(39) Suntivich, J.; May, K. J.; Gasteiger, H. A.; Goodenough, J. B.; Shao-Horn, Y. A Perovskite Oxide Optimized for Oxygen Evolution Catalysis from Molecular Orbital Principles. *Science* **2011**, *334* (6061), 1383–1385. https://doi.org/10.1126/science.1212858.
(40) Nemudry, A.; Rudolf, P.; Schöllhorn, R. Topotactic Electrochemical Redox Reactions of the Defect Perovskite SrCoO2.5+x. *Chem. Mater.* **1996**, *8* (9), 2232–2238. https://doi.org/10.1021/cm950504+.
(41) Suntivich, J.; Gasteiger, H. A.; Yabuuchi, N.; Nakanishi, H.; Goodenough, J. B.; Shao-Horn, Y. Design Principles for Oxygen-Reduction Activity on Perovskite Oxide Catalysts for Fuel Cells and Metal–air Batteries. *Nat. Chem.* **2011**, *3* (7), 546–550. https://doi.org/10.1038/nchem.1069.
(42) Gong, K.; Du, F.; Xia, Z.; Durstock, M.; Dai, L. Nitrogen-Doped Carbon Nanotube Arrays with High Electrocatalytic Activity for Oxygen Reduction. *Science* **2009**, *323* (5915), 760–764. https://doi.org/10.1126/science.1168049.

(43) Zhou, M.; Wang, H.-L.; Guo, S. Towards High-Efficiency Nanoelectrocatalysts for Oxygen Reduction through Engineering Advanced Carbon Nanomaterials. *Chem. Soc. Rev.* **2016**, *45* (5), 1273–1307. https://doi.org/10.1039/C5CS00414D.
(44) Seitz, L. C.; Dickens, C. F.; Nishio, K.; Hikita, Y.; Montoya, J.; Doyle, A.; Kirk, C.; Vojvodic, A.; Hwang, H. Y.; Norskov, J. K.; et al. A Highly Active and Stable IrOx/SrIrO3 Catalyst for the Oxygen Evolution Reaction. *Science* **2016**, *353* (6303), 1011–1014. https://doi.org/10.1126/science.aaf5050.
(45) Jung, J.-I.; Risch, M.; Park, S.; Kim, M. G.; Nam, G.; Jeong, H.-Y.; Shao-Horn, Y.; Cho, J. Optimizing Nanoparticle Perovskite for Bifunctional Oxygen Electrocatalysis. *Energy Env. Sci* **2016**. https://doi.org/10.1039/C5EE03124A.
(46) Lee, D. U.; Park, M. G.; Park, H. W.; Seo, M. H.; Ismayilov, V.; Ahmed, R.; Chen, Z. Highly Active Co-Doped LaMnO 3 Perovskite Oxide and N-Doped Carbon Nanotube Hybrid Bi-Functional Catalyst for Rechargeable Zinc–air Batteries. *Electrochem. Commun.* **2015**, *60*, 38–41. https://doi.org/10.1016/j.elecom.2015.08.001.
(47) Elumeeva, K.; Masa, J.; Sierau, J.; Tietz, F.; Muhler, M.; Schuhmann, W. Perovskite-Based Bifunctional Electrocatalysts for Oxygen Evolution and Oxygen Reduction in Alkaline Electrolytes. *Electrochimica Acta* **2016**, *208*, 25–32. https://doi.org/10.1016/j.electacta.2016.05.010.
(48) Elumeeva, K.; Masa, J.; Tietz, F.; Yang, F.; Xia, W.; Muhler, M.; Schuhmann, W. A Simple Approach towards High-Performance Perovskite-Based Bifunctional Oxygen Electrocatalysts. *ChemElectroChem* **2016**, *3* (1), 138–143. https://doi.org/10.1002/celc.201500353.
(49) Zhu, Y.; Zhou, W.; Shao, Z. Perovskite/Carbon Composites: Applications in Oxygen Electrocatalysis. *small* **2017**.
(50) Liu, J.; Jin, X.; Song, W.; Wang, F.; Wang, N.; Song, Y. Facile Preparation of Modified Carbon Black-LaMnO3 Hybrids and the Effect of Covalent Coupling on the Catalytic Activity for Oxygen Reduction Reaction. *Chin. J. Catal.* **2014**, *35* (7), 1173–1188. https://doi.org/10.1016/S1872-2067(14)60066-8.
(51) Yu, P. T.; Gu, W.; Makharia, R.; Wagner, F. T.; Gasteiger, H. A. The Impact of Carbon Stability on PEM Fuel Cell Startup and Shutdown Voltage Degradation. *ECS Trans.* **2006**, *3* (1), 797–809. https://doi.org/10.1149/1.2356199.
(52) Datsyuk, V.; Kalyva, M.; Papagelis, K.; Parthenios, J.; Tasis, D.; Siokou, A.; Kallitsis, I.; Galiotis, C. Chemical Oxidation of Multiwalled Carbon Nanotubes. *Carbon* **2008**, *46* (6), 833–840. https://doi.org/10.1016/j.carbon.2008.02.012.
(53) Soares, C. O.; Silva, R. A.; Carvalho, M. D.; Jorge, M. E. M.; Gomes, A.; Rangel, C. M.; da Silva Pereira, M. I. Oxide Loading Effect on the Electrochemical Performance of LaNiO3 Coatings in Alkaline Media. *Electrochimica Acta* **2013**, *89*, 106–113. https://doi.org/10.1016/j.electacta.2012.11.040.
(54) Bauer, A.; Song, C.; Ignaszak, A.; Hui, R.; Zhang, J.; Chevallier, L.; Jones, D.; Rozière, J. Improved Stability of Mesoporous Carbon Fuel Cell Catalyst Support through Incorporation of TiO2. *Electrochimica Acta* **2010**, *55* (28), 8365–8370. https://doi.org/10.1016/j.electacta.2010.07.025.

(55) Kim, H. J.; Jackson, D. H. K.; Lee, J.; Guan, Y.; Kuech, T. F.; Huber, G. W. Enhanced Activity and Stability of TiO2-Coated Cobalt/Carbon Catalysts for Electrochemical Water Oxidation. *ACS Catal.* **2015**, *5* (6), 3463–3469. https://doi.org/10.1021/acscatal.5b00173.
(56) Maldonado, S.; Morin, S.; Stevenson, K. J. Structure, Composition, and Chemical Reactivity of Carbon Nanotubes by Selective Nitrogen Doping. *Carbon* **2006**, *44* (8), 1429–1437. https://doi.org/10.1016/j.carbon.2005.11.027.
(57) McCrory, C. C. L.; Jung, S.; Peters, J. C.; Jaramillo, T. F. Benchmarking Heterogeneous Electrocatalysts for the Oxygen Evolution Reaction. *J. Am. Chem. Soc.* **2013**, *135* (45), 16977–16987. https://doi.org/10.1021/ja407115p.
(58) Singh, C.; Shaffer, M. S.; Windle, A. H. Production of Controlled Architectures of Aligned Carbon Nanotubes by an Injection Chemical Vapour Deposition Method. *Carbon* **2003**, *41* (2), 359–368.
(59) Maldonado, S.; Stevenson, K. J. Influence of Nitrogen Doping on Oxygen Reduction Electrocatalysis at Carbon Nanofiber Electrodes. *J. Phys. Chem. B* **2005**, *109* (10), 4707–4716. https://doi.org/10.1021/jp044442z.
(60) Cushing, B. L.; Kolesnichenko, V. L.; O'Connor, C. J. Recent Advances in the Liquid-Phase Syntheses of Inorganic Nanoparticles. *Chem. Rev.* **2004**, *104* (9), 3893–3946. https://doi.org/10.1021/cr030027b.
(61) Garsany, Y.; Singer, I. L.; Swider-Lyons, K. E. Impact of Film Drying Procedures on RDE Characterization of Pt/VC Electrocatalysts. *J. Electroanal. Chem.* **2011**, *662* (2), 396–406. https://doi.org/10.1016/j.jelechem.2011.09.016.
(62) Wiberg, G. K. H.; Mayrhofer, K. J. J.; Arenz, M. Investigation of the Oxygen Reduction Activity on Silver – A Rotating Disc Electrode Study. *Fuel Cells* **2010**, *10* (4), 575–581. https://doi.org/10.1002/fuce.200900136.
(63) Schmidt, T. J.; Gasteiger, H. A.; Stäb, G. D.; Urban, P. M.; Kolb, D. M.; Behm, R. J. Characterization of High-Surface-Area Electrocatalysts Using a Rotating Disk Electrode Configuration. *J. Electrochem. Soc.* **1998**, *145* (7), 2354–2358. https://doi.org/10.1149/1.1838642.
(64) Wang, Y.; Alsmeyer, D. C.; McCreery, R. L. Raman Spectroscopy of Carbon Materials: Structural Basis of Observed Spectra. *Chem. Mater.* **1990**, *2* (5), 557–563. https://doi.org/10.1021/cm00011a018.
(65) Tuinstra, F.; Koenig, J. L. Characterization of Graphite Fiber Surfaces with Raman Spectroscopy. *J. Compos. Mater.* **1970**, *4* (4), 492–499. https://doi.org/10.1177/002199837000400405.
(66) Pantea, D.; Darmstadt, H.; Kaliaguine, S.; Sümmchen, L.; Roy, C. Electrical Conductivity of Thermal Carbon Blacks: Influence of Surface Chemistry. *Carbon* **2001**, *39* (8), 1147–1158. https://doi.org/10.1016/S0008-6223(00)00239-6.
(67) Baratto, C.; Lottici, P. P.; Bersani, D.; Antonioli, G.; Gnappi, G.; Montenero, A. Sol-Gel Preparation of α-Fe2O3 Thin Films: Structural Characterization by XAFS and Raman. *J. Sol-Gel Sci. Technol.* *13* (1–3), 667–671. https://doi.org/10.1023/A:1008694519106.

(68) Park, E.; Ostrovski, O.; Zhang, J.; Thomson, S.; Howe, R. Characterization of Phases Formed in the Iron Carbide Process by X-Ray Diffraction, Mossbauer, X-Ray Photoelectron Spectroscopy, and Raman Spectroscopy Analyses. *Metall. Mater. Trans. B 32* (5), 839–845. https://doi.org/10.1007/s11663-001-0071-1.
(69) Pels, J. R.; Kapteijn, F.; Moulijn, J. A.; Zhu, Q.; Thomas, K. M. Evolution of Nitrogen Functionalities in Carbonaceous Materials during Pyrolysis. *Carbon* **1995**, *33* (11), 1641–1653. https://doi.org/10.1016/0008-6223(95)00154-6.
(70) Biniak, S.; Szymański, G.; Siedlewski, J.; Świtkowski, A. The Characterization of Activated Carbons with Oxygen and Nitrogen Surface Groups. *Carbon* **1997**, *35* (12), 1799–1810. https://doi.org/10.1016/S0008-6223(97)00096-1.
(71) Allen, G. C.; Curtis, M. T.; Hooper, A. J.; Tucker, P. M. X-Ray Photoelectron Spectroscopy of Iron–oxygen Systems. *J. Chem. Soc. Dalton Trans.* **1974**, *0* (14), 1525–1530. https://doi.org/10.1039/DT9740001525.
(72) Marcus, P.; Grimal, J. M. The Anodic Dissolution and Passivation of NiCrFe Alloys Studied by ESCA. *Corros. Sci.* **1992**, *33* (5), 805–814.
(73) A. Jain; S.P. Ong; G. Hautier; W. Chen; W.D. Richards; S. Dacek; S. Cholia; D. Gunter; D. Skinner; G. Ceder; et al. The Materials Project: A materials genome approach to accelerating materials innovation https://materialsproject.org/#apps/pourbaixdiagram/{"chemsys"%3A["Fe"]} (accessed Oct 14, 2016).
(74) Wiggins-Camacho, J. D.; Stevenson, K. J. Effect of Nitrogen Concentration on Capacitance, Density of States, Electronic Conductivity, and Morphology of N-Doped Carbon Nanotube Electrodes. *J. Phys. Chem. C* **2009**, *113* (44), 19082–19090. https://doi.org/10.1021/jp907160v.
(75) Rice, R. J.; McCreery, R. L. Quantitative Relationship between Electron Transfer Rate and Surface Microstructure of Laser-Modified Graphite Electrodes. *Anal. Chem.* **1989**, *61* (15), 1637–1641. https://doi.org/10.1021/ac00190a010.
(76) Cline, K. K.; McDermott, M. T.; McCreery, R. L. Anomalously Slow Electron Transfer at Ordered Graphite Electrodes: Influence of Electronic Factors and Reactive Sites. *J. Phys. Chem.* **1994**, *98* (20), 5314–5319. https://doi.org/10.1021/j100071a023.
(77) Yang, Z.; Yao, Z.; Li, G.; Fang, G.; Nie, H.; Liu, Z.; Zhou, X.; Chen, X.; Huang, S. Sulfur-Doped Graphene as an Efficient Metal-Free Cathode Catalyst for Oxygen Reduction. *ACS Nano* **2012**, *6* (1), 205–211. https://doi.org/10.1021/nn203393d.
(78) Dai, L.; Xue, Y.; Qu, L.; Choi, H.-J.; Baek, J.-B. Metal-Free Catalysts for Oxygen Reduction Reaction. *Chem. Rev.* **2015**, *115* (11), 4823–4892. https://doi.org/10.1021/cr5003563.
(79) Guo, D.; Shibuya, R.; Akiba, C.; Saji, S.; Kondo, T.; Nakamura, J. Active Sites of Nitrogen-Doped Carbon Materials for Oxygen Reduction Reaction Clarified Using Model Catalysts. *Science* **2016**, *351* (6271), 361–365. https://doi.org/10.1126/science.aad0832.
(80) Yang, H. B.; Miao, J.; Hung, S.-F.; Chen, J.; Tao, H. B.; Wang, X.; Zhang, L.; Chen, R.; Gao, J.; Chen, H. M.; et al. Identification of Catalytic Sites for Oxygen

Reduction and Oxygen Evolution in N-Doped Graphene Materials: Development of Highly Efficient Metal-Free Bifunctional Electrocatalyst. *Sci. Adv.* **2016**, *2* (4), e1501122. https://doi.org/10.1126/sciadv.1501122.

(81) Terrones, M.; Ajayan, P. M.; Banhart, F.; Blase, X.; Carroll, D. L.; Charlier, J. C.; Czerw, R.; Foley, B.; Grobert, N.; Kamalakaran, R.; et al. N-Doping and Coalescence of Carbon Nanotubes: Synthesis and Electronic Properties. *Appl. Phys. A* **2002**, *74* (3), 355–361. https://doi.org/10.1007/s003390201278.

(82) Cheon, J. Y.; Kim, J. H.; Kim, J. H.; Goddeti, K. C.; Park, J. Y.; Joo, S. H. Intrinsic Relationship between Enhanced Oxygen Reduction Reaction Activity and Nanoscale Work Function of Doped Carbons. *J. Am. Chem. Soc.* **2014**, *136* (25), 8875–8878. https://doi.org/10.1021/ja503557x.

(83) Shinagawa, T.; Garcia-Esparza, A. T.; Takanabe, K. Insight on Tafel Slopes from a Microkinetic Analysis of Aqueous Electrocatalysis for Energy Conversion. *Sci. Rep.* **2015**, *5*, 13801. https://doi.org/10.1038/srep13801.

(84) Yang, H.-H.; McCreery, R. L. Elucidation of the Mechanism of Dioxygen Reduction on Metal-Free Carbon Electrodes. *J. Electrochem. Soc.* **2000**, *147* (9), 3420–3428. https://doi.org/10.1149/1.1393915.

(85) Xu, J.; Huang, W.; McCreery, R. L. Isotope and Surface Preparation Effects on Alkaline Dioxygen Reduction at Carbon Electrodes. *J. Electroanal. Chem.* **1996**, *410* (2), 235–242. https://doi.org/10.1016/0022-0728(96)04545-7.

(86) Maldonado, S.; Stevenson, K. J. Direct Preparation of Carbon Nanofiber Electrodes via Pyrolysis of Iron(II) Phthalocyanine: Electrocatalytic Aspects for Oxygen Reduction. *J. Phys. Chem. B* **2004**, *108* (31), 11375–11383. https://doi.org/10.1021/jp0496553.

(87) Forslund, R. P.; Mefford, J. T.; Hardin, W. G.; Alexander, C. T.; Johnston, K. P.; Stevenson, K. J. Nanostructured LaNiO3 Perovskite Electrocatalyst for Enhanced Urea Oxidation. *ACS Catal.* **2016**, *6* (8), 5044–5051. https://doi.org/10.1021/acscatal.6b00487.

(88) Zhou, W.; Sunarso, J. Enhancing Bi-Functional Electrocatalytic Activity of Perovskite by Temperature Shock: A Case Study of LaNiO3−δ. *J. Phys. Chem. Lett.* **2013**, *4* (17), 2982–2988. https://doi.org/10.1021/jz401169n.

(89) Lee, D. U.; Park, H. W.; Park, M. G.; Ismayilov, V.; Chen, Z. Synergistic Bifunctional Catalyst Design Based on Perovskite Oxide Nanoparticles and Intertwined Carbon Nanotubes for Rechargeable Zinc–Air Battery Applications. *ACS Appl. Mater. Interfaces* **2015**, *7* (1), 902–910. https://doi.org/10.1021/am507470f.

(90) Hu, J.; Liu, Q.; Shi, Z.; Zhang, L.; Huang, H. LaNiO 3 -Nanorod/graphene Composite as an Efficient Bi-Functional Catalyst for Zinc–air Batteries. *RSC Adv.* **2016**, *6* (89), 86386–86394. https://doi.org/10.1039/C6RA16610E.

(91) Materials Project https://materialsproject.org/#apps/pourbaixdiagram/{“chemsys”%3A[“C”]} (accessed Nov 20, 2016).

(92) Persson, K. A.; Waldwick, B.; Lazic, P.; Ceder, G. Prediction of Solid-Aqueous Equilibria: Scheme to Combine First-Principles Calculations of Solids with Experimental Aqueous States. *Phys. Rev. B* **2012**, *85* (23), 235438.
(93) Lyon, J. L.; Stevenson, K. J. Anomalous Electrochemical Dissolution and Passivation of Iron Growth Catalysts in Carbon Nanotubes. *Langmuir* **2007**, *23* (22), 11311–11318. https://doi.org/10.1021/la7019186.
(94) Miller, J. R.; Simon, P. MATERIALS SCIENCE: Electrochemical Capacitors for Energy Management. *Science* **2008**, *321* (5889), 651–652. https://doi.org/10.1126/science.1158736.
(95) Augustyn, V.; Simon, P.; Dunn, B. Pseudocapacitive Oxide Materials for High-Rate Electrochemical Energy Storage. *Energy Environ. Sci.* **2014**, *7* (5), 1597. https://doi.org/10.1039/c3ee44164d.
(96) Wang, G.; Zhang, L.; Zhang, J. A Review of Electrode Materials for Electrochemical Supercapacitors. *Chem Soc Rev* **2012**, *41* (2), 797–828. https://doi.org/10.1039/C1CS15060J.
(97) Wang, F.; Xiao, S.; Hou, Y.; Hu, C.; Liu, L.; Wu, Y. Electrode Materials for Aqueous Asymmetric Supercapacitors. *RSC Adv.* **2013**, *3* (32), 13059. https://doi.org/10.1039/c3ra23466e.
(98) Liu, Y.; Dinh, J.; Tade, M. O.; Shao, Z. Design of Perovskite Oxides as Anion-Intercalation-Type Electrodes for Supercapacitors: Cation Leaching Effect. *ACS Appl. Mater. Interfaces* **2016**, *8* (36), 23774–23783. https://doi.org/10.1021/acsami.6b08634.
(99) Zhu, L.; Liu, Y.; Su, C.; Zhou, W.; Liu, M.; Shao, Z. Perovskite SrCo0.9Nb0.1O3−δ as an Anion-Intercalated Electrode Material for Supercapacitors with Ultrahigh Volumetric Energy Density. *Angew. Chem.* **2016**, *128* (33), 9728–9731. https://doi.org/10.1002/ange.201603601.
(100) Che, W.; Wei, M.; Sang, Z.; Ou, Y.; Liu, Y.; Liu, J. Perovskite LaNiO 3-δ Oxide as an Anion-Intercalated Pseudocapacitor Electrode. *J. Alloys Compd.* **2018**, *731*, 381–388. https://doi.org/10.1016/j.jallcom.2017.10.027.
(101) Lang, X.; Mo, H.; Hu, X.; Tian, H. Supercapacitor Performance of Perovskite La $_{1-x}$ Sr $_{x}$ MnO $_{3}$. *Dalton Trans* **2017**, *46* (40), 13720–13730. https://doi.org/10.1039/C7DT03134C.
(102) Kuznetsov, D. A.; Han, B.; Yu, Y.; Rao, R. R.; Hwang, J.; Román-Leshkov, Y.; Shao-Horn, Y. Tuning Redox Transitions via Inductive Effect in Metal Oxides and Complexes, and Implications in Oxygen Electrocatalysis. *Joule* **2017**. https://doi.org/10.1016/j.joule.2017.11.014.
(103) Grenier, J.-C.; Ghodbane, S.; Demazeau, G.; Pouchard, M.; Hagenmuller, P. Le Cobaltite de Strontium Sr2Co2O5 : Caracterisation et Proprietes Magnetiques. *Mater. Res. Bull.* **1979**, *14* (6), 831–839. https://doi.org/10.1016/0025-5408(79)90145-4.
(104) Qiu, L.; Lee, T. H.; Liu, L.-M.; Yang, Y. L.; Jacobson, A. J. Oxygen Permeation Studies of SrCo0.8Fe0.2O3 − δ. *Solid State Ion.* **1995**, *76* (3), 321–329. https://doi.org/10.1016/0167-2738(94)00296-5.

(105) Laiho, R.; Lisunov, K. G.; Lähderanta, E.; Petrenko, P. A.; Salminen, J.; Stamov, V. N.; Stepanov, Y. P.; Zakhvalinskii, V. S. Low-Field Magnetic Properties of LaMnO3+δ with 0.065≤δ≤0.154. *J. Phys. Chem. Solids* **2003**, *64* (12), 2313–2319. https://doi.org/10.1016/S0022-3697(03)00266-X.
(106) Alexander, C. T.; Abakumov, A. M.; Forslund, R. P.; Johnston, K. P.; Stevenson, K. J. Role of the Carbon Support on the Oxygen Reduction and Evolution Activities in LaNiO3 Composite Electrodes in Alkaline Solution. *ACS Appl. Energy Mater.* **2018**, *1* (4), 1549–1558. https://doi.org/10.1021/acsaem.7b00339.
(107) L'vov, B. V.; Ugolkov, V. L. Peculiarities of CaCO3, SrCO3 and BaCO3 Decomposition in CO2 as a Proof of Their Primary Dissociative Evaporation. *Thermochim. Acta* **2004**, *410* (1–2), 47–55. https://doi.org/10.1016/S0040-6031(03)00372-1.
(108) Dann, S. E.; Currie, D. B.; Weller, M. T.; Thomas, M. F.; Al-Rawwas, A. D. The Effect of Oxygen Stoichiometry on Phase Relations and Structure in the System La1-xSrxFeO3-δ ($0 \leq X \leq 1$, $0 \leq \delta \leq 0.5$). *J. Solid State Chem.* **1994**, *109* (1), 134–144. https://doi.org/10.1006/jssc.1994.1083.
(109) Nemudry, A.; Weiss, M.; Gainutdinov, I.; Boldyrev, V.; Schöllhorn, R. Room Temperature Electrochemical Redox Reactions of the Defect Perovskite SrFeO2.5+x. *Chem. Mater.* **1998**, *10* (9), 2403–2411. https://doi.org/10.1021/cm980090v.
(110) Cook, R.; Sammells, A. On the Systematic Selection of Perovskite Solid Electrolytes for Intermediate Temperature Fuel Cells. *Solid State Ion.* **1991**, *45* (3–4), 311–321. https://doi.org/10.1016/0167-2738(91)90167-A.
(111) Woodward, P. M. Octahedral Tilting in Perovskites. II. Structure Stabilizing Forces. *Acta Crystallogr. B* **1997**, *53* (1), 44–66. https://doi.org/10.1107/S0108768196012050.
(112) Mitchell, J. F.; Argyriou, D. N.; Potter, C. D.; Hinks, D. G.; Jorgensen, J. D.; Bader, S. D. Structural Phase Diagram of La1-xSrxMnO3: Relationship to Magnetic and Transport Properties. *Phys. Rev. B* **1996**, *54* (9), 6172–6183. https://doi.org/10.1103/PhysRevB.54.6172.
(113) Chmaissem, O.; Dabrowski, B.; Kolesnik, S.; Mais, J.; Jorgensen, J. D.; Short, S. Structural and Magnetic Phase Diagrams of La 1 − X Sr X MnO 3 and Pr 1 − Y Sr Y MnO 3. *Phys. Rev. B* **2003**, *67* (9). https://doi.org/10.1103/PhysRevB.67.094431.
(114) James, M.; Avdeev, M.; Barnes, P.; Morales, L.; Wallwork, K.; Withers, R. Orthorhombic Superstructures within the Rare Earth Strontium-Doped Cobaltate Perovskites: Ln1−xSrxCoO3−δ (Ln=Y3+, Dy3+–Yb3+; 0.750⩽x⩽0.875). *J. Solid State Chem.* **2007**, *180* (8), 2233–2247. https://doi.org/10.1016/j.jssc.2007.04.029.
(115) Inoue, I. H. Electrostatic Carrier Doping to Perovskite Transition-Metal Oxides. *Semicond. Sci. Technol.* **2005**, *20* (4), S112–S120. https://doi.org/10.1088/0268-1242/20/4/013.
(116) Armstrong, A. R.; Holzapfel, M.; Novák, P.; Johnson, C. S.; Kang, S.-H.; Thackeray, M. M.; Bruce, P. G. Demonstrating Oxygen Loss and Associated

Structural Reorganization in the Lithium Battery Cathode Li[Ni0.2Li0.2Mn0.6]O2. *J. Am. Chem. Soc.* **2006**, *128* (26), 8694–8698. https://doi.org/10.1021/ja062027+.

(117) Tripkovic, A. V.; Popovi, K. D.; MomEilovic', J. D.; DraEi, D. M. Kinetic and Mechanistic Study of Methanol Oxidation on a Pd 111) Surface in Alkaline Media. 12.

(118) Brousse, T.; Taberna, P.-L.; Crosnier, O.; Dugas, R.; Guillemet, P.; Scudeller, Y.; Zhou, Y.; Favier, F.; Bélanger, D.; Simon, P. Long-Term Cycling Behavior of Asymmetric Activated carbon/MnO2 Aqueous Electrochemical Supercapacitor. *J. Power Sources* **2007**, *173* (1), 633–641. https://doi.org/10.1016/j.jpowsour.2007.04.074.

(119) Lankhorst, M. H. R.; Bouwmeester, H. J. M.; Verweij, H. High-Temperature Coulometric Titration of La1−xSrxCoO3−δ: Evidence for the Effect of Electronic Band Structure on Nonstoichiometry Behavior. *J. Solid State Chem.* **1997**, *133* (2), 555–567. https://doi.org/10.1006/jssc.1997.7531.

(120) Chernova, N. A.; Roppolo, M.; Dillon, A. C.; Whittingham, M. S. Layered Vanadium and Molybdenum Oxides: Batteries and Electrochromics. *J. Mater. Chem.* **2009**, *19* (17), 2526. https://doi.org/10.1039/b819629j.

(121) Brezesinski, T.; Wang, J.; Tolbert, S. H.; Dunn, B. Ordered Mesoporous α-MoO3 with Iso-Oriented Nanocrystalline Walls for Thin-Film Pseudocapacitors. *Nat. Mater.* **2010**, *9* (2), 146–151. https://doi.org/10.1038/nmat2612.

(122) Brezesinski, K.; Wang, J.; Haetge, J.; Reitz, C.; Steinmueller, S. O.; Tolbert, S. H.; Smarsly, B. M.; Dunn, B.; Brezesinski, T. Pseudocapacitive Contributions to Charge Storage in Highly Ordered Mesoporous Group V Transition Metal Oxides with Iso-Oriented Layered Nanocrystalline Domains. *J. Am. Chem. Soc.* **2010**, *132* (20), 6982–6990. https://doi.org/10.1021/ja9106385.

(123) Xiong, H.; Yildirim, H.; Shevchenko, E. V.; Prakapenka, V. B.; Koo, B.; Slater, M. D.; Balasubramanian, M.; Sankaranarayanan, S. K. R. S.; Greeley, J. P.; Tepavcevic, S.; et al. Self-Improving Anode for Lithium-Ion Batteries Based on Amorphous to Cubic Phase Transition in TiO2 Nanotubes. *J. Phys. Chem. C* **2012**, *116* (4), 3181–3187. https://doi.org/10.1021/jp210793u.

(124) Supercapacitor carbons http://dx.doi.org/10.1016/j.mattod.2013.09.005 (accessed May 16, 2018).

(125) Gu, J.; Jin, C.; Bian, Z.; Liu, X.; Li, S.; Tang, S.; Yuan, D. Asymmetric Capacitors Based on TiO<Subscript>2</Subscript> and Mesoporous MnO<Subscript>2</Subscript> Electrodes Using Neutral Aqueous Electrolyte. *J. Nanoparticle Res.* **2017**, *19* (9), 322. https://doi.org/10.1007/s11051-017-4015-3.

(126) Chen, P.-C.; Shen, G.; Shi, Y.; Chen, H.; Zhou, C. Preparation and Characterization of Flexible Asymmetric Supercapacitors Based on Transition-Metal-Oxide Nanowire/Single-Walled Carbon Nanotube Hybrid Thin-Film Electrodes. *ACS Nano* **2010**, *4* (8), 4403–4411. https://doi.org/10.1021/nn100856y.

(127) Alexander, C. T.; Mefford, J. T.; Saunders, J.; Forslund, R. P.; Johnston, K. P.; Stevenson, K. J. Anion-Based Pseudocapacitance of the Perovskite Library La1–

xSrxBO3−δ (B = Fe, Mn, Co). *ACS Appl. Mater. Interfaces* **2019**. https://doi.org/10.1021/acsami.8b19592.
(128) Zhang, S.; Pan, N. Supercapacitors Performance Evaluation. *Adv. Energy Mater.* **2015**, *5* (6), 1401401. https://doi.org/10.1002/aenm.201401401.
(129) Xing, W.; Qiao, S.; Wu, X.; Gao, X.; Zhou, J.; Zhuo, S.; Hartono, S. B.; Hulicova-Jurcakova, D. Exaggerated Capacitance Using Electrochemically Active Nickel Foam as Current Collector in Electrochemical Measurement. *J. Power Sources* **2011**, *196* (8), 4123–4127. https://doi.org/10.1016/j.jpowsour.2010.12.003.
(130) Nan, H.; Hu, X.; Tian, H. Recent Advances in Perovskite Oxides for Anion-Intercalation Supercapacitor: A Review. *Mater. Sci. Semicond. Process.* **2019**, *94*, 35–50. https://doi.org/10.1016/j.mssp.2019.01.033.
(131) Augustyn, V.; Simon, P.; Dunn, B. Pseudocapacitive Oxide Materials for High-Rate Electrochemical Energy Storage. *Energy Environ. Sci.* **2014**, *7* (5), 1597–1614. https://doi.org/10.1039/c3ee44164d.
(132) Hahn, B. P.; Long, J. W.; Rolison, D. R. Something from Nothing: Enhancing Electrochemical Charge Storage with Cation Vacancies. *Acc. Chem. Res.* **2013**, *46* (5), 1181–1191. https://doi.org/10.1021/ar200238w.
(133) Mo, H.; Nan, H.; Lang, X.; Liu, S.; Qiao, L.; Hu, X.; Tian, H. Influence of Calcium Doping on Performance of LaMnO 3 Supercapacitors. *Ceram. Int.* **2018**, *44* (8), 9733–9741. https://doi.org/10.1016/j.ceramint.2018.02.205.
(134) Zhu, L.; Liu, Y.; Su, C.; Zhou, W.; Liu, M.; Shao, Z. Perovskite SrCo0.9Nb0.1O3−δ as an Anion-Intercalated Electrode Material for Supercapacitors with Ultrahigh Volumetric Energy Density. *Angew. Chem. Int. Ed. 55* (33), 9576–9579. https://doi.org/10.1002/anie.201603601.
(135) Wang, W.; Lin, B.; Zhang, H.; Sun, Y.; Zhang, X.; Yang, H. Synthesis, Morphology and Electrochemical Performances of Perovskite-Type Oxide LaxSr1-xFeO3 Nanofibers Prepared by Electrospinning. *J. Phys. Chem. Solids* **2019**, *124*, 144–150. https://doi.org/10.1016/j.jpcs.2018.09.011.
(136) Li, Z.; Zhang, W.; Yuan, C.; Su, Y. Controlled Synthesis of Perovskite Lanthanum Ferrite Nanotubes with Excellent Electrochemical Properties. *RSC Adv.* **2017**, *7* (21), 12931–12937. https://doi.org/10.1039/C6RA27423D.
(137) Che, W.; Wei, M.; Sang, Z.; Ou, Y.; Liu, Y.; Liu, J. Perovskite LaNiO 3-δ Oxide as an Anion-Intercalated Pseudocapacitor Electrode. *J. Alloys Compd.* **2018**, *731*, 381–388. https://doi.org/10.1016/j.jallcom.2017.10.027.
(138) Ho, K.-H.; Wang, J. Hydrazine Reduction of LaNiO3 for Active Materials in Supercapacitors. *J. Am. Ceram. Soc.* **2017**, *100* (10), 4629–4637. https://doi.org/10.1111/jace.14997.
(139) Ling, T.; Da, P.; Zheng, X.; Ge, B.; Hu, Z.; Wu, M.; Du, X.-W.; Hu, W.-B.; Jaroniec, M.; Qiao, S.-Z. Atomic-Level Structure Engineering of Metal Oxides for High-Rate Oxygen Intercalation Pseudocapacitance. *Sci. Adv.* **2018**, *4* (10), eaau6261. https://doi.org/10.1126/sciadv.aau6261.
(140) Li, Z.; Zhang, W.; Wang, H.; Yang, B. Two-Dimensional Perovskite LaNiO3 Nanosheets with Hierarchical Porous Structure for High-Rate Capacitive Energy

Storage. *Electrochimica Acta* **2017**, *258*, 561–570. https://doi.org/10.1016/j.electacta.2017.11.099.

(141) Moitra, D.; Anand, C.; Ghosh, B. K.; Chandel, M.; Ghosh, N. N. One-Dimensional BiFeO3 Nanowire-Reduced Graphene Oxide Nanocomposite as Excellent Supercapacitor Electrode Material. *ACS Appl. Energy Mater.* **2018**, *1* (2), 464–474. https://doi.org/10.1021/acsaem.7b00097.

(142) Liu, Y.; Wang, Z.; Veder, J.-P. M.; Xu, Z.; Zhong, Y.; Zhou, W.; Tade, M. O.; Wang, S.; Shao, Z. Highly Defective Layered Double Perovskite Oxide for Efficient Energy Storage via Reversible Pseudocapacitive Oxygen-Anion Intercalation. *Adv. Energy Mater.* **2018**, *8* (11), 1702604. https://doi.org/10.1002/aenm.201702604.

(143) Pan, Z.; Jiang, Y.; Yang, P.; Wu, Z.; Tian, W.; Liu, L.; Song, Y.; Gu, Q.; Sun, D.; Hu, L. In Situ Growth of Layered Bimetallic ZnCo Hydroxide Nanosheets for High-Performance All-Solid-State Pseudocapacitor. *ACS Nano* **2018**, *12* (3), 2968–2979. https://doi.org/10.1021/acsnano.8b00653.

(144) Forslund, R. P.; Hardin, W. G.; Rong, X.; Abakumov, A. M.; Filimonov, D.; Alexander, C. T.; Mefford, J. T.; Iyer, H.; Kolpak, A. M.; Johnston, K. P.; et al. Exceptional Electrocatalytic Oxygen Evolution via Tunable Charge Transfer Interactions in La 0.5 Sr 1.5 Ni 1−x Fe X O 4±δ Ruddlesden-Popper Oxides. *Nat. Commun.* **2018**, *9* (1), 3150. https://doi.org/10.1038/s41467-018-05600-y.

(145) Corrigan, D. A. The Catalysis of the Oxygen Evolution Reaction by Iron Impurities in Thin Film Nickel Oxide Electrodes. *J. Electrochem. Soc.* **1987**, *134* (2), 377–384. https://doi.org/10.1149/1.2100463.

(146) Louie, M. W.; Bell, A. T. An Investigation of Thin-Film Ni–Fe Oxide Catalysts for the Electrochemical Evolution of Oxygen. *J. Am. Chem. Soc.* **2013**, *135* (33), 12329–12337. https://doi.org/10.1021/ja405351s.

(147) Cao, Y.; Lin, B.; Sun, Y.; Yang, H.; Zhang, X. Sr-Doped Lanthanum Nickelate Nanofibers for High Energy Density Supercapacitors. *Electrochimica Acta* **2015**, *174*, 41–50. https://doi.org/10.1016/j.electacta.2015.05.131.

(148) Moriga, T.; Usaka, O.; Imamura, T.; Nakabayashi, I.; Matsubara, I.; Kinouchi, T.; Kikkawa, S.; Kanamaru, F. Synthesis, Crystal Structure, and Properties of Oxygen-Deficient Lanthanum Nickelate LaNiO3−x ($0 \leq X \leq 0.5$). *Bull. Chem. Soc. Jpn.* **1994**, *67* (3), 687–693. https://doi.org/10.1246/bcsj.67.687.

(149) Crespin, M.; Levitz, P.; Gatineau, L. Reduced Forms of LaNiO 3 Perovskite. Part 1.—Evidence for New Phases: La 2 Ni 2 O 5 and LaNiO 2. *J. Chem. Soc. Faraday Trans. 2 Mol. Chem. Phys.* **1983**, *79* (8), 1181–1194.

(150) Hayward, M. A.; Green, M. A.; Rosseinsky, M. J.; Sloan, J. Sodium Hydride as a Powerful Reducing Agent for Topotactic Oxide Deintercalation: Synthesis and Characterization of the Nickel(I) Oxide LaNiO2. *J. Am. Chem. Soc.* **1999**, *121* (38), 8843–8854. https://doi.org/10.1021/ja991573i.

(151) Alonso, J. A.; Martínez-Lope, M. J. Preparation and Crystal Structure of the Deficient Perovskite LaNiO 2.5, Solved from Neutron Powder Diffraction Data. *J. Chem. Soc. Dalton Trans.* **1995**, No. 17, 2819–2824.

(152) Tassel, C.; Kageyama, H. Square Planar Coordinate Iron Oxides. *Chem. Soc. Rev.* **2012**, *41* (6), 2025–2035. https://doi.org/10.1039/C1CS15218A.
(153) Tsujimoto, Y.; Tassel, C.; Hayashi, N.; Watanabe, T.; Kageyama, H.; Yoshimura, K.; Takano, M.; Ceretti, M.; Ritter, C.; Paulus, W. Infinite-Layer Iron Oxide with a Square-Planar Coordination. *Nature* **2007**, *450* (7172), 1062–1065. https://doi.org/10.1038/nature06382.
(154) Liu, T.-C.; Pell, W. G.; Conway, B. E.; Roberson, S. L. Behavior of Molybdenum Nitrides as Materials for Electrochemical Capacitors Comparison with Ruthenium Oxide. *J. Electrochem. Soc.* **1998**, *145* (6), 1882–1888. https://doi.org/10.1149/1.1838571.
(155) Hunter, J. C. Preparation of a New Crystal Form of Manganese Dioxide: λ-MnO2. *J. Solid State Chem.* **1981**, *39* (2), 142–147.
(156) Gogotsi, Y.; Penner, R. M. Energy Storage in Nanomaterials – Capacitive, Pseudocapacitive, or Battery-Like? *ACS Nano* **2018**, *12* (3), 2081–2083. https://doi.org/10.1021/acsnano.8b01914.
(157) Bielski, B. H. J.; Allen, A. O. Mechanism of the Disproportionation of Superoxide Radicals. *J. Phys. Chem.* **1977**, *81* (11), 1048–1050. https://doi.org/10.1021/j100526a005.
(158) Jain, A.; Ong, S. P.; Hautier, G.; Chen, W.; Richards, W. D.; Dacek, S.; Cholia, S.; Gunter, D.; Skinner, D.; Ceder, G.; et al. Commentary: The Materials Project: A Materials Genome Approach to Accelerating Materials Innovation. *APL Mater.* **2013**, *1* (1), 11002. https://doi.org/10.1063/1.4812323.
(159) Lee, Y.-L.; Kleis, J.; Rossmeisl, J.; Shao-Horn, Y.; Morgan, D. Prediction of Solid Oxide Fuel Cell Cathode Activity with First-Principles Descriptors. *Energy Environ. Sci.* **2011**, *4* (10), 3966. https://doi.org/10.1039/c1ee02032c.
(160) Liu, T.-C.; Pell, W. G.; Conway, B. E.; Roberson, S. L. Behavior of Molybdenum Nitrides as Materials for Electrochemical Capacitors Comparison with Ruthenium Oxide. *J. Electrochem. Soc.* **1998**, *145* (6), 1882–1888. https://doi.org/10.1149/1.1838571.